NASA Conference Publication 3228

Space Electrochemical Research and Technology

Proceedings of a conference held at
NASA Lewis Research Center
Cleveland, Ohio
April 14–15, 1993

NASA

NASA Conference Publication 3228

Space Electrochemical Research and Technology

Proceedings of a conference held at
NASA Lewis Research Center
Cleveland, Ohio
April 14–15, 1993

NASA
National Aeronautics and
Space Administration

Office of Management

Scientific and Technical
Information Program

1993

PREFACE

This document contains the proceedings of NASA's fourth Space Electrochemical Research and Technology (SERT) Conference, held at the NASA Lewis Research Center on April 14 and 15, 1993. The objective of the conference was to assess the present status and general thrust of research and development in those areas of electrochemical technology required to enable NASA missions into the next century. The conference provided a forum for the exchange of ideas and opinions of those actively involved in the field, in order to define new opportunities for the application of electrochemical processes in future NASA missions. Papers were presented in three technical areas: advanced secondary batteries, fuel cells, and advanced concepts for space power.

SPACE ELECTROCHEMICAL RESEARCH AND TECHNOLOGY

April 14-15, 1993

Contents

Section One
Advanced Secondary Batteries

Section Two
Fuel Cells

Section Three
Advanced Concepts for Space Power

Section
One

Advanced Secondary Batteries

AEROSPACE APPLICATIONS OF BATTERIES

Shahid Habib
NASA Headquarters
Washington, DC

ABSTRACT

NASA has developed battery technology to meet the demanding requirements for aerospace applications; specifically, the space vacuum, launch loads, and high duty cycles. Because of unique requirements and operating environments associated with space applications, NASA has written its own standards and specifications for batteries.

INTRODUCTION

Since 1958, over 300 NASA spacecraft have used primary or secondary batteries. Primary batteries provide energy to critical systems on launch vehicles and portable equipment used by humans in space. Secondary battery systems supply power, usually 28 V DC, when spacecraft are in darkness. When a spacecraft is in sunlight, photovoltaic cells power the satellite and darkness. When a spacecraft is in sunlight, photovoltaic cells power the satellite and charge the secondary battery.

The orbit determines the duty cycle for a secondary battery. Low Earth orbit applications are the most demanding because the spacecraft passes through the Earth's shadow on almost every orbit. Since a typical orbit period is 95 min, the battery must be recharged rapidly. Satellites in higher orbits need batteries less frequently--these orbits have longer periods and are more often totally in sunlight. A typical spacecraft has a design lifetime of three years. (Table 1)

NASA has used nickel-cadmium batteries for over 160 satellites to low Earth orbit, geostationary orbit, and the nearby planets. Some recent NASA applications are Topex/Poseidon, the Tracking and Data Relay Satellite, and Mars Observer. The Hubble Space Telescope uses nickel-hydrogen batteries, and the Extravehicular Mobility Unit used on Shuttle missions has a silver-zinc primary battery. Descriptions of these applications follow. NASA also uses many other battery chemistries.

TOPEX/POSEIDON SPACECRAFT

To increase our understanding of global ocean circulation, the Topex/Poseidon spacecraft (Figure 1) carries two radar altimeters for making very precise measurements of sea level. The French space agency, Centre National d'Etudes Spatiales (CNES), and NASA built the altimeters. The designs permit correction of measurement errors induced by the atmosphere and ionosphere. Uncertainty in the orbital position limits the accuracy to about 14cm, even though the satellite is at a high altitude for low drag and uses both laser and microwave Doppler tracking methods. On August 10, 1992, an Ariane rocket launched Topex/Poseidon from Kourou, French Guiana into a 66 degree inclination orbit.

Topex/Poseidon uses NASA's Multimission Modular Spacecraft (MMS), a design first used in 1980 for the Solar Maximum Mission. Because the Instrument Module always faces the Earth, the single panel of solar cells that provides at least 2260 W of power has gimbals to track the

sun. The Modular Power System (MPS) contains the power conditioning electronics and three batteries with 22 NASA 50 Ah Ni-Cd cells (Figure 2). Topex/Poseidon is the sixth mission to use this battery; the first was Landsat 4 in 1982. NASA initiated the design effort for this battery in 1975. From a total production of over 1400 cells, industry has made 23 flight batteries plus 20 test or spare units. References 1 and 2 define the design. The only qualified cell supplier is Gates Aerospace Batteries.

TRACKING AND DATA RELAY SATELLITE

From its geostationary orbit the Tracking and Data Relay Satellite (TDRS) links NASA controllers on the ground with satellites in low Earth orbits (Figure 3). For example, TDRS provides voice, television, and data communications to and from the Space Shuttle. Two TDRS satellites are stationed over the Atlantic and the other two over the Pacific. Except for a small zone over the Indian Ocean, TDRS allows continuous communications between a satellite and the ground. A ground station at White Sands, New Mexico controls all four satellites. TDRS receives high rate data at up to 300 Mbps through two large K-band antennas dedicated to (pointed at) specific satellites. There is also a low rate S-band service that can be shared by up to 20 user satellites.

Each TDRS satellite has two solar arrays supplying 1700 W while tracking the sun. Three Ni-Cd batteries can supply 1400 W while TDRS is in darkness for a 1.3 hr period per day. The batteries are reconditioned by completely discharging the cells just before the two 45-day periods per year when they are needed.

MARS OBSERVER

Mars Observer began its trip to Mars in October 1992 and will arrive in August 1993 (Figure 4). After a four month period for checkout and orbit adjustments, the spacecraft will map the surface and profile the atmosphere using a complementary instrument set covering spectral regions from radio waves through gamma rays. The mapping phase will continue for at least a full Mars year or 22 months. The 117 minute mapping orbit is nearly circular and polar. Darkness periods vary seasonally between 36 and 42 minutes.

The solar array power is 1130 W when initially deployed and 930 W when fully deployed at Mars. The batteries provide approximately 500 W for the spacecraft during launch, maneuvers, orbit insertion, and occultations. There are two 42 Ah Ni-Cd batteries; the cells are similar to the NASA 50 Ah cell. Because there are only 17 cells per battery, an electronic circuit produces the desired 28 V output to the spacecraft. The backups were 37 Ah Ni-Cd batteries with an advanced design.

HUBBLE SPACE TELESCOPE

The Hubble Space Telescope (HST) (Figure 5), launched three years ago, makes observations at ultraviolet wavelengths and with higher angular resolution than any telescope that must look through the Earth's atmosphere. HST's major accomplishments include observations of the early stages of star formation, and the development of a major storm in Saturn's atmosphere. HST has a very accurate attitude control system that points the telescope toward a star, galaxy, or planet while the articulated solar arrays follow the sun. After a Shuttle servicing mission in

December 1993, HST will be more productive and reliable with its new solar arrays and gyroscopes, a new Wide Field and Planetary Camera with corrective optics for improved resolution, and separate corrective optics for the other instruments.

To meet a 15-year lifetime requirement, the original HST design had Ni-Cd batteries in units that could be replaced on orbit. Given problems with Ni-Cd batteries and a 4-year launch delay for other reasons, NASA decided to substitute Ni-H_2 batteries (Figure 6). Each of HST's 6 parallel batteries has 22 cylindrical cells. Actual capacity is 75 to 80 Ah per battery, and in normal operation the depth of discharge is less than 10 percent. NASA plans to use Ni-H_2 batteries on other large spacecraft.

EXTRAVEHICULAR MOBILITY UNIT

Astronauts performing space walks wear a special suit known as an Extravehicular Mobility Unit (EMU). This system provides essential life support--a pure oxygen environment at a differential pressure of 4.2 pounds per square inch, water vapor and carbon dioxide removal, and temperature control while the astronaut is outside the Shuttle (Figure 7). The major components of the EMU are the hard upper torso with the life support systems, lower torso (legs), arms, helmet, and liquid cooling and ventilation garment. Each component comes in several sizes that are custom fitted to astronauts. The EMU, which can be reused during a Shuttle mission, is designed for a 15-year lifetime.

A silver zinc battery provides power for monitoring and controlling the life support systems, circulating fluids, and communicating with Shuttle. The EMU has a 16.5 V (11 cell) battery rated at 27 Ah. Each EMU has a new battery that is filled and charged just before launch. The battery capacity allows continuous operation of the EMU for up to 7 hours and can be recharged in orbit with Shuttle power. A recent series of tests (5) allowed the wet life of these batteries to be extended from 135 to 166 days or about 3 Shuttle missions.

AEROSPACE FLIGHT BATTERY SYSTEMS PROGRAM

The origin of the NASA Aerospace Flight Battery Systems Program was the Administrator's concern over battery-related launch delays and even the shorting of a battery prior to a launch. NASA formed a Steering Committee in 1985 to review battery requirements for future missions and to investigate ways to increase the safety, reliability, and performance of space power systems. The Steering Committee participated in the development of a program plan for a NASA-wide effort with objectives, tasks, a budget, and a schedule.

The program objectives are to enhance cell/battery safety and reliability, maintain current battery technology, increase fundamental understanding of primary and secondary cells, support development of advanced technology for flight use, reduce battery technology related risk, and ensure that safe and reliable batteries are available for NASA's future missions. The technical approach employed in the program establishes technical guidelines for procurement, design, production, testing, and operation; opens and maintains communications lines among NASA field installations and the aerospace battery community; qualifies advanced technologies; and implements independent cell verification. The program recently redefined some tasks in response to continuing problems with the production of Ni-Cd cells.

The program's sponsor is the Engineering Division in the Office of Safety and Mission

Quality at NASA Headquarters. NASA's Lewis Research Center (LeRC) has overall program management responsibility. Specific projects (Figure 8) are assigned to various NASA field installations. The program has tasks addressing battery systems technology, secondary batteries, primary batteries, and program management. Reference 4 has a general history and overview of this program.

The Battery Systems Technology Task addresses handbooks, training, a data base, and the NASA Battery Workshops. Under this task, Goddard Space Flight Center (GSFC) is preparing a Handbook for Nickel-Hydrogen Batteries and a Handbook for the Handling and Storage of Nickel-Cadmium Batteries that will become the basis for the training effort by Kennedy Space Center (KSC). LeRC is developing the data base that will compile knowledge gained from manufacturing, ground testing, and flight experience. This effort includes a computer bulletin board for problem reporting, technical notes, test reports, and policy documents. The Marshall Space Flight Center (MSFC) conducts the NASA Aerospace Battery Workshop, (see NASA Conference Publications 3119 and 3140).

To provide independent checks and balances, NASA invested in expanded and improved battery test facilities at GSFC, the Jet Propulsion Laboratory (JPL), and the Naval Weapons Support Center in Crane, Indiana. Crane currently places its test data into a computer data base. In addition, LeRC is developing a method for non-destructive evaluation by impedance spectroscopy of secondary cells, and MSFC is establishing procedures for destructive physical analysis.

The Secondary Battery Technology Task includes both Ni-Cd and Ni-H_2 battery activities. The Ni-Cd efforts specifically address the cell quality and reliability problems that surfaced in the late 1980's. In the near term, GSFC will convert the existing NASA Ni-Cd specification, Reference 5, into a guidelines document and where necessary strengthen the technical and quality assurance requirements. Gates will manufacture cells with modified plates and separators for a statistically designed experiment that evaluates nickel attack level, positive plate loading, and negative plate loading. GSFC and Crane began testing cells developed by Hughes and SAFT about two years ago. Additional cells from SAFT and Sanyo will enter testing at Crane in 1993.

The far-term solution is advanced Ni-Cd cells with electrochemically impregnated plates and non-nylon separators (similar to the Topex backups and the Hughes cells under test at Crane) or Ni-H_2 cells. LeRC leads the effort for Ni-H_2 evaluation that demonstrated the advantages of a 26 percent KOH electrolyte concentration and a catalyzed wall wick for aerospace applications. GSFC will prepare a guideline document for Ni-H_2 cells.

JPL leads an effort to develop computer models of the Ni-Cd and Ni-H_2 electrochemical systems. The initial Ni-Cd model, available now, uses the table look-up approach to predict battery performance, specifically voltage and efficiency vs. temperature and state-of-charge. Predictions made by the second version, with a one dimensional electrochemical model, generally match test data, although the model needs some modifications and additional verifications. The goal is models that can be used to develop accelerated test methods for determining battery quality and reliability.

The objective of the Primary Battery Task is improved performance, reliability, and safety, particularly for cells used on Shuttle missions. As the leader for this task, Johnson Space Center (JSC) prepared a Primary Battery Design and Safety Handbook. JSC investigated Yardney's patented thermal short circuit protection method for Lithium K-cells but found the performance

degradation unacceptably high. Both JSC and JPL obtained promising test results on some $LiSOCl_2$ cells. JSC supported development on two $Zr-O_2$ cells with capacities of 9-12 and 150-200 Ah that exceeded performance goals for capacity and specific energy at discharge rates of 1 to 6 A.

SUMMARY

Batteries used in several current space programs are described. NASA's unique requirements for aerospace batteries have necessitated the writing of their own standards and the establishment of a Steering Committee for oversight of the requirements, safety and reliability of these systems.

REFERENCES

1. GSFC 74-150000, Specification for the Manufacturing of Aero-Space Nickel-Cadmium Storage Cells.

2. NASA 50 Ah Ni-Cd Battery Manual, NASA CR 166701.

3. EMU Ag-Zn Battery Wet-life Extension Test, in The 1991 NASA Aerospace Battery Conference, NASA Conference Publication 3140, 1992, pp. 249-260.

4. Manzo, M. and O'Donnell, P. NASA Flight Battery Program, An Update, in the 1991 NASA Aerospace Battery Conference, NASA Conference Publication 3140, 1992, pp. 7-18.

5. NHB 8073.1, NASA Specification for Manufacturing and Performance Requirements of NASA Standard Aerospace Nickel-Cadmium Cells.

FIGURES

Table 1. Typical Aerospace Battery Duty Cycles

Aerospace Application (orbit)	Minimum Charge Time	Maximum Discharge Time	Cycles per Year
Low Earth	60 min	35 min	6000
Geostationary	22.7 hr	1.3 hr	90

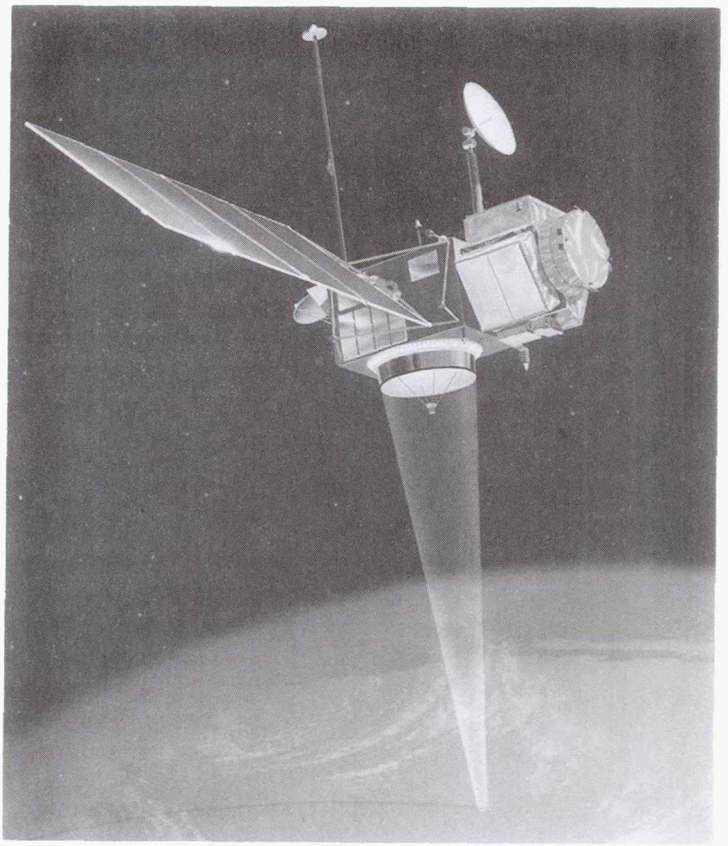

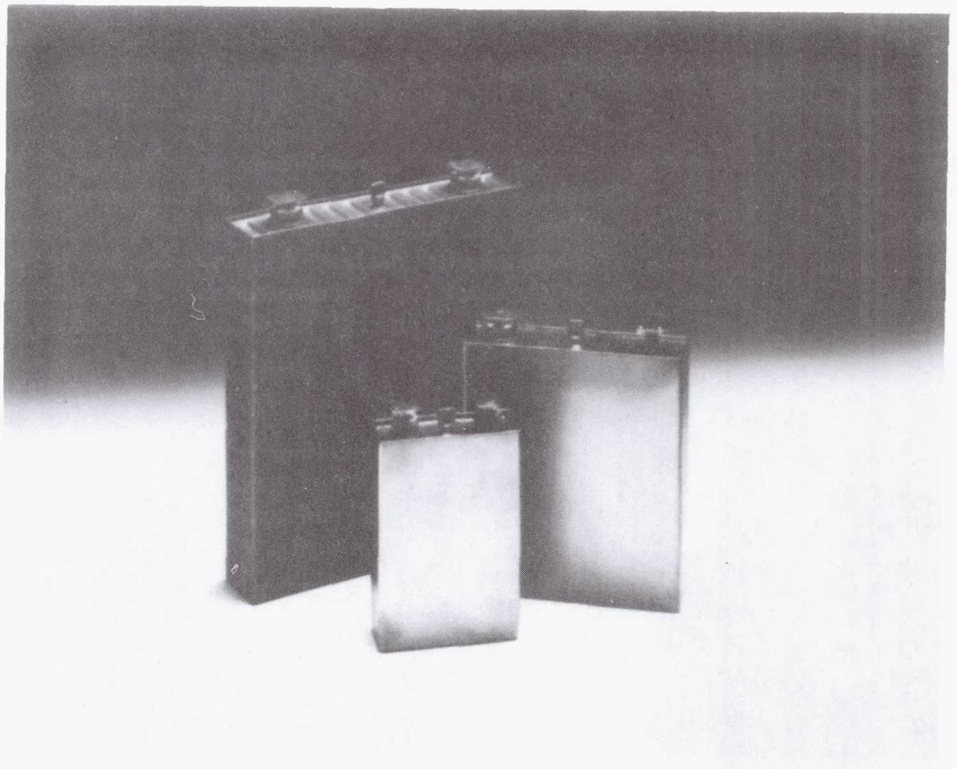

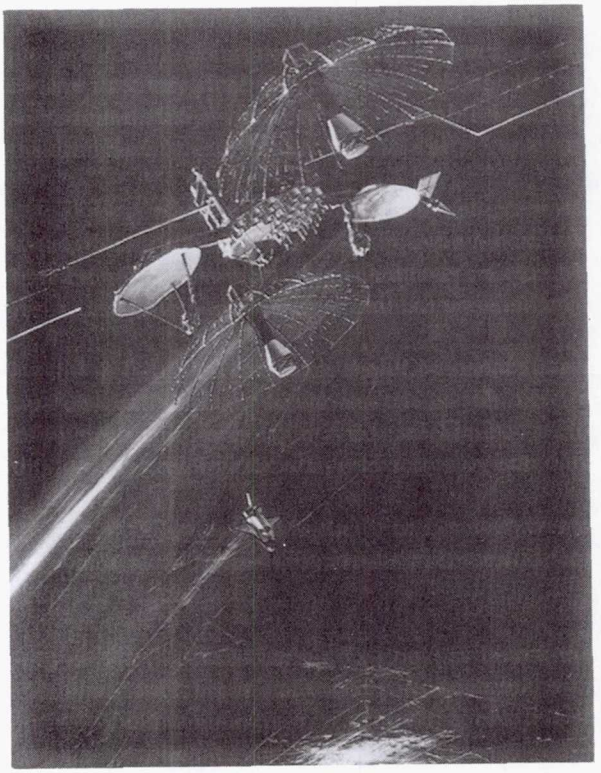

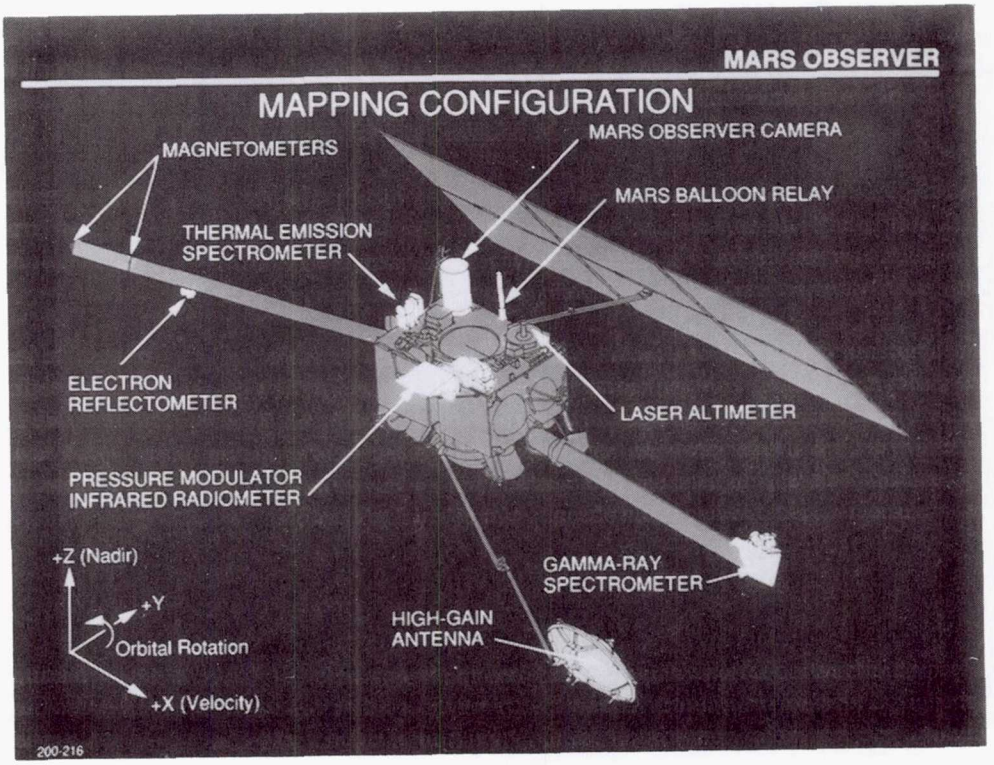
MARS OBSERVER
MAPPING CONFIGURATION
MAGNETOMETERS
MARS OBSERVER CAMERA
MARS BALLOON RELAY
THERMAL EMISSION SPECTROMETER
ELECTRON REFLECTOMETER
LASER ALTIMETER
PRESSURE MODULATOR INFRARED RADIOMETER
+Z (Nadir)
+Y
Orbital Rotation
+X (Velocity)
GAMMA-RAY SPECTROMETER
HIGH-GAIN ANTENNA
200-216

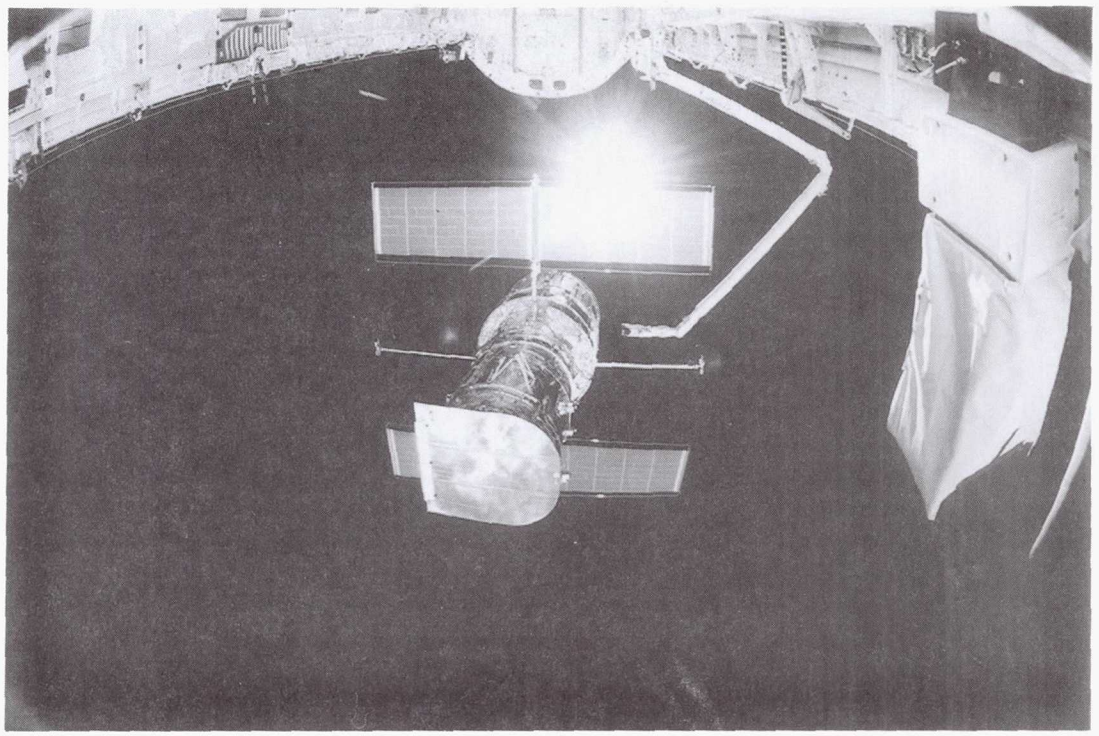

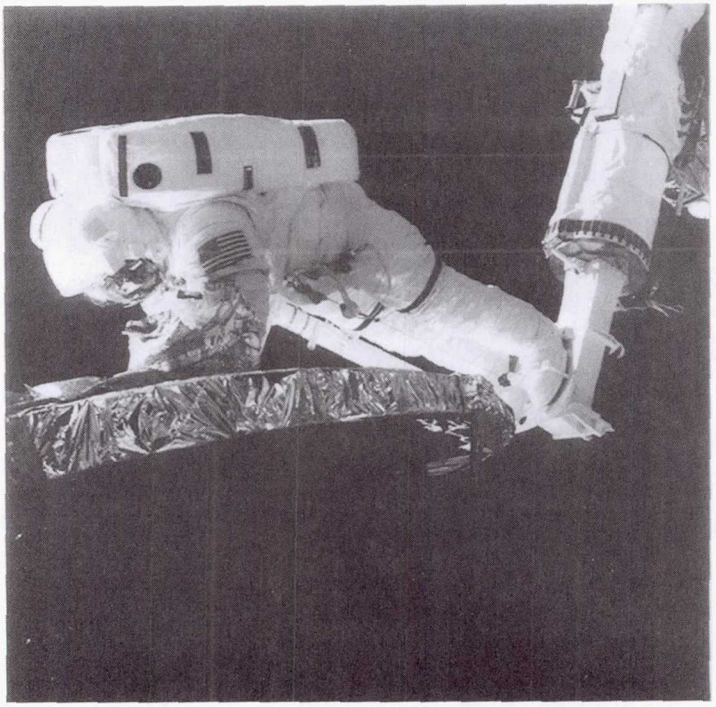

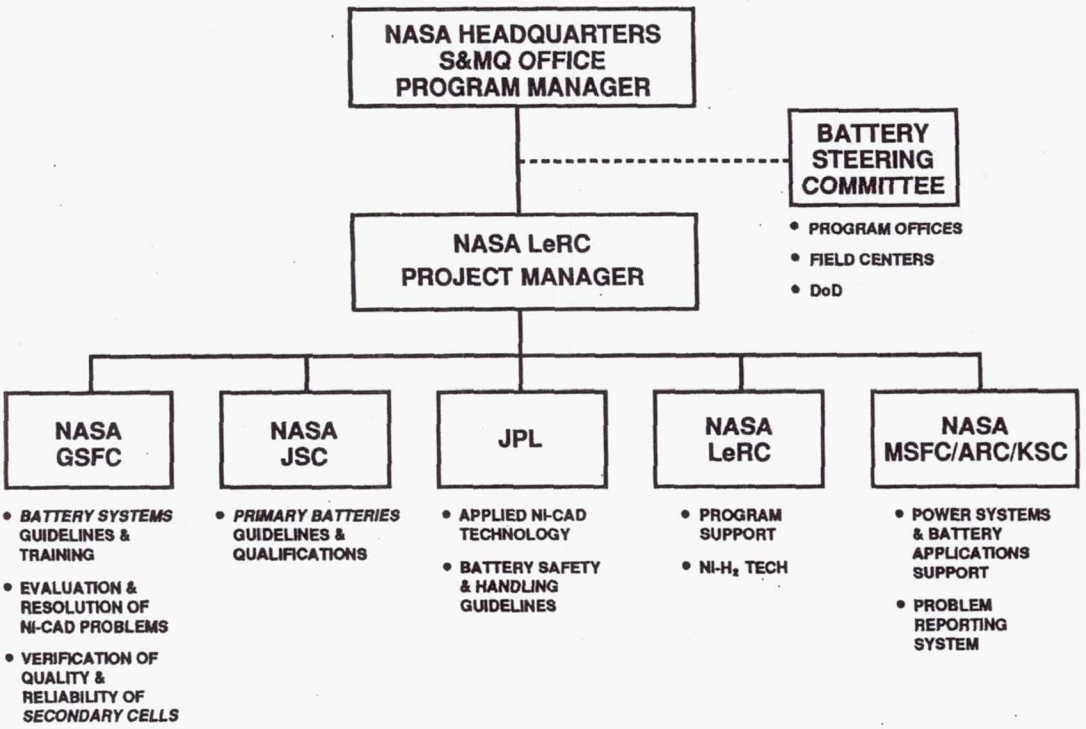
NASA HEADQUARTERS
S&MQ OFFICE
PROGRAM MANAGER
BATTERY
STEERING
COMMITTEE
• PROGRAM OFFICES
• FIELD CENTERS
• DoD
NASA LeRC
PROJECT MANAGER
NASA
GSFC
• BATTERY SYSTEMS GUIDELINES & TRAINING
• EVALUATION & RESOLUTION OF NI-CAD PROBLEMS
• VERIFICATION OF QUALITY & RELIABILITY OF SECONDARY CELLS
NASA
JSC
• PRIMARY BATTERIES GUIDELINES & QUALIFICATIONS
JPL
• APPLIED NI-CAD TECHNOLOGY
• BATTERY SAFETY & HANDLING GUIDELINES
NASA
LeRC
• PROGRAM SUPPORT
• NI-H2 TECH
NASA
MSFC/ARC/KSC
• POWER SYSTEMS & BATTERY APPLICATIONS SUPPORT
• PROBLEM REPORTING SYSTEM

APPLICATIONS OF X-RAY ABSORPTION FINE STRUCTURE TO THE *IN SITU* STUDY OF THE EFFECT OF COBALT IN NICKEL HYDROUS OXIDE ELECTRODES FOR FUEL CELLS AND RECHARGEABLE BATTERIES

Sunghyun Kim, Donald A. Tryk, Daniel A. Scherson

Department of Chemistry
Case Western Reserve University
Cleveland, OH 44106-7078

Mark R. Antonio

Argonne National Laboratory
Chemistry Division
Argonne, IL 60439

ABSTRACT

Electronic and structural aspects of composite nickel-cobalt hydrous oxides have been examined in alkaline solutions using *in situ* X-ray absorption fine structure (XAFS). The results obtained have indicated that cobalt in this material is present as cobaltic ions regardless of the oxidation state of nickel in the lattice. Furthermore, careful analysis of the Co K-edge Extended X-ray absorption fine structure data reveals that *the co-electrodeposition procedure generates a single phase, mixed metal hydrous oxide, in which cobaltic ions occupy nickel sites in the NiO_2 sheet-like layers and not two intermixed phases each consisting of a single metal hydrous oxide.*

INTRODUCTION

Nickel oxide electrodes have found widespread application in a variety of energy storage and energy generation devices,including rechargeable batteries and fuel cells.[1] The addition of certain metal cations to the nickel hydrous oxide lattice can profoundly affect its electrochemical characteristics.[1] In particular, cobalt has been found to shift the potential associated with the oxidation of $Ni(OH)_2$ to NiOOH[2] and to improve the charge acceptance of nickel oxide electrodes used in alkaline batteries.[1] In contrast, composite nickel oxide films involving iron as the guest metal exhibit high electrocatalytic activity for oxygen evolution and, as such, may be of practical value in alkaline water electrolysis.[3,4]

The studies presented herein have been aimed at elucidating the structural and electronic properties of composite nickel-cobalt hydrous oxides using *in situ* X-ray absorption fine structure (XAFS) as a probe of the host (Ni) and guest (Co) metal sites in the lattice.

Basic aspects of XAFS as applied to the study of electrochemical interfaces have been amply reviewed in the literature[5] and will not be discussed here. This technique can provide structural information without relying on long range order. This factor is of crucial importance, as high charge storage capacities can only be achieved by using materials in high area form, which are in many cases amorphous or consist of particles that are too small to achieve sufficient coherence for standard X-ray diffraction techniques to be very useful. Furthermore, high intensity X-rays in the energy range of interest can penetrate through thin electrolyte layers and low-Z window materials, such as organic polymers and thin aluminum sheets. This provides a means of performing measurements *in situ*, that is, with the electrode under potential control in an appropriately designed electrochemical cell.

EXPERIMENTAL

Pure metal (either nickel or cobalt) and nickel-cobalt composite hydrous oxides were prepared by cathodic (galvanostatic) electrodeposition[2,6] from solutions of the corresponding metal nitrates on a solid graphite electrode. After deposition, the films were rinsed with water and characterized in the spectroelectrochemical cell first by cyclic voltammetry and subsequently by XAFS in deaerated 1.0 M KOH. The cell for *in situ* fluorescence XAFS experiments employed in this study has been described elsewhere.[7]

In situ XAFS measurements for the pure Ni and Ni/Co hydrous oxide films were conducted in the discharged (i.e., reduced) and partially and nominally fully charged (i.e., oxidized) states. For the latter experiments, the potential was first scanned to a value more positive than the onset of oxygen evolution and then reversed to a value sufficiently negative for the current to drop essentially to zero but still positive with respect to the onset of NiOOH reduction. This strategy made it possible to eliminate problems associated with oxygen bubble formation during spectral acquisition. For measurements involving partially oxidized films, the potential was scanned up to a value on the rising part of the $Ni(OH)_2$ oxidation peak and then reversed to a no-current voltage condition.

All experiments were performed at beam-line IV-2 at the Stanford Synchrotron Research Laboratory. Details regarding these measurements as well as the method employed in the analysis of the EXAFS data have been given in previous work.[8]

RESULTS AND DISCUSSION

I. ELECTROCHEMISTRY

The cyclic voltammogram of a composite 9:1 Ni/Co hydrous oxide in 1.0 *M* KOH, shown in curve a, Figure 1, displayed characteristic oxidation and reduction peaks associated with the $Ni(OH)_2$/NiOOH redox process. In agreement with the observations of Corrigan,[2] but at variance with those of Cordoba et al.[4], the overpotential for oxygen evolution was larger for this composite oxide than for a pure nickel hydrous oxide prepared using the same procedure (see curve b, Figure 1). Also in harmony with earlier data[4] are the shifts in the $Ni(OH)_2$/NiOOH redox features in the negative direction (ca. 50 mV) induced by the presence of Co in the Ni hydrous oxide lattice. As pointed out by Corrigan and Bendert,[2] no voltammetry features associated with the $Co(OH)_2$/CoOOH redox couple can be identified for this composite Ni/Co film. This is particularly interesting, as the redox peaks of pure Co hydrous oxide in this same electrolyte occur at a potential of 0.09 V and thus more negative than those observed for a pure Ni film and therefore should be clearly discernable in the voltammogram.

II. XANES

A. Nickel K-edge

The Ni K-edge XANES for the composite Ni/Co hydrous oxide film in the reduced (fully discharged) and oxidized (nominally charged) state recorded at -0.3 and +0.3 V vs. SCE, in 1.0 *M* KOH are shown in Curves a and b, Fig. 2, respectively. These curves are nearly identical to those reported by Pandya et al.[9] for pure Ni hydrous oxide in 1.0 *M* KOH. Particularly noticeable is the shift in the overall absorption edge region toward higher X-ray energies for the oxidized (Ni^{3+}) film compared to the reduced (Ni^{2+}) film, including the peak at about 8363 eV. As discussed by Pandya et al.[9] the pre-edge feature at about 8332 eV is ascribed to the $1s \rightarrow 3d$ electronic transition,for which the intensity is found to be larger

for the oxidized than for the reduced state. It must be stressed that in both cases this spectral feature is relatively small and therefore consistent with a slightly distorted octahedral environment.

B. Cobalt K-edge

The Co K-edge XANES for the Ni/Co composite film in the oxidized and reduced states are very similar (see Curves a and b, Fig. 3) displaying a very small pre-edge peak. This observation provides strong evidence that the nature of the cobalt sites is not modified by the structural and electronic changes in the lattice associated with redox processes involving the nickel sites. A comparison between these curves and those obtained for pure cobalt hydrous oxide films (prepared using the same electrodeposition method: see curve c in this figure)[8] clearly shows that the cobalt sites in the latter composite hydrous oxide can be assigned to Co^{3+}. This is somewhat surprising since Co^{2+} in a pure cobalt hydrous oxide film undergoes oxidation at a potential only slightly more negative than that observed for the $Ni(OH)_2/NiOOH$ couple.[4] As is well known, however, the nature of the ligands can profoundly alter the redox potential of the Co^{3+}/Co^{2+} couple, e.g., $E^o[Co(NH_3)_6]^{2+/3+} = 0.108$ V, while $E^o[Co(H_2O)_6]^{2+/3+} = 1.83$ V.[10] It can therefore be concluded that *the environment of the cobaltic ions in the hydrated nickel oxide lattice is such that the potential required for their reduction is shifted to much more negative values.* Such a claim has been been made earlier in the literature, although without much substantiation.[11] Additional evidence for the presence of Co^{3+} sites in these composite hydrous oxides was obtained from the *in situ* Co K-edge EXAFS data (*vide infra*).

III. EXAFS

A. Nickel K-edge

The Fourier transforms (FTs) (without phase shift correction) of the $k^3\chi(k)$ Ni K-edge EXAFS for the Ni/Co hydrous oxide films in the reduced (-0.30 V vs. SCE) and oxidized (+0.30 V) states (see Curves a and b, Fig. 4, respectively) are very similar to those reported by Pandya et al.[9,12,13] for the oxidized and reduced forms of battery-type nickel hydrous oxide electrodes. In accordance with their observations, the Ni-O and Ni-Ni distances within the sheet-like NiO_2 layers (1st and 2nd major shells, respectively) were found to be somewhat smaller for the nominally oxidized film, d(Ni-O) = 1.92 ± 0.02 Å, $d(Ni\text{-}Ni)_1$ = 2.82 ± 0.02 Å, shown in Curve b, Fig. 4, compared to its reduced counterpart, d(Ni-O) = 2.09 ± 0.02 Å, $d(Ni\text{-}Ni)_1 = 3.11 \pm 0.02$ Å. The close similarity between the results obtained for the pure and composite Ni/Co hydrous oxide films indicates that within the sensitivity of this technique, the presence of cobalt at a nominally 10 metal-atom percent does not appear to significantly affect the structure of the nickel hydrous oxide.

Unlike the behavior observed for composite Ni/Fe hydrous oxide films in the nominally fully oxidized state, for which contributions due to Ni^{2+} were invariably observed, the Ni-Ni shell for a fully oxidized 9:1 composite Ni/Co film displayed a single well-defined shell attributed to Ni^{3+} sites. This affords unambiguous evidence that under these conditions *the nickel in Ni/Co films can be completely oxidized, leaving no residual Ni^{2+} ions in the lattice.*

C. Cobalt K-Edge

A number of interesting conclusions can be drawn from the analysis of the FT of the $k^3\chi(k)$ Co K-edge EXAFS spectra of these composite Ni/Co films (see Figure 5). In particular, the best fit to the Co K-edge EXAFS data yielded a value of d(Co-O) = 1.90 ± 0.02 Å and thus, within experimental error, is

identical to d(Co-O) in crystalline CoOOH, i.e., 1.90 Å.[14] This observation is consistent with the presence of cobaltic sites in the lattice, as proposed on the basis of the XANES data. More noteworthy, however, is the fact that composite Ni/Co films purposely charged only partially (obtained at +0.32 V: see curve c, Figure 5) displayed clearly resolvable Co-Ni shells associated with Co^{3+}-Ni^{2+} and Co^{3+}-Ni^{3+} interactions. These results clearly indicate that *the co-electrodeposition procedure generates a single phase, mixed metal hydrous oxide, in which cobaltic ions occupy nickel sites in the NiO_2 sheet-like layers and not two intermixed phases each consisting of a single metal hydrous oxide.*

LITERATURE

1. McBreen, J. In *Modern Aspects of Electrochemistry*, Conway, B.; White, R.; Bockris, J. O'M, Eds.; Plenum Press: New York, 1991, Vol. 23.
2. Corrigan, D. A.; Bendert, R. M. *J. Electrochem. Soc.* **1989**, *136*, 723.
3. Corrigan, D. A. *J. Electrochem. Soc.* **1987**, *134*, 377.
4. Cordoba, S. I.; Carbonio, R. E.; Lopez Teijelo, M.; Macagno, V. A. *Electrochim. Acta* **1986**, *31*, 1321.
5. Abruna, H. D. In *Electrochemical Interfaces*, Abruna, H. D. Ed.; VCH: New York, 1991, Chapter 1.
6. Burke, L. D.; Twomey, T. A. M. *J. Power Sources* **1984**, *12*, 203.
7. Kim, S.; Bae, I. T.; Sandifer, M.; Ross, P. N.; Carr, R.; Woicik, J.; Antonio, M. R.; Scherson, D. A. *J. Am. Chem. Soc.* **1991**, *113*, 9063.
8. Kim S.; Tryk, D. A.; Antonio, M. R.; Scherson, D. A. *J. Phys. Chem.* submitted, March 1993.
9. Pandya, K. I.; Hoffman, R. W.; McBreen, J.; O'Grady, W. E. *J. Electrochem. Soc.* **1990**, *137*, 383.
10. Milazzo, G.; Caroli, S. *Tables of Standard Electrode Potentials*, Wiley: New York, **1978**, pp. 337.
11. Weininger, J. L. In *The Nickel Electrode*, Gunther, R. G.; Gross, S.; Eds., Proceedings of the Symposium, The Electrochemical Society, 1982.
12. McBreen, J.; O'Grady, W. E.; Pandya, K. I.; Hoffman, R. W.; Sayers, D. E. *Langmuir* **1987**, *3*, 428.
13. Pandya, K. I.; O'Grady, W. E.; Corrigan, D. A.; McBreen, J.; Hoffman, R. W. *J. Phys. Chem.* **1990**, *94*, 21.
14. Delaplane, R. G.; Ibers, J. A.; Ferraro, J. R.; Rush, J. J. *J. Chem. Phys.* **1969**, *50*, 1920.

ACKNOWLEDGEMENTS

This work was supported in part by the Department of Energy through a subcontract from Lawrence Berkeley Laboratory. Additional funding was provided by Eveready Battery Co., Westlake, Ohio.

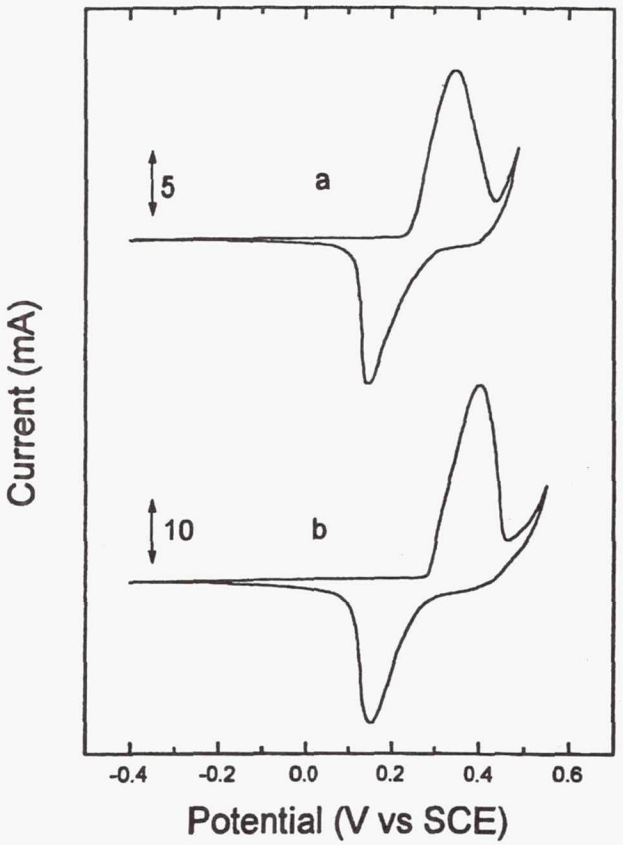

Fig. 1 Cyclic voltammetry curves for composite 9:1 Ni/Co (curve a) and a pure Ni (curve b) hydrous oxide electrode in deaerated 1.0 M KOH.
Scan rate: 5mV s^{-1}. Cross sectional electrode area: 0.74 cm^2.

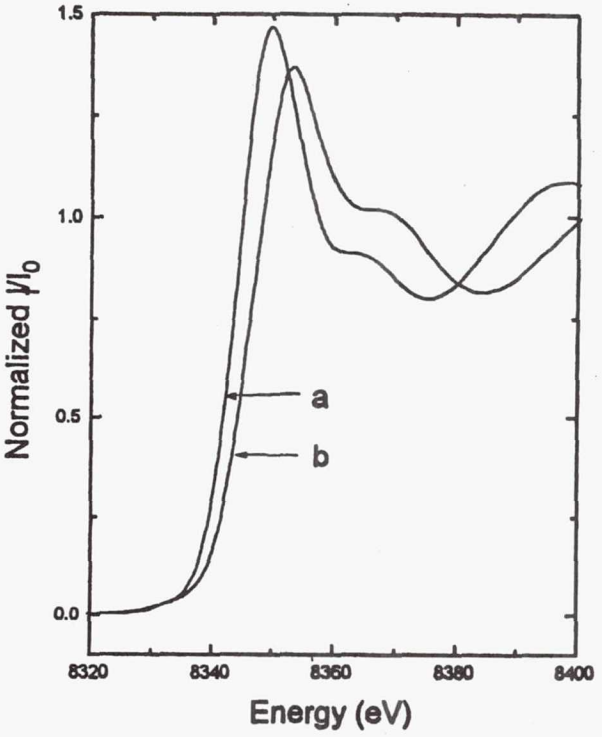

Fig. 2 Ni K-edge XANES for a composite 9:1 Ni/Co hydrous oxide film in the fully discharged (Curve a) and nominally fully oxidized (Curve b) recorded at -0.3 V and +0.3 V vs SCE, respectively in 1.0 M KOH.

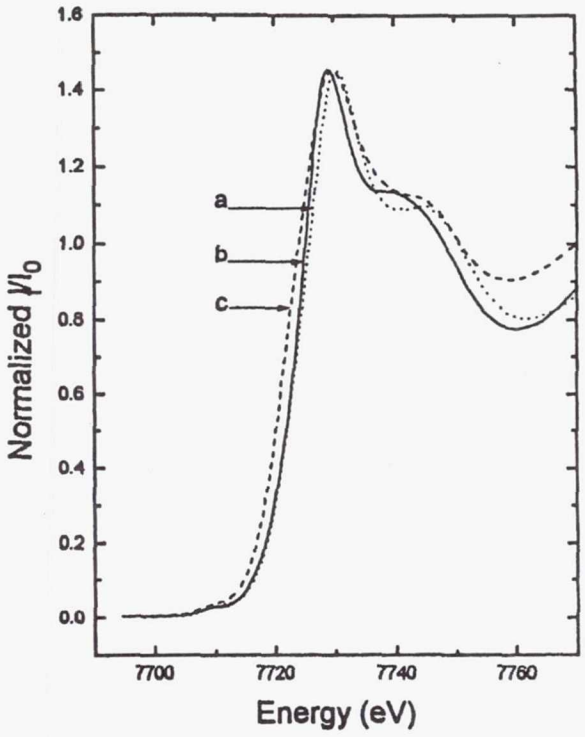

Fig. 3 Co K-edge XANES for a composite 9:1 Ni/Co hydrous oxide film in the oxidized (0.3V) and reduced (-0.3V) states (Curves a and b, respectively). Also shown in in this figure are the corresponding spectra for a pure Co hydrous film prepared by the same electrodeposition procedure described in the Experimental Section in the reduced state (Curve c).

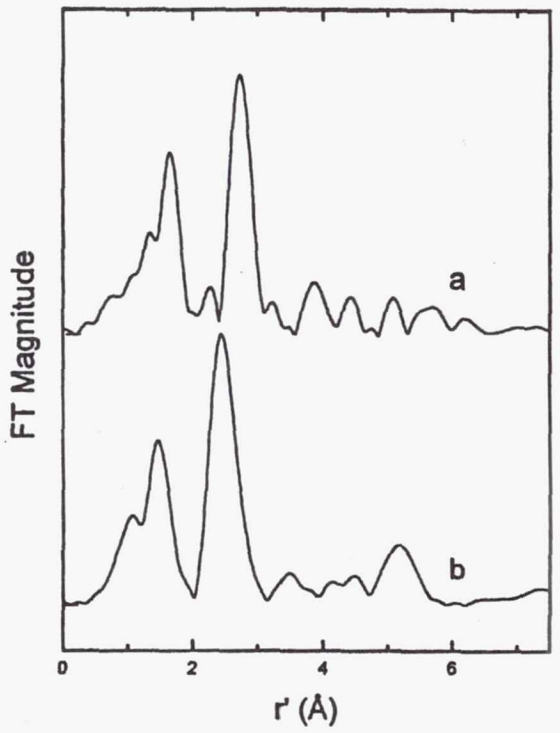

Fig. 4 Phase-uncorrected FT for the $k^3\chi(k)$ Ni K-edge EXAFS for 9:1 Ni/Co hydrous oxide films in the reduced (-0.3 V vs SCE, Curve a), and oxidized (+0.30 V, Curve b) states.

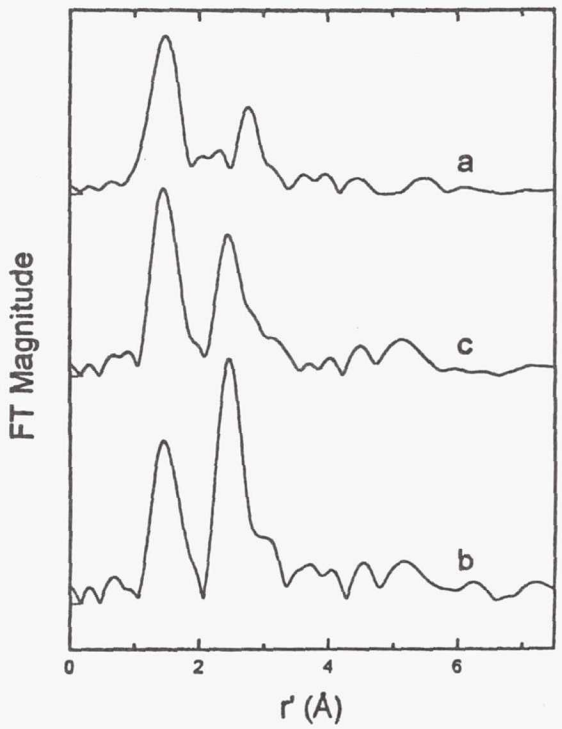

Fig. 5 Phase-uncorrected FT for the $k^3\chi(k)$ Co K-edge EXAFS for 9:1 Ni/Co hydrous oxide films in the reduced (Curve a), fully oxidized (Curve b) and partially oxidized (obtained at +0.32 V, Curve c) states. Other conditions are given in the Caption Figure 2.

REVIEW OF SUPER Ni/Cd CELL DESIGNS AND PERFORMANCE

Bruce Abrams-Blakemore

Eagle-Picher. Inc.
Colorado Springs, CO 80911

ABSTRACT

Eagle-Picher Industries, Inc., in cooperation with Hughes Aircraft Company, began production of the Super Nickel-Cadmium cell in 1989. Since that time the Super Nickel-Cadmium cell has been deployed in a wide variety of satellites. This paper will review one of those programs and provide a performance update. We will discuss storage requirements and capacity histories for the various Super NiCad Cell designs.

INTRODUCTION

The Super NiCad was first introduced in 1989 by Hughes Aircraft Company for use in the LESAT satellite. The cell is manufactured at Eagle-Picher Industries in Colorado Springs, Colorado. The Super NiCad differs from standard nickel cadmium cells in several ways:

1. The positive plate is made by an electrochemical-chemical deposition process. This process is based on the Air Force patented buffered deposition process.

2. The positive plate loading target is in the range of 1.65 g/cc void. This is lower than the standard NiCad positive loading which is in the range of 2.0 g/cc void.

3. The negative electrode in the Super NiCad has similar loading levels to the standard NiCad but is produced by an aqueous electrochemical chemical deposition method.

4. The negative to positive ratio is much higher in the Super NiCad normally exceeding a theoretical negative to positive of 1.8. This allows for precharge in the range of 40% of excess negative capacity.

5. Finally, the Super NiCad incorporates an impregnated zirconia separator. This separator is as wettable as the nylon used in standard NiCads, however it is much more resistant to the alkaline environment.

Because of the unique design there are some special storage considerations with Super NiCad:

1. Unlike the standard NiCad, the Super NiCad should never be stored under short-circuit.

2. The Super NiCad is best stored under trickle charge.

3. When constant charging during storage is impractical, the Super NiCad can be periodically "topped-off."

4. When any type of charging is impractical, the Super NiCad is best stored open-circuited and completely discharged at low temperature.

The Super NiCad was developed to correct observed failure mechanisms of the standard nickel cadmium cells. It was anticipated that the changes discussed above would provide some performance advantages:

1. The deposition method and loading limits were to provide better active material utilization, better ability to withstand deep discharge and less plate expansion over cycle life.

2. The negative manufacturing process was designed to improve active material utilization and decrease plate deterioration, thereby minimizing cadmium migration.

3. The higher precharge had better gas management as its goal, additionally there was the expected benefit of better overcharge protection.

4. The zirconia separator was chosen in order to avoid the oxidation to carbonate that was seen with the nylon separator.

The purpose of this paper is to explore functioning Super NiCad programs and determine how well the cells have met performance goals. Specific data will be drawn from the SMEX 9 AH program. We will first look at the beginning of life (BOL) performance characteristics. Next we will discuss cell performance during accelerated life cycle testing. Finally, we will briefly discuss cell performance in flight.

ACCEPTANCE AND STRESS TESTING

Beginning of Life

All Super NiCad cells that are destined for flight or accelerated life cycling are sent through an acceptance test regime (see Figure 1). The test is based on the NASA approved flight cell acceptance test. It involves testing at 0° C, 10° C and 22° C. Charge currents are varied from trickle charge (C/20) to rapid charge (C/2). The cells are normally discharged at a C/2 current, but there are tests to demonstrate charge retention (self-discharge rate) and high current discharge performance (at 5C). In addition to the electrical testing, representative plates are subjected to a destructive stress test (see Figure 2).

Since the normal satellite operating temperature is around 10° C, all capacity qualification testing is performed at this temperature. The Super NiCads have demonstrated from 85 to 95% utilization at this early stage of cell life.

ACCEPTANCE TESTING PROCEDURE

Capacity Test at 10° C

- Cells are shorted down to 0.010 volt maximum, 16 hour stand.
- Cells are soaked at 10° C for 4 hours.
- C/10 charge for 20 hours, 1 hour open-circuit stand, C/2 discharge to 1.0 volt.

Overcharge and Capacity Test at 0° C

- Cells are shorted down to 0.010 volt maximum, 12 hour minimum.
- Cells are soaked at 0° C for 4 hours.
- C/20 charge for 72 hours, 1 hour open-circuit stand, C/2 discharge to 1.0 volt.

High Current Discharge Test at 22° C

- Cells are shorted down to 0.010 volt maximum, 12 hours minimum.
- Cells are soaked at 22° C for 4 hours.
- C/10 charge for 20 hours, 5C pulse discharge for 10 seconds, C/2 discharge to 1.0 volt.

Charge Retention (Discharged) Test at 22° C

- Cells are shorted down for 12 hours.
- C/10 charge for 10 minutes, open-circuit for 24 hours, minimum voltage 1.15 volts.

Figure 1. Description of EPI Acceptance Test.

EPI POSITIVE ELECTRODE STRESS TEST

- Hot Formation: 5C rate, 70° C, 20% KOH, 2 cycles.
- Pre-Stress: Weight, thickness and visual appearance characterization.
- Initial Capacity: Charge at 5C for 12 min., C/2 for 1 hour. Discharge at C rate to 1.0 V vs. Ni sheet.
- 200 Cycles: Charge at 10C for 12 minutes. Discharge at 10C for 8 min. Diode clamped to -1.0 V.
- Ending Capacity: 5 Cycles, same as initial capacity.
- Visual appearance.
- Scrub, rinse, and dry.
- Weight loss and swelling.

Figure 2. Stress Test Regime.

After 200 stress cycles (charge and discharge at 10°C) the plates show less than 3% thickness growth and no blistering. By comparison, electrodes for standard NiCads seldom survive the stress test intact.

Cell voltages at 0°C do not exceed 1.50 volts on overcharge at C/20 (see Figure 3).

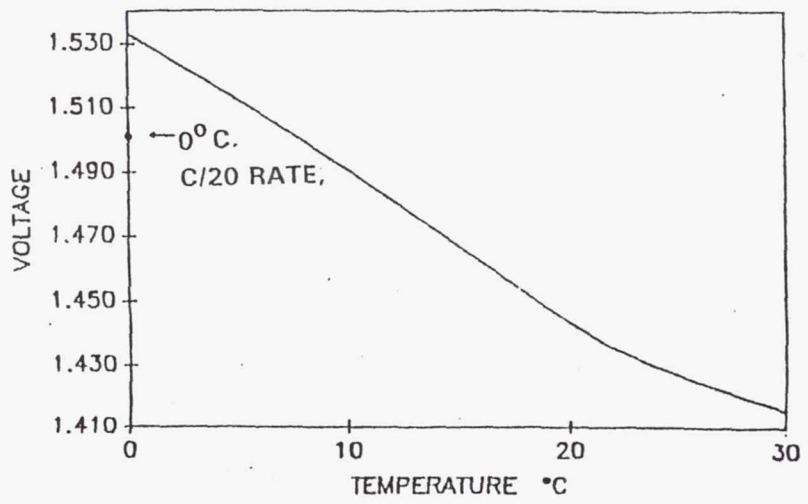

Figure 3. Typical Super NiCad End-of-Charge Voltage vs. Temperature, C/10 Rate.

Typically all cells of a given lot perform within a 20 millivolt range.

Figure 4 depicts average cell performance values for the SMEX acceptance test.

SMEX AVERAGE ACCEPTANCE TEST RESULTS		
	0°C Test	10°C Test
Average Capacity	11.55 AH	11.76 AH
Average EOC Voltage	1.491	1.4824
Average EOC Pressure	2.5 psi	11.4 psi
Average Final Voltage after 10 Second 5C Discharge: 1.1429 V		

Figure 4. Results of SMEX acceptance testing.

ACCELERATED LIFE CYCLING

The super NiCad has been tested in both simulated LEO and GEO orbits and has passed all NASA requirements to date.

FLIGHT PERFORMANCE

The super NiCad has demonstrated end-of-charge voltages in the ranges of 1.40 to 1.48 and end-of-discharge voltages in the ranges of 1.18 to 1.21. These end-of-charge voltages are approximately 20 millivolts lower than those seen in standard nickel cadmium cells and the discharge voltages are similarly higher than those seen in standard nickel cadmium cells.

Initial flight data for the SMEX program agree with the trends that were suggested by the accelerated testing.

CONCLUSION

Beginning-of-life test data show increased active material utilization in the super NiCad design, as anticipated. Cell voltages and pressures are well within acceptable limits. Stress testing indicates that the Super NiCad positive has a longer theoretical life than the standard Nickel cadmium positive.

Accelerated life cycling has provided a positive picture of the long term Super NiCad performance. Super NiCad cells have surpassed the life normally expected in a standard NiCad. All super NiCads currently in flight are performing well and within all specified limits.

THERMODYNAMICS OF NICKEL-CADMIUM AND NICKEL-HYDROGEN BATTERIES

Digby D. Macdonald and Mark L. Challingsworth
Center for Advanced Materials
The Pennsylvania State University
517 Deike Building
University Park, PA 16802

ABSTRACT

Thermodynamic parameters for Nickel-Cadmium (NiCad) and Nickel-Hydrogen (NiH_2) batteries are calculated for temperatures ranging from 273.15K (0°C) to 373.15K (100°C). For both systems, we list equilibrium and thermoneutral voltages for the cells, and in the case of the NiH_2 battery, these data are provide for hydrogen fugacities ranging from 0.01 to 100 (atm) to simulate the full discharged and charged states. The quality of the input thermodynamic data are assessed and the effect of assuming different cell reactions is analyzed.

INTRODUCTION

Nickel-cadmium (NiCad) and nickel-hydrogen (NiH_2) batteries are used extensively in aerospace systems, because of their relatively high energy and power densities and their excellent cycling capabilities [1-4]. However, given the severe demands placed on cycling performance for satellites in low earth orbit (LEO) and recognizing the need to keep battery weight to an absolute minimum, efforts continue to improve the cycle life particularly to high depths of discharge. The current standard in this regard for NiH_2 batteries is a cycle life of 30,000 cycles to 50% loss in capacity (of the nickel electrode) at 50% depth of discharge. The cycle life of NiCad batteries is not as favorable (generally a few thousand cycles), so that these systems are commonly not employed where cycle life is the key operational characteristic.

It is well recognized that the cycle lives of NiCad and NiH_2 batteries are limited by irreversible structural and physicochemical changes that occur in the porous nickel electrodes as the batteries are cycled between the charged and discharged states. Although the mechanistic details of the degradation processes are not well-understood, various models have been developed that provide a good phenomenological simulation of the loss of capacity [5,6]. However, a complete understanding of the degradation mechanisms requires a careful analysis of the cell thermodynamics so that the voltage and energy efficiencies can be placed on a rational basis. Thermodynamic data for a variety of alkaline batteries has been published previously by Pound, Singh, and Macdonald [7] and for sealed NiCad batteries by Hodge et al [8]. The present work recalculates and expands the thermodynamic database for the

NiCad and NiH_2 systems by deriving values for relevant parameters (equilibrium cell and thermoneutral potentials) over a wide range of temperature (0°C – 100°C) and, in the case of NiH_2, hydrogen pressure (0.01 – 100 atm).

BATTERY THERMODYNAMICS

Following conventional formalism, the cell reactions for NiCad and NiH_2 batteries can be written as

$$Cd + 2\,NiOOH + 2H_2O = Cd(OH)_2 + 2Ni(OH)_2 \tag{1}$$

and

$$\frac{1}{2}H_2 + NiOOH = Ni(OH)_2 \tag{2}$$

respectively, assuming that the charged nickel active material is NiOOH, or as

$$Cd + 2NiOOH \cdot H_2O = Cd(OH)_2 + 2Ni(OH)_2 \tag{1'}$$

and

$$\frac{1}{2}H_2 + NiOOH \cdot H_2O = Ni(OH)_2 + H_2O \tag{2'}$$

if $NiOOH \cdot H_2O$ is assumed to be the active material at the nickel positive electrode [8]. The equilibrium voltages for these four reactions are given by the Nernst equation as

$$\Delta E^{e}_{cell} = \Delta E^{o}_{cell} + \frac{2.303RT}{F} \log a_{H_2O} \tag{3}$$

$$\Delta E^{e}_{cell} = \Delta E^{o}_{cell} + \frac{2.303RT}{F} \log f^{1/2}_{H_2} \tag{4}$$

$$\Delta E^{e}_{cell} = \Delta E^{o}_{cell} \tag{3'}$$

and

$$\Delta E^{e}_{cell} = \Delta E^{o}_{cell} + \frac{2.303RT}{F} \log f^{1/2}_{H_2} - \frac{2.303RT}{F} \log a_{H_2O} \tag{4'}$$

where f_{H_2} is the fugacity of hydrogen, a_{H_2O} is the activity of water, and the standard cell voltages are given by

$$\Delta E^{o}_{cell} = -\Delta G^{o}_{cell} / nF \tag{5}$$

ΔG^{o}_{cell}, n, and F are the change in standard Gibbs energy for the cell, the number of electrons involved in the cell reaction, and Faraday's constant, respectively. The change in standard Gibbs energy for the cell is

$$\Delta G^{o}_{cell} = \sum_{\text{Products}} \nu_P \Delta_f G^{o}_P - \sum_{\text{Reactants}} \nu_R \Delta_f G^{o}_R \tag{6}$$

where $\Delta_f G^{o}_I$ is the standard Gibbs energy of formation of component I, n is the stoichiometric coefficient for the reaction, and subscripts P and R refer to "products" and "reactants," respectively, in the cell reactions (i.e. Reactions (1), (2), (1′), and (2′)).

A full assessment of the thermodynamics of a battery requires the estimation of the thermoneutral potential of the cell, defined as

$$\Delta E^{T}_{cell} = -\Delta H_{cell} / nF \tag{7}$$

and hence

$$\Delta E^{T}_{cell} = \Delta E^{e}_{cell} - T\left(\frac{\partial \Delta E^{e}_{cell}}{\partial T}\right) \tag{8}$$

Using standard thermodynamic identities, we derive expressions for ΔE^{T}_{cell} for the four cells of interest as

$$\Delta E^{T}_{cell,1} = -\frac{\Delta H^{o}_1}{2F} - \frac{RT^2}{F}\left[\frac{\partial \ln a_{H_2O}}{\partial T}\right] \tag{9}$$

$$\Delta E^{T}_{cell,2} = -\frac{\Delta H^{o}_2}{F} \tag{10}$$

$$\Delta E^{T}_{cell,1'} = -\frac{\Delta H^{o}_{1'}}{2F} \tag{11}$$

and

$$\Delta E^{T}_{cell,2'} = -\frac{\Delta H^{o}_{2'}}{F} + \frac{RT^2}{F}\left[\frac{\partial \ln a_{H_2O}}{\partial T}\right] \tag{12}$$

where ΔH^{o}_k is the change in standard enthalpy for Reaction k. Note that a term involving the fugacity of hydrogen does not appear in Equations (10) and (11) [corresponding to Reactions (2) and (2′)], because we have assumed that f_{H_2} is a constant, independent of temperature.

THERMODYNAMIC DATA

The thermodynamic data employed in this study are summarized in Tables 1 and 2, together with the sources from which they were taken. Heat capacities for $Ni(OH)_2$, $Cd(OH)_2$, $NiOOH \cdot H_2O$, and NiOOH had to be estimated using C_p^o/S^o ratios, which are found to be constant for given classes of compounds [7]. The value adopted for the Gibbs energy of formation for $Cd(OH)_2$ was adjusted slightly from that given by Naumov et al (Ref. (a), Table 1), 474.5 kJ/mol, so as to yield the observed equilibrium voltage for the NiCad battery [1.45V (2)]. The accuracies of the various thermodynamic quantities summarized in Table 1 are largely unknown and are difficult to estimate without detailed information on the original experiments from which they are derived.

Noting that heat capacities are generally expressed in the form

$$C_p^o = A + BT + CT^{-2} \tag{13}$$

we derived expressions for the Gibbs energy and enthalpy of formation of any given compound at temperature T as follows.

$$\Delta_f G_T^o = \Delta_f G_{T_o}^o - (T - T_o)\Delta_f S_{T_o}^o + A_f\left[T - T_o - T\ln\left(\frac{T}{T_o}\right)\right] + B_f\left[\frac{T^2 - T_o^2}{2} - T(T - T_o)\right] + C_f\left[\frac{1}{T} - \frac{1}{T_o}\right]\left[\frac{T}{2}\left(\frac{1}{T} + \frac{1}{T_o}\right) - 1\right] \tag{14}$$

$$\Delta_f H_T^o = \Delta_f H_{T_o}^o + A_f(T - T_o) + \frac{B_f}{2}\left[T^2 - T_o^2\right] - C\left(\frac{1}{T} - \frac{1}{T_o}\right) \tag{15}$$

and

$$\Delta_f S_T^o = \left(\Delta_f H_T^o - \Delta_f G_T^o\right)/T \tag{16}$$

where $\Delta_f S_{T_o}^o$ and $\Delta_f H_{T_o}^o$ are the entropy and enthalpy of formation at the reference temperature (T_o = 298.15K) and A_f, B_f, and C_f are the coefficients in Equation (13) for the formation of the compound of interest.

Thermodynamic parameters of formation calculated using Equations (14) to (16) for various active components in NiCad and NiH_2 batteries are summarized in Table 3 as a function of temperature from 273.15K (0°C) to 373.15K

(100°C). Note that no values are given for Cd and H_2 because, by definition, the parameters of formation are zero at all temperatures.

Calculation of the equilibrium and thermoneutral cell voltages requires a knowledge of the activity of water, which for 8 molal KOH can be expressed as (7)

$$\ln a_{H_2O} = -6.345750 + 6.125771 \text{ x } 10^3 / T - 2.093874 \text{ x } 10^6 / T^2 + 2.324516 \text{ x } 10^8 / T^3 \quad (17)$$

The activity of water for this electrolyte ranges from 0.514 at 263.15K to 0.618 at 393.15K.

The data summarized in Table 3 were used to estimate equilibrium and thermoneutral cell voltages for NiCad and NiH_2 batteries as a function of temperature, as given in Tables 4-7. We should note, at this point, that the thermodynamic data for $NiOOH \cdot H_2O$ are poorly known, so that lower confidence should be placed in the potentials calculated from Reactions (1′) and (2′) than is those calculated from Reactions (1) and (2). Accordingly, in this work, we will emphasize the thermodynamic calculations that involve NiOOH as the oxidized, active material at the positive electrodes of NiCad and NiH_2 batteries.

DISCUSSION

As seen from the data summarized in Tables 4 and 5, the equilibrium potentials for NiCad and NiH_2 batteries with 8m KOH electrolyte decrease with increasing temperature and, for the latter system at any given temperature, increase with increasing hydrogen partial pressure. The dependence of ΔE^e_{cell} on temperature results directly from the entropy and heat capacity changes for the cell reactions as well as from the change in water activity in the electrolyte, whereas the dependence on hydrogen pressure (in the case of NiH_2 batteries) results directly from the thermodynamics of the negative electrode. We also note that much larger changes in ΔE^e_{cell} with temperature are predicted if the oxidized nickel phase is assumed to be $NiOOH \cdot H_2O$ rather than NiOOH, but the poor quality of the data for the former precludes any in-depth analysis of this difference.

Thermoneutral potentials for NiCad and NiH_2 batteries are listed in Tables 6 and 7. The thermoneutral voltage corresponds to that voltage that the cell would have to operate at so that the entropic dissipation of energy is zero. Of course, the data calculated in this work do not include the various irreversible sources of energy dissipation, associated with heat generation due to the internal cell resistance and arising from the reactions occurring at the

electrodes on charging and discharging. These irreversible effects are best treated using irreversible thermodynamic methods of the type proposed by Ratjke et al [9].

For both the NiCad and NiH_2 batteries, the thermoneutral voltage is greater than the equilibrium cell voltage at equivalent temperatures and hydrogen pressure (for the NiH_2 system). This relationship arises from the fact that the entropy changes for the cell reactions on discharge are negative, corresponding to exothermic processes. Likewise, on charging both cells are endothermic provided that the voltage lies between ΔE^{e}_{cell} and ΔE^{T}_{cell}.

Finally, we note that the equilibrium cell potentials calculated in this work for the NiH_2 battery are in good agreement with our previous calculations and with experimental data [7]. A similar comparison cannot be made with experimental data for NiCad batteries because we have used these data to adjust the Gibbs energy of formation of $Cd(OH)_2$ used in the calculations. However, it is worth noting that our equilibrium cell potential at 25°C (1.45V) is significantly more positive than that calculated by Hodge et al [8] (1.29V). This difference may be attributed to the large uncertainty in the Gibbs energy of formation for $NiOOH \cdot H_2O$ [8] and to the fact that Hodge et al [8] did not apply a correction for the activity of water. Clearly, the calculated value of Hodge et al [8] is much lower than the open circuit voltage of 1.45V quoted by Halpert [2]. Because irreversible processes within the cell are expected to reduce the measured open circuit voltage below the equilibrium cell voltage, it is evident that the calculations of Hodge et al (8) are at odds with experiment.

REFERENCES

1. P.C. Milner and U.B. Thomas, in "Advances in Electrochemistry and Electrochemical Engineering," Vol. 5, p. 1 (Interscience, N.Y., 1967).
2. G. Halpert, J. Power Sources, 15, 119 (1985).
3. J.K. McDermott, J. Power Sources, 18, 265 (1986).
4. L. Miller, J. Brill, and G. Dodson, J. Power Sources, 29, 533 (1990).
5. D.D. Macdonald, B.G. Pound, and S.J. Lenhart, J. Power Sources, 29, 447 (1990).
6. D.D. Macdonald, M. Urquidi-Macdonald, S.D. Bhatka, and B.G. Pound, J. Electrochem. Soc., 138, 1359 (1991).
7. B.G. Pound, R.P. Singh, and D.D. Macdonald, J. Power Sources, 18, 1 (1986).
8. B.J.R. Hodge, R. Bonnaterre, and F. Putois, J. Power Sources, 7, 211 (1975).
9. S.K. Ratkje, T. Ikeshoji, and K. Syverud, J. Electrochem. Soc., 137, 2088 (1990).

TABLE 1

Thermodynamic Properties of Components at 298.15K

Component	$\Delta_f G^o$ (kJ/mol)	$\Delta_f H^o$ (kJ/mol)	$\Delta_f S^o$ (f) (J/K.mol)	S^o (J/K.mol)	$\Delta_f C_p^o$ (a,b,f) (kJ/mol)
Ni	0	0	0	29.87 (f)	16.987 + 0.02946T
Cd	0	0	0	51.756 (a)	22.217 + 0.012301T
O_2	0	0	0	205.03 (f)	$29.957 + 0.00414T - 1.674 \times 10^5 T^{-2}$
H_2	0	0	0	130.574 (a)	$27.2797 + 0.0032635T + 0.50208 \times 10^5 T^{-2}$
H_2O	-237.178 (a)	-285.828 (d)	-163.174	69.915 (a)	$10.669 + 0.042284T - 6.90308 \times 10^5 T^{-2}$
$Ni(OH)_2$	-459.070 (b)	-541.799 (d)	-277.474	88.0 (f)	$18.106 - 0.03686T + 1.1719 \times 10^{-5} T^{-2}$
NiOOH	-321.7 (b)	-391.231 (d)	-233.207	66.98 (b)	$30.186 - 0.03523T + 1.423 \times 10^5 T^{-2}$
$NiOOH \cdot H_2O$	-564.422 (c)	-629.859 (d)	-219.478	150.624 (c)	$87.388 - 0.082844T + 8.661 \times 10^5 T^{-2}$
$Cd(OH)_2$	-482.347	-571.642 (d)	-299.496	87.864 (a)	$12.726 - 0.0197T + 1.17192 \times 10^5 T^{-2}$

(a) G.B. Naumov, et al, Handbook of Thermodynamic Data, USGS-WRD-74-001, US Geol. Survey, 1974.

(b) P.G. Pound, R.P. Singh, & D.D. Macdonald, J. Power Sources, 18, 1 (1986).

(c) B.J.R. Hodge et al, J. Power Sources, 7, 211 (1975).

(d) Estimated from $\Delta_f H^o = \Delta_f G^o + T\Delta_f S^o$.

(e) Calculated for the formation reaction from the elements.

(f) D.D. Wagman et al, J. Phys. Chem. Ref. Data, 11, Suppl. No. 2 (1982).

TABLE 2

Heat Capacities of Active Compounds (a,b,f, Table 1)

Compound	C_p^o (kJ/mol)
H_2O	$52.928 + 47.614 \times 10^{-3} T - 7.238 \times 10^5 T^{-2}$
$Ni(OH)_2$	92.33
NiOOH	90.77
$NiOOH \cdot H_2O$	200.09
$Cd(OH)_2$	92.18

TABLE 3

Thermodynamic Parameters of Formation for Active Components in NiCad and NiH_2 Batteries as a Function of Temperature

Temperature (K)	Gibbs Energy (J/mol)	Enthalpy (J/mol)	Entropy (J/K-mol)
	$Ni(OH)_2$		
273.15	-466014.9	-541988.4	-278.1382
283.15	-463234.9	-541909.9	-277.8557
293.15	-460457.7	-541835.1	-277.5959
298.15	-459070	-541799	-277.474
303.15	-457682.9	-541763.9	-277.3572
313.15	-454910.5	-541696.4	-277.1382
323.15	-452140.1	-541632.6	-276.9376
333.15	-449371.7	-541572.5	-276.7544
343.15	-446605	-541516.1	-276.5875
353.15	-443839.8	-541463.4	-276.436
363.15	-441076.2	-541414.3	-276.299
373.15	-438313.8	-541368.9	-276.1758
	NiOOH		
273.15	-327593.5	-391776.8	-234.9745
283.15	-325230.3	-391554.5	-234.237
293.15	-322874.9	-391337	-233.5396
298.15	-321700	-391230	-233.205
303.15	-320526.8	-391124.2	-232.8793
313.15	-318185.7	-390915.9	-232.2536
323.15	-315851.2	-390712	-231.66
333.15	-313522.9	-390512.6	-231.0964
343.15	-311200.5	-390317.4	-230.5608
353.15	-308883.8	-390126.4	-230.0517
363.15	-306572.3	-389939.7	-229.5673
373.15	-304266	-389757	-229.1063
	$NiOOH \cdot H_2O$		
273.15	-570232.1	-631718.9	-225.1038
283.15	-567888.4	-630963.5	-222.763
293.15	-565571.2	-630224	-220.5461
298.15	-564422	-629860	-219.481
303.15	-563278.9	-629499.7	-218.4432
313.15	-561010.3	-628789.9	-216.4453
323.15	-558764.1	-628093.9	-214.5448
333.15	-556539.2	-627411.5	-212.7346
343.15	-554334.6	-626742	-211.0085
353.15	-552149.4	-626085.1	-209.3611
363.15	-549982.6	-625440.3	-207.7873
373.15	-547833.4	-624807.5	-206.2827

TABLE 3 (continued)

Temperature (K)	Gibbs Energy (J/mol)	Enthalpy (J/mol)	Entropy (J/K-mol)
		$Cd(OH)_2$	
273.15	-489876.4	-571855.4	-300.1235
283.15	-486862.4	-571767.8	-299.8593
293.15	-483851.4	-571683.2	-299.6129
298.15	-482347	-571642	-299.496
303.15	-480843.3	-571601.5	-299.383
313.15	-477837.8	-571522.6	-299.1684
323.15	-474834.8	-571446.4	-298.9677
333.15	-471834	-571372.9	-298.7802
343.15	-468835.5	-571302.1	-298.6049
353.15	-465839	-571233.7	-298.441
363.15	-462844.4	-571167.9	-298.2878
373.15	-459851.5	-571104.5	-298.1446
		H_2O	
273.15	-241078.8	-286186.8	-165.1239
283.15	-239514.8	-286051.7	-164.3391
293.15	-237955.6	-285906.4	-163.5557
298.15	-237178	-285830	-163.165
303.15	-236401.7	-285751.3	-162.7751
313.15	-234852.9	-285587	-161.9981
323.15	-233309.6	-285414	-161.2256
333.15	-231771.8	-285232.7	-160.458
343.15	-230239.5	-285043.4	-159.6957
353.15	-228712.8	-284846.5	-158.939
363.15	-227191.8	-284642.2	-158.188
373.15	-225676.6	-284430.8	-157.4429

TABLE 4

Calculated Equilibrium Cell Voltages for NiCad Batteries as a Function of Temperature

T/K	ΔE^{e}_{cell} (V) Reaction (1)	Reaction (1′)
273.15	1.461	1.459
283.15	1.457	1.438
293.15	1.453	1.418
298.15	1.450	1.408
303.15	1.448	1.397
313.15	1.444	1.377
323.15	1.439	1.356
333.15	1.435	1.334
343.15	1.430	1.313
353.15	1.425	1.292
363.15	1.420	1.270
373.15	1.415	1.248

TABLE 5

Calculated Equilibrium Cell Voltages for NiH_2 Batteries as a Function of Temperature and Hydrogen Pressure

	pH_2/atm				
T/K	0.01	0.1	1.0	10.0	100.0
			Reaction 2		
273.15	1.380	1.408	1.435	1.462	1.489
283.15	1.374	1.402	1.430	1.458	1.487
293.15	1.368	1.397	1.426	1.455	1.484
298.15	1.365	1.394	1.424	1.453	1.483
303.15	1.361	1.391	1.422	1.452	1.482
313.15	1.355	1.386	1.417	1.448	1.479
323.15	1.348	1.381	1.413	1.445	1.477
333.15	1.342	1.375	1.408	1.441	1.474
343.15	1.335	1.369	1.403	1.437	1.471
353.15	1.329	1.364	1.399	1.434	1.469
363.15	1.322	1.358	1.394	1.430	1.466
373.15	1.315	1.352	1.389	1.426	1.463
			Reaction (2′)		
273.15	1.459	1.432	1.405	1.378	1.351
283.15	1.440	1.412	1.384	1.356	1.327
293.15	1.420	1.391	1.362	1.333	1.304
298.15	1.410	1.381	1.351	1.322	1.292
303.15	1.401	1.371	1.341	1.311	1.281
313.15	1.382	1.351	1.320	1.289	1.258
323.15	1.362	1.330	1.298	1.266	1.234
333.15	1.342	1.309	1.276	1.243	1.210
343.15	1.322	1.288	1.254	1.220	1.186
353.15	1.302	1.267	1.232	1.197	1.162
363.15	1.282	1.246	1.210	1.174	1.138
373.15	1.262	1.225	1.188	1.151	1.114

TABLE 6

Calculated Thermoneutral Cell Voltages for NiCad Batteries as a Function of Temperature

T/K	ΔE^{T}_{cell} (V) Reaction (1)	Reaction (1′)
273.15	1.580	2.033
283.15	1.574	2.040
293.15	1.570	2.046
298.15	1.569	2.050
303.15	1.568	2.053
313.15	1.568	2.059
323.15	1.569	2.065
333.15	1.572	2.071
343.15	1.575	2.077
353.15	1.580	2.083
363.15	1.585	2.089
373.15	1.591	2.095

TABLE 7

Calculated Thermoneutral Cell Voltages for NiH_2 Batteries as a Function of Temperature and Hydrogen Pressure

	pH_2/atm				
T/K	0.01	0.1	1.0	10.0	100.0
			Reaction 2		
273.15	1.611	1.584	1.557	1.530	1.503
283.15	1.615	1.586	1.558	1.530	1.502
293.15	1.618	1.589	1.560	1.531	1.502
298.15	1.620	1.590	1.561	1.531	1.501
303.15	1.621	1.591	1.561	1.531	1.501
313.15	1.625	1.594	1.563	1.532	1.501
323.15	1.628	1.596	1.564	1.532	1.500
333.15	1.632	1.599	1.566	1.533	1.500
343.15	1.635	1.601	1.567	1.533	1.499
353.15	1.639	1.604	1.569	1.533	1.498
363.15	1.642	1.606	1.570	1.534	1.498
373.15	1.645	1.608	1.571	1.534	1.497
			Reaction (2′)		
273.15	2.065	2.038	2.011	1.983	1.956
283.15	2.081	2.053	2.025	1.997	1.969
293.15	2.094	2.065	2.036	2.007	1.978
298.15	2.100	2.071	2.041	2.012	1.982
303.15	2.106	2.076	2.046	2.016	1.986
313.15	2.116	2.085	2.054	2.023	1.992
323.15	2.124	2.092	2.060	2.028	1.996
333.15	2.131	2.098	2.065	2.032	1.999
343.15	2.137	2.103	2.069	2.035	2.001
353.15	2.142	2.107	2.072	2.037	2.002
363.15	2.156	2.110	2.074	2.038	2.002
373.15	2.149	2.112	2.075	2.038	2.001

HIGH SPECIFIC ENERGY, HIGH CAPACITY NICKEL-HYDROGEN CELL DESIGN

James R. Wheeler
Eagle Picher Industries
Joplin, Missouri 64801

ABSTRACT

A 3.5 inch rabbit-ear-terminal nickel-hydrogen cell has been designed and tested to deliver high capacity at steady discharge rates up to and including a C rate. Its specific energy yield of 60.6 wh/kg is believed to be the highest yet achieved in a slurry-process nickel-hydrogen cell, and its 10°C capacity of 113.9 AH the highest capacity yet of any type in a 3.5 inch diameter size. The cell also demonstrated a pulse capability of 180 amps for 20 seconds. Specific cell parameters and performance are described. Also covered is an episode of capacity fading due to electrode swelling and its successful recovery by means of additional activation procedures.

CELL DESCRIPTION

A development program was initiated with the objective of maximizing power and specific energy for 3.5 inch diameter nickel-hydrogen cells while still retaining the long-cycle life and ruggedness of the positive slurry electrode. Eagle-Picher designed cells to meet this objective as part of a joint project with a major aerospace company. We have now completed and tested a 100 ampere-hour cell design in two separator versions. One version has a single layer of Zircar (zirconia-fiber cloth) separator for each positive electrode (hereafter termed -3 cells), and the other version has a single asbestos separator (-5 cells), but they are otherwise identical and were made from the same lots of electrodes and other components.

The electrolyte quantity for single layer Zircar is just slightly larger than the single layer asbestos version, and this should ensure at least equal cycle life. At Eagle Picher, single-layer Zircar cells in an on-going life test have exceeded 20,000 cycles at a depth of discharge of 15%. End of discharge and charge voltages have thus far been stable.

A photograph of a sample cell (both versions are externally the same) and a table of weights and dimensions are provided by Figure 1 and Table 1. All of the cells were equipped with strain-gage pressure monitors.

The internal cell design is a dual stack with a back-to-back electrode configuration and continuous leads to rabbit-ear terminals. The rabbit-ear terminal is a feature which permits a shorter battery height and therefore a shorter thermal path when the cells are vertically mounted. Thus, the high specific energy can be further improved at the battery level by reducing the length of cell sleeve mountings and cell inter-connections. If the cells are mounted parallel to a base plate, the rabbit-ear terminals help there as well because the cells can be rotated to minimize the length of the interconnects.

The positive electrodes are slightly thicker and more porous than Eagle-Picher's standard high-bend-strength slurry plaque. They are approximately double the bend-strength of dry sinter, but only about 3/4 the strength of the standard slurry product. Bend strength may be considered a measure of the resistance of the electrode to plate swelling.

Four Zircar cells and three asbestos cells were built. The electrolyte concentration was set at about 39% in order to maximize the specific energy of the cell. It was hoped that this high concentration would not be so great as to cause the positive electrodes to swell, since it has proved compatible with the standard electrodes in the past. As we were to learn later, this was not the case.

A catalyzed wall wick is incorporated for improved thermal operation and gas management, making the cell suitable for either LEO or GEO applications. The final electrolyte levels for the two versions were about the same, with the single Zircar version holding, on average, only 1% more per cell than the single asbestos version.

The pressure vessel is Inconel 718. MEOP translates to a minimum burst safety factor of 2.5. The actual maximum pressure reached by the highest Zircar version cell under conditions of severe overcharge was 3% greater than the value for the asbestos.

INITIAL CELL TESTING

Four Zircar-separator cells and three asbestos cells were built. After activation, the cells were tested to the customer's performance specification, which conservatively assumed a rated capacity of 90 AH. For the initial acceptance testing therefore, standard capacity charges were 9 amps for 16 hours. The discharge rate used was 68 amps. Performance data are summarized in tables 2 and 3. Average discharge voltage performance for each type of cell is shown by the curves in Figure 2. Mid-discharge values (45 minutes) are comparable to those achieved in shorter 3.5 inch cells, indicating that the internal bussing has an adequate cross-section. The voltage advantage of Zircar over asbestos is apparent, and is essentially the same for the single Zircar configuration as would be expected from a double Zircar design.

Testing also included a 180 amp pulse test (See Figure 2). The pulse was conducted after a 16 hour, 9 amp charge and 15 minutes of the 68 amp discharge. Pulse duration was 20 seconds. Minimum terminal voltages reached at the end of the pulse were 1.17 V for the Zircar version cells, and 1.13 V for the asbestos cells.

The Zircar version achieved 60.1 watt-hours per kilogram at 10°C to 1.0 V at a discharge rate of 68 amps (C/1.47 for a 100AH nominal rating). (Watt-hour values were not merely estimated on mid-point voltages, but were actually measured by the automated data collection software.) In the same test the asbestos version achieved 59.0 watt-hours per kilogram. Capacities would have been greater and discharge voltage higher at a more-normal C/2 rate. They would also likely have been higher had the cells been charged closer to a true C/10 rate, i.e. at 10 amps rather than 9.

Without the strain gages, the values would be 60.6 wh/kg and 59.4 wh/kg respectively. These are believed to be the highest energy densities yet achieved at the cell level for nickel-hydrogen cells with slurry-process positive electrodes. The performance exceeds other large cells recently reported, including some 83AH cells [1] and the 90AH HST cells [2]. The evolution of size and power of slurry-type cells at Eagle-Picher is shown in Figure 3. The progression in efficiency has paralleled a rather steady increase in cell size and increasing operating pressures over the last 10 years.

Capacity retention at 10°C was measured by charging the cells for 16 hours at 9.0 amps, and, after an open circuit stand of 72 hours, discharging at 68 amps to 1.0 V. The percentages of capacity retained, when compared to the standard 10°C test, were 84.6% for Zircar, and 85.8% for asbestos. These are in the expected range for nickel-precharged cells.

SUBSEQUENT TESTING

After initial acceptance tests 6 of the 7 cells were shipped to the customer, with one asbestos cell being retained in cold storage at Eagle Picher. At the customer's facility the cells were subjected to characterization tests with a nominal rating of 100AH. The testing included discharges at 74.5 amps and 100 amps. Counting the initial acceptance and conditioning testing, 51 full-depth cycles had been performed on the cells when, within a few cycles of the end of this period, the cells declined in capacity from an initial value of about 114 AH to about 102 AH at 10°C The cells were returned to Eagle Picher at this point, where the low capacity condition was confirmed. There was no evidence of a second plateau in the discharge curve.

A destructive physical analysis (DPA) was performed on one of the single Zircar cells. The results showed that the positive electrodes had expanded in thickness about 12% above their initial installed thickness. This condition is consistent with the literature [3] [4] indicating a correlation of positive electrode swelling with high electrolyte concentration. Analysis of the electrolyte in the cell components confirmed the high concentration at an average of 39.31%. It showed that the electrolyte distribution was uniform among the four quadrants of the stack, but that each separator had given up about a third of its electrolyte to its corresponding positive electrode. It was therefore decided to remove the fill-tube welds, open all of the cells, and reactivate them, this time fixing concentration at a lower value of 35%.

To replace the cell destroyed in the DPA, the cell with asbestos separator that had been stored (S/N 5-3) was added to the group. Although this cell was never shipped to the customer and did not see the additional cycles, it was opened and reactivated with the other five in order to achieve the same electrolyte concentration as the others.

Following reactivation the cells were rapid-cycled at 10°C using 10 amp charges for 16 hours and high rate (78 amp) discharges, followed by a resistor-let-down to less than 0.01 volts. A chart of rapid-cycle performance is shown in figure 4. The initial performance was disappointing (about 92 AH), but with continued cycling the capacity rose steadily. After 24 full-depth cycles the capacities of the Zircar cells were again above 100 AH. Note that the discharge rate of 78 amps

was greater than the 68 amps used in the initial acceptance tests, and the charge rate was also greater by 1 amp. It can be seen that the replacement asbestos cell (S/N 5-3) was initially higher than the others and remained fairly level in capacity until about cycle 12, whereupon it appeared to rejoin the other two asbestos cells in performance. This cell however developed a leak due to the reopening process and had to be repaired. In the process of repairing a damaged fill tube, a small piece of aluminum from a fixture fell into the cell. This may affect the future performance of this cell.

At cycle 16, due to small leaks in the activation plumbing on some of the cells, it was decided to reset the nickel precharge, which in effect meant adding a small amount of hydrogen. This had a positive effect on capacities. Following cycle 28, the cells were removed from the test fixtures and welded off. This involved another setting of nickel precharge similar to the last. Following pinch-off the cells were subjected to one additional 10°C rapid cycle, this time at the lower discharge rate of 74.5 amps. The capacity jumped about 5 AH after pinch-off. It is probable that this is due partly to the lower discharge rate (74.5 amps versus 78 amps) and possibly because capacities were somewhat hydrogen-limited prior to that time due to plumbing leakage. (Pinch-off involves some hydrogen addition). The cells were then subjected to an abbreviated acceptance test using 10 amp charges for 16 hours and 74.5 discharges, a lower discharge rate than for the 28 rapid cycles just completed.

Performance data for the 25 rapid cycles and the final mini-ATP are summarized in Table 4. It is clear that much of the original high-capacity performance has been restored. Charge retention at 10°C was also confirmed at 86% to 88%.

PLANS

The cells are being returned to the customer and will be cycled to confirm the latest results. Vibration testing is also planned. Life testing is then planned for up to 15 years and will be to a GEO regime (real-time eclipse cycling to an 80% depth of discharge with shortened sun-times).

CONCLUSIONS

By using single-layer separator and slightly thicker, slightly more-porous positive electrodes, specific energies of 3.5 inch nickel-hydrogen cells can exceed 60 watt-hours per kilogram and provide good, all-around performance, even at discharge rates of C/1.28. The use of single layer Zircar separator appears promising, but requires further validation through life-testing.

The testing demonstrates that a 3.5 inch-diameter cell can be made to yield capacities above 110 AH . This is important to spacecraft designers who are requiring larger-capacity batteries for many applications. If these higher-power requirements can be satisfied by a 3.5 inch design, thermal characteristics will be better than with a larger-diameter cell.

It was also demonstrated that a swollen-positive-electrode condition can be corrected through application of activation techniques. The long-term efficacy of this requires confirmation through cycle-testing. Such testing is planned for these cells.

ACKNOWLEDGMENT

The professional assistance of Paul Daugherty in collecting and assessing data for this paper, and of David Cooke for cell construction and testing, are gratefully acknowledged.

1. T. M. Yang, C. W. Koehler, A. Z. Applewhite, "An 83AH Nickel Hydrogen Battery for Geosynchronous Satellite Applications," 24th IECEC Washington, D.C., Vol. 3, p. 1375

2. Jeffrey C. Brewer, Thomas H. Whitt, J. Roy Lanier, Jr., "Hubble Space Telescope Nickel-Hydrogen Batteries Testing and Flight Performance," 26th IECEC, p. 257, Vol 3

3. J. J. Smithrick, and S. W. Hall, "Validation Test of Advanced Technology for IPV Nickel-Hydrogen Flight Cells - Update," 27th Intersociety Energy Conversion Engineering Conference Proceedings, IECEC '92, San Diego, CA, 1992, Vol. 1, p.1.215

4. H. S. Lim, and S. A. Verzwyvelt, "KOH Concentration Effect on Cycle Life of Nickel Hydrogen Cells, III. Cycle Life Test," Journal of Power Sources, Vol. 22, Mar-Apr 1988, pp. 213-220

CELL DESCRIPTION	TYPE SEPARATOR	
	Single Zircar	Single Asbestos
Weight (grams)*	2279	2236
Cell Length (in) Dome to Dome	10.97	10.97
Cell Length (in) Overall	11.56	11.56
* strain gage weight subtracted (17g)		

TABLE 1

CAPACITIES TO 1.0V (AH) AT 68 AMPS	SEPARATOR TYPE	
	Zircar	Asbestos
30°C	81.3	82.9
20°C	99.1	99.7
10°C	113.9	111.3
0°C	117.6	113.1
-10°C	115.6	108.2

TABLE 2

PERFORMANCE DATA	TYPE SEPARATOR	
	Zircar	Asbestos
180 Amp Pulse, Minimum Voltages	1.173	1.130
WH/Kg	60.1	59.0
WH/Kg*	60.6	59.4
* Strain gage weight subtracted		

TABLE 3

Capacities to 1.0V (AH) at 74.5 Amps (Post-Reactivation)	SEPARATOR TYPE	
	Zircar	Asbestos
30°C	77.8	81.0
10°C	107.6	101.8
0°C	117.8	109.1

TABLE 4

FIGURE 1

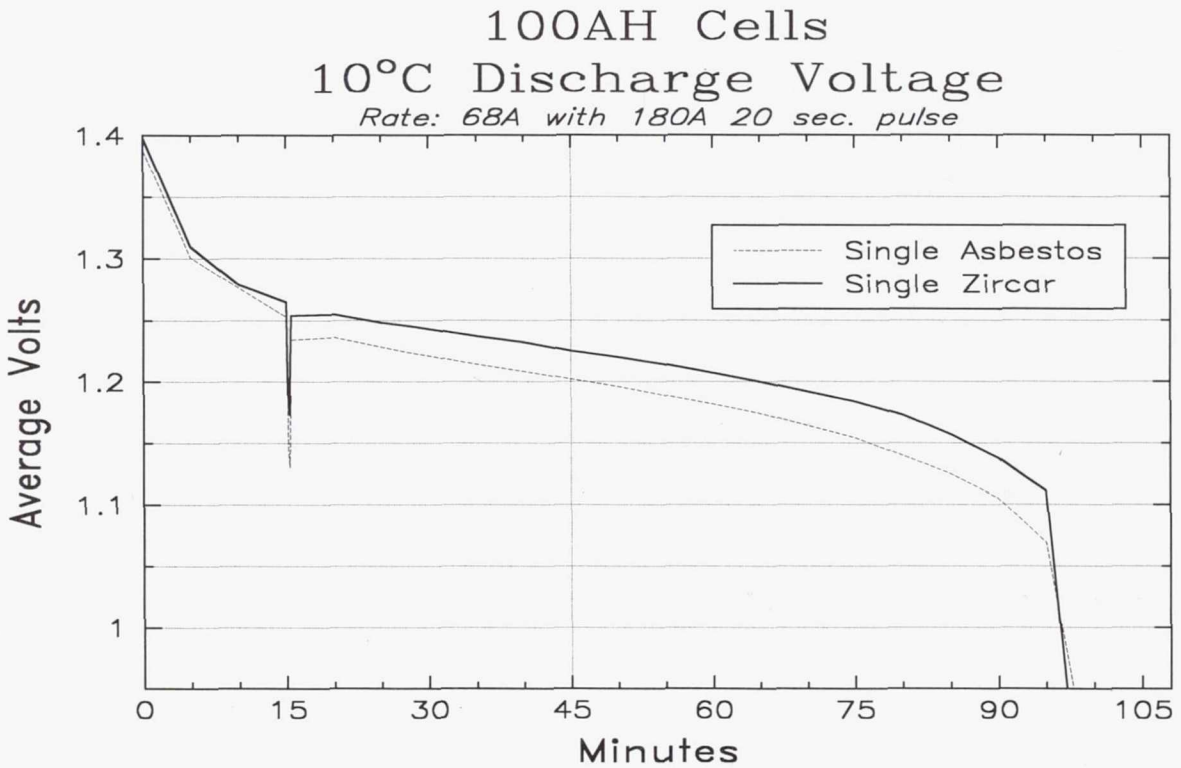

FIGURE 2

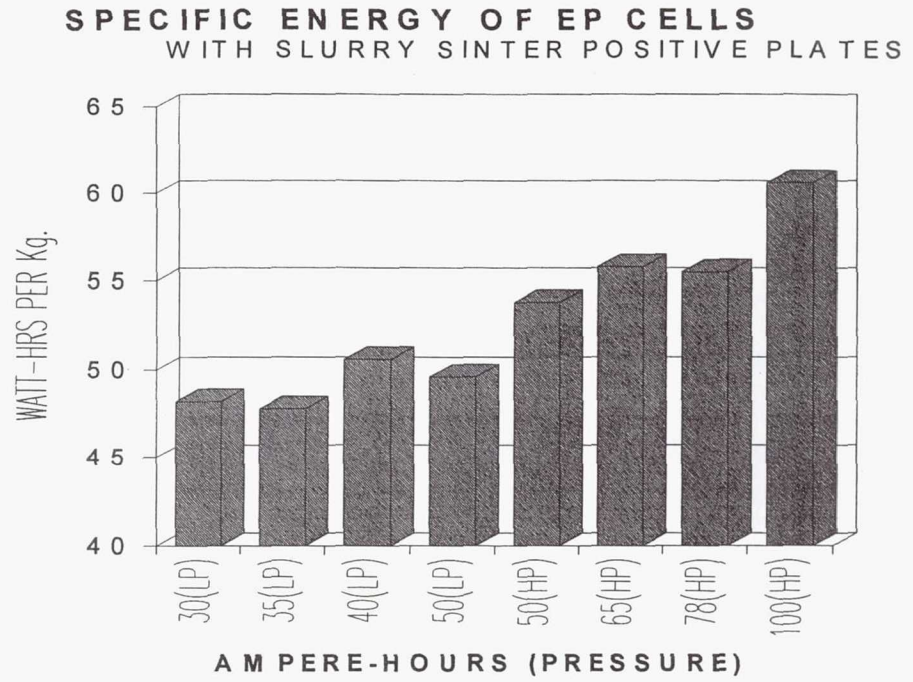

FIGURE 3

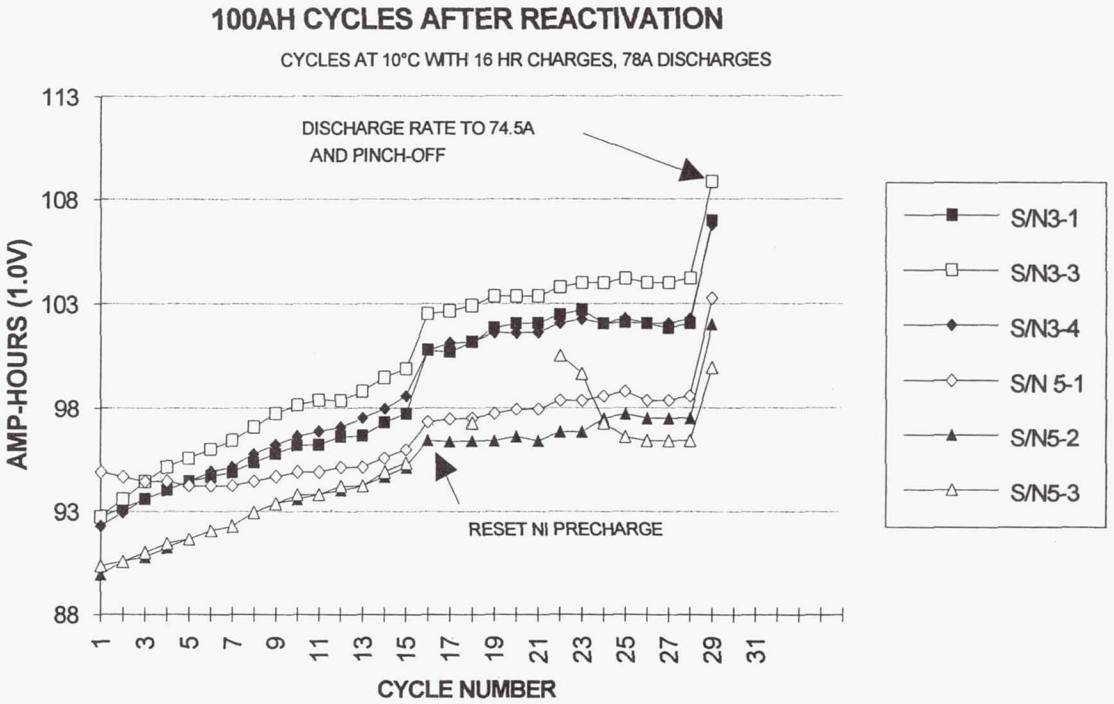

FIGURE 4

HIGH SURFACE AREA, LOW WEIGHT COMPOSITE NICKEL FIBER ELECTRODES

By Bradley A. Johnson, Richard E. Ferro, Greg M. Swain,
and Bruce J. Tatarchuk

Department of Chemical Engineering and
Space Power Institute
Auburn University, Alabama, 36849

ABSTRACT

The energy density and power density of light weight aerospace batteries utilizing the nickel oxide electrode are often limited by the microstructures of both the collector and the resulting active deposit in/on the collector. Heretofore, these two microstructures have been intimately linked to one another by the materials used to prepare the collector grid as well as the methods and conditions used to deposit the active material. Significant weight and performance advantages have been demonstrated by Britton[1] and Reid[2] at NASA-LeRC using FIBREX nickel mats of ca. 28-32 μm diameter. Work in our laboratory has investigated the potential performance advantages offered by nickel fiber composite electrodes[3,4,5] containing a mixture of fibers as small as 2 μm diameter (Available from Memtec America Corporation). These electrode collectors possess in excess of an order of magnitude more surface area per gram of collector than FIBREX nickel. The increase in surface area of the collector roughly translates into an order of magnitude thinner layer of active material. Performance data and advantages of these thin layer structures will be presented. Attributes and limitations of their electrode microstructure to independently control void volume, pore structure of the $Ni(OH)_2$ deposition , and resulting electrical properties will be discussed.

INTRODUCTION

The secondary nickel-hydrogen (Ni/H_2) battery is a hybrid of the secondary Ni-Cd battery and the H_2/O_2 fuel cell; a combination of the two best performing electrodes from these two systems. The Ni/H_2 battery possesses many advantages over other battery systems which include (1) long cycle life, (2) stability to overcharge and (3) a built-in state-of-charge indicator (cell pressure). However, the energy density and power density of light weight aerospace batteries utilizing the nickel hydroxide electrode are often limited because they must be designed with large void volumes to avoid clogging of the conductive pathways with precipitant during electrochemical impregnation.

Previous research has concentrated on increasing the porosity of powder sinters while attempting to maintain acceptable structural integrity and electrical conductivity.

Other attempts have been to impregnate the powder sinter substrate more efficiently with active material resulting in an increase of the electrochemical utilization. More recently, work has involved the impregnation of FIBREX (™ National Standards) nickel fibers which has been shown to possess superior performance characteristics, especially in terms of weight savings compared with plaque-based materials[1]. Our laboratory has investigated the potential performance advantages offered by nickel fiber composite electrodes[2,3] using nickel fibers as small as 2 μm. The supposition was that the incorporation of small diameter nickel fibers (2 μm) into FIBREX, or the use of the stand alone small diameter fiber composite electrode, would result in a significant increase in the surface area available for deposition of the active material without a significant reduction in void volume. Superior performance characteristics of the nickel fiber composite electrode have been demonstrated. By controlling the microstructure of both the collecting grid and the active deposit, the performance of the traditional nickel hydroxide electrode has been enhanced. Furthermore, the electrochemical impregnation at a reduced effective current density results in a much thinner layer of active material, which is more electrochemically accessible.

The key advantages of using small nickel fibers versus sintered nickel plaques or FIBREX include an order of magnitude higher specific surface area per gram of fiber. This not only provides increased area for the active deposit, but also increases electrochemical accessibility to the active material. Additionally, there is a low ohmic resistance within the microstructure due to the sinter bonded fibers and low mass transport resistance within the microstructure voids resulting in easier transport of electrolytes. Moreover, this electrode can be prepared with adjustable porosities and void volumes to enhance inter- and intra-electrode transport while accommodating the required precipitation of chemical products at the cathode. Finally, its electronic properties are independent of any mechanical pressing.

EXPERIMENTAL METHODS

A. ELECTRODE STRUCTURE AND PREPARATION

Sintered fiber mats were produced using small nickel fibers and cellulose. The nickel fibers had diameters of approximately 2 μm and were 2-3 mm in length. The cellulose, a mixture of soft and hardwoods, was 20-30 μm in diameter and 100 to 1000 μm in length. These materials were then incorporated into a paper preform. This was done by first thoroughly mixing the metal fibers in an industrial blender. They were then agitated with the cellulose fibers until all fibers were uniformly dispersed. The solution of dispersed fibers was then further diluted and formed into a 16 cm diameter paper preform on a sheet mold. The preform was then pressed and allowed to dry in air.

Once the paper preforms were fabricated, circular discs ca. 19 mm were cut from the preforms. Four of these discs were pressed together and placed on top of a 1 mil thick nickel foil. This structure was then sintered at 1323 K for 30 minutes under a hydrogen atmosphere. The sintering creates many intimate electrical contacts per fiber and provides the mechanical stability required to withstand stress associated with swelling and

contraction of the active material during cycling. Additionally, during the sintering process, virtually all of the cellulose gasifies, resulting in large pores and voids inside the electrode microstructure.

The electrochemical impregnation of the $Ni(OH)_2$ active material was carried out using the methods described by Britton[1]. The electrode was placed in an acidic solution of 1.5 M $Ni(NO_3)_2$, 0.175 M $Co(NO_3)_2$, and 0.075 M $NaNO_3$. Using current densities in the range of 5-10 mA/cm² of geometrical surface area for 3-6 hours, a loading of 1.9 ± 0.4 g $Ni(OH)_2$/cc was achieved. The electrochemical reduction of nitrate produces hydroxide ions in the vicinity of the bare metal fibers. Nickelous ions in solution combine with the hydroxide ions to form nickel hydroxide, which precipitates out of solution onto the surface of the fibrous network. After impregnation, the structure is rinsed with distilled water, dried in an over at 393K for 1 hour, and stored under ambient conditions for a minimum of 12 hours.

B. ELECTRODE EVALUATION

Cycle-life testing was performed in a half cell arrangement as described by Britton[1]. A platinum gauze counter electrode was used and all potentials are reported versus a saturated calomel electrode (SCE). All measurements were made at room temperature in 26 wt% KOH. Cyclic voltametry and cyclic chronopotentiometry were performed using a EG&G Princeton Applied Research Model 273 Potentiostat/Galvanostat. During cyclic chronopotentiometry, a current of C/2 was used, while discharge current varied from C/2 to 3C. The C-Rate is defined as being the theoretical rate at which all active material will be reduced in a period of 1 hour. From these measurements, conditioning times, capacities, and efficiencies were determined.

Scanning electron micrographs were obtained with a JEOL 440 Microscope. Both impregnated and non-impregnated electrodes were examined to determine the overall effects of impregnation on the electrode microstructure. Furthermore, SEM was utilized to confirm the sintering of metal contacts and to view the overall fiber distribution.

DICUSSION AND RESULTS

Figures 1 and 2 show SEM micrographs of the nickel fiber composite electrode before and after impregnation, respectively. In the micrograph of the bare electrode, the sintered contacts between the individual fibers along with the sizable void volume can be seen (Fig. 1). The large number of sintered joints provides high conductivity pathways and mechanical strength. The impregnated electrode possesses a relatively thin and conformal coating over the entire electrode surface (Fig. 2). The active material possesses many apparent defects and grain boundaries and exhibits regions of apparent high crystallinity. The high surface area and large void volume of the electrode allows for a considerable loading of active material while maintaining a sizable void volume.

Table 1 compares the physical properties of the electrode microstructures examined during the course of this research before and after impregnation. The two columns of data most noteworthy are the values for FIBREX and those for the nickel fiber

composite electrode. The composite electrode is thinner, possesses a 10 fold increase in specific surface area and is slightly more porous than FIBREX. After impregnation, the nickel fiber composite electrode possesses a higher weight of active material per unit void volume, a higher volume percent loading and a thinner layer of active material compared with FIBREX. Differences in surface area and active deposit thickness result from the smaller diameter fibers used in the composite electrode. It is important to note that while the electrodes possessing stainless steel fibers have a significantly larger surface area than FIBREX, the performance data was poor due to the weak adhesion of the active material to stainless steel. The incorporation of small diameter nickel fibers into FIBREX improves the physical properties of the electrode, however, the nickel fiber composite electrode possesses the most desirable properties.

Figure 3 shows typical charge and discharge curves for impregnated FIBREX and nickel composite electrodes. The loading level per unit void volume is 1.52 g/cc and 1.69 g/cc, respectively. Again, the larger surface area of the composite electrode results in the ability to deposit a considerable amount of active material while maintaining a sizable void volume. In both cases, charging was performed at a C/2 rate while discharging was performed at a 3C/2 rate. It can be seen that the potential during charging (oxidation) at the two electrodes is ca. 0.8 and 0.5 V, respectively. The more positive potential plateau at the FIBREX electrode is indicative of a higher ohmic resistance and/or mass transport resistance and suggests that much of the current being passed is going toward oxygen evolution; a parasitic side reaction which reduces the overall charge/discharge efficiency. The more negative potential plateau observed at the nickel fiber composite electrode reflects less ohmic loss and suggests that a higher percentage and the current passes is going toward the oxidation of the active material to form the oxyhydroxide rather than toward oxygen evolution, although it is likely that even at this potential oxygen evolution is occurring to some degree. Upon reversal of the current to initiate the discharge process, it can be seen that the electrode potential of FIBREX quickly drops and plateaus at a more negative potential compared with the nickel fiber electrode. Again, this difference is likely due to the increased ohmic loss within the FIBREX electrode. The most noteworthy difference between the two electrodes is the increased capacity present at the composite electrode. The percent utilization at the composite electrode is greater than 200%. The maximum utilized capacity was usually reached within 5 to 10 cycles which compares most favorably with the greater than 200 number of cycles often required for many commercially available electrodes.

Table 2 contains the specifications used in the charge and discharge cycles. The FIBREX-containing electrodes contain a larger amount of active material and consequently, a higher rating (mA-hr). This active deposit is relatively thick compared with that estimated for the nickel fiber composite electrode. The increased thickness produces more mass transport impedance and results in a reduced efficiency. Most importantly, the utilization typically observed at the FIBREX electrodes, containing small metal fibers, is near 200%. However, a 300% utilization is routinely observed at the nickel fiber composite electrode. A less efficient utilization is observed at the stainless steel composite electrode because of the poor adhesion of the active material.. The active material was observed to detach from off the electrode during cycling.

The effect of the discharge rate on the utilization was examined and is shown in Figure 4. Data for a FIBREX and two nickel fiber composite electrodes are shown; one with a low loading of 0.66 g/cc and one with a high loading of 1.69 g/cc. All charging cycles were performed at C/2 and each data point was obtained after 5 cycles. The data for the FIBREX electrode show the expected trend of decreasing utilization of the active material with increasing rate. This decrease is due to the deficiency of protons within the active material near the reaction sites and to the mass transport impedance through the thick film. On the contrary, the data for the nickel fiber composite electrodes show an increasing trend of utilization with discharge rate up to a rate near 2C where the utilization begins to decrease. Higher utilizations are observed at the composite electrode with the lower loading, as would be expected.

Figure 5 shows a plot of the percent utilization versus the cycle number for a typical impregnated composite electrode. The plot shows how the conditioning time is short at the composite electrode as full utilization is reached within the first 10 cycles. The utilization is approaching 280% after 10 cycles and remains relatively constant for the first 500 cycles. In each cycle, the charging step was performed at a C/2 rate and the discharging was performed at a 3C/2 rate. After 500 cycles, the utilization begins to decrease and by the time 1000 cycles have been performed, the utilization is near 150%. The percent utilization is defined as the ratio of the charge passed during the reduction of the active material (discharging), before the electrode potential decreases to -0.2 V vs. SCE, to the charge passed during oxidation of the active material (charging).

Figure 6 lists some of the possible reactions which might be occurring to give rise to the anomalous increase in capacity. At present, we have not identified the source of the increased capacity but we are currently conducting a detailed mechanistic study of the nickel hydroxide/oxyhydroxide redox process at the composite electrode. One possibility involves the generation of hydrogen at the nickel electrode for extended periods of time during the discharge cycle. The discharge cycle tests, described herein, were always performed for a defined period of time regardless of the electrode potential value. In many cases, the electrode potential decreased to ca. -1.2 V vs. SCE and remains there for extended periods of time during the discharge cycle in order to maintain the desired current flow. Consequently, significant quantities of hydrogen were produced. In this same potential region, bare nickel substrate is exposed due to the reduction of nickel hydroxide. The bare substrate provides sites for the dissociative chemisorption and or oxidation of hydrogen which can then be injected into the active material adjacent to these reaction sites. The injected protons may increase the ability to discharge residual or isolated capacity by increasing the proton concentration which supports conductivity[4]. The limiting step in the reduction of nickel oxyhydroxide to nickel hydroxide is known to be the proton transfer. Increasing the availability of protons in the active material will result in an increased utilization. The hydrogen gas generated can also be occluded within the pores and defects of the active material and react chemically with isolated nickel oxyhydroxide to reduce it back to nickel hydroxide as part of a self discharge mechanism[5,6].

All of the cycle tests reported herein were conducted during exposure to the atmosphere. CO_2 will readily dissolve in alkaline solution to form CO_3^{2-} anions. These

anions may affect the overall performance by intercalating and assisting in the compensation of the excess charge introduced by the presence of Co^{3+} and higher nickel oxides[7]. It is also possible that the CO_3^{2-} anions can be reduced to a hydrocarbon species. Another possible reaction which may contribute to the charge passed during discharge is the reduction of carbon in the presence of excess protons to form methane. The carbon forms on the electrode surface because of the incomplete gasification of the cellulose during the sintering process. This is only speculation at this point as the potentials at which these two reactions occur at a substantial rate have not been identified. Additional sources for the extra capacity may also involve the chemical reaction of occluded oxygen with the lower oxide to form the higher oxide. If this reaction were to occur at an appreciable rate in competition with the electrochemical reduction during discharge, then additional capacity could be obtained. This chemical reaction may have more of an influence on the performance of the composite electrode given the thin and conformal nature of the active material deposit. Also, oxygen reduction may occur concomitant with the reduction of the higher oxide[8]. Finally, some additional capacity will result from the oxidation of the bare nickel substrate.

ACKNOWLEDGEMENTS

NASA-LeRC Electrochemical Technology Branch,
Contract # NAG3-1154
Doris Britton
Patricia O'Donnell
Peggy Reid

REFERENCES

1. D.L. Britton, "Lightweight Fibrous Nickel Electrode for Nickel Hydrogen Battery", NASA-TM-100958, 1988.

2. D. Kohler, J. Zabasajja, A. Krishnagopalan, B. Tatarchuk, J. Electrochem. Soc., 137, 136 (1990).

3. D. Kohler, J. Zabasajja, F. Rose, B. Tatarchuk, J. Electrochem. Soc., 137, 1750, (1990).

4. A.H. Zimmerman, in Proceedings of the Symposium on Nickel Hydroxide Electrodes, eds. D.A. Corrigan and A.H. Zimmerman, Electrochemical Society, vol 90-4, 1980, p. 311.

5. Z. Mao and R.E. White, J. Electrochem. Soc., 139, 1282 (1992).

6. A. Visintin, S. Srinivasan, A.J. Appleby and H.S. Lim, J. Electrochem. Soc., 139, 985 (1992).

7. C. Delmas, Y. Borthomiell, and C. Fauce, in Nickel Hydroxide Electrodes, eds. D.A. Corrigan and A.H. Zimmerman, Electrochemical Society, vol. 90-4, 1980, p.119.

8. D.T. Sawyer and L.V. Interrante, J. Electroanal. Chem., 2, 310 (1961).

Table 1. Physical properties of fiber based electrode microstructures before and after impregnation.

	FIBREX	FIBREX/SS	FIBREX/Ni	Steel	Nick.
			BEFORE IMPREGNATION		
Thickness (mils)	35	35	35	19	19
Surf. Area/ Weight (cm^2/g)	160.5	292.8	276.7	2535	2297
Density (g/cm^3)	0.49	0.55	0.55	0.33	0.35
Porosity (%)	94.4	93.7	93.7	95.8	95.8
			AFTER IMPREGNATION		
Wt. of $Ni(OH)_2$ /cm^3 of Void	0.42	0.21	0.67	1.12	0.66
Porosity (%)	80.9	86.7	74.1	66.0	75.9
Loading (vol %)	14.3	7.53	21.0	30.8	20.5
Effective Thickness of $Ni(OH)_2$ (μm)	17.1	6.49	2.64	3.51	2.47

Table 2. Specifications used for the different electrode microstructures during cycle testing.

	FIBREX	FIBREX+SS	STEEL	FIBREX+NI	NICKEL
Weight	124.6 mg	138.7 mg	28.70 mg	185.0 mg	31 mg
$Ni(OH)_2$ Weight	85.32 mg	65.88 mg	63.80 mg	120.5 mg	44 mg
Rating (mA-hr)	24.67	19.04	18.44	34.84	12.7
CHARGE (C/2)					
Act. Cur.	12.33 mA	9.52 mA	9.22 mA	17.42 mA	6.36mA
Time (s)	7200	7200	7200	7200	7200
Cur/wt. (A/g)	0.144	0.144	0.144	0.144	0.144
DISCHARGE (3C/2)					
Act. Cur.	35.99 mA	28.56 mA	27.66 mA	52.26 mA	19.1mA
Time (s)	1200	4800	1120	4800	7440
Cur/wt.	0.433	0.433	0.433	0.433	0.433
Capacity (ma-hr)	45.3	38.08	8.61	69.68	39.43
% Util.	50%	200%	36.67%	200%	310%

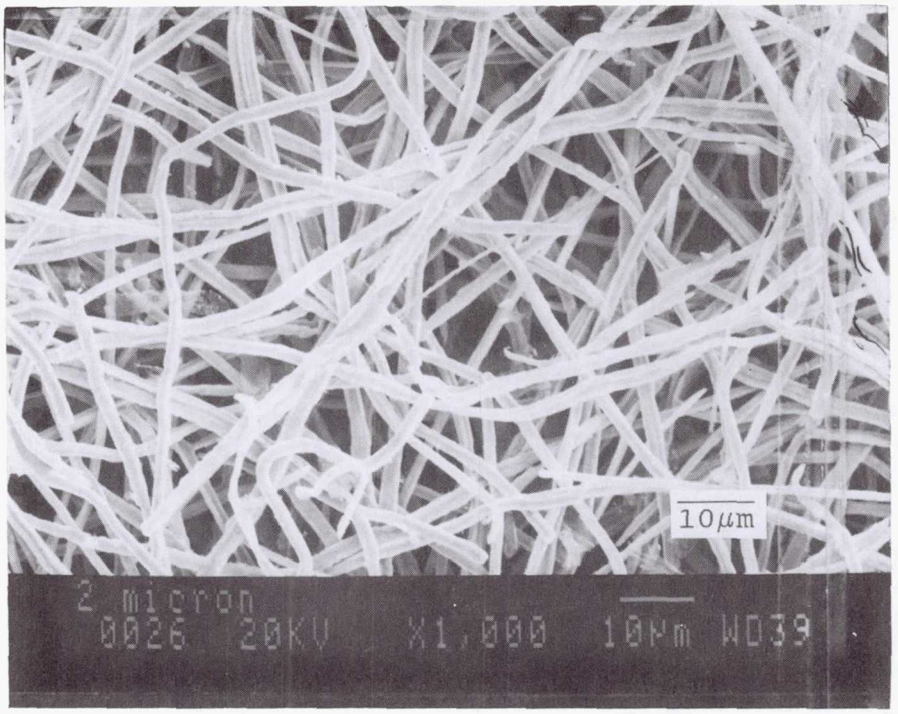

Figure 1. SEM micrograph of a bare nickel fiber composite electrode.

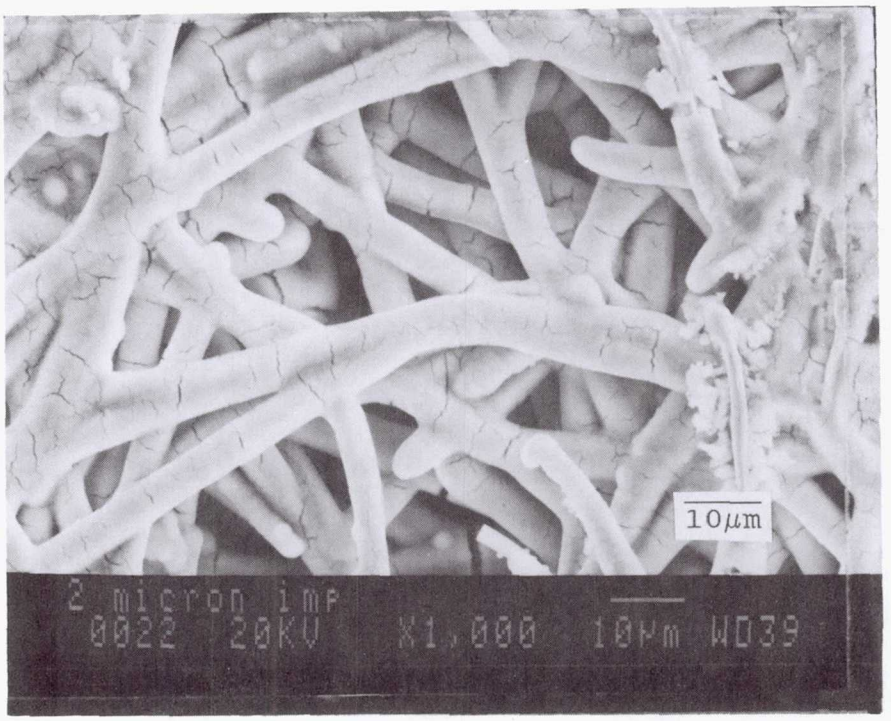

Figure 2. SEM micrograph of an impregnated nickel fiber composite material.

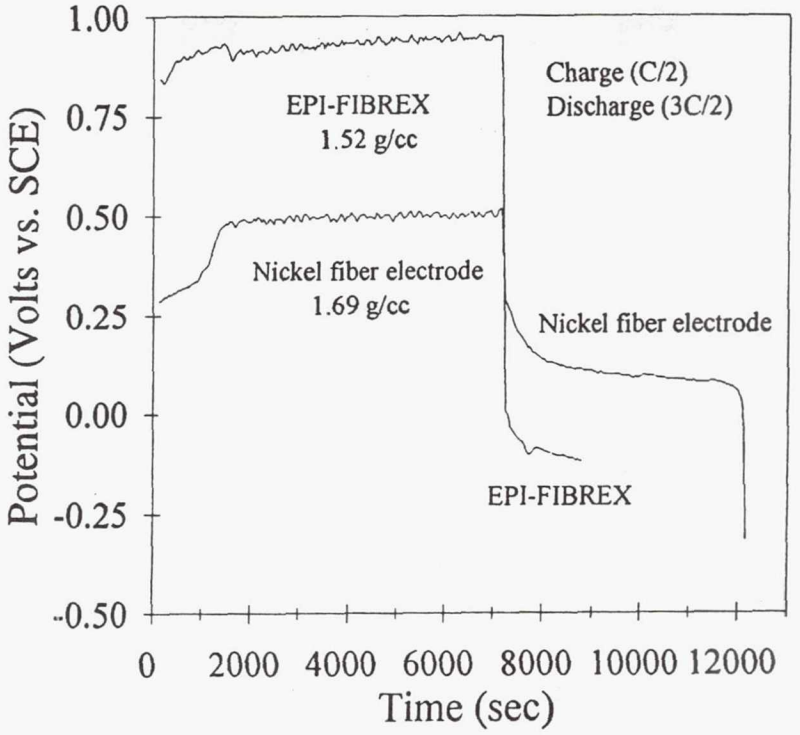

Figure 3. Charge and discharge curves for impregnated Eagle-Picher (FIBREX based) and nickel fiber composite electrodes in 26 wt% KOH.

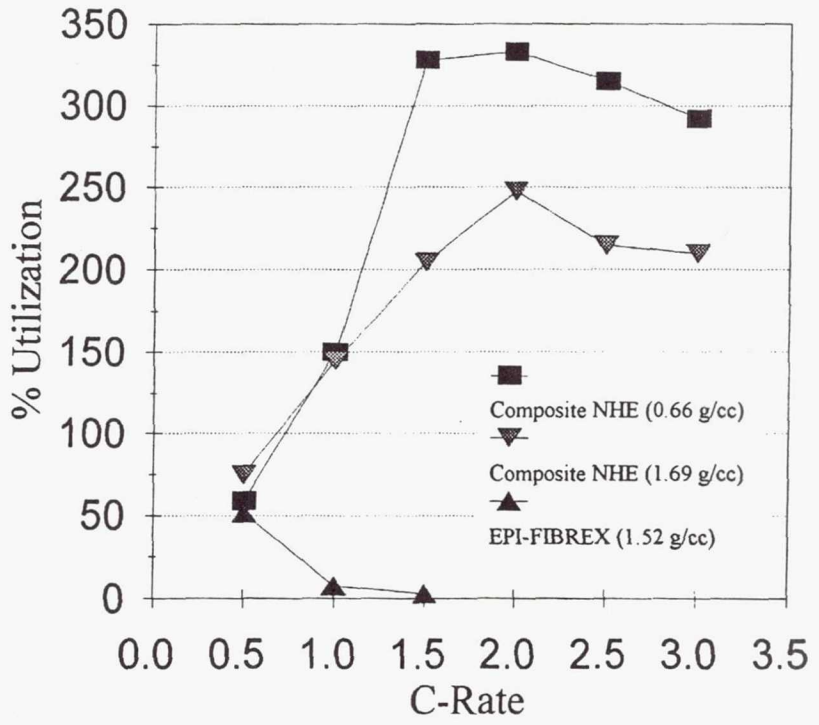

Figure 4. Plot of the percent utilization versus discharge rate for an impregnated Eagle-Picher (FIBREX-based) and an impregnated nickel fiber composite electrode at two different loading levels in 26 wt% KOH. Charging performed at C/2.

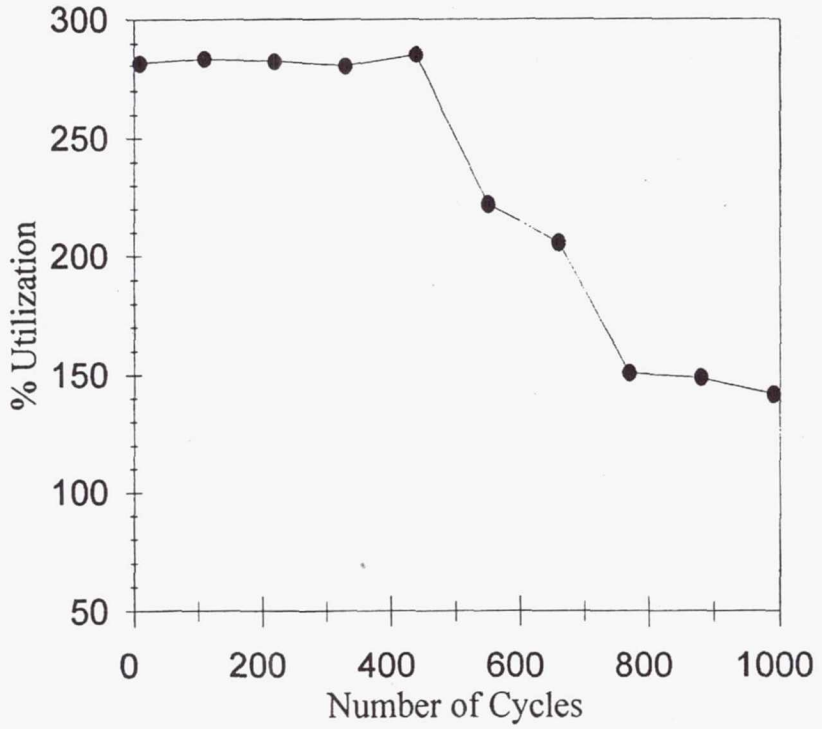

Figure 5. Plot of the percent utilization versus the cycle number for an impregnated nickel fiber composite electrode in 26 wt% KOH. Charging performed at C/2 and discharging at 3C/2.

A. Chemical Reaction: Lower Oxide + O_2/OH^- ↔ Higher Oxide
B. Growth and conditioning of active material formed on the substrate.
C. Injection of H^+/H generated during HER at sites on the composite electrode into the active material. Increased ability to discharge residual capacity by raising proton concentration which supports conductivity. Influx of protons from remaining charged active material or from H_2 generated at current collector.
D. Cycle tests performed in open atmosphere Intercalation of anions-charge neutralization within active material.

Figure 6. Possible reaction schemes to account for the "anomalous" capacity observed.

OVONIC NICKEL METAL HYDRIDE BATTERIES FOR SPACE APPLICATIONS

S. Venkatesan, D. A. Corrigan, M. A. Fetcenko,
P. R. Gifford, S. K. Dhar, and S. R. Ovshinsky

OVONIC BATTERY COMPANY,
Troy, Michigan 48084

ABSTRACT

Ovonic nickel-metal hydride (NiMH) rechargeable batteries are easily adaptable to a variety of applications. Small consumer NiMH cells have been developed and are now being manufactured by licensees throughout the world. This technology has been successfully scaled up in larger prismatic cells aimed at electric vehicle applications. Sealed cells aimed at satellite power applications have also been built and cycle tested by OBC and other outside agencies. Prototype batteries with high specific energy (over 80 Wh/kg), high energy density (245 Wh/L), and excellent power capability (400 W/kg) have been produced. Ovonic NiMH batteries have demonstrated an excellent cycle life of over 10,000 cycles at 30% DOD. Presently, Ovonic Battery Company is working on an advanced version of this battery for space applications as part of an SBIR contract from NASA.

INTRODUCTION

Space power requirements include high gravimetric and volumetric energy densities, long cycle life, and high reliability. Nickel-cadmium and nickel-hydrogen batteries are currently used for most space applications. However, these systems do have several disadvantages. The environmental impact related to the manufacture of nickel-cadmium batteries is coming under increasing scrutiny. The high cost of nickel-hydrogen batteries makes it difficult to justify their use of many applications. Further, improvements in gravimetric and volumetric energy densities for each system would be desirable.

The Ovonic nickel-metal hydride battery offers a viable alternative to the existing batteries with an opportunity for significant gains in energy density [1-3]. They have roughly twice the gravimetric and volumetric energy density of nickel-cadmium batteries. They are made with nontoxic environmentally acceptable materials. The viability of this technology has been demonstrated in consumer cell applications with batteries now being manufactured and sold around the world through licensees. Licensees of Ovonic Battery Company include Varta (Germany), Hitachi Maxell (Japan), Gold Peak (Hong Kong), Samsung (Korea), Gates Energy Products and Harding Industries.

Considerable ongoing development is aimed at larger prismatic cells for electric vehicle applications [1-3]. Last year, Ovonic Battery Company was awarded the first development contract by the United States Advanced Battery Consortium, a consortium of the big three auto companies, DOE, and EPRI to develop electric vehicle batteries.

In this paper, we describe the performance characteristics of Ovonic nickel-metal hydride cells as they apply to space applications.

RESULTS AND DISCUSSION

Previously [4], the high energy density of Ovonic nickel-metal hydride technology was demonstrated in small wound consumer cells. Gravimetric and volumetric energy densities of 70 Wh/kg and 210 Wh/L, respectively, were attained. More recently, even higher energy density was demonstrated in larger prismatic cells. Results from a 50 Ah prismatic cell showing 80 Wh/kg and 245 Wh/L are shown in Fig. 1. Presently, several proprietary approaches are being pursued at Ovonic Battery Company aimed at a specific energy well in excess of 100 Wh/kg.

In collaboration with Eagle-Picher Industries [5], we have produced prismatic cells specifically designed for satellite applications. Figure 2 shows a diagram of the OBC aerospace cells. These cells delivered 5 Ah discharged at 5 A (C-rate), which corresponds to a specific energy of 55 Wh/kg. The energy density delivered represents a two-fold improvement over the NiCd version of the cell in Fig. 2 which is rated at 2.5 Ah. The next generation of cells being fabricated at OBC under the ongoing NASA contract work will have a specific energy of 70 Wh/kg due primarily to improvements in the positive electrode energy density.

Ovonic NiMH cells also exhibit excellent high rate capability. Previously, we have demonstrated up to 400 W/kg in large prismatic cells aimed at electric vehicle applications [1-3]. The high rate performance of OBC aerospace cells is shown in Fig. 3. The dependence of discharge capacity on the discharge current up to 20 A (4-C rate) is shown. These cells deliver 80% of their rated capacity at the 4-C discharge rate.

Ovonic NiMH have a wide operating temperature range as previously reported [1-3]. Figure 4 shows the discharge performance of OBC aerospace cells over a range of temperatures. The discharge performance is virtually identical between 10 and 30°C.

Ovonic NiMH cells have been tested by Eagle-Picher [5] and Rockwell International [6,7] to determine cycle life under simulated LEO conditions (35% DOD). Rockwell International reported having achieved over 10,000 cycles when the tests were terminated for other reasons [7]. From this test, they projected a cycle life well over 17,000 cycles for Ovonic NiMH cells. In tests of Ovonic aerospace cells, Eagle-Picher attained over 7,000 cycles to 37% DOD. Charge-discharge curves are compared for cycles 89, 4900, and 7900 in Fig. 5.

Resistance to abusive overcharge and overdischarge conditions is a unique feature of the Ovonic NiMH technology which should provide for improved reliability in actual operation in spacecraft applications. Intrinsic overcharge protection is provided via an oxygen recombination cycle where oxygen evolved at the positive electrode is recombined at the negative electrode. Intrinsic overdischarge protection is provided via a hydrogen recombination cycle where hydrogen evolved at the positive electrode is recombined at the negative electrode. Previous results [4] have shown Ovonic NiMH cells can be repeated overcharged and/or overdischarged by 15% or more for hundreds of cycles without damage.

Ovonic nickel-metal hydride system is a viable alternative to provide for improved energy densities beyond those currently provided by nickel-cadmium and nickel-hydrogen systems now in use. There should be no sacrifice in cycle life or reliability. However, disadvantages such as environmental concerns related to the NiCd system or high costs related to the nickel-hydrogen system can be overcome.

REFERENCES

1. S. R. Ovshinsky, P. R. Gifford, S. Venkatesan, M. A. Fetcenko, D. A. Corrigan, and S. K. Dhar, Proceedings of the 11th International Electric Vehicle Symposium, Florence, Italy, September, 1992.

2. S. R. Ovshinsky, S. K. Dhar, S. Venkatesan, M. A. Fetcenko, P. R. Gifford, and D. A. Corrigan, Proceedings of the 10th International Seminar on Primary and Secondary Battery Technology and Applications, Deerfield Beach, Florida, March 1993.

3. S. Venkatesan, D. A. Corrigan, P. R. Gifford, M. A. Fetcenko, S. K. Dhar, and S. R. Ovshinsky, Proceedings of the 8th Annual Battery Conference on Applications and Advances, Long Beach, California, January, 1993.

4. M. A. Fetcenko, S. Venkatesan, S. K. Dhar, S. R. Ovshinsky, and T. Tsang, Proceedings of the 3rd International Rechargeable Battery Seminar, Deerfield Beach, Florida, March 1992.

5. J. Brill, D. Coates, P. Bemis, S. Venkatesan, M. A. Fetcenko, S. R. Ovshinsky, AIAA/Utah State University Conference on Small Satellites, August, 1990.

6. B. M. Otzinger, NASA Battery Workshop, Huntsville, Alabama, December, 1990.

7. B. M. Otzinger, Proceedings of the 6th Annual Battery Conference on Applications and Advances, California State University, Long Beach, California, January, 1991; B. M. Otzinger, Rockwell International, personal communication, January 1992.

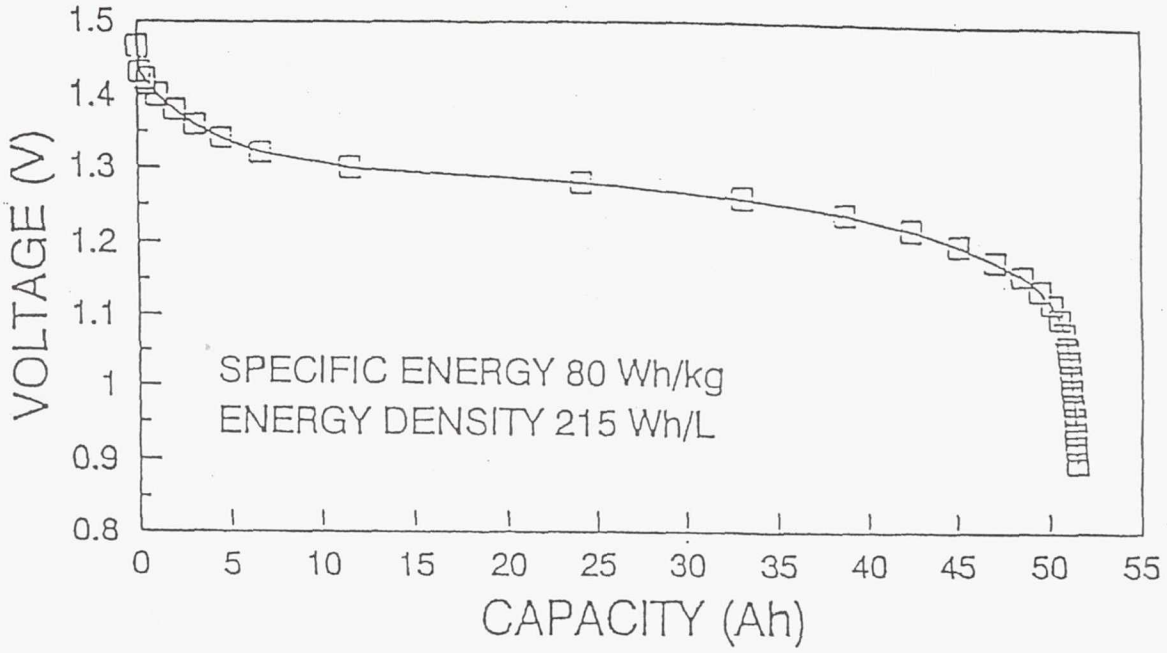

Figure 1. Discharge voltage versus time curve for advanced design 50 Ah EV prototype cell demonstrating 80 Wh/kg gravimetric energy density.

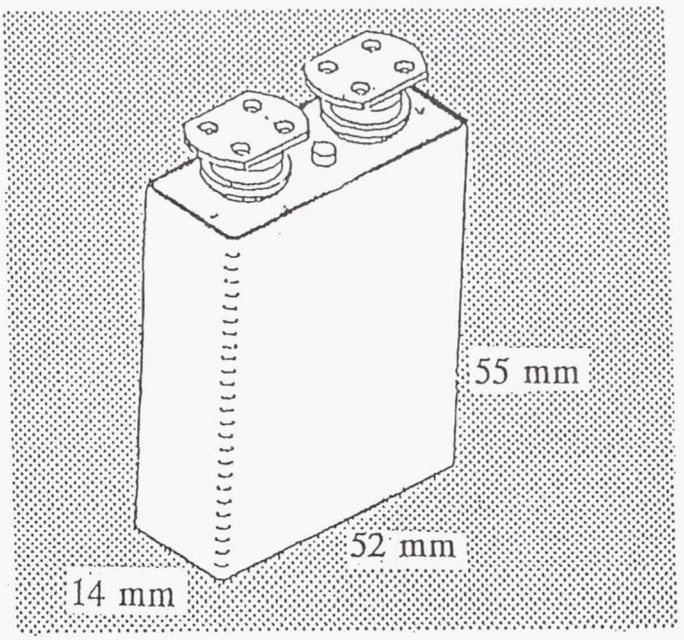

FIGURE 2

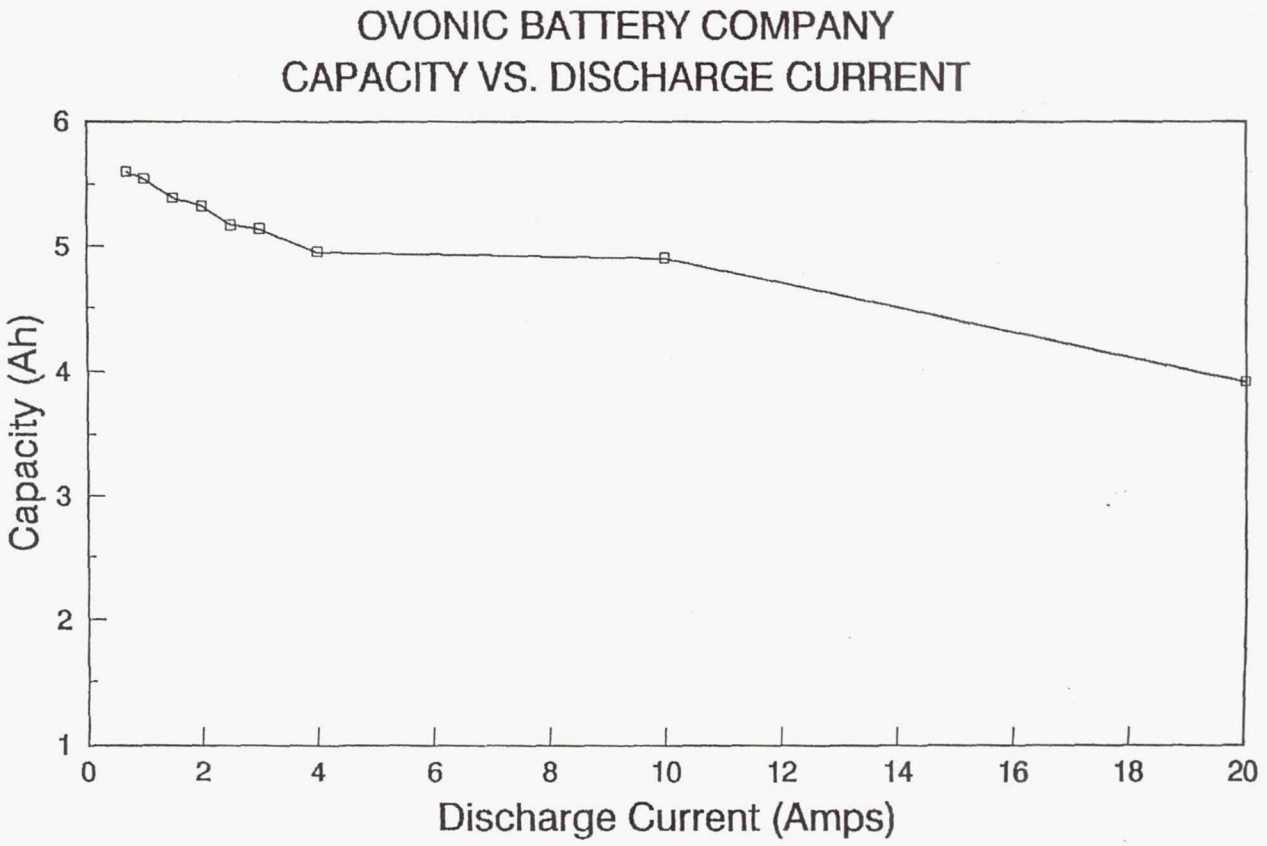

FIGURE 3

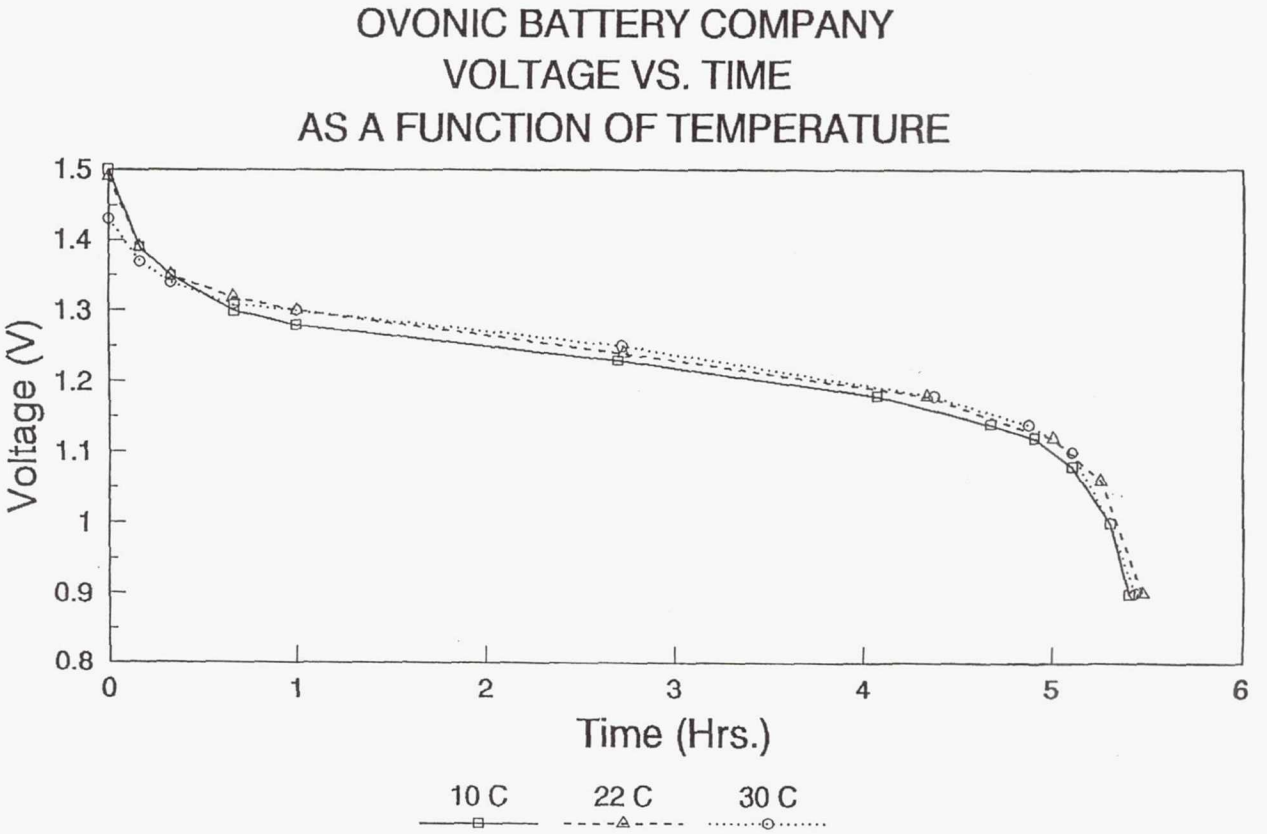

FIGURE 4

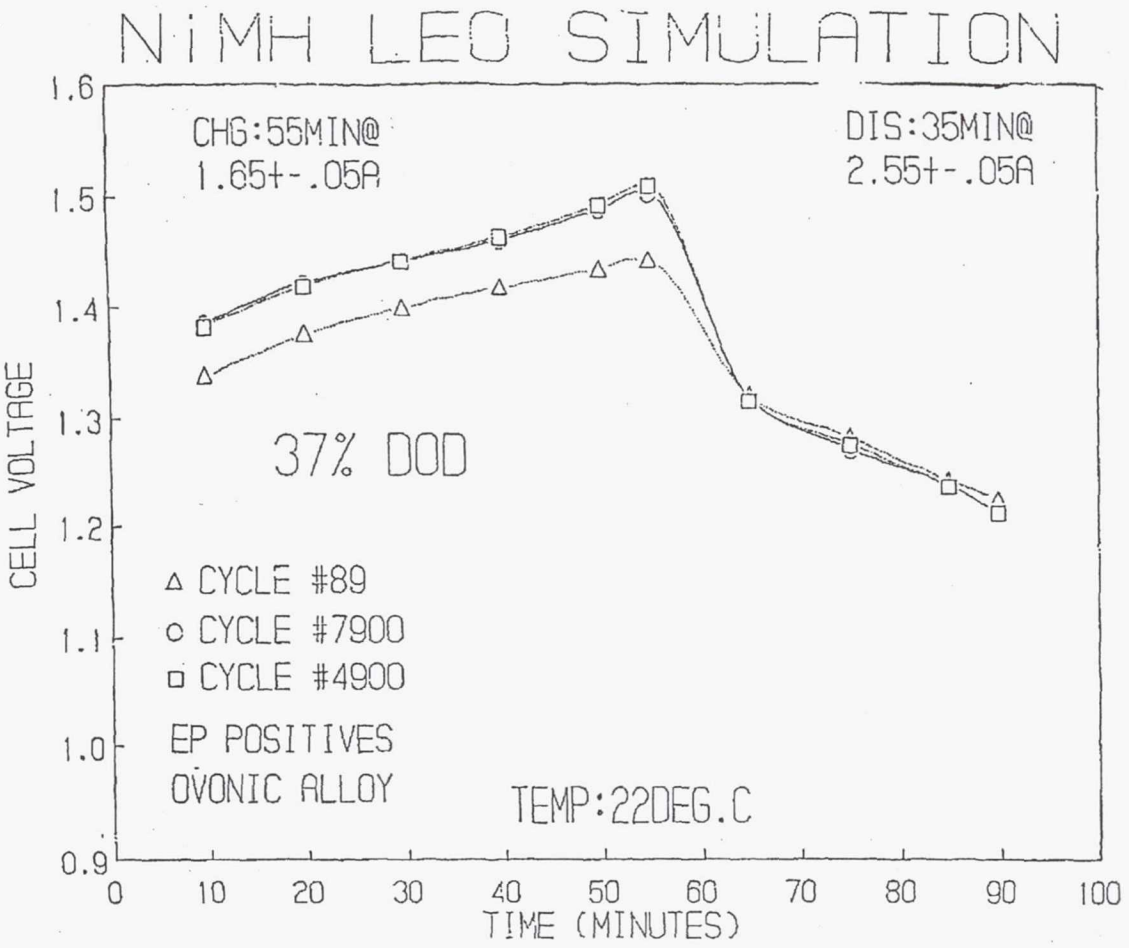
NiMH LEO SIMULATION
CHG:55MIN@
1.65+-.05A
DIS:35MIN@
2.55+-.05A
37% DOD
△ CYCLE #89
○ CYCLE #7900
□ CYCLE #4900
EP POSITIVES
OVONIC ALLOY
TEMP:22DEG.C
CELL VOLTAGE
TIME (MINUTES)
1.6
1.5
1.4
1.3
1.2
1.1
1.0
0.9
0
10
20
30
40
50
60
70
80
90
100

FIGURE 5

ALLOYS FOR HYDROGEN STORAGE IN NICKEL/HYDROGEN AND NICKEL/METAL HYDRIDE BATTERIES

Anaba Anani, Arnaldo Visintin, Konstantin Petrov and Supramaniam Srinivasan
Center for Electrochemical Systems and Hydrogen Research
Texas Engineering Experiment Station
Texas A&M University System
College Station, TX 77843-3402

James J. Reilly and John R. Johnson
Department of Applied Science
Brookhaven National Laboratory
Upton, NY 11973

Ricardo B. Schwarz and Paul B. Desch
Center for Materials Science
Los Alamos, NM 87545

ABSTRACT

Since 1990, there has been an ongoing collaboration among the authors in the three laboratories to (1) prepare alloys of the AB_5 and AB_2 types, using arc-melting/annealing and mechanical alloying/annealing techniques; (2) examine their physico-chemical characteristics (morphology, composition); (3) determine the hydrogen absorption/desorption behavior (pressure-composition isotherms as a function of temperature); and (4) evaluate their performance characteristics as hydride electrodes (charge/discharge, capacity retention, cycle life, high rate capability). This review article presents the work carried out on representative AB_5 and AB_2 type modified alloys (by partial substitution or with small additives of other elements). The purpose of the modification was to optimize the thermodynamics and kinetics of the hydriding/dehydriding reactions and enhance the stabilities of the alloys for the desired battery applications. The results of our collaboration, to date, demonstrate that (1) alloys prepared by arc-melting/annealing and mechanical alloying/annealing techniques exhibit similar morphology, composition and hydriding/dehydriding characteristics; (2) alloys with the appropriate small amounts of substituent or additive elements: (i) retain the single phase structure, (ii) improve the hydriding/dehydriding reactions for the battery applications, and (iii) enhance the stability in the battery environment; and (3) the AB_2 type alloys exhibit higher energy densities than the AB_5 type alloys but the state-of-the-art, commercialized batteries are predominantly manufactured using AB_5 type alloys.

RATIONALE FOR INVESTIGATIONS AND CRITERIA FOR ALLOY SELECTION

The interest in alloys for hydrogen storage in nickel/hydrogen and, particularly, in nickel/metal hydride batteries is gaining momentum because of the high performance characteristics of these batteries, in respect to energy efficiency, energy density, high rate charge/discharge capability and cycle life. Previous studies at CESHR, TEES-TAMUS have shown that the high rate of self-discharge in nickel/hydrogen batteries is due to the direct reduction of the nickel oxyhydroxide to nickel oxide (1-4). In these batteries, hydrogen is stored as a compressed gas and because of the high pressure of hydrogen the rate of transport to the nickel oxide electrode is quite rapid. In order to elucidate the mechanism of the self-discharge reaction and find methods for its inhibition, microcalorimetric and electrochemical techniques were used. These studies showed that the rate of self-discharge is proportional to the hydrogen pressure in the battery and the activity of nickel oxyhydroxide. Several types of potential inhibitors were incorporated in the nickel oxide electrode, during its fabrication or added to the electrolyte, to elucidate their effects on the rate of self-discharge. Though some additives such as lead, cobalt, and cadmium were found to have some effect, the rate of self-discharge could not be reduced significantly. Thus, this work showed that the only way in which the self-discharge could be reduced was by lowering the pressure of hydrogen in the pressure vessel. This is not feasible because it would increase the weight and volume of the nickel/hydrogen battery; thus, it was thought at that time that one approach would be to use hydrides for hydrogen storage in nickel/hydrogen batteries. By using this

approach, the hydrogen pressure could be considerably reduced and hence the rate of self-discharge considerably decreased. The added advantage is that hydrogen stored as hydrides requires a considerably smaller volume than hydrogen stored as compressed gas; further, there could also be a better packing and, hence, an improvement in the thermal management of this battery.

During the last five years, there has been a great incentive for developing nickel/metal hydride batteries. Use of nickel/metal hydride, rather than nickel/hydrogen batteries, can reduce the weight and thereby increase the specific energy, but the main impetus for developing nickel/metal hydride batteries is due to the impending legislations to curtail the production of nickel/cadmium batteries, because of the highly toxic nature of cadmium. The nickel/metal hydride batteries which are being developed, manufactured and commercialized, particularly in Japan, have a wide variety of applications: lap-top computers, cellular phones, video-cameras, etc. There is also great interest in developing nickel/metal hydride batteries as power sources for electric vehicles. The advantages of the nickel/metal hydride batteries are: (1) that their energy densities, in terms of weight or volume, are better than those for the nickel/cadmium battery; (2) their rate capabilities are approaching that of the nickel/cadmium batteries; and (3) the lifetimes of these batteries, which are still in the infant stage of development, are approaching at least 1,000 cycles (5,6).

For the aforementioned type of applications, there has been, in recent times, great interest in two types of alloys for hydrogen storage - the AB_5 type and the AB_2 type alloys. Since the 1960s, research on these hydrides has been fairly extensive at Brookhaven National Laboratory in New York (7) and Phillips Research Laboratory in Eindhoven (8). The pioneering work on the AB_2 type alloys have been carried out at Energy Conversion Devices - a subsidiary of this company, Ovonics, has been formed recently and is presently heavily engaged in developing nickel/metal hydride batteries, particularly for the electric vehicle application (9). In these alloys, the A component is the one which forms the stable hydride. The B component performs several functions: (1) it could play a catalytic role in enhancing the hydriding/dehydriding characteristics; (2) it can alter the equilibrium pressures for the hydrogen absorption/desorption and raise it or lower it to the desired levels; and (3) it could also add to the stability of the alloys because some of the A components could be readily oxidized. The AB_5 type alloys have a hexagonal structure while the AB_2 type alloys have a cubic structure. Most of the alloys of both these types, which have been successfully used or are being developed, are multi-component. In the AB_5 type alloy, the parent alloy is $LaNi_5$, while in the AB_2 type it is $TiNi_2$ or $ZrNi_2$. However, either the partial substitution by or a small addition of other elements alters the hydriding/dehydriding characteristics of these alloys, as required for gas phase hydrogen storage and for hydride electrodes. The roles of these substituents or additives could be to: (1) increase or decrease the crystal lattice constant and thereby change the equilibrium pressure for hydrogen absorption/desorption; (2) decrease the hysteresis during hydrogen absorption/desorption; (3) catalyze the hydriding/dehydriding reactions; and/or (4) improve the stability of these alloys by preventing oxide formation on one or more of the components.

Since 1990, there has been an ongoing collaboration among the authors in the three institutions to: (1) prepare alloys of the AB_5 and AB_2 types using arc-melting and mechanical alloying techniques; (2) examine their physicochemical characteristics - morphology, composition; (3) determine the hydrogen absorption/desorption behavior (pressure-composition isotherms as a function of temperature); and (4) evaluate their performance characteristics as hydride electrodes (charge/discharge, capacity retention, cycle life, high rate capability). This review article illustrates the results of the several types of investigations, which have been carried out on some selected AB_5 and AB_2 alloys (10-13). In most cases, the alloys were prepared by the arc-melting and annealing technique, but in some cases also by the mechanical alloying and annealing technique. A comparison of the physicochemical characteristics, including the hydriding/dehydriding reaction, was also made on the same alloy prepared by the two methods.

PREPARATION AND PHYSICOCHEMICAL CHARACTERIZATION OF ALLOYS

The AB_2 and AB_5 alloys were prepared by arc-melting of the constituent elements followed by annealing in an argon atmosphere ; for the AB_2 type alloys, annealing was carried out at 800° C for three days and for the AB_5 type alloys it was at 1000° C for 36 hours. The alloys were pulverized mechanically into powders about 100 mesh. The method of mechanical alloying (14) was used to prepare some selected alloys of the AB_5 type. Mechanical alloying is a high energy ball-milling process that repeatedly cold-welds and fractures powder particles. The microstructure that forms during mechanical alloying consists of layers of the starting material; the thickness of the material decreases with increase in mechanical alloying time leading to true alloy formation down to atomic levels.

Phases formed are usually meta-stable both in structure and morphology and amorphousity (nano-crystallinity) is easily obtained by controlling the alloying time. Alloys were prepared using powder elements of puritronic quality, obtained from Johnson Mathey Company. A laboratory size Spex 8000 mixer/mill was used to mechanically alloy mixtures of the constituent elements contained in a tungsten carbide vial. Alloying was carried out in a high purity helium atmosphere glove box in powder charge batches of 5 grams each. Multiple mechanical alloying runs were combined to obtain 20 to 30 gram sample powders. In our investigations, over thirty alloys have been prepared and characterized. A representative list of the alloys, which were prepared using the arc-melting and/or mechanical alloying technique, is found in Table 1.

PHYSICOCHEMICAL CHARACTERIZATION OF ALLOYS

Structural Characterization Using X-ray Diffraction Techniques

Structure and phase identity of the alloy samples were characterized by x-ray diffraction utilizing a Scintag diffractometer with Cu-K α-radiation. Typical x-ray diffractograms for the alloys, prepared by arc-melting and annealing and by mechanical alloying and annealing, are shown in Figures 1 and 2. These figures also illustrate that the incorporation of small quantities of substituents and/or additives do not effect the single phase structure of the alloys. It is also worth mentioning that if the annealing treatment is not carried out on the mechanically alloyed samples, broad diffraction peaks are observed. However, sharp peaks are obtained by annealing because a nano-crystalline (amorphous) to crystalline transformation takes place. Depending on the temperature and time of annealing, the entire amorphous state can be transformed to an entirely crystallized state. The lattice constants and cell volumes for the selected alloys, as extracted from the x-ray data for the alloys, are tabulated in Table 1. A striking result is that the cell volume for the AB_2 type alloy is nearly twice that for the AB_5 type. This is reflected in the considerably lower equilibrium pressures for hydrogen absorption/desorption for the AB_2 type alloys than for the AB_5 type alloys. The incorporation of substituents or additives can alter the lattice constants and cell volumes, and, hence, the equilibrium pressures for hydrogen absorption/desorption.

Morphologic and Compositional Characterization Using Scanning Electron Microscopy - Energy Dispersive X-ray Analysis

An analysis of the morphology, composition and distribution of the elements was made using SEM-EDAX techniques. A JSM Model 6400 Scanning Electron Microscope (equipped with a Noran 1-2 EDX unit) was used for the study. The SEM-EDAX studies confirm the x-ray diffraction studies in respect to morphology and the homogeneity of the alloys. A typical SEM photograph, which illustrates the homogeneity of the alloys, is shown in Figure 3. The compositions of these alloys were very close to that of the starting composition and the examinations, carried out at high resolution levels, revealed the homogeneity of the alloys, in respect to structure and composition.

Evaluation of Alloys for Hydrogen Storage from Gas-Phase Pressure-Composition-Temperature Isotherms

The pressure-composition-temperature isotherms for hydrogen absorption/desorption are generally measured by using a modified Sievert's type apparatus. The principles of the hydrogen absorption/desorption reaction may be represented by Figure 4. With increase of pressure, there will be an increase in the amount of hydrogen absorption in the single-phase (α-phase) region. Hydrogen absorption is in the solid solution region and Sievert's Law is obeyed, i.e. the amount of hydrogen absorption is proportional to the hydrogen pressure. Once the formation of the single-phase alloy is completed, the second phase starts forming, (i.e. the β-phase) and this forms from the outer surface and migrates towards the interior of the alloy. This is a two-phase region and for an ideal system there would be plateau pressure in the pressure-composition isotherm. Once the β-phase is completely formed, if any more hydrogen is to be introduced, this will again have to be with a significant increase of pressure. During desorption from the β-phase solid solution region, a decrease of pressure causes a decrease of the hydrogen content. The hydrogen desorption starts from the outer surface giving rise to the α-phase formation and this case is exactly the reverse during the absorption phenomenon (Figure 4). For an ideal case, there will be very little hysteresis in the hydrogen absorption and desorption isotherms, but in general there will be a slightly lower pressure in the two-phase region during desorption. Once the β-phase has been completely transformed into the α-phase (the solid solution region), with decrease of pressure there will be a decrease in the hydrogen content. The AB_5 type of alloy generally

exhibits a plateau pressure (P) that would be determined by the thermodynamics of the hydrogen absorption/desorption reactions. With increasing temperature, the plateau pressures will increase and the capacity for hydrogen absorption will decrease in this two phase region. Using the Vant-Hoff equation,

$$\ln P = \frac{\Delta H}{RT} - \frac{\Delta S}{R} \qquad (1)$$

one could calculate the enthalpy (ΔH) for the absorption/desorption reactions as well as the entropy change (ΔS) for the reaction. The enthalpy change is generally of the order of about 10 kcal/mole.

With the AB_2 type alloys, plateau pressures are hardly observed, which could be due to some multi-phase alloy formation in the intermediate range. However, the pressures during which the absorption/desorption occur could be considerably below one atmosphere. For hydrogen storage this will be a disadvantage, but for the hydride electrodes, even though there is a considerable slope in the intermediate region of the pressure-composition isotherm, this is not a disadvantage, because at a sacrifice of, say, less than 40 or 50 mV, the coulombic capacity for the hydriding/dehydriding reaction corresponds close to the maximum hydrogen content (i.e., one atom of hydrogen for each atom of the metal). In the Sievert's type experiments, one can calculate the amount of hydrogen (H) absorbed by using the equation:

$$(H) = \frac{2\upsilon\,\Delta P}{RT} - \Sigma c \equiv \frac{2\upsilon\,\Delta\tau}{RT}\,\varphi - \Sigma c \qquad (2)$$

where R and T have their usual meanings, υ is the volume of reservoir, $\varphi = 0.01098$ is the slope of the pressure vs. transducer reading curve, Δt is the change in transducer reading, and Σc is a correction factor accounting for hydrogen in the gaseous phase in equilibrium with the solid hydride phase.

The useful hydrogen content for hydrogen storage, say, from the gas phase, can be considered to be in the region between pressures of 0.5 and 5 atmospheres. In practice, for the AB_5 type alloys, the range of hydrogen pressures to obtain the maximum capacity for hydrogen absorption could be even smaller. The degree of slant may be expressed by the equation:

$$S = \log \left(\frac{P_{H/M} = 0.75}{P_{H/M} = 0.25} \right) \qquad (3)$$

where $P_{H/M} = 0.75$ and $P_{H/M} = 0.25$ are the pressures at H/metal ratios corresponding to 0.75 and 0.25, respectively. An optimum hydrogen storage alloy is defined in these terms to be one with a high hydrogen capacity and a low degree of slant.

Typical hydrogen absorption/desorption isotherms for an alloy prepared at Brookhaven National Laboratory (BNL 3) are shown in Figure 5. This figure illustrates a reasonably low plateau pressure and minimum hysteresis. Further, this alloy also shows a considerable wide range over which hydrogen is absorbed and it approximately corresponds to one atom of hydrogen for each atom of metal. Table 1 summarizes the results of the hydrogen absorption/desorption characteristics of some alloys, prepared using both the arc-welding and the mechanical alloying techniques. Figure 6 shows the hydrogen absorption behavior for the alloy prepared by the mechanical alloying technique before and after annealing. Due to the amorphous nature of the alloy prior to annealing, the hydrogen absorption/desorption characteristics are not satisfactory. However, the annealing causes a transformation from the amorphous to the crystalline structure and produces grain boundaries, which are necessary for the migration of the hydrogen into the alloy; thus, the absorption/desorption characteristics are considerably improved. Figure 7 shows a comparison of the hydrogen absorption isotherms for the same alloy prepared by the mechanical alloying and by the arc-melting techniques. One can note from this figure that the characteristics are very similar, in respect to the plateau pressures; however, the alloy prepared by mechanical alloying showed a lower hydrogen content. This could, however, be improved very probably by extending the time for mechanical alloying. The incorporation of tin improves the hydrogen absorption/desorption behavior and cycle life (15). It also has some effect of lowering the plateau pressure. In addition, the substitution of neodymium increases the crystal lattice parameters and also lowers the plateau pressure (8).

EVALUATION OF ALLOYS AS HYDRIDE ELECTRODES

Charge/Discharge and Cycle Life Behavior

Reactions which occur during the charging and discharging of hydride electrodes in alkaline electrolytes may be represented as follows:

$$M + H_2O + e^- \Leftrightarrow M\text{–}H_{ads} + OH^-_{int} \quad (4)$$

$$M - H_{ads} \Leftrightarrow M\underline{H} \quad (5)$$

$$OH^-_{int} \rightarrow OH^-_{bulk} \quad (6)$$

$$M\underline{H} \Leftrightarrow MH \quad (7)$$

$$2\,H_{ads} \rightarrow H_2 \uparrow \quad (8)$$

$$M + H_2O + e^- \Leftrightarrow MH + OH^- \quad (9)$$

The first step (Eq. 4) is the charge transfer reaction, which gives rise to the formation of the adsorbed hydrogen and hydroxide ions at the interface. The second step (Eq. 5) involves the dissolution of H in the alloy and the diffusion of the absorbed hydrogen into the bulk alloy, while the hydroxide ions diffuse into the bulk of the electrolyte (Eq. 6). The third step (Eq. 7) is the recrystallization of the condensed phase. During overcharging, one could have hydrogen evolution (Eq. 8), and for practical purposes, this has to be avoided in the nickel/metal hydride batteries. The complete electrode reaction is represented by Eq. 9. The phase changes, which occur during this reaction, are identical in the gas-phase hydrogen storage. The hydride electrodes for this work were generally prepared by mixing the powder with 100 micron particle size copper powder and pressing into pellets onto nickel screens. Nickel wires were spot-welded onto the electrodes for current collection. In more recent work, instead of using copper powder, high surface area carbon with Teflon was used for the fabrication of the electrodes. The main purpose of the copper or carbon additive is to enhance the electronic conductivity of the electrode because during hydriding the electronic conductivity decreases. The Teflon serves the purpose of a binder. The typical charge/discharge behavior of the electrode, prepared with the BNL 3 material, is shown in Figure 8. This material exhibited very favorable characteristics. In terms of cycle life, a limited number of studies have been carried out to date, but one example is given in Figure 9 to show the advantages of using high surface area carbon, rather than copper, as an additive (16). Very probably, the advantage of carbon over copper is that copper could undergo some dissolution in the strong alkaline environment, whereas carbon is quite stable. There is also an enhanced capacity when using carbon as an additive. This could be connected with the very high surface area of carbon (BET surface area of about 100 or 200 m^2/g).

Charge/Discharge Rate Capabilities

For several applications, it is desirable for the hydride electrodes to be able to function at relatively high charge/discharge rates. A study was conducted on the LANL-3 material to demonstrate the performance as a function of the discharge rate (Figure 10). This figure shows that even at the 3C rate of charge that about 90% of the capacity could be obtained without any significant loss in the potential of the electrode. Such studies have been conducted on several of the electrodes with the other alloys listed in Table 1 and one may conclude that fast discharge rates, nearly as high as those in the nickel/cadmium battery, can be obtained with these materials. Of the materials tested to date, the one which has shown the best behavior is the BNL 4 material which is of the AB_2 type.

Capacity Retention

The capacity retention is an essential criterion for secondary batteries; this parameter gives a measure of the self-discharge rate of the batteries. As mentioned in the first section, the self-discharge rate on the nickel/hydrogen battery is quite high, about 10% per day. This value is about 1% per day for the nickel/cadmium battery. Capacity retention studies were conducted by fully charging the battery and leaving it for different periods of storage time.

After the desired periods, the remaining capacities were determined by completely discharging the batteries. Typical plots of the capacity retention and of the electrode potential, as a function of storage time, for the PRL 1 material are shown in Figure 11. Figure 12 shows the capacity retention as a function of storage time for several of the alloys tested in this work. An intuitive guess is that there should be a relationship between the dissolution pressure and the self-discharge rate. Table 2 demonstrates the correlation between the desorption pressures and the self-discharge rate after five days for some of the alloys. Here again, the AB_2 type alloys may have some advantages over AB_5 type ones because of their considerably lower plateau pressures, but as seen from Table 1, it is clear that even the AB_5 type alloys can be modified with substituents and/or additives to lower the plateau pressure to a level of about 0.1 to 1.0 atm. From this article, one may conclude that hydride electrodes could function optimally with alloys having plateau pressures or even sloping pressures in the range of .1 and .9 atm.

CONCLUSIONS

1. Modified alloys, prepared by partial substitution of the A and B components and by incorporation of minimal amounts of additives, retain the single phase structure, and provide the necessary changes in the physicochemical characteristics to attain high hydrogen storage capacities at relatively low equilibrium pressures.

2. Alloys prepared by the two methods (arc-melting/annealing and ball milling/annealing) yield very similar hydrogen absorption/desorption characteristics both in the gas phase and as hydride electrodes. The alloy prepared by mechanical alloying attained the maximum electrochemical capacity without prior activation.

3. The AB_5 type alloys, unlike the AB_2 type alloys, exhibit minimal hysteresis and degree of slant of the pressure-composition isotherm for hydrogen absorption/desorption. Thus, for storage of hydrogen from the gas phase (as in Ni/H_2 batteries), the AB_5 type alloys have a distinct advantage.

4. The AB_2 type alloys absorb/desorb hydrogen at lower pressures and have higher hydrogen storage capacities that the AB_5 type alloys and hence show a higher level of performance as hydride electrodes.

5. A modified LaNi5 alloy incorporating Ce or Nd and Sn exhibits excellent hydrogen storage behavior from the gas phase and also as a hydride electrode.

ACKNOWLEDGEMENTS

This work was sponsored by the Office of Research and Development under contract No. 88*F674300 and the NASA Center for Space Power at Texas A&M University (Contract P.O. 58-529211-X113). Special thanks are also due to Dr. Hong S. Lim of Hughes Aircraft Company and Mr. Joe Stockel of the U. S. Government Office of Research and Development for their encouragement and discussions of this work.

REFERENCES

1. Y.J. Kim, S. Srinivasan and A. J. Appleby, J. Appl. Electrochemistry , 20 (1990) 377.

2. K. A. Murugesamoorthi, S. Srinivasan and A. J. Appleby, J. Appl. Electrochemistry , 21 (1991) 95.

3. Y.J. Kim, A. Visintin, S. Srinivasan and A. J. Appleby, J. Appl. Electrochemistry, 139 (1991), 351.

4. Z. Mao, A. Visintin, H. S. Lim and A. J. Appleby, J. Appl. Electrochemistry, 22, (1992) 409.

5. T. Sakai, K. Muta, H. Miyamura, N. Kuriyama, and H. Ishikawa, in D. A. Corrigan and S. Srinivasan (eds), Proceedings of the Symposium on "Hydrogen Storage Materials, Batteries and Electrochemistry", The Electrochemical Society, Pennington, NJ, 92-5 (1992), 59.

6. I. Matsumoto, M. Ikoma, A. Ohata, H. Matsuda and Y. Toyoguchi, Extended Abstract of 183rd Meeting of the Electrochemical Society, The Electrochemical Society, Princeton, NJ, 93-1, (1993) 39.

7. J. J. Reilly, in D. A. Corrigan and S. Srinivasan (eds) Proceedings of the Symposium on "Hydrogen Storage Materials, Batteries and Electrochemistry", The Electrochemical Society, Pennington, NJ, 92-5 (1992), 24.

8. H. H. Van Mal, K. H. J. Buschow, and A. R. Miedema, J. Less Common Metals, 35, (1974), 65.

9. M. A. Fetcenko, S. Venkatesan and S.R. Orkinsky,in D. A. Corrigan and S. Srinivasan (eds), Proceedings of the Symposium on "Hydrogen Storage Materials, Batteries and Electrochemistry", The Electrochemical Society, Pennington, NJ, 92-5 (1992), 76.

10. A. Anani, A. Visintin, S. Srinivasan and A. J. Appleby, in D. A. Corrigan and S. Srinivasan (eds), Proceedings of the Symposium on "Hydrogen Storage Materials, Batteries and Electrochemistry", The Electrochemical Society, Pennington, NJ, 92-5 (1992), 105.

11. A. Anani, A. Visintin, S. Srinivasan and A. J. Appleby, Extended Abstract of 183rd Meeting of the Electrochemical Society, The Electrochemical Society, Princeton, NJ, 93-1 (1993) 82.

12. A. Visintin, K. Petrov, S. Srinivasan A. J. Appleby J. J. Reilly, J. R. Johnson and H. S. Lim, Extended Abstract of 183rd Meeting of the Electrochemical Society, The Electrochemical Society, Princeton, NJ, 93-1, (1993) 79.

13. A. Anani, A. Visintin, S. Srinivasan, P. B. Desch and R. B. Schwarz, to be submitted to the Journal of the Electrochemical Society.

14. R. B. Schwarz, R. R. Petrich and C. K. Saw, J. Non-Crystalline Solids, 76, (1985) 281.

15. D. Chandra and F. E. Lynch, Rare Earths, Extraction, Preparation and Applications, ed. R. G. Bautista and M. M. Wonf. The Minerals, Metals and Materials Society, (1989), 83-89.

16. K. Petrov, A. Visintin, S. Srinivasan and A. J. Appleby, Extended Abstract of 183rd Meeting of the Electrochemical Society, The Electrochemical Society, Princeton, NJ (1993) 41.

TABLE 1

Crystallographic Parameters, Hydrogen Storage Characteristics
and Coulomhic Capacities of Electrodes for Some Selected
AB_5 and AB_2 Alloys

COMPOSITION	I D	Lattice Const. a/c (A^o)	Cell Volume $(A^o)^3$	Plateau Pressure (atm)	H_2 Storage H/atom Pressure Range 0.5 - 5.0 atm	H_2 Capacity (mAh/g)
$LaNi_5$	LANL-1	5.009/3.97	86.31	1.6	0.916	341
$MmNi_{3.55}Mn_{0.4}Al_{0.3}Co_{0.75}$	MBC-1	4.977/4.05	86.99	0.8-1.5	0.833	316
$La_{0.8}Nd_{0.2}Ni_{2.5}Co_{2.4}Si_{0.1}$	PRL-1	5.020/3.98	87.08	0.96	0.721	273
$La_{0.8}Nd_{0.2}Ni_{2.9}Co_{2.4}Mo_{0.1}Si_{0.1}$	PRL-2	5.028/3.98	87.35			
$LaNi_{4.8}Co_{0.5}Si_{0.1}$	BNL-1	5.012/4.00	87.05	2.4	0.99	354
$La_{0.8}Ce_{0.2}Ni_{2.9}Co_{2.4}Mo_{0.1}Si_{0.1}$	BNL-2	5.004/4.01	86.95	0.6	0.716	207
$La_{0.8}Ce_{0.2}Ni_{4.8}Sn_{0.25}$	BNL-3			1.08	0.933	335
$La_{0.8}Nd_{0.2}Ni_{4.75}Co_{0.5}Sn_{0.25}$	LANL-2	5.042/4.02	88.48	0.57	0.75	257
$La_{0.8}Nd_{0.2}Ni_{4.75}Co_{0.5}Sn_{0.25}$	BNL-8	5.044/4.02	88.76	0.6	0.792	272
$La_{0.8}Nd_{0.2}Ni_{4.5}Co_{0.5}Sn_{0.25}$	LANL-3	5.044/4.02	88.56	0.8	0.75	259
$Ti_{0.51}Zr_{0.49}V_{0.67}Ni_{1.18}Cr_{0.21}$	BNL-4	4.959/8.06	172.3		0.82	350

Table 2

Relationship between Desorption Pressures and Self-Discharge

for PRL-1, BNL-1, 2, and 3 Alloys

Alloy Identification	Desorption pressure (atm)	Self-Discharge after 5 days (%)
BNL-2	0.61	10
BNL-3	0.96	12
PRL-1	0.96	15
BNL-1	2.44	40

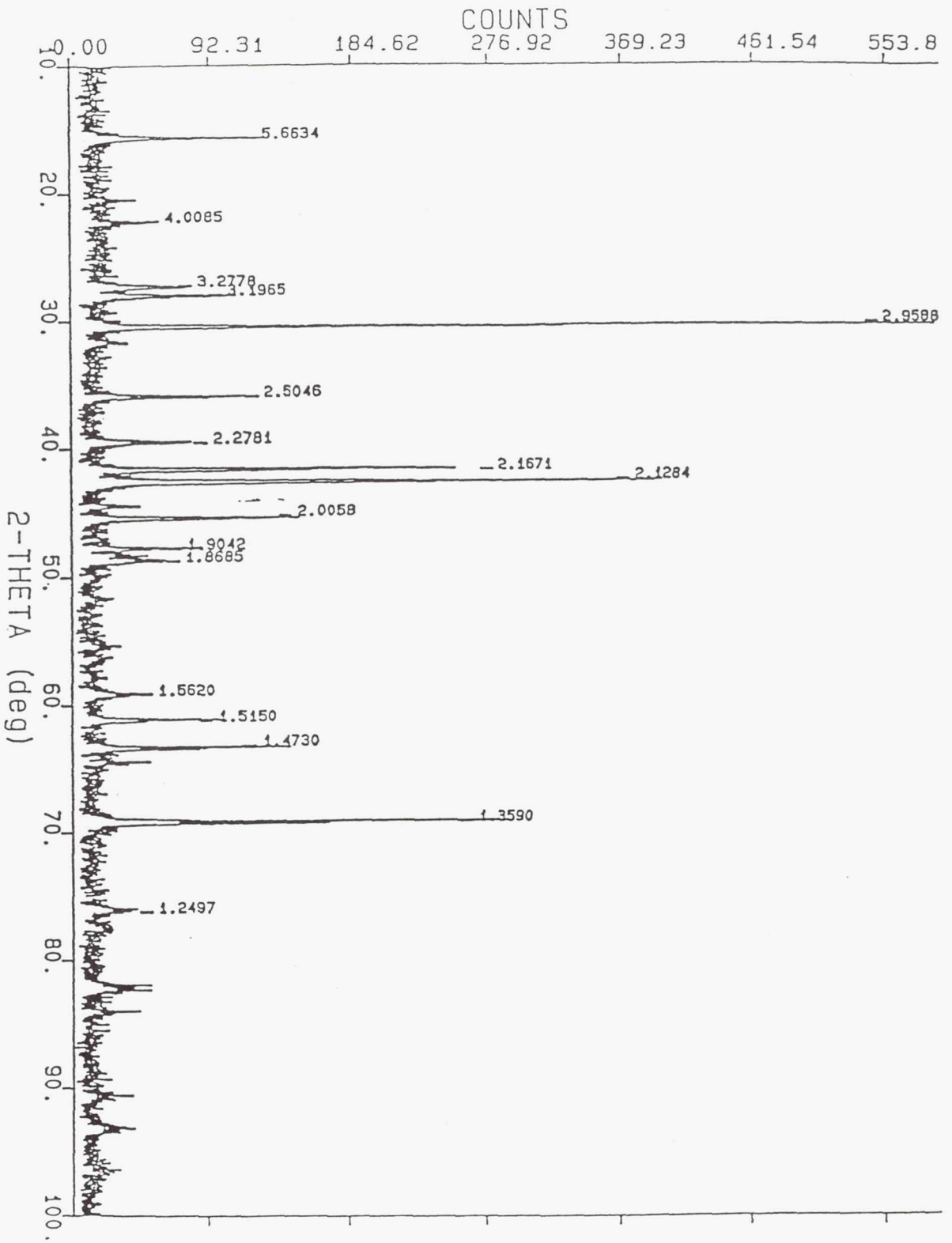

Figure 1.—X-ray diffraction pattern for BNL-1 alloy, prepared by arc-melting and annealing. Numbers above peaks represent d-spacing in A^{o}.

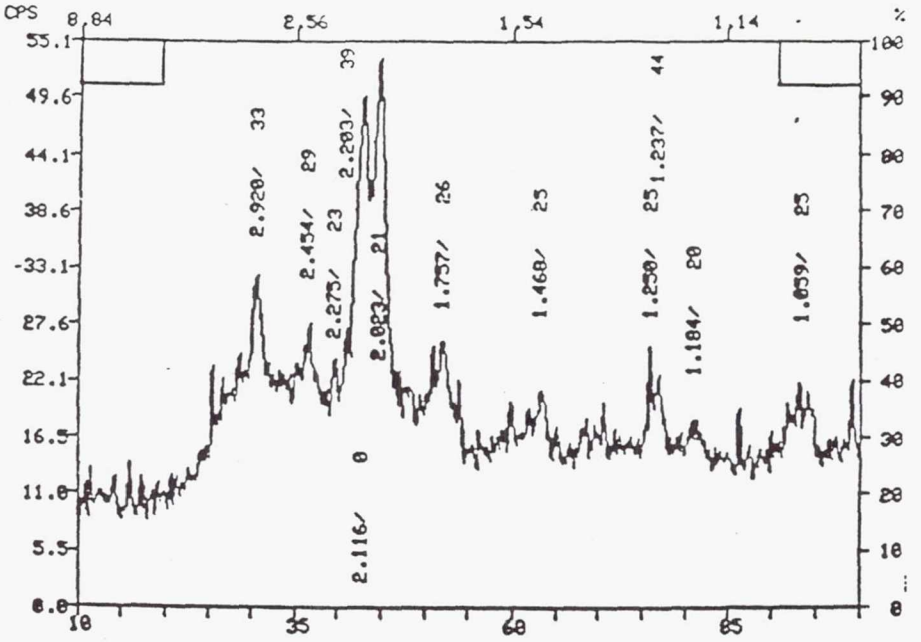

(a) Prepared by mechanical alloying.

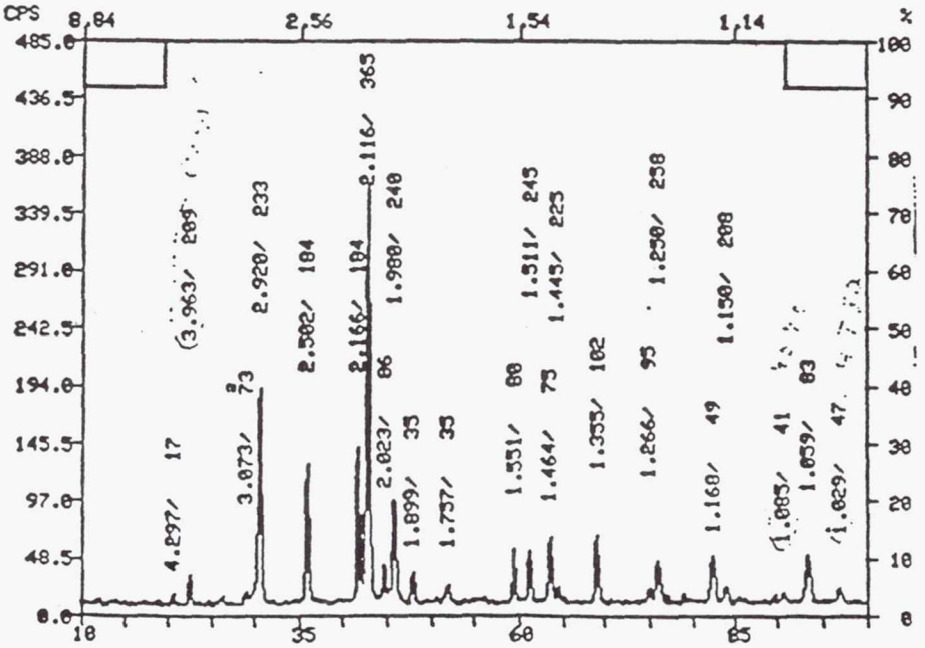

(b) Prepared by mechanical alloying and annealing.

Figure 2.—X-ray diffraction pattern of $LaNi_5$ alloy.

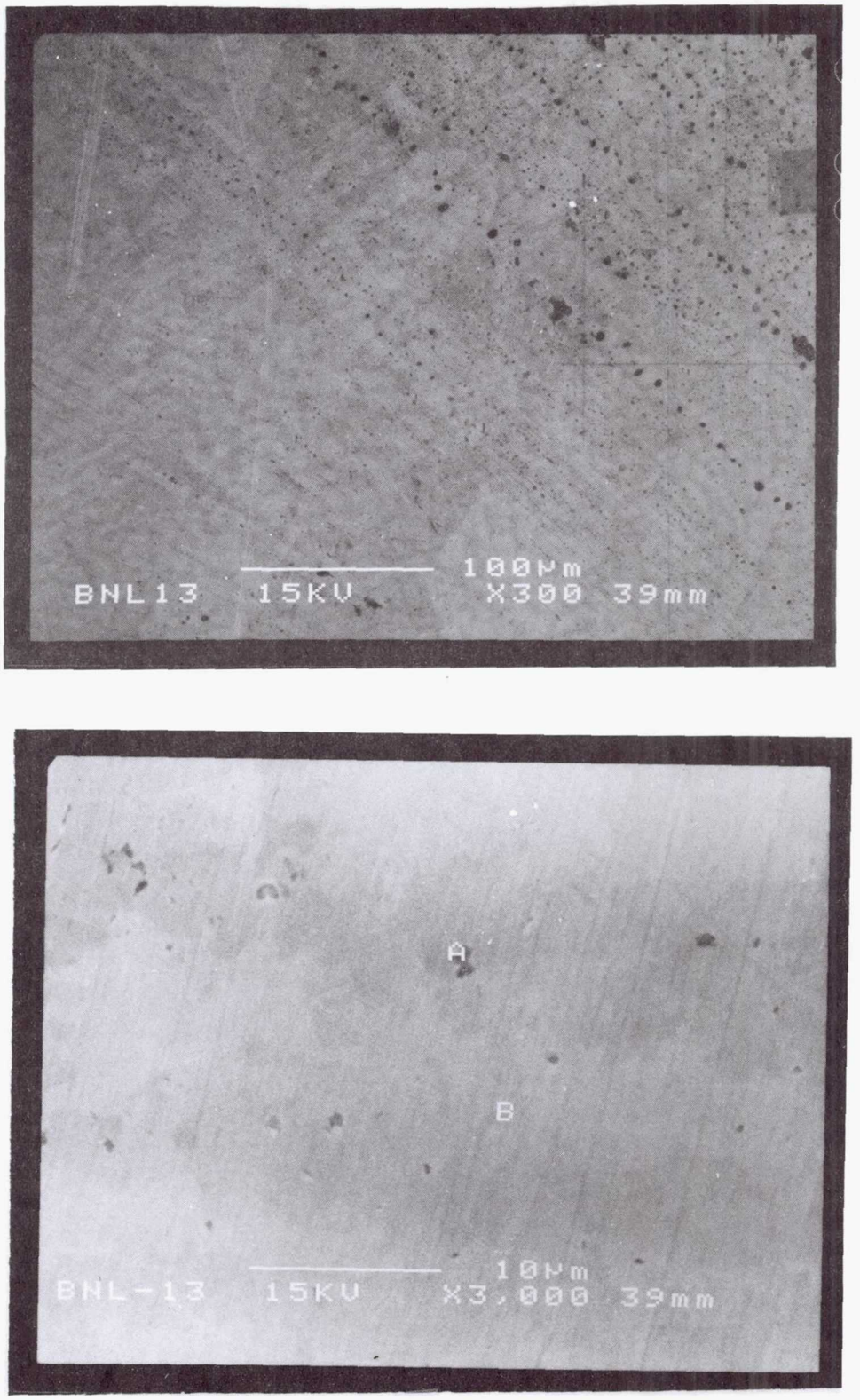

Figure 3.—Scanning electron micrographs for BNL-1 alloy, prepared by arc-melting.

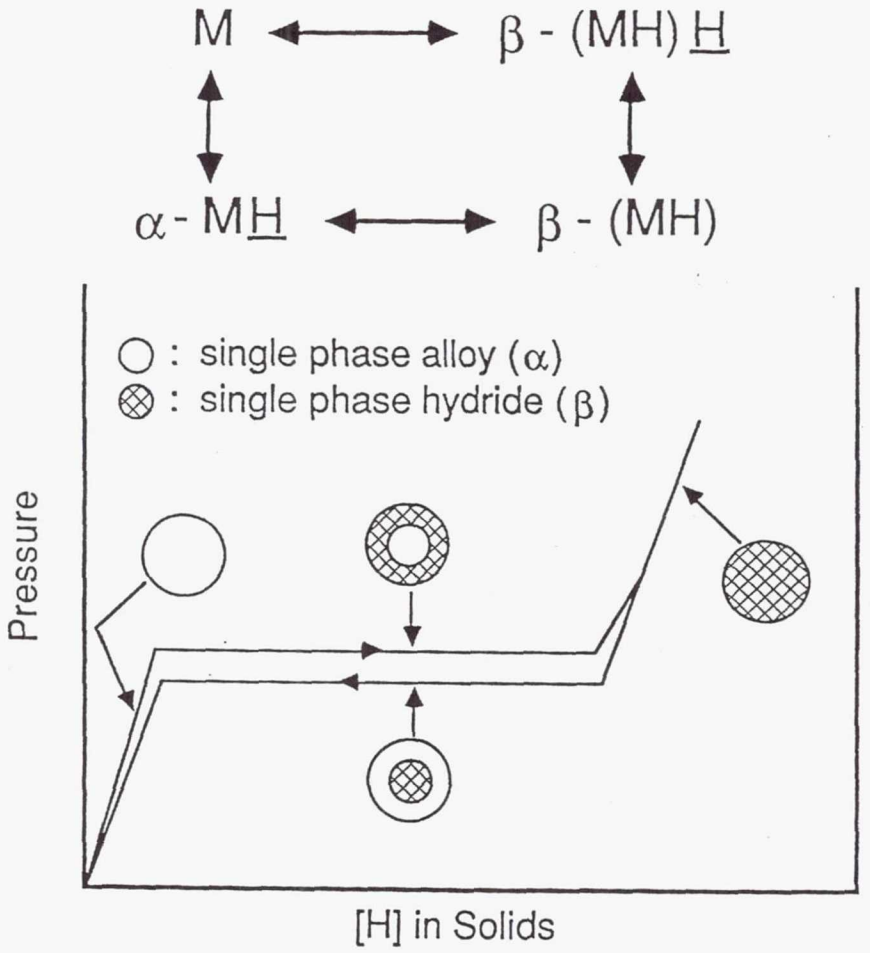

Solid Solution : Sievert's Law

$P_{H_2} = f([H])$

Mixed Phase : van't Hoff Relation

$P_{H_2} \neq f([H])$

Figure 4.—Principles of hydrogen gas-phase absorption/desorption.

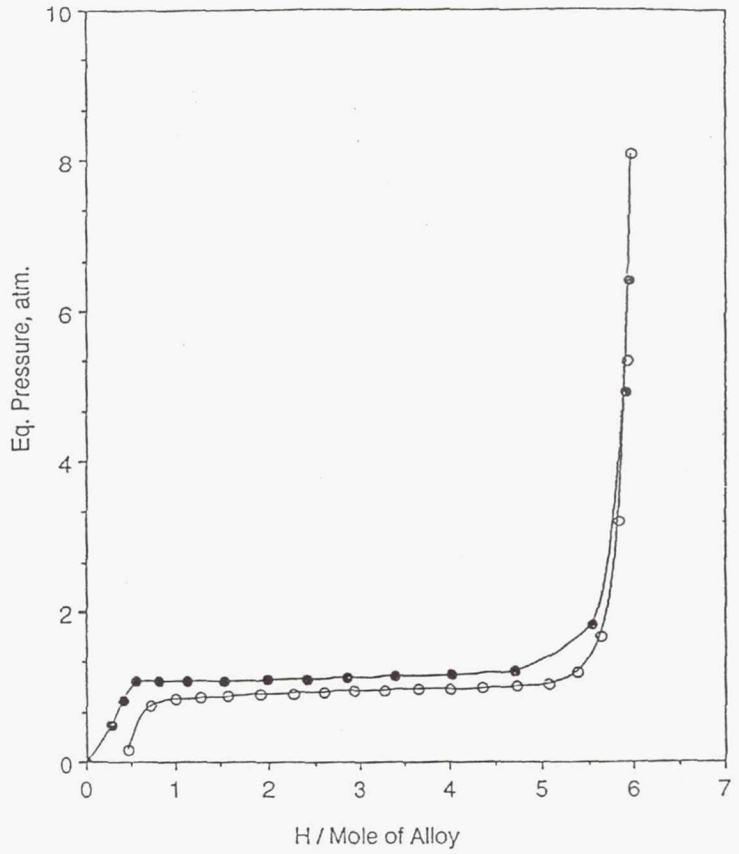

Figure 5.—Typical gas phase absorption/desorption isotherms showing minimal hysteresis effect. BNL-3; 25 °C open circle denotes desorption; solid circle denotes absorption.

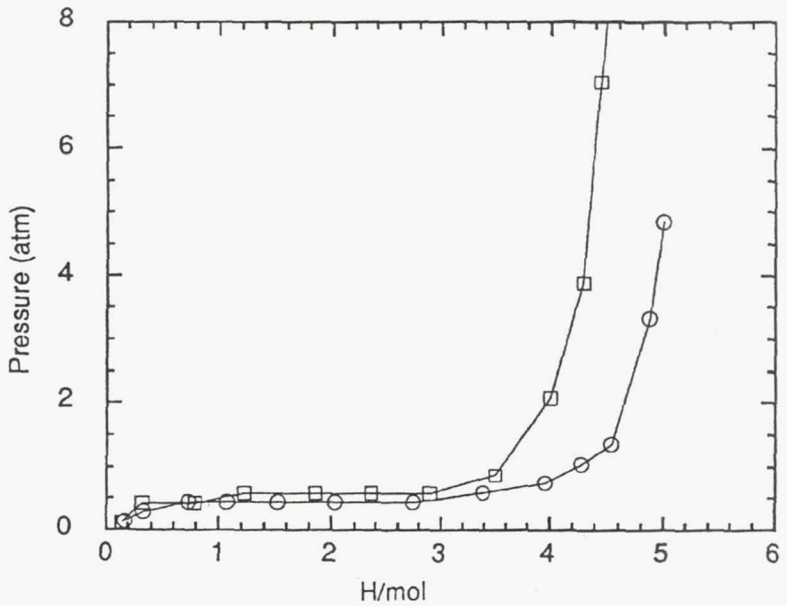

Figure 6.—Comparison of hydrogen absorption isotherms at 25 °C for the AB_5 type material. Open circle denotes arc-melted BNL-8. Square denotes mechanically alloyed and annealed LANL-2.

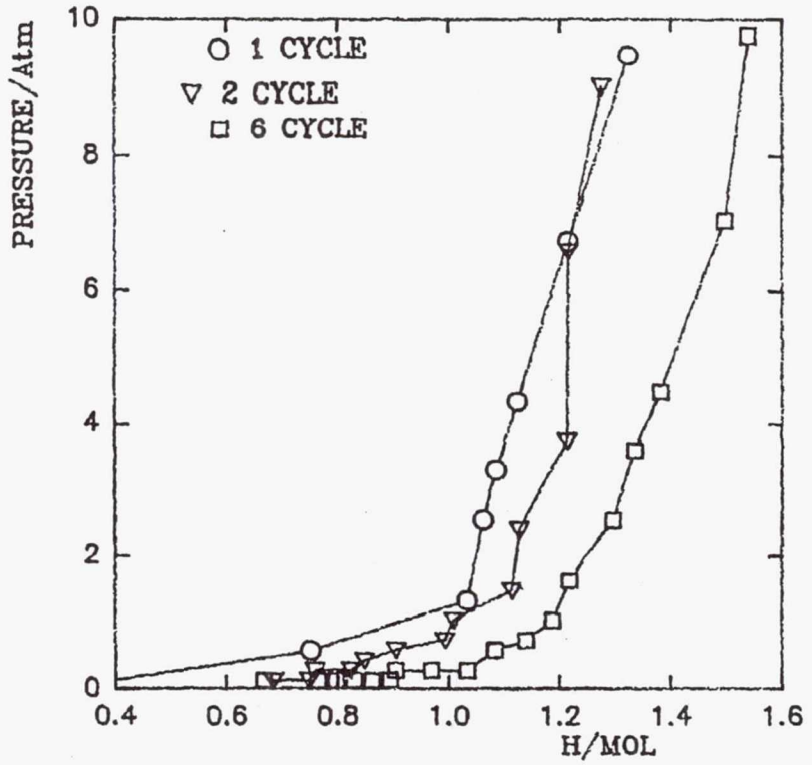

(a) Prepared over a 20 hr period using tungsten carbide vial.

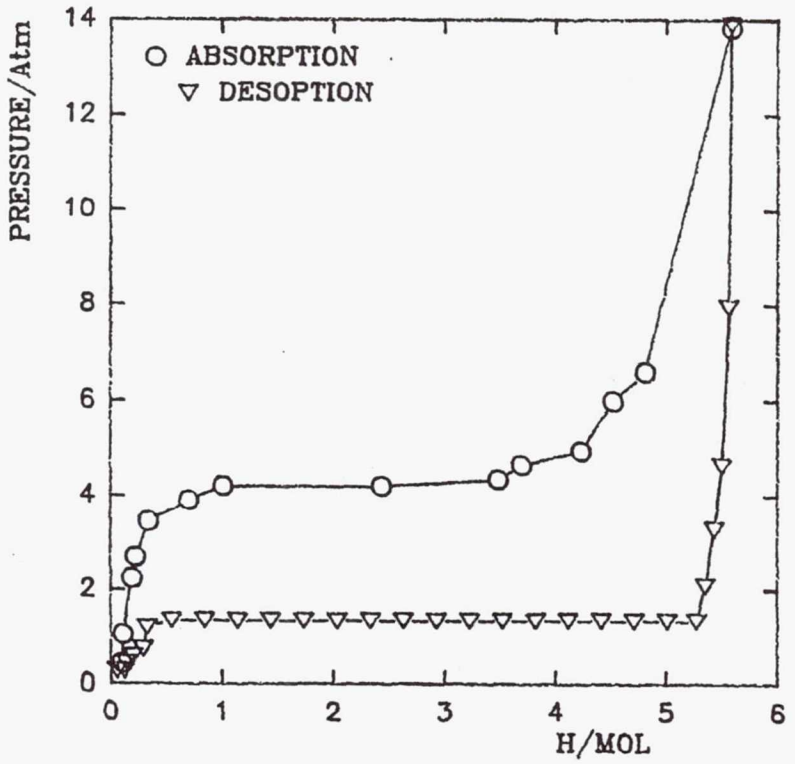

(b) Annealed at 700 °C for 15 min.

Figure 7.—Gas-phase absorption/desorption isotherms for $LaNi_5$, prepared by mechanical alloying.

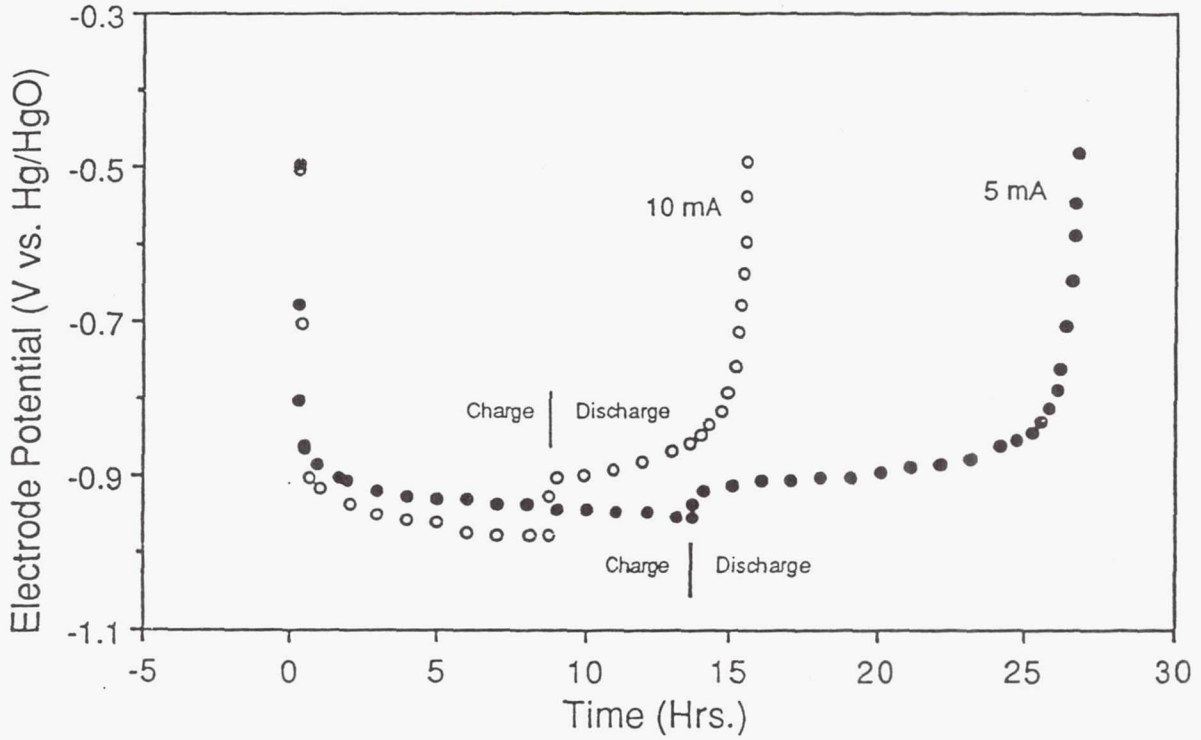

Figure 8.—Charge/discharge behavior of the electrode prepared with the BNL 3 material.

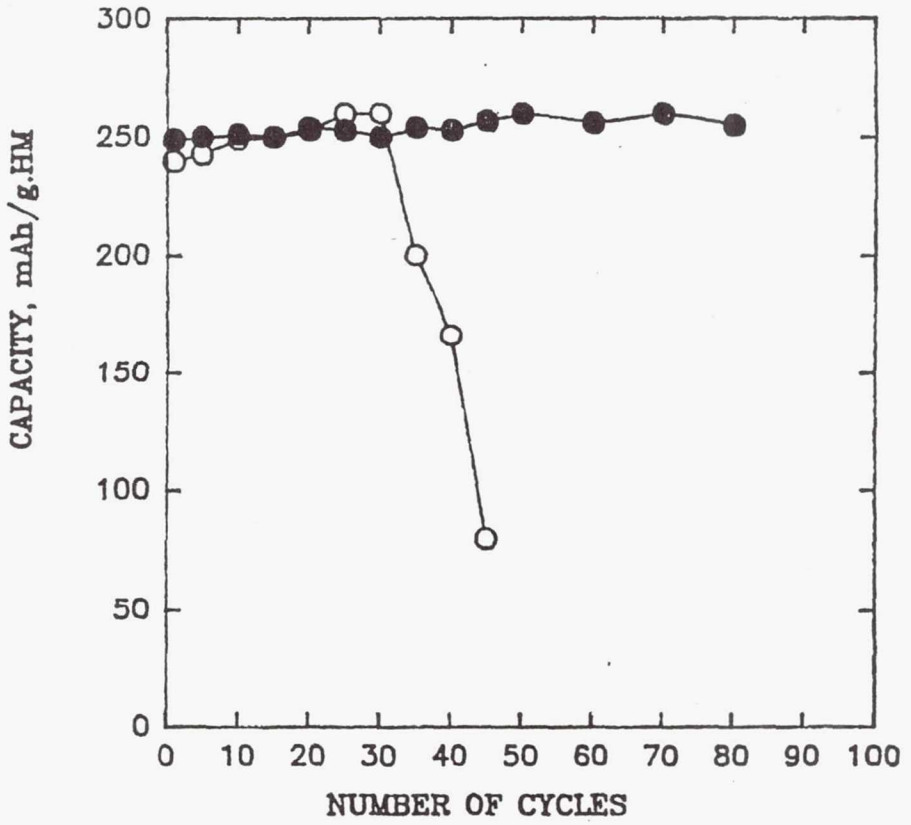

Figure 9.—Effect of additive to active material (LANL-3) on the cycle life of electrode. Open circle denotes LANL-3 + Teflonized acetylene black; solid circle denotes LANL-3 + Cu powder; 25 °C; 8 M KOH.

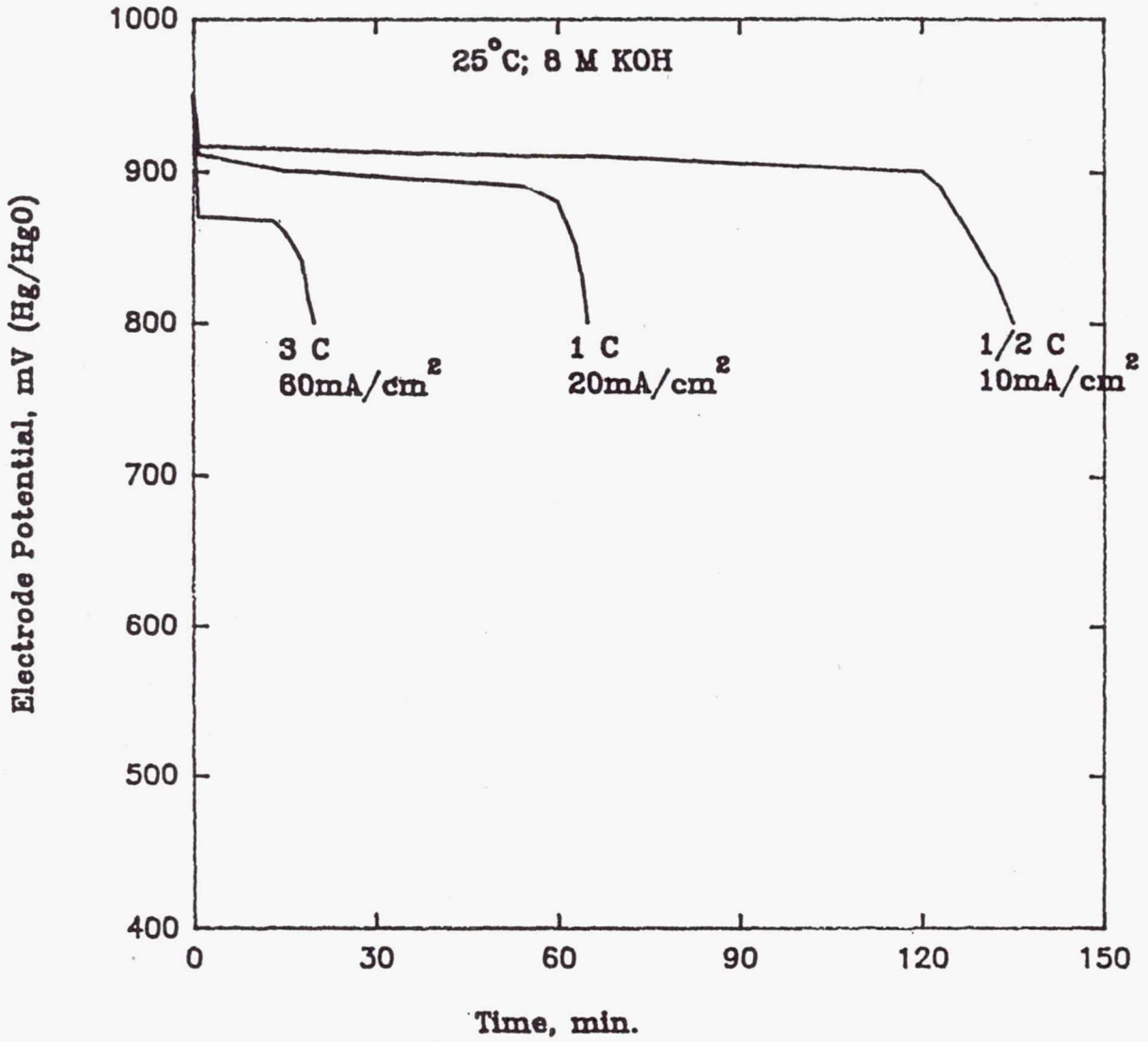

Figure 10.—Electrode potential versus time during discharge at different rates for electrodes with LANL-3 hydride material. Additive–Vulcan + 40% PTFE.

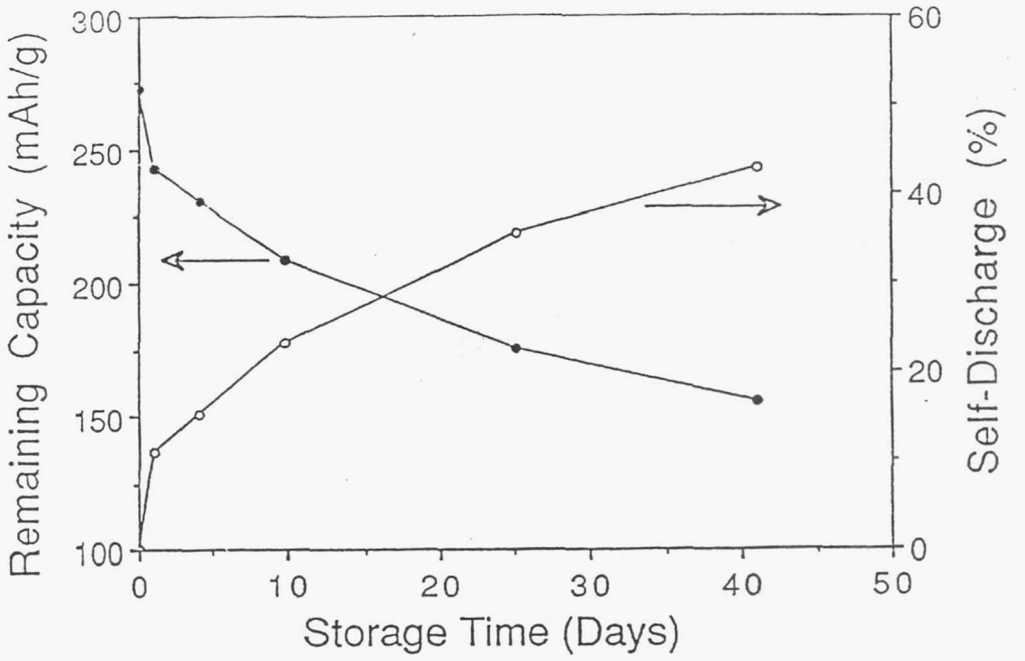

(a) Capacity retention.

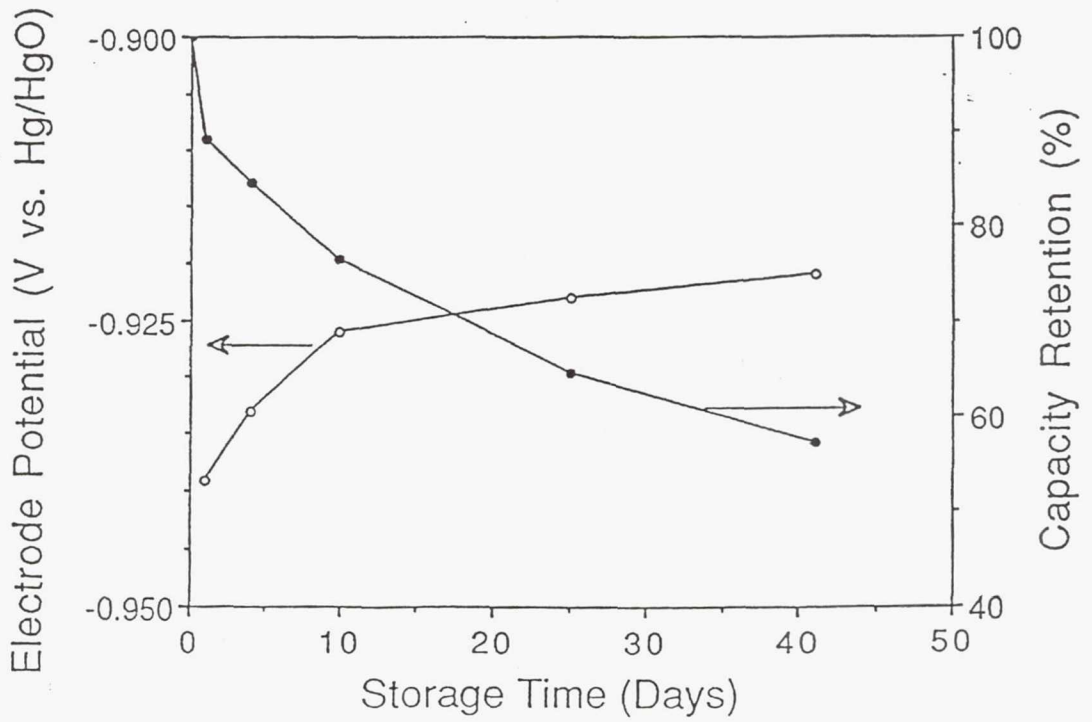

(b) Electrode potential and capacity retention.

Figure 11.—PRL-1 sample as a function of storage time.

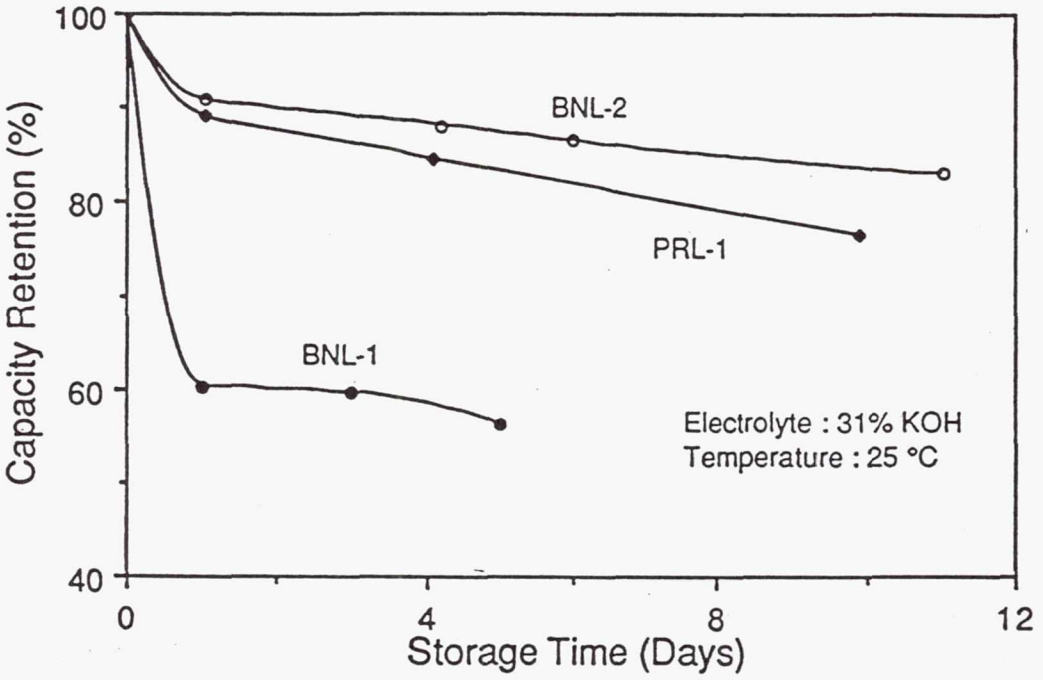

Figure 12.—Comparison of the capacity retention capabilities for the PRL-1, BNL-1, and BNL-2 alloy electrode samples.

STATUS OF THE DEVELOPMENT OF RECHARGEABLE LITHIUM CELLS

G. Halpert, S. Surampudi, D. Shen, C-K Huang, S. Narayanan, E. Vamos and D. Perrone

Jet Propulsion Laboratory

California Institute of Technology

Pasadena, California 91109

ABSTRACT

The progress in the development of the ambient temperature Lithium - Titanium Disulfide rechargeable cell under development at the Jet Propulsion Laboratory is described in this paper. Originally aimed at achieving a specific energy of 100 Wh/kg, 'AA' cells have demonstrated 125 Wh/kg at the C/3 discharge rate. The results of evaluating cell design parameters are discussed and cycling test data are also included in the paper. Safety tests results at various overcharge and over discharge conditions and rates proved to be uneventful. The test results of cell with built-in overcharge mechanism proved the concept was feasible. Replacing the lithium foil electrode with a Li_xC resulted in a capacity at 1mA/cm^2 of 200 mAh/gm and 235 mAh/gm at 0.167 mA.

INTRODUCTION

Ambient temperature Lithium - Titanium Disulfide (Li-TiS_2) rechargeable cells have been under development at the Jet Propulsion Laboratory. The effort sponsored by Code C at NASA Headquarters is aimed at high specific energy rechargeable cells that can reduce mass, and/or volume and or increase mission capability in planetary spacecraft applications. The need for a long cycle life lithium rechargeable battery has also been a goal of this effort. The program goals were 100 Wh/kg, 1000 cycles at 50% depth of discharge at the C/5 rate, 5 years of active storage life and safe under electrical abuse conditions.

The approach has been to prepare materials, components and cells to gain an understanding of how the variations in design, composition and structure affect performance and life. During the development a number of cathode materials were studied in a comprehensive evaluation process before selecting titanium disulfide for its specific energy and cycle life capability. More than seventy-five different and solvent combination electrolytes were subjected to complex impedance, microcalorimetry and electrochemical measurements before selecting a solution of 2-methyl tetrahydrofuran/ethylene carbonate/2-methyl furan (2-MeTHF/EC/2-MeF) containing 1.5 moles of lthium hexafluoroarsenate ($LiAsF_6$). The initial evaluation cells were a 150 mAh spiral wound design . These were scaled-up to 1 Ah size spiral wound cells. The volume of electrolyte was found to be essential to long life.

The objectives of this effort were to determine the effect of stack compression, overcharge protection and electrical abuse on the performance and safety of the Li-TiS_2 cell. Additionally an alternate Li_xC electrode prepared from commercial graphite was evaluated as a replacement for Lithium foil as the anode.

PERFORMANCE

Examples of the performance of these cells is given in Figures 1-4. Figure 1 shows the voltage on charge (C/10) and discharge (C/5). Charge is terminated at 2.5 volts and discharge at 1.7 volts. The sloping voltage has the advantage of providing a measure of state of charge. Figure 2 provides a measure of the specific energy at various discharge rates. Note that the 1 Ah cell achieved a specific energy of greater than 125 Wh/Kg at rates as high as C/2. Figure 3 illustrates 965 cycles achieved at 50% depth of discharge (to 2.2 volts) in a cell comprising the 2-MeTHF/EC/2-MeF/$LiAsF_6$ electrolyte and a cathode:anode ratio of 4:1. The cycle life at 100% depth of discharge (to 1.7 volts) shown in Figure 4 was 335 cycles. This is not significantly less than that achieved with commercial Ni-Cd cells.

CELL DESIGN PARAMETERS

The parameters addressed during the development process this year included: pack tightness, final selection of electrolyte composition, separator type, electrode capacity ratio and case polarity. More than 100 experimental 1 Ah spiral wrapped cells were assembled in house and 50 'AA' (1Ah) cells were procured from EIC to determine the effect of these parameters on performance.

The effect of varying the pack tightness on end of discharge voltage is given in Figure 5. The pack was tightened using a 10 mil Teflon sheet wrapped around the spiral. The tight pack utilized 2 layers around the spiral, the medium 1 layer and the loose pack did not use a Teflon layer. Although there is a significant difference in the early cycles, the performance appears to be similar after 250 cycles, probably because of the expansion of the cathode and film on the lithium foil. However, the tight pack voltage was higher throughout and therefore was judged to be a superior configuration.

Results of the evaluation of four different separators is shown in Figure 6. The Celgard microporous polyethylene (PE) and polypropylene (PP) appear to provide similar results. The microporous polypropylene was selected to minimize the lithium dendrite growth. The thermal separator, a wax -coated polypropylene material, was selected to evaluate the properties of a separator that would serve as a fuse and shut down the cell if the temperature became unsafe. These also provided more than 400 cycles at 50% DOD.

The summary of the design parameter study, including work previously performed is given in Table 1. The anode:cathode ratio of 4:1 has been shown to provide consistent long cycle life cells. Three electrolytes including that described above have proven to capable of providing long life. Only 6 cc of the electrolyte were found to be necessary. The optimum ethylene/propylene/diene terpolymer (EPDM) binder in the TiS_2 cathode was found to be 1%. There was little difference in performance with a floating or case positive polarity.

SAFETY EVALUATION TESTS

Experimental and EIC 1 Ah cells were subjected to short, circuit, overcharge, over discharge, and combinations thereof. The results of the short circuit test is given in Figure 7. Peak current rose to 25 amps within 2 minutes and then dropped to near zero current immediately after. The temperature followed the current, rising to 220 ^{o}F, then tapering to 95^{o} F within 30 minutes. There were no ventings, explosions or other safety incidents during these tests. Table 2 provides a summary of the results of inadvertent electrical abuse tests which occurred during cell testing when a computer failed. Even after overcharging 5 times and over discharging 10 times the capacity after 200 - 500 cycles, the cells were in tact and did not vent.

OVERCHARGE PROTECTION STUDIES

From an operational point of view cells in a series string require overcharge protection to prevent a cell from being overcharged when degradation results in cell imbalance in the string. Ni-Cds cells utilize their inherent oxygen recombination capability to allow cells in a string to be balanced during overcharge. Lithium rechargeable cells do not inherently have this capability. Three additives were included in Li-TiS_2 cells to create a shuttle reaction that could provide overcharge protection. Tetracyanoethylene (TCNE), N-butylferrocene, suggested by EIC and JPL's tetramethylphenylenediamine (TMPD) were evaluated. Figure 8 shows the result of adding TMPD to a cell. The additive provided 10-15% capacity at 2.9 volts thus protecting the cell during that period. TCNE did not provide adequate protection. N-butylferrocene from, early measurements appears to be comparable to or better than TMPD.

LITHIUM/CARBON ANODES

Replacement of lithium foil electrodes with an alternative lithium anode to enhance safety has been of interest. The performance targets for this material were 250 mAh/g and >2mA/cm^2 with good mechanical stability. One of areas JPL's effort has centered on is the development of a lithium/carbon alloy (Li_xC). Several carbon materials, including pitch coke, petroleum coke, graphite fiber and graphite were evaluated as potential candidates. The rate capability of Li_x C using the graphite material is shown in Table 3. At 1 mA/cm^2 a capacity of 200 mAh/g was achieved. At the lower rates, higher capacities to 235 mAh/g were found. A discharge curve is given in Figure 9. As expected the voltage of this experimental cell was below the lithium foil electrode cells. The Li_xC electrode was only 72 mv below the Lithium electrode potential at the start of the discharge and increased to 264 mv at the end of the discharge. Thus, it had a discharge curve comparable to that of the lithium foil cells.

SUMMARY

Ambient temperature rechargeable Li-TiS_2 cells have demonstrated a capability of 125 Wh/kg at rates greater than C/2 and almost 1000 cycles at 50% depth of discharge. Design studies identified that a tight pack provided a more consistent and higher operating voltage. Microporous PE or PP were found to be suitable as separator material. The electrolyte and anode:cathode ratios among other parameters were also specified. Significant electrical abuse did not result in a venting or explosion. Overcharge protection was shown to a possible in these cells. A Li_6C alloy was found to be a suitable replacement for lithium foil with predictable reduction in specific energy for the loss in lithium metal.

ACKNOWLEDGMENT

The work described herein was carried out at the Jet Propulsion Laboratory, California Institute of Technology, under a contract with the National Aeronautics and Space Administration (Code C).

(1-2

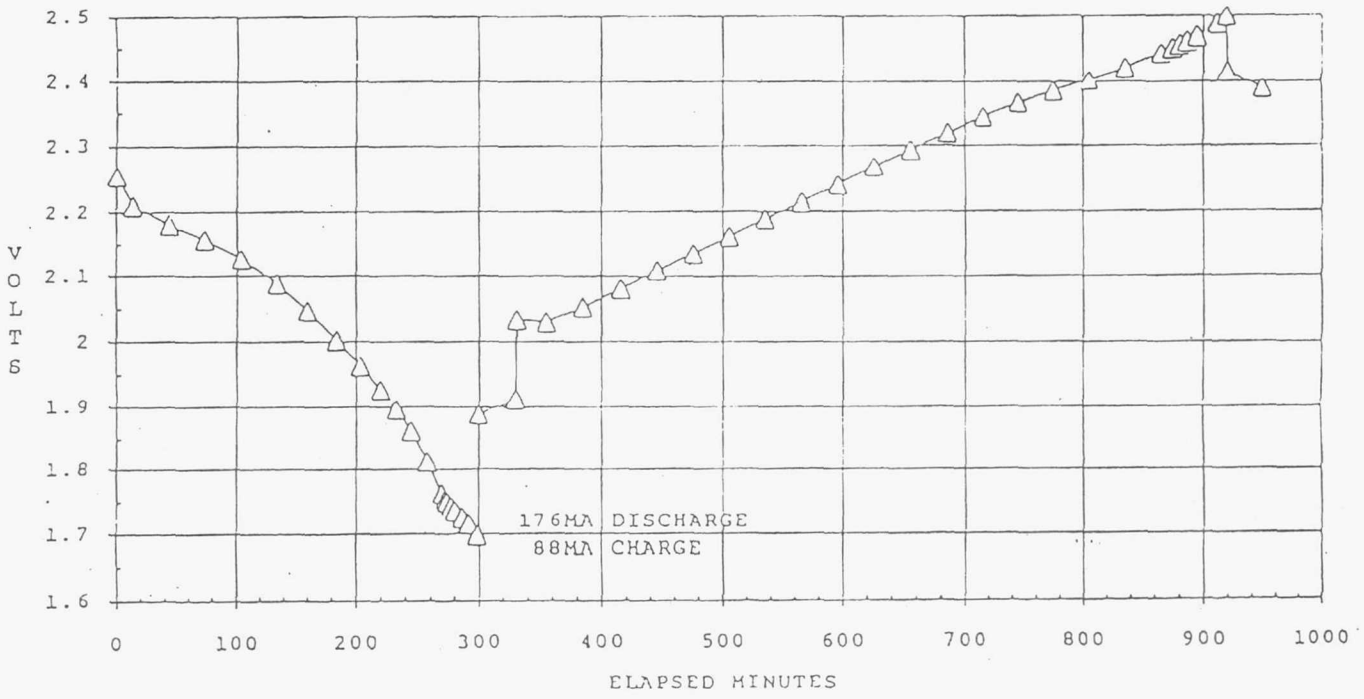

Figure 1: Li-TiS_2 Charge/Discharge Curve

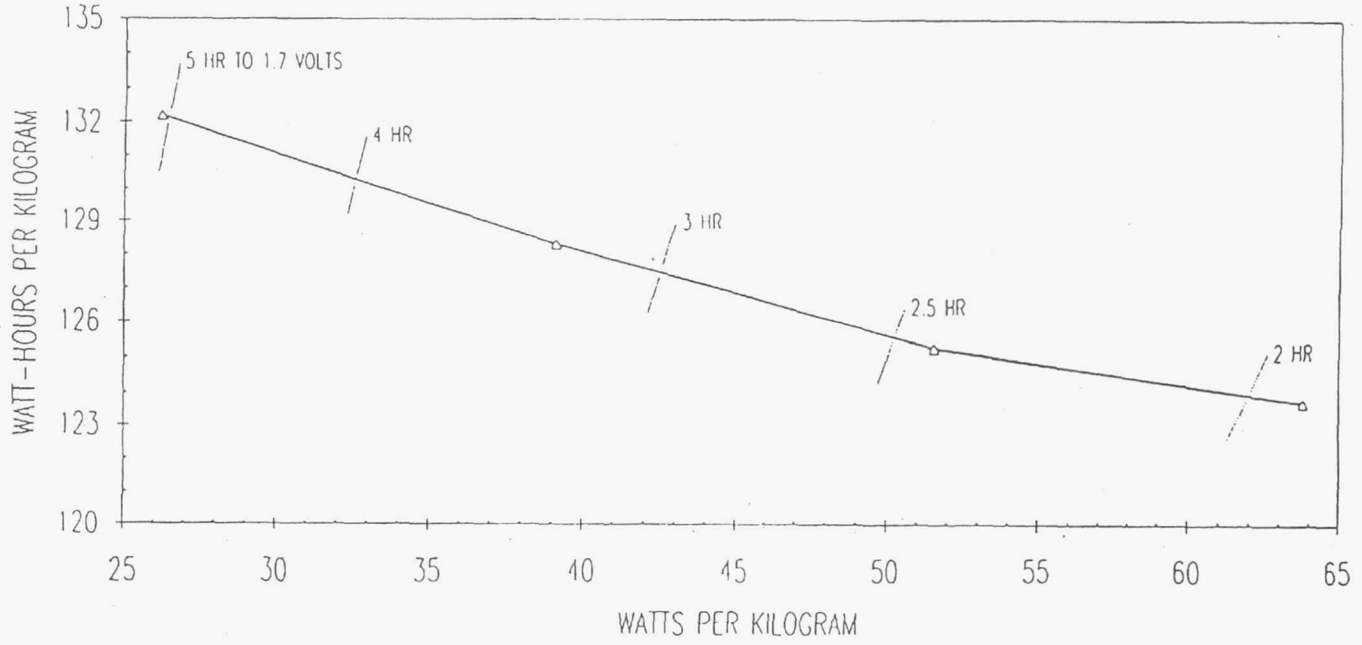

Figure 2: Performance of a Typical 1 Ah Li-TiS_2 Cell

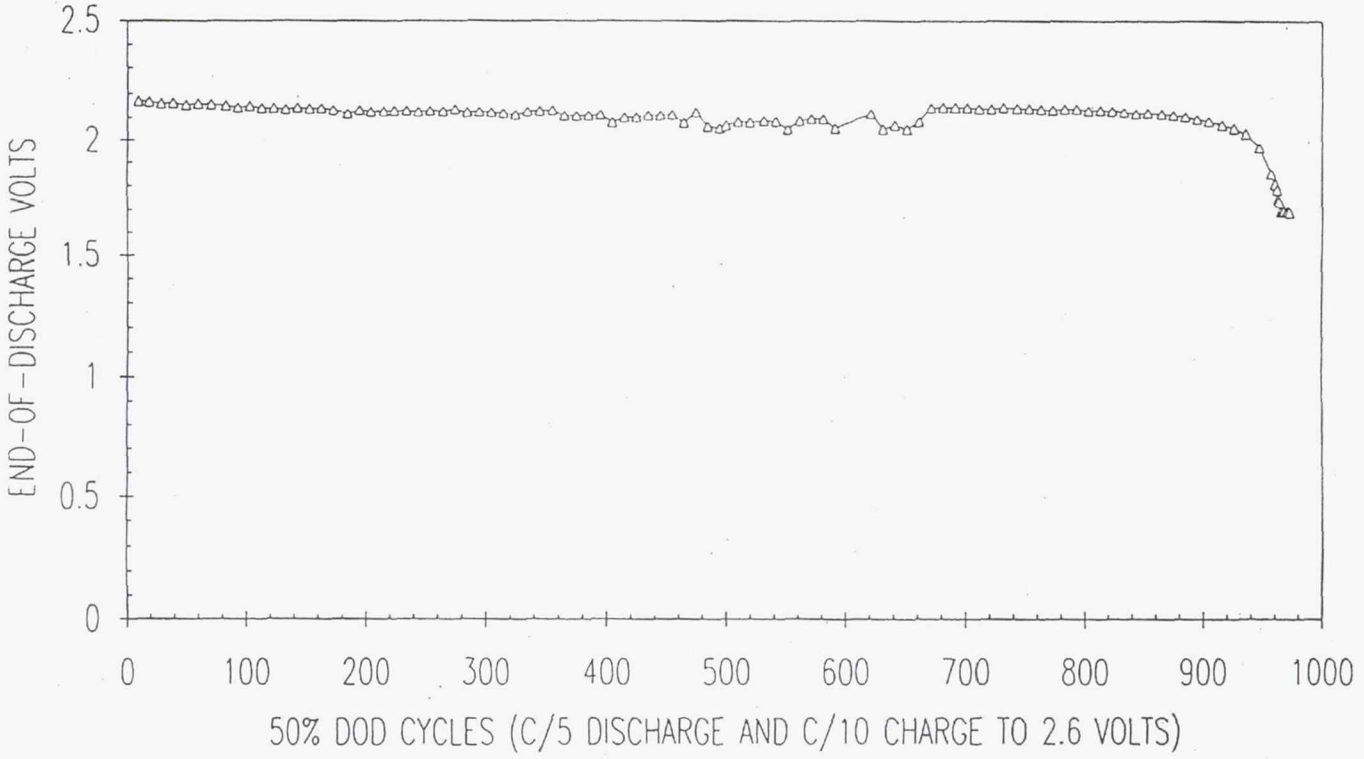

Figure 3: Cycle Life of a Li-TiS_2 Cell at 50% Depth of Discharge

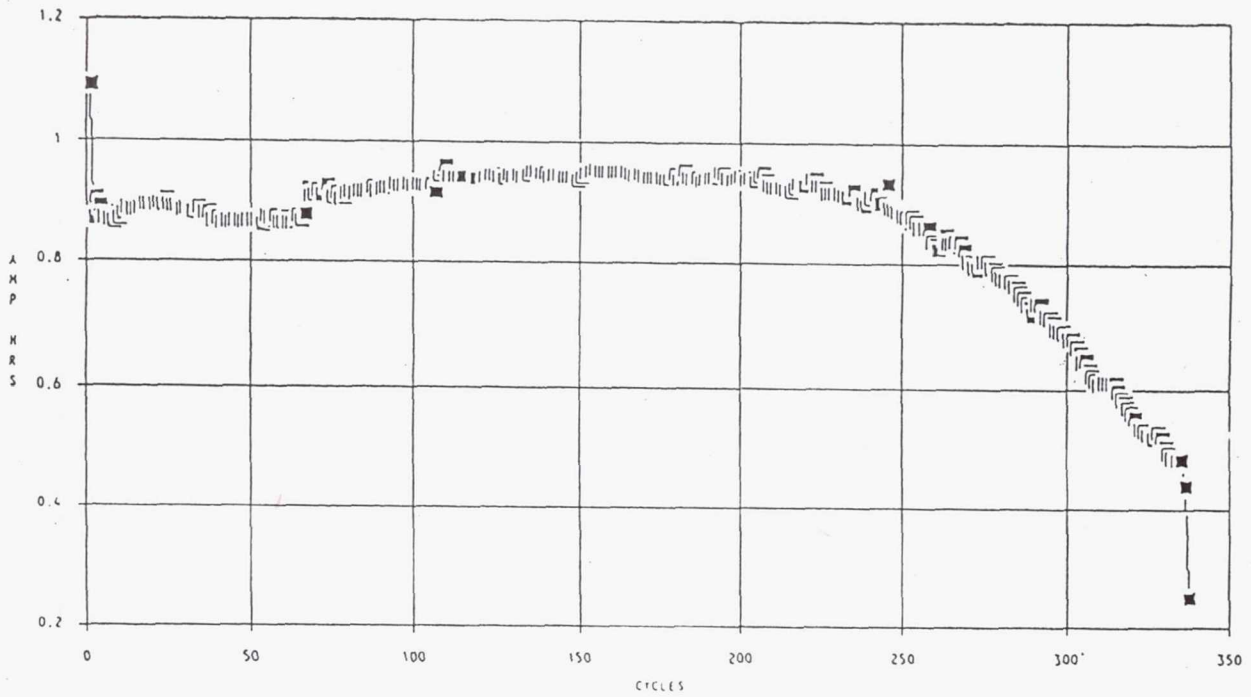

Figure 4: Cycle Life of a Li-TiS_2 Cell at 100% Depth of Discharge

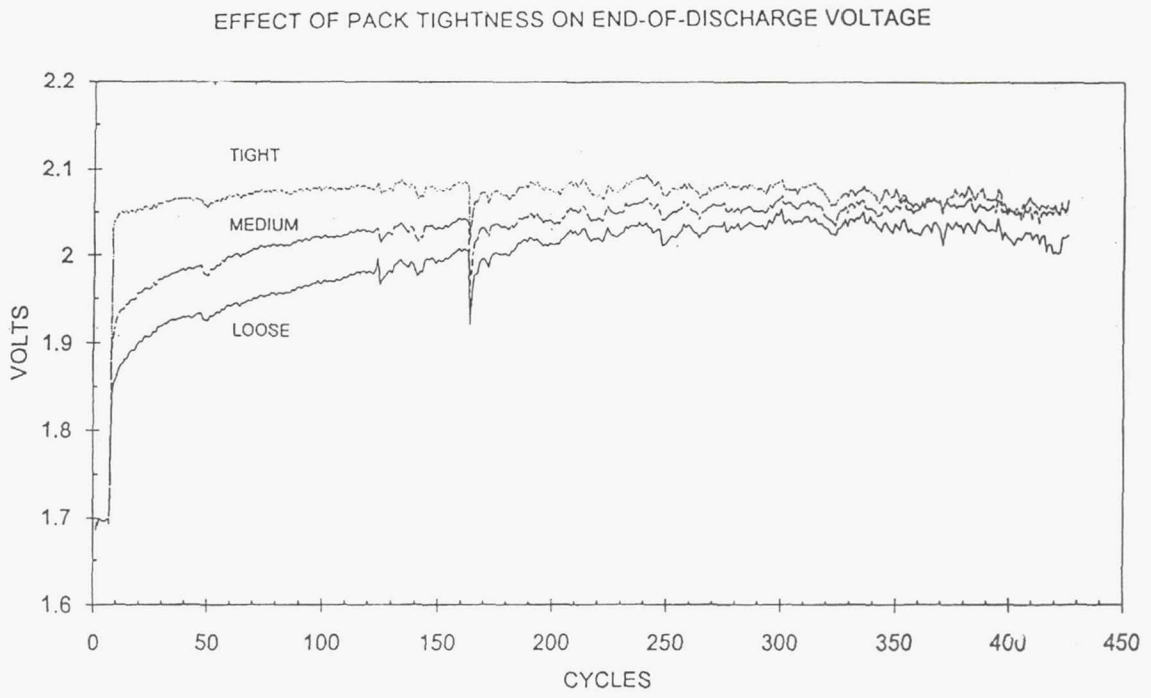

Figure 5: Effect of Pack Tightness on End-of-Discharge Voltage

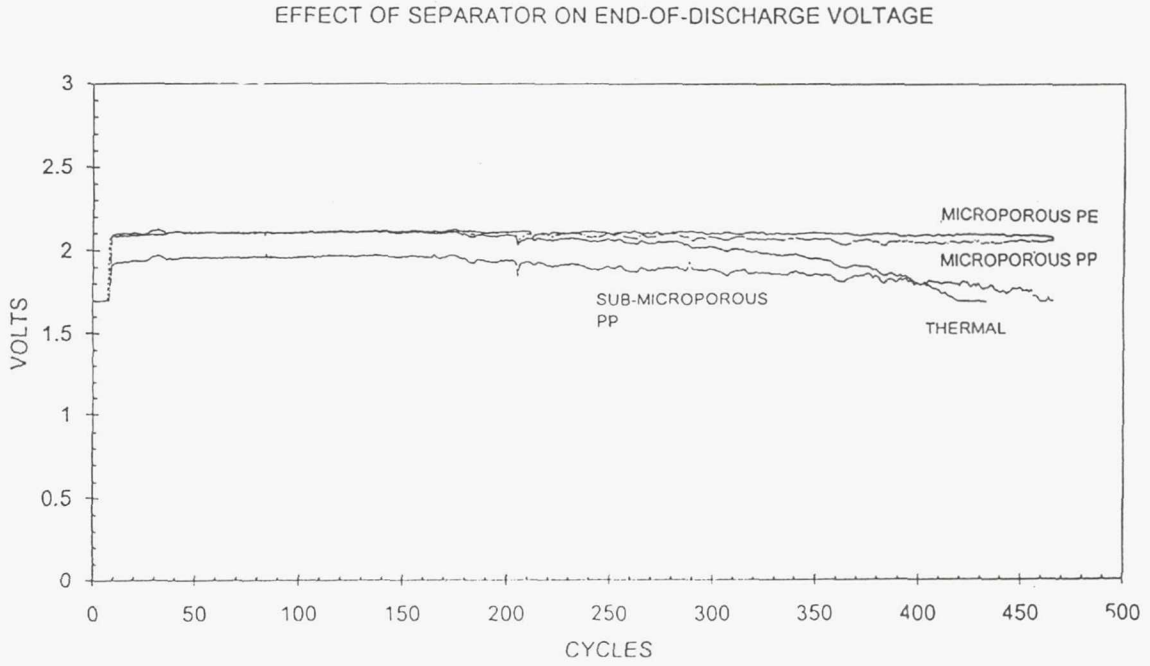

Figure 6: Effect of Separator on End-of-Discharge Voltage

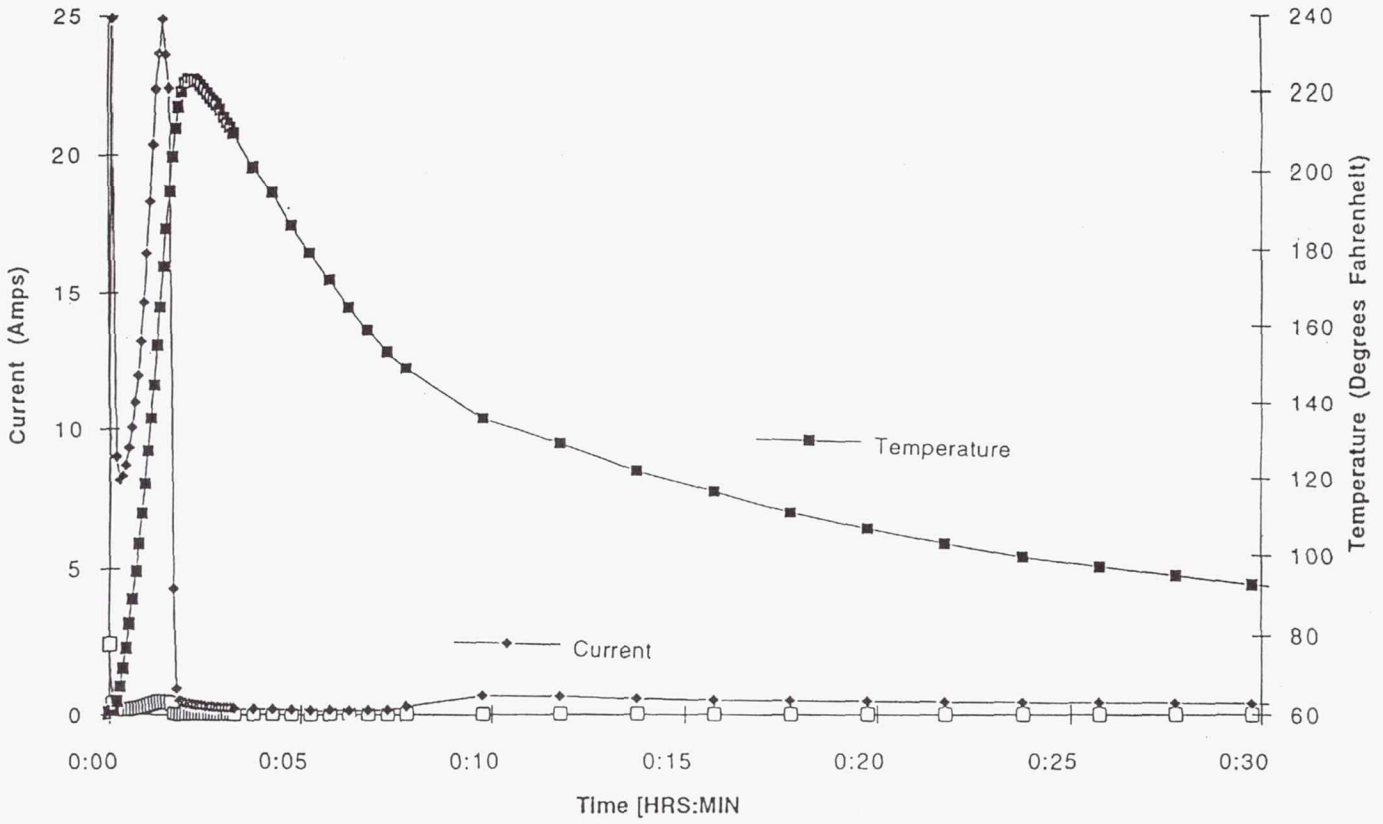

Figure 7: Short Circuit of a 1Ah 'AA' Li-TiS_2 Cell

. 70-75% OF THEORETICAL CAPACITY (STABILIZED IN 5 CYCLES)

. OVERCHARGE PERFORMANCE:

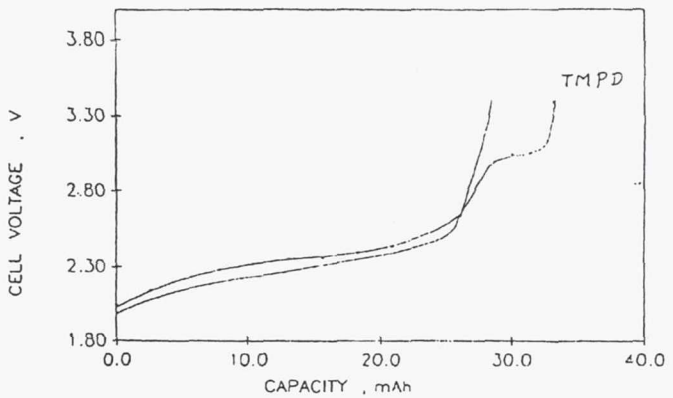

. 25 CYCLES WITH STABILIZED CAPACITY

* COMPATIBLE WITH THE CELL
* 10-15% OVERCHARGE PROTECTION AT THE NORMAL CHARGE RATE

Figure 8: Results of adding TMPD to a cell for Overcharge Protection

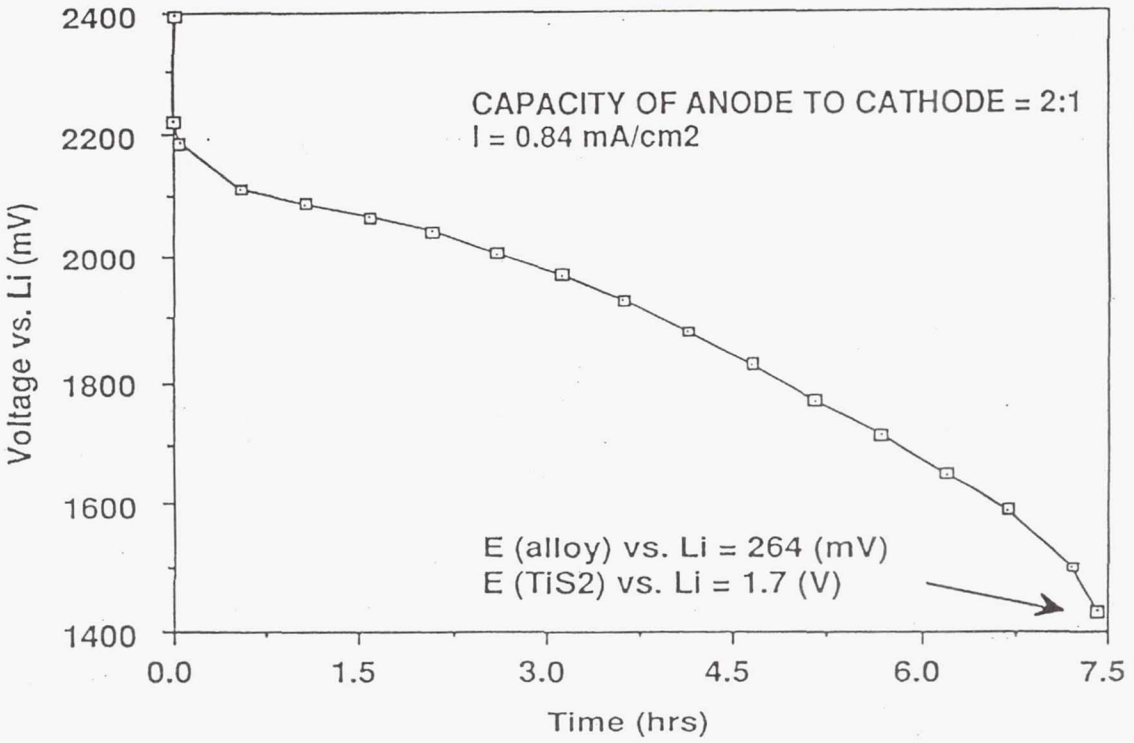

Figure 9: Discharge Curve of a Li_xC-TiS_2 Cell

Table 1: Cell Design Parameters

DESIGN PARAMETERS	VARIATIONS
ANODE TO CATHODE CAPACITY RATIO	4 : 1
PACK TIGHTNESS	Tight
TYPE OF ELECTROLYTE Salt: 1.5 M $LiAsF_6$	10% EC + 88% 2-MeTHF + 2% 2-MeF THF + 2-MeTHF + 2% 2-MeF, DIOX + 2-MeTHF + THF + 2% 2-MeF
QUANTITY OF ELECTROLYTE	6 c. c.
SEPARATOR	Microporous Polypropylene Microporous Polyethylene
BINDER CONCENTRATION	1 % by weight
CASE POLARITY	floating or positive.

Table 2: Results of Electrical Abuse Tests on Li-TiS_2 cells

CYCLE #	TYPE OF ABUSE	RATE	ABUSE %	EVENT
200	OVERCHARGE	C/10	400	NONE
400	OVERCHARGE	C/10	500	NONE
550	OVERCHARGE	C/10	500	NONE
400	OVERDISCHARGE	C/5	1000	NONE
500	OVERDISCHARGE	C/5	1000	NONE

Table 3: Rate Capability of a Li_xC Anode

CURRENT (mA/cm2)	CAPACITY (mAh/gm)
0.167	235
0.333	214
0.667	208
1.000	200

IMPEDANCE MEASUREMENTS ON A SPIRAL-WOUND NICKEL/METAL HYDRIDE CELL CYCLED IN A SIMULATED LEO ORBIT

Margaret A. Reid
National Aeronautics and Space Administration
Lewis Research Center
Cleveland, OH 44135

ABSTRACT

A spiral-wound size C cell was cycled at 25°C in a Low Earth Orbit regime (LEO) at 50% depth of discharge (DOD) with approximately 5% overcharge. The nominal capacity was 3.5 AH. The cell was cycled for 2000 cycles. Capacity checks and impedance measurements over the complete range of state of charge were made upon receipt and after 500, 1000 and 2000 cycles. The capacity of the cell was essentially unchanged until after the impedance measurements at 2000 cycles. Only small changes in the impedance parameters were observed, but there was somewhat more scatter in the data after 2000 cycles. When the cell was returned to LEO cycling after 2000 cycles, only 38% of the capacity could be obtained. It is believed that the cell failed because of an equipment failure at the end of the final impedance measurements which allowed an overdischarge.

INTRODUCTION

Nickel-metal hydride cells have been under intensive development in the last few years, and several manufacturers are selling these for both commercial markets [1, 2] and for space applications [3]. We are initiating testing of these for low-earth orbit applications. Since spiral-wound cells are readily available, we began with cycling and impedance measurements on an Ovonics size C cell with a nominal capacity of 3.5 AH.

EXPERIMENTAL

Short leads were soldered onto the two ends of the cell. The capacity was measured by charging at a C/10 rate for 16 hours and discharging at a C/4 rate to a cut-off voltage of 1.0 V. The initial capacity was 3.38 AH. A value of 3.4 AH was used in the computer program that controlled the cycling. Open circuit voltage decay measurements when the cell was new gave a loss of about 18% of capacity in 24 hours and 26% in 48 hours.

After the initial capacity check, the cell was charged and the impedances measured at various depths of discharge. Measurements were made on the fully charged cell and then at increments of 10% DOD until the cell was fully discharged. (Additional measurements were taken at 1%, 3% and 5% DOD after 500 cycles). A program developed by Dr. Stephen Lipka of Florida Atlantic University, CYCLER, was used to automate the charging, discharging and impedance measurements. The program was written in Pascal and run on a DOS 286 computer with a PAR 273 potentiostat and a Solartron 250 Frequency Response Analyzer. A Hewlett-Packard 3455A digital voltmeter was used to monitor the cell voltage. The computer was programmed to cut off the charging and discharge currents if a limiting voltage was reached in order to prevent overdischarge and overcharge. The change of voltage with time on open circuit after discharge was used to determine when the cell had reached a quasi-equilibrium state.

The desired depth of discharge was obtained by starting each measurement in the fully charged state and discharging to the calculated depth of discharge at a 20% LEO rate (0.343 C). Impedance measurements were taken at the quasi-equilibrium voltage described below. A true equilibrium voltage is never reached. After the discharge current is interrupted, the voltage rises abruptly, then more gradually, eventually falling due to self-discharge. We assume that the maximum voltage reached corresponds to a quasi-equilibrium state. The time that it takes to reach this maximum varies with the depth of discharge. At low depths of discharge the time is brief, and at high depths of discharge it is very long, on the order of days before self-discharge is appreciable. In order for the computer to determine when quasi-equilibrium has been reached, a parameter, δ, is defined as the rate of change of the voltage vs time. Ideally, quasi-equilibrium would be reached when $\delta = 0$. However it is impractical to wait to take the impedance measurements until the voltage stops rising completely, especially at high depths of discharge. Because of the different times required to reach quasi-equilibrium at different states of charge, the value of δ is set for each DOD based on prior observation of the voltage-time curve. The value selected may also depend on the type of cell under study (and how long one is willing to wait before taking the measurement). The rate of change of voltage with time is calculated by the computer program, and when this falls below δ, the impedance measurements are carried out at this quasi-equilibrium voltage. For the fully charged cell, δ was set at 0.005 mV/min, and this was decreased as the depth of discharge was increased. For 10% DOD, δ was set at 0.001 mV/min, and at 50% DOD and below was 0.00022 mV/min. Typical equilibration times using these values were about 20 minutes for a fully charged cell, 1-2 hours at 30% DOD, and 4-6 hours below 50% DOD.

After each measurement the cell was recharged by adding the capacity withdrawn on the prior discharge plus an additional 10% of the capacity of the cell.

The capacity on receipt was 3.38 AH. After the initial impedance measurements, the capacity had increased to 3.47 AH. The cell was then cycled for 500 LEO cycles at 50% DOD using a 55 minute charge time and a 35 minute discharge time. Approximately 5% overcharge was used. This corresponds to a 0.573 C charge rate and a 0.857 C discharge rate. The cutoff voltage on discharge was 1.00 V. The capacity and impedance measurements were then repeated. Measurements were repeated again after 1000 cycles and 2000 cycles.

After the cell failed, it was opened in order to determine the area and thickness of the individual electrodes for comparison of the impedances with those of boilerplate Ni/H_2 cells on a unit area basis. The nickel electrode was about 40 mils thick with an area of about 94 cm^2. (The initial thickness was probably smaller). The hydride electrode was about 15 mils thick with an area of about 113 cm^2. Attempts to make further measurements with the hydride electrode were unsuccessful due to its disintegration when current was applied.

EXPERIMENTAL RESULTS

The capacity remained essentially constant, increasing slightly to 3.49 AH before cell failure at the end of the impedance measurements at 2000 cycles.

Initial analysis of the data was done using the conventional circuit shown in Fig. 1 with the ohmic resistance in series with a parallel combination of a capacitor representing the double-layer capacitance or adsorption capacitance and a resistor representing the kinetic resistance of the electrode. The ohmic resistance of the cell was about 16.5 $\pm$ 0.5 mOhms and did not vary with the DOD or cycle number. Little change in the other impedance parameters was observed until very low depths of

discharge, similar to observations on boilerplate Ni/H_2 cells. Table I lists the parameters for the cells at 2000 cycles.

After 2000 cycles the impedances were essentially the same as at 1000 cycles, with slightly larger values at the lowest frequencies. At the higher states of charge there was an indication of the start of a second RC circuit. At the lower states of charge, there was slightly more scatter. Figures 2-5 show the comparisons for 5%, 20%, 70% and 90% DOD.

DISCUSSION

Very little data is available in the literature as yet on the impedances of hydride electrodes and nickel-metal hydride cells. Kuriyama et al measured impedances of electrodes made from an alloy powder ($MmNi_{3.5}Co_{0.7}Al_{0.8}$) pressed with a PFE/PFP binder, both with and without a copper coating on the alloy particles. Agerwal and Orazem measured impedances of a $LaNi_5$ solid electrode. The electrodes in the Ovonics cell studied here are made from an alloy containing Ni, Ti, V, Zr and other trace elements.

In order to obtain an estimate of the impedance of the hydride electrode in this cell, the data were put on a unit area basis and the complex plane plots compared to those of the boilerplate Ni/H_2 cells that we are also testing. This is shown in Fig. 6 for the two cells at a 20% DOD. The boilerplate Ni electrodes have capacities of about 0.033 AH/cm^2 compared to about 0.037 AH/cm^2 of the Ni electrodes in the metal hydride cell. If we assume that the impedance of the hydrogen electrode in the boilerplate Ni/H_2 cells is negligible [8], and that the impedances of the two nickel electrodes are about the same at corresponding states of charge, then the increased impedance of the hydride cell over that of the boilerplate Ni/H_2 cell can be attributed to the hydride electrode. An estimate of the impedance of the hydride electrode calculated from the differences at each frequency is shown in Figure 7. Although these are very approximate calculations, they suggest that the impedance of the metal hydride electrode is not negligible, in contrast to that of the gaseous hydrogen electrode in a typical Ni/H_2 cell.

A confirmation that these estimated values for the impedance of the metal hydride electrode are reasonable can be obtained by comparison of this data with that of Agerwal and Orazem (Fig. 8). The impedance data are of the same form at that found by these authors, (i.e., an ohmic resistance in series with a single parallel RC circuit which includes a diffusion impedance) although they worked with a different alloy electrode ($LaNi_5$) and used a solid rod rather than a powdered electrode. Estimating the true surface area of the powdered alloy from published literature data using a surface area of about 2000 cm^2/g and a capacity of about 400 mAH/g [8], our impedances calculated with respect to the true surface area are of the same order of magnitude as those of Agerwal and Orazem, where the surface area was 1.5 cm^2.

The data of Kuriyama et al were measured on a bonded hydride electrode with a binder of polyperfluoroethylene/polyperfluoropropylene (10% by weight) and have an additional semicircle in the complex plane plots, believed to be due to the contact resistance between the alloy and the current collector. The remaining portion of the curve is similar to our curves, but insufficient data is given to make a more detailed comparison.

Spectroscopic analysis of the Ni electrode after dismantling showed a Zr content of about 1%. This is consistent with the findings of earlier researchers that the Zr dissolves extensively (and preferentially) from this alloy in 31% KOH at 70°[3]. Since nickel electrodes commonly last for thousands of

cycles before failure, the failure is presumably caused by changes in the hydride electrode, either as a result of the cycling or from the failure of the equipment. It would be of interest to see if the metal ions that have precipitated in or on the Ni electrode have an effect on the cycle life, but this cannot be studied without measurements on the individual electrodes in situ.

More information about the changes brought about by cycling and the mechanism of failure might be obtained if both the nickel electrode and the hydride electrode are isolated from the case so that the case can be used as a quasi-reference electrode [8]. Studies will be initiated shortly on cells of this type which will allow the contributions of the individual electrodes to be determined.

Since the cell impedance did not change appreciably during the 2000 cycles that the cells were cycled, it cannot be determined from this limited study whether impedance can be used as a diagnostic criteria for metal hydride cells, especially in this situation where the negative electrode is connected to the case.

CONCLUSION

Impedances of the spiral-wound metal hydride cell changed only slightly over the course of 2000 LEO cycles. Both the nickel electrode and the metal hydride electrode apparently contribute to the impedance of the cell, with the larger portion probably due to the Ni electrode. In the absence of a reference electrode, the contributions of each electrode to the impedance cannot be determined. Future measurements will be made with cells constructed with the hydride electrode not connected to the case. This arrangement allows the case to be used as a quasi-reference electrode, and thus the effects of cycling can be determined for the individual electrodes.

REFERENCES

1. M. Fetcenko, S. Venkatesan, S. Dhar, S. Ovshinsky and R. Tsang, Proceedings of the 3rd International Rechargeable Battery Seminar, Deerfield Beach, Florida, March 1992.

2. S. Ovshinsky, P. Gifford, S. Venkatesan, D. Corrigan and S. Dhar, Proceedings of the Tenth International Seminar on Primary and Secondary Battery Technology and Application, Deerfield Beach, FL, March 1993.

3. Sealed Metal-Hydride Batteries for Aerospace Applications, D. Coates, R.D. Wright, pp. 199-209, Proceedings of the Symposium on Hydrogen Storage Materials, Batteries, and Electrochemistry, Eds. D.A. Corrigan and S. Srinivasan, The Electrochemical Society, Pennington, N.J., Vol. 92-5.

4. N. Kuriyama, T. Sakai, H. Miyamura, I. Uehara, H. Ishikawa and T. Iwasaki, J. Electrochem. Soc., 139 (1992) L72-L73.

5. M.G.S.R.Thomas, P.G. Bruce and J.B. Goodenough, J. Electrochem. Soc., 132 (1985) 1521-1528.

6. B.K. Zoitos, D.L. Hudson, P.D. Bennett and V.J. Puglisi, pp. 168-178, Proceedings of the Symposium on Hydrogen Storage Materials, Batteries, and Electrochemistry, Eds. D.A. Corrigan and S. Srinivasan, The Electrochemical Society, Pennington, N.J., Vol. 92-5.

7. P. Agerwal, M. Orazem and A. Hiser, pp. 120-137, Proceedings of the Symposium on Hydrogen Storage Materials, Batteries, and Electrochemistry, Eds. D.A. Corrigan and S. Srinivasan, The Electrochemical Society, Pennington, N.J., Vol. 92-5.

8. M.A. Reid, J. Power Sources, 29, 467-76 (1990).

9. J.J. Reilly, pp 24-45, Proceedings of the Symposium on Hydrogen Storage Materials, Batteries, and Electrochemistry, Eds. D.A. Corrigan and S. Srinivasan, The Electrochemical Society, Pennington, N.J., Vol. 92-5.

Table I.—Selected impedance parameters at 2000 cycles using the standard circuit model.

DOD	R_{ohm}, mOhm	R_{kin}, mOhm	Capacitance, Farads	Slope, mOhm $sec^{-1/2}$
5	15.1	14.3	~2000	2.66
20	15.3	14.3	~4000	2.95
70	15.5	20.9	~6000	2.31
90	15.3	42.1	~8000	1.44

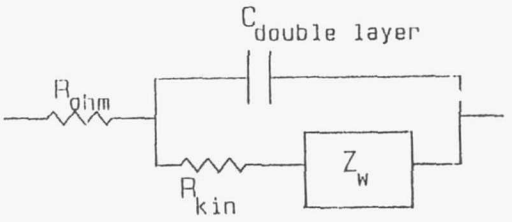

Figure 1.—Simplified circuit model for analysis of impedance parameters.

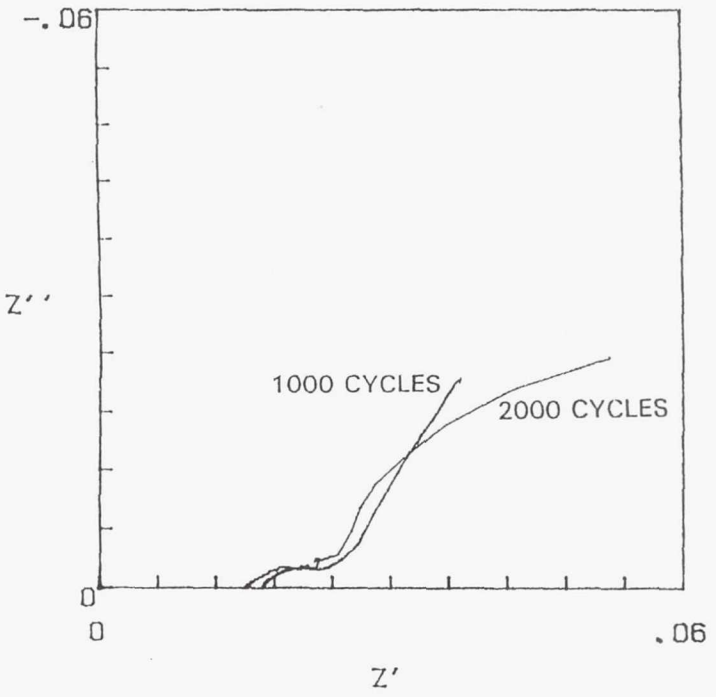

Figure 2.—Complex plane plots at 5 percent DOD for 1000 and 2000 cycles. V = 1.395.

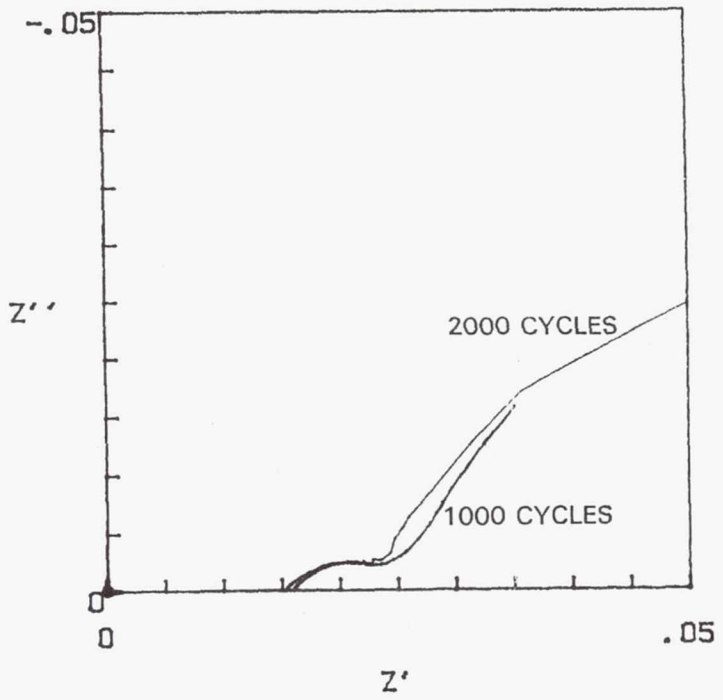

Figure 3.—Complex plane plots at 20 percent DOD for 1000 and 2000 cycles. V = 1.340.

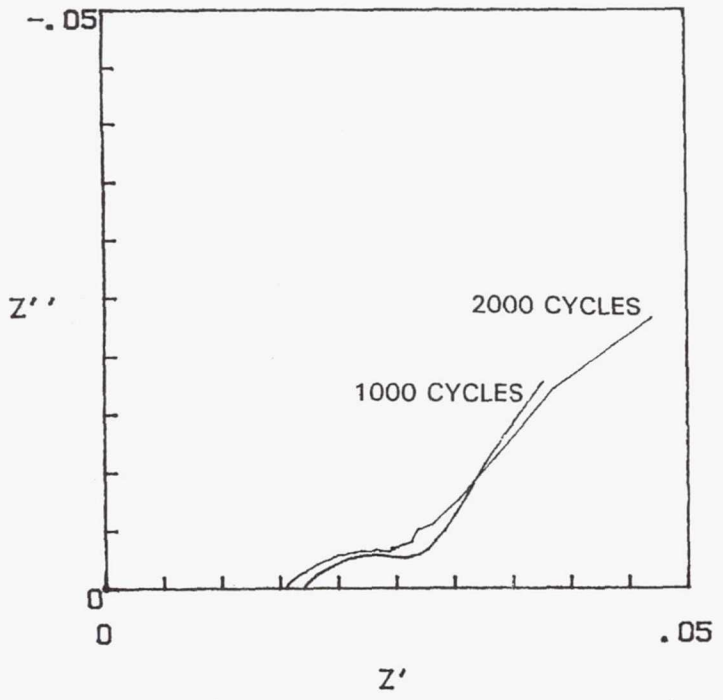

Figure 4.—Complex plane plots at 70 percent DOD for 1000 and 2000 cycles. V = 1.262.

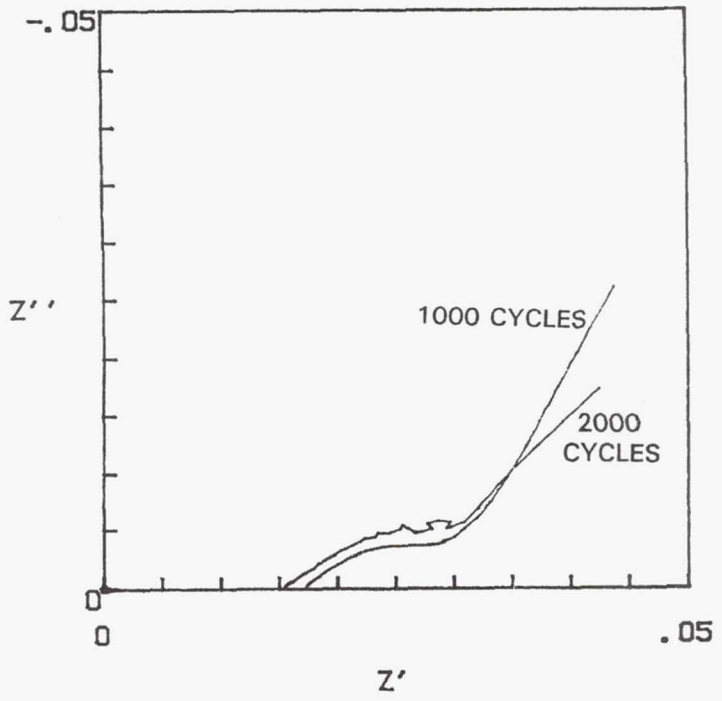

Figure 5.—Complex plane plots at 90 percent DOD for 1000 and 2000 cycles. V = 1.206.

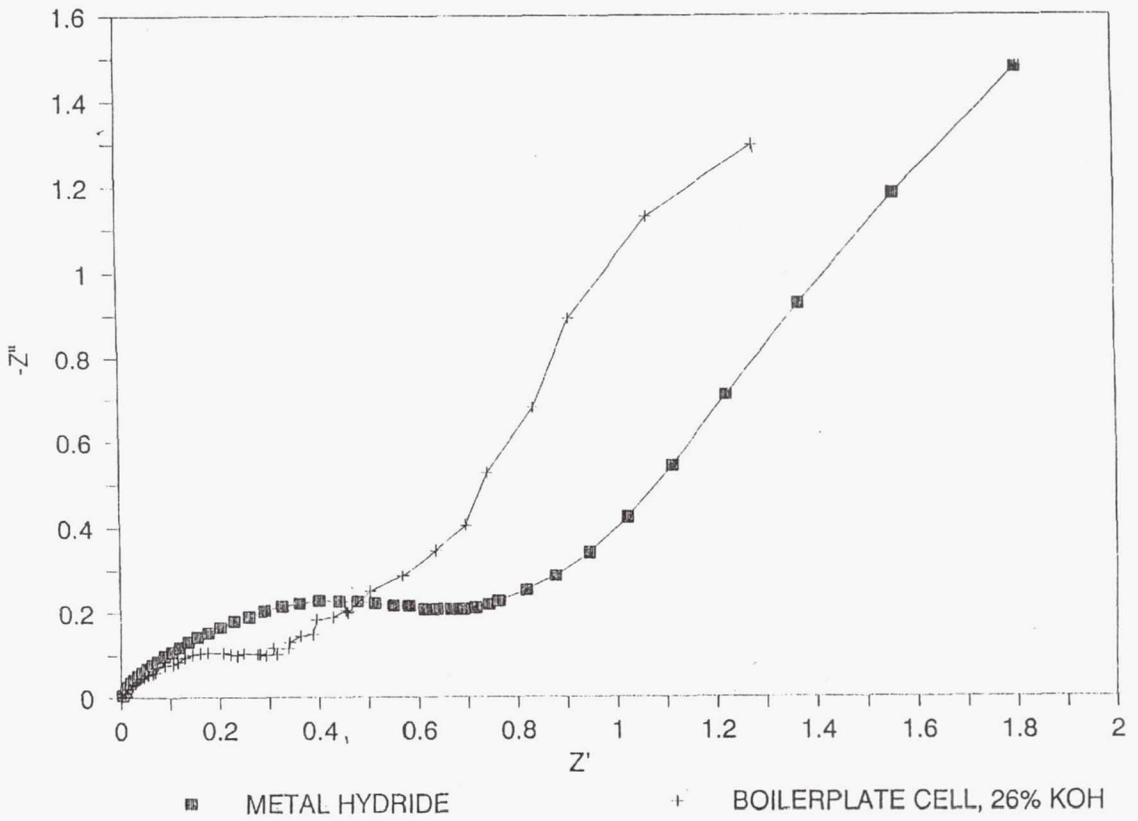

Figure 6.—Comparison of impedances of boilerplate Ni/H_2 cell and Ni/MH cell on a unit projected area basis. 20 percent DOD, 1000 LEO cycles.

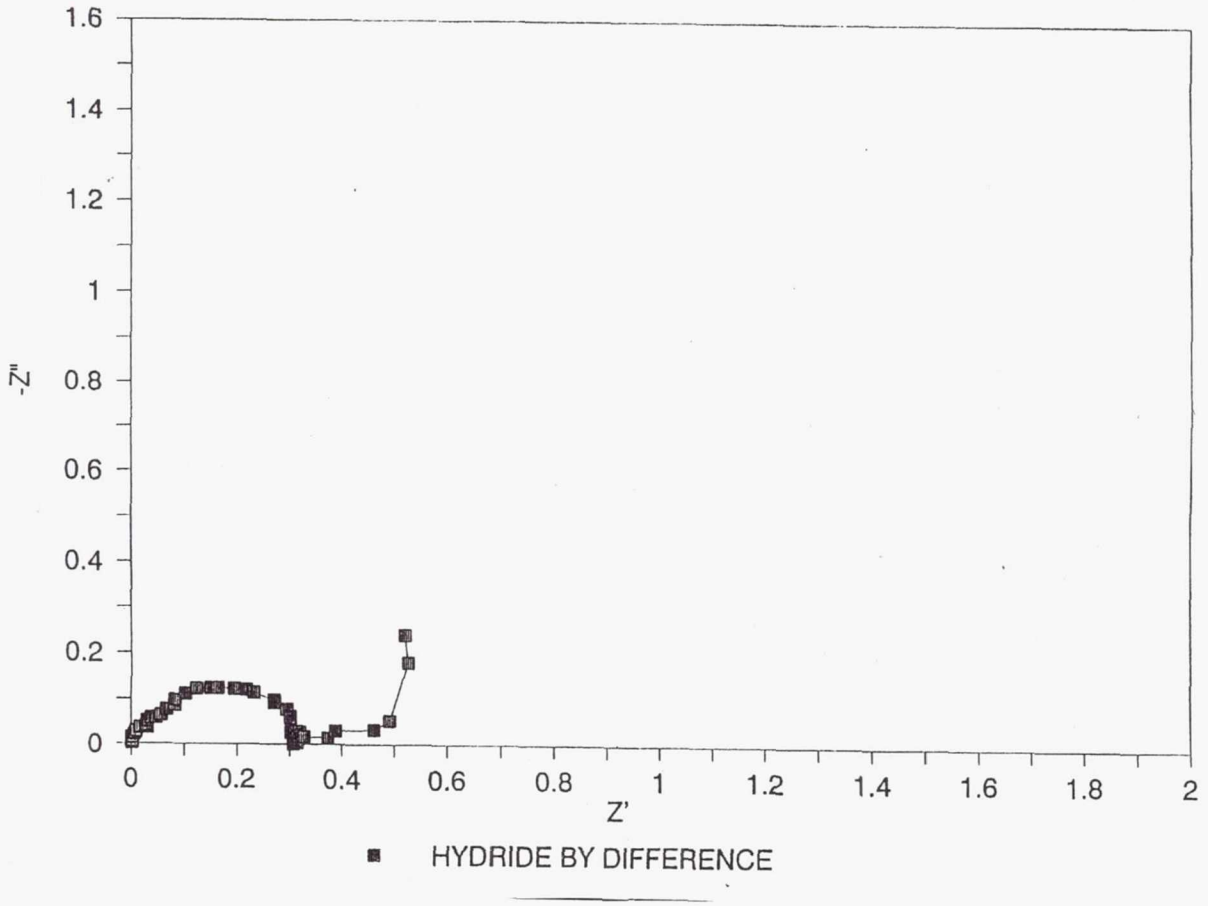

Figure 7.—Estimated impedance of the metal hydride electrode at 20 percent DOD by difference between Ni/MX cell and boilderplate Ni/H_2 cell. After 1000 LEO cycles.

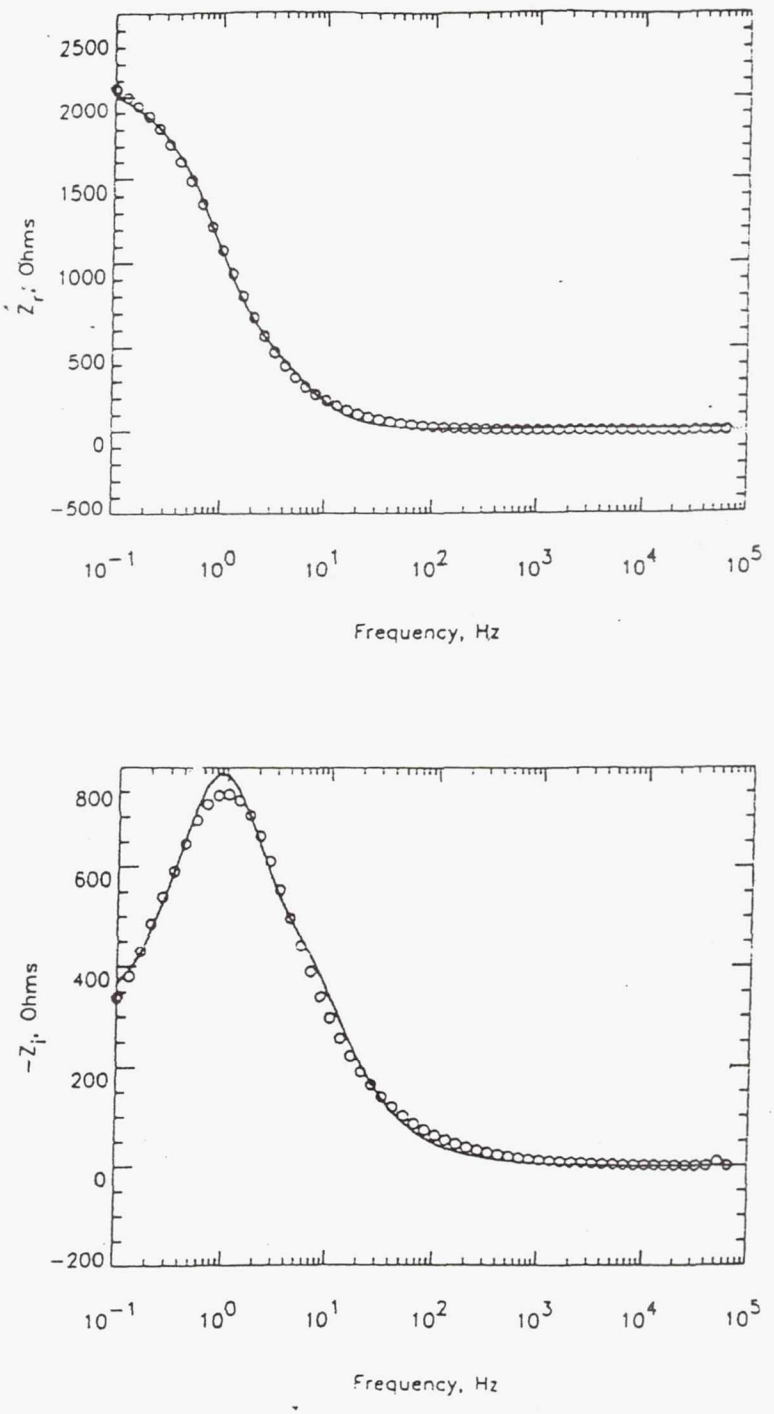

(a) Agerwal and Orazem.

Figure 8.—Comparison of estimated impedance of metal hydride electrode at 20 percent DOD (estimated true surface area of about 20 000 cm^2) with literature data of Agerwal and Orazem for a partially charged electrode (1.5 cm^2 rod).

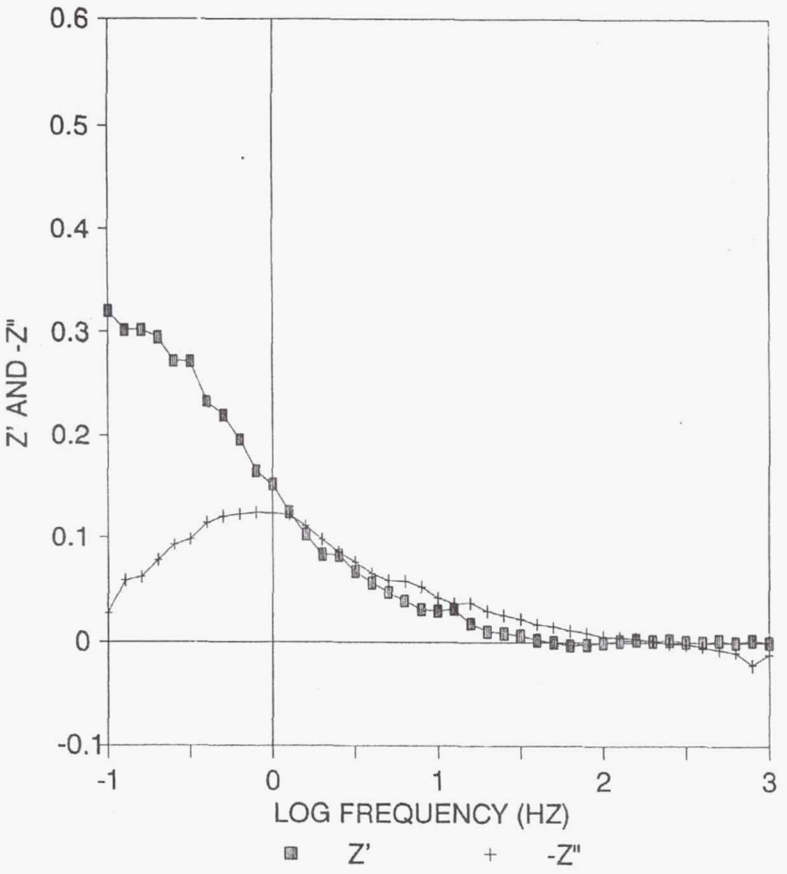

(b) This study.

Figure 8.—Concluded.

NASA LEWIS ADVANCED IPV NICKEL-HYDROGEN TECHNOLOGY

John J. Smithrick
and
Doris L. Britton
National Aeronautics and Space Administration
Lewis Research Center
Cleveland, Ohio 44135

ABSTRACT

Individual pressure vessel (IPV) nickel-hydrogen technology was advanced at NASA Lewis and under Lewis contracts. Some of the advancements are as follows: (1) to use 26 percent potassium hydroxide electrolyte to improve cycle life and performance, (2) to modify the state-of-the-art cell design to eliminate identified failure modes and further improve cycle life, and (3) to develop a lightweight nickel electrode to reduce battery mass, hence reduce launch and/or increase satellite payload.

A breakthrough in the LEO cycle life of individual pressure vessel nickel-hydrogen battery cells was reported. The cycle life of boiler plate cells containing 26 percent KOH electrolyte was about 40,000 accelerated LEO cycles at 80 percent DOD compared to 3,500 cycles for cells containing 31 percent KOH. Results of the boiler plate cell tests have been validated at NWSC, Crane, Indiana. Forty-eight ampere-hour flight cells containing 26 and 31 percent KOH have undergone real time LEO cycle life testing at an 80 percent DOD, 10°C. The three cells containing 26 percent KOH failed on the average at cycle 19,500. The three cells containing 31 percent KOH failed on the average at cycle 6,400.

Validation testing of NASA Lewis 125 Ah advanced design IPV nickel-hydrogen flight cells is also being conducted at NWSC, Crane, Indiana under a NASA Lewis contract. This consists of characterization, storage, and cycle life testing. There was no capacity degradation after 52 days of storage with the cells in the discharged state, on open circuit, 0°C, and a hydrogen pressure of 14.5 psia. The catalyzed wall wick cells have been cycled for over 22,694 cycles with no cell failures in the continuing test. All three of the noncatalyzed wall wick cells failed (cycles 9,588, 13,900 and 20,575).

Cycle life test results of the Fibrex nickel electrode has demonstrated the feasibility of an improved nickel electrode giving a higher specific energy nickel-hydrogen cell. A nickel-hydrogen boiler plate cell using an 80 mil thick, 90 percent porous Fibrex nickel electrode has been cycled for 10,000 cycles at 40 percent DOD.

INTRODUCTION

The state of development of individual pressure vessel nickel-hydrogen battery cells is such that they are acceptable for geosynchronous orbit (GEO) applications since not many cycles are required over the life of the battery system (1000 cycles, 10 years). There are 20 communication satellites in GEO using IPV nickel-hydrogen batteries [1]. For the demanding Low-Earth-Orbit (LEO) applications, however, the current cycle life at moderate-to-deep depths-of-discharge (40 to 80 percent) should be improved. Battery cycle life has a major impact on life cycle cost for LEO applications such as Space Station Freedom (30 year life). The primary drivers are transportation to orbit and battery cost.

IPV nickel-hydrogen technology was advanced at NASA Lewis and under Lewis contracts. Some of the advancements are as follows: (1) to use 26 percent potassium hydroxide electrolyte to improve cycle life and performance, (2) to modify the state-of-the-art cell designs to eliminate identified failure modes and further improve cycle life and (3) to develop a lightweight nickel electrode to reduce battery mass, hence reduce launch cost and/or increase satellite payload.

The influence of potassium hydroxide electrolyte concentration on cycle life was investigated at Hughes Aircraft Company under a NASA Lewis Contract. Hughes reported a breakthrough in LEO cycle

life [2, 3]. Boiler plate cells containing 26 percent KOH were cycled for about 40,000 accelerated cycles at 80 percent depth-of-discharge (DOD) at 23°C, compared to 3,500 cycles for cells containing 31 percent KOH. These results are in the process of being validated using flight hardware and real time LEO test under a NASA Lewis Contract with the Naval Weapons Support Center, Crane, Indiana.

The advanced design for an IPV nickel-hydrogen cell was conceived with the intention of improving cycle life at moderate-to-deep depths-of-discharge (40 to 80 percent). The approach was to review IPV nickel-hydrogen cell designs and results of cycle life tests conducted in-house and by others to identify areas where improvements could result in a longer life [4 - 10]. The feasibility of the design was demonstrated using 6 Ah boiler plate cells [11]. The advanced design is in the process of being validated using 125 Ah flight cells and real time test under a NASA Lewis Contract with the NWSC, Crane, Indiana.

A lightweight nickel electrode using a thick, porous, fiber substrate has been evaluated in-house using boiler plate cells. The thickness is 80 mils, porosity 90 percent, active material loading level 1.6 g /cm^3 void volume.

In this report results of validation tests will be updated [12,13].

MEASUREMENTS AND PROCEDURES

For both the 48 and 125 Ah cells, the quantities measured every 2.4 min for each cell during charge and discharge and their accuracies are: current (± 2.0 percent), voltage (± 0.001 percent), pressure (± 1 percent), and temperature (± 1 percent). Charge and discharge ampere-hour capacities are calculated from current and time. Charge-to-discharge ratio (ampere-hours into cell on charge to ampere-hours out on discharge) is calculated from the capacities. Cell charge and discharge currents are calculated from the voltage measured across a shunt, using an integrated digital voltmeter. Cell pressure is measured using a strain gauge located on the cell dome. The temperature is measured using a thermistor located on the center of the pressure vessel dome. The thermistor is mounted using a heat sink compound to insure good thermal contact.

To verify the performance of lightweight nickel electrodes in boiler plate hardware, a nickel-hydrogen cell was assembled at NASA Lewis. The quantities measured during charge and discharge are: current (± 2.0 percent), voltage (± 0.001 percent), and time (± 1 percent). The charge and discharge ampere-hours and watt-hours are calculated from current and time on every scan. Every 18 sec, the data is saved and stored to a data collector. The data can be retrieved for data and graphical output. The percent utilization is calculated by using the ratio of the measured discharge capacity to the theoretical calculated capacity based on the weight of the active material deposited. End-of-life failure is defined as the point where the discharge voltage degrades to 0.5 V.

For the 48 Ah cells, prior to cell final hydrogen gas adjustment, the nickel electrodes were positively charged, which results in a 0 psia hydrogen gas pressure. After completion of acceptance testing the cells were discharged at the C/10 rate (4.8 A) to 0.1 V or less. The cells were shipped to NWSC, Crane, Indiana, where they were stored at 10°C under trickle charge at C/200 for 31 days. After storage the discharge ampere-hour capacity acceptance test was repeated. The capacity was measured after charging the cells at the C/2 rate (24 A) for 2.0 hr, then C/10 for 6 hr followed by a 0.5 hr open circuit stand. The discharge capactiy was measured to 1.0 V at each of the following rates: C2, C, 1.4, and 2 C.

Prior to undergoing cycle life testing, the capacity retention after a 72 hr open circuit stand (10°C) was measured for each cell. For the cycle life test the cells were connected electrically in series to form a six cell pack. The cycle regime was a 90 min LEO orbit consisting of a 54 min charge at a constant 0.93 C rate (44.7 A) followed by a 36 min discharge at a 1.33 C rate (64 A). The charge to discharge ratio was 1.048. The depth-of-discharge was 80 percent of name plate capacity (48 Ah). During the cycle life test the cooling plate temperature was maintained at 10±2°C. Cell failure for this test was defined to occur when the discharge voltage degrades to 1.0 V during the course of the 36 min discharge.

For the 125 Ah cells, after completion of activation by the manufacturer, the precharge hydrogen pressure was set to 0 psig (14.5 psia) with the nickel electrodes in the fully discharged state. After completion of the acceptance testing the cells were discharged at the C/10 rate (12.5 A) to 0.1 V or less and the terminals were shorted. The cells were shipped to NWSC, Crane, where they were stored at open circuit, and discharged at 0°C for 52 days. After storage the discharge ampere-hour capacity acceptance test was repeated. The capacity was measured after charging the cells at the C/2 rate (62.5 A) for 2 hr then C/10 for 6 hr followed by a 0.5 hr open circuit stand. The discharged capacity was measured to 1.0 V for each of the following rates: C/2, C, 1.4 C, and 2 C.

Prior to undergoing cycle life testing the capacity retention after a 72 hr open circuit stand (10°C) was measured for each cell. For the cycle life test the cells were connected electrically in series to form a six cell pack. The cycle regime is a 90 min LEO orbit consisting of a 54 min charge at a constant 0.69 C rate (87 A) followed by a 36 min discharge at a C rate (125 A). The charge-to-discharge ratio was 1.04. The depth-of-discharge was 60 percent of name plate capacity (125 Ah). During the cycle life test the cooling plate temperature was maintained at 10±2°C. Cell failure for this test was defined to occur when the discharge voltage degrades to 1.0 V during the course of the 36 min discharge.

The boiler plate cell was cycle life tested using a 90 min cycle regime at 40 percent DOD. The continuous test regime consists of charging at a constant 0.48 C rate for 55 min immediately followed by discharge at a constant 0.69 C rate for 35 min. Cell capacities are measured every 1000 cycles, by charging at the C rate for 80 min followed by discharging at the 0.69 C rate to 0.5 V. Failure of the cell occurs when the discharge voltage degrades to 0.5 V during the course of the constant current 35 min discharge at the 0.69 C rate.

EXPERIMENTAL

TEST FACILITY - The facility is capable of testing 45 battery packs with maximum of 10 cells electrically connected in series per pack. Each pack has its own charge and discharge power supply controlled by a computer which is programmed to satisfy the particular test requirements. During testing, each pack is scanned every 2.4 min to compare data such as voltage, temperature, and pressure with programmed limits. If a parameter is out of limit, an alarm will be initiated and a message will be typed out identifying the cell and parameter. The data is recorded on a 132 mB disc drive and if requested can be obtained in report form. The cell temperature during a test is controlled by a recirculating cooler that circulates a solution of water and ethylene glycol through a cooling plate.

CELL DESCRIPTION - 48 Ah Flight Cells - Six Air Force/Hughes recirculating design IPV nickel-hydrogen flight cells manufactured by Hughes are undergoing testing. Three of the cells contain 26 percent KOH electrolyte (test cells). The other three (control cells) are identical to the test cells but they contain 31 percent KOH. Both the test and control cells contain an equal number of components. The name plate capacity is 48 A-hr. The cell is illustrated in Fig. 1. It consists of a stack of nickel electrodes, separators, hydrogen electrodes, and gas screen assembled in a non-back-to-back electrode configuration. In this configuration electrodes of different types directly face each other. The stack is packaged in a cylindrical pressure vessel, with hemispherical end caps. This is made of Inconel 718 and lined with zirconium oxide which serves as a wall wick. The components are shaped in a pineapple slice pattern. Like electrodes are connected electrically in parallel. The separators consist of two layers of zircar, which extend beyond the electrodes to contact the wall wick. Hence, the electrolyte which leaves the stack during cycling will be wicked back. The gas screens are polypropylene. The nickel electrode consists of a dry sinter plaque containing a nickel screen substrate which was electrochemically impregnated by the alcoholic Pickett process [14].

CELL DESCRIPTION - 125 Ah Advanced Flight Cells - Six 125 Ah advanced design IPV nickel-hydrogen flight cells fabricated by Eagle-Picher, Joplin according to NASA Lewis specification are undergoing cycle life testing. The nickel electrodes were fabricated at Eagle-Picher, Colorado Springs and were impregnated with active material by the alcoholic Pickett process [14]. Three of the cells (test cells) contain all of the advanced design features as described in [15]. The other three cells (control cells) are the same as the test cells except they do not have catalyst on the wall wick. All six cells contain 26 rather than 31 percent KOH electrolyte.

The test cell design is illustrated in Fig. 2. The new features of this design which are not incorporated in the state-of-the-art Air Force/Hughes or COMSAT/Intelsat Cells are: (1) use of 26 rather than 31 percent KOH electrolyte which improves cycle life [2, 3, and 16], (2) use of a catalyzed wall wick located on the inside surface of the pressure vessel wall which chemically recombines oxygen generated at the end of charge and on overcharge with hydrogen to form water. State-of-the-art nickel-hydrogen cells recombine the oxygen on the catalyzed hydrogen electrode surface in the stack. The catalyzed wall wick should improve oxygen and thermal management [17], (3) use of serrated edge separators to facilitate gaseous oxygen and hydrogen flow within the cell, while still maintaining physical contact with the wall wick for electrolyte management, (4) use of a floating rather than fixed stack (SOA) to accommodate nickel electrode expansion due to charge/discharge cycling. This is accomplished by use of Belleville disc springs located at each end of the stack. The significant improvements resulting from these innovations are extended cycle life, enhanced oxygen, thermal and electrolyte management, and accommodation of some of the nickel electrode expansion.

LIGHTWEIGHT NICKEL ELECTRODE - The lightweight nickel electrodes evaluated were fabricated from Fibrex nickel fiber substrates. The substrates contain 50 percent nickel fibers, 35 percent nickel powder and 15 percent cobalt powder. The porosity was 90 percent and the thickness was 80 mils. They were electrochemically impregnated by Eagle-Picher using the aqueous process to a loading level of 1.6 g/cm^3.

CELL DESCRIPTION - For Testing Lightweight Nickel Electrodes - The cycle test was conducted using a boiler plate cell with a 5- by 5-cm active area. The components of the cell consist of a stack of nickel electrode, separator, hydrogen electrode, and gas screen. The nickel electrode is made from an 80 mil thick, 90 percent porous Fibrex nickel electrode loaded to 1.6 g/cm^3 void volume. The separator consists of three layers of 6-mil thick beater treated asbestos separator. The hydrogen electrode was made by Life Systems, Incorporated and consists of a mixture of platinum and Teflon applied to a gold plated nickel screen. The gas screen, located behind the hydrogen electrode, is 60 mil thick nickel Exmet which was compressed to 40 mil to fit into the cavity designed for the hydrogen electrode and gas screen. An electrolyte reservoir plate (ERP), which is incorporated into the cell, is made of 125 mil-thick foam metal. The current collectors are gold plated nickel. A graphic representation of the unit cell cross section is shown in Fig. 3. After assembly, the entire stack is vacuum-filled with 26 percent KOH electrolyte. The electrolyte is allowed to stand in the stack overnight, then the excess electrolyte is drained. The stack is placed in a pressure vessel which is evacuated and filled with hydrogen to 3.4 atm (50 psi).

RESULTS AND DISCUSSION

48 Ah FLIGHT CELLS - Storage Test - The nickel-hydrogen battery could undergo a planned or unplanned storage due to delays prior to launch. This may have an effect on performance. The influence of storage (31 days, trickle charged at C/200, 10°C) on the capacity of the 48 Ah IPV nickel-hydrogen flight cells containing 26 and 31 percent KOH electrolyte is shown in Fig. 4. The spread in the data indicate there is no significant capacity loss after 31 days for either the 26 or 31 percent KOH cells.

48 Ah FLIGHT CELLS - Performance Test - A comparison of the average discharge voltage (three cells) as a function of time for the cells containing 26 and 31 percent KOH was made and is shown in Fig. 5. The voltage for the 26 percent KOH cells is higher than for the the 31 percent KOH cells up to about an 82 percent DOD. The discharge rate was 1.4 C (67.2 A) and the cell temperature was maintained at 10°C. The ampere-hour capacity for these cells is shown in Table I (1.4 C, 10°C). The capacity on the average for the 26 percent KOH cells was about 10 percent lower than the 31 percent KOH cells. The tradeoff for this relatively small decrease in initial capacity is a significant increase in cycle life. It should be noted that the data in Table I is for a 100 percent DOD. In an actual application the DOD will be much less. For instance the DOD for Space Station Freedom will be about 35 percent. In this operating region the cells containing 26 percent KOH have a higher discharge voltage, and still have adequate capacity reserve.

48 Ah FLIGHT CELLS - Cycle Test - The influence of LEO cycling at 80 percent DOD on the end

of discharge voltage for the 48 Ah IPV nickel-hydrogen flight cells containing 26 percent KOH is summarized in Fig. 6. The three cells containing 26 percent KOH failed on the average at cycle 19,500 (cycle 15,314, 19,518, and 23,659). The influence of cycling on the end of charge pressure for the 26 percent KOH cells is shown in Fig. 7. The pressure increase per 1000 cycles if 23.3 PSI. The pressure increase could be indicative of nickel plaque corrosion which converts nickel to active material. The increase in pressure will result in a shift in the beginning of life state-of-charge versus pressure curve.

The influence of LEO cycling at 80 percent DOD on the end of discharge voltage for the cells containing 31 percent KOH is shown in Fig. 8. The three cells containing 31 percent KOH failed on the average at cycle 6,400 (cycles 3,729, 4,165 and 11,355). The failure mode for each cell was characterized by degradation of discharge voltage to 1.0 V. No cell failed due to an electrical short. A comparison of the discharge curve at the beginning and end of life for Cell 1, which failed at cycle 3,729, is shown in Fig. 9. This information also shows a voltage degradation. The ampere-hour capacity decrease for cell 1 was about 33 percent (1.4 C rate, 10°C), for cell 2, 33 percent, and for cell 3, 36 percent. The influence of cycling on the end of charge pressure for the 31 percent KOH cells is shown in Fig. 10. The pressure change can be correlated with the discharge voltage change due to cycling. The pressure increase per 1000 cycles is 23.3 PSI. The pressure increase is the same as for the 26 percent KOH.

The cycle life of the cells containing 26 percent KOH was a factor of 3 to 4 better than those with 31 percent KOH. The superior performance of the 26 percent KOH cells compared to the 31 percent cells is in agreement with boiler plate cell results reported previously (2 and 3). It is attributed to crystallographic change of active material [16]. Gamma NiOOH is converted to beta NiOOH in 26 percent KOH. Beta NiOOH has a lower capacity but longer life.

48 Ah FLIGHT CELLS - Destructive Physical Analysis - Destructive physical analysis (DPA) of all three of the 31 percent KOH cells was completed and documented at Hughes under a NASA Lewis contract [18]. DPA of the 26 percent cells is in process. A summary of the DPA results of the 31 percent KOH cells is as follows: All three cells failed during cycling due to a decrease in voltage and nickel-electrode capacity. The capacity decrease was confirmed by measuring nickel-electrode capacity in flooded electrolyte cells. Some observations which could cause the capacity decrease are nickel-electrode expansion, rupture and corrosion of the nickel-electrode substrate, active material redistribution, and accumulation of electrochemically undischarged active material with cycling. Cell 3 appears to have failed by gradual wear-out due to these changes. Some of the electrodes from cells 1 and 2 showed a premature capacity fading which was responsible for early failure. However, chemical analysis of these electrodes did not show anomalous results. The mechanism of the premature capacity fading is not fully understood by the present DPA. No cells failed due to an electrical short. All cells showed some increase in internal resistance after the cycle test; however, this increase itself does not appear to be the direct cause of failure. All cells showed a decrease in discharge voltage and an increase in charge voltage after the cycle test.

125 Ah ADVANCED FLIGHT CELLS - Cell Performance - For a representative 125 Ah advanced catalyzed wall wick nickel-hydrogen flight battery cell the voltage and pressure during charge and discharge are shown in Fig. 11 (beginning of life). The discharge rate was 0.69 C (87 A) and the temperature was a nominal 10°C. The mid-discharge voltage was 1.248 V. The pressure, as expected, varies linearly with the state-of-charge. It should be noted, however, that the pressure could increase with charge/discharge cycling causing a shift in the state-of-discharge curve.

The effect of discharge rate on ampere-hour capacity for a representative cell of each type is shown in Fig. 12. The capacity decreased slightly (1 percent) over the range of C/2 to 1.4 C, after which point it decreased rapidly. In a nickel-hydrogen cell the gaseous hydrogen comes into contact with the nickel electrodes resulting in a capacity loss due to self discharge. The capacity retention of the cells after a 72 hr open circuit stand at 10°C is shown in Fig. 13. The data shows no significant difference in capacity retention between the catalyzed and noncatalyzed wall wick cells. The capacity retention for the catalyzed wall wick cells on the average is 84 percent and for the noncatalyzed wall wick cells is 85 percent.

125 Ah ADVANCED FLIGHT CELLS - Storage Test - The effect of storage (52 days, discharged, open circuit, 0°C) on the capacity of the six 125 Ah flight IPV nickel-hydrogen cells is summarized in Fig. 14. The spread in the data shows no significant capacity loss for either the catalyzed or noncatalyzed wall wick cells due to the 52 day storage. Actually, there was a slight average increase in capacity for both the catalyzed and noncatalyzed wall wick sells.

125 Ah ADVANCED FLIGHT CELLS - Cycle Test - The influence of LEO cycling at 60 percent DOD on the end of discharge voltage for the 125 Ah catalyzed wall wick IPV nickel-hydrogen flight cells is summarized in Fig. 15. After 22,694 cycles there has been no cell failure in the continuing test. The influence of cycling on the end of charge pressure for the catalyzed wall wick cells is shown in Fig. 16. No pressure for cell 2 is available because the cell had a bad strain gauge. For cells 1 and 3 the pressure increased relatively rapidly up to about cycle 1400 then decreased. The average pressure increase at cycle 1400 is about 11 percent higher than at the beginning of life.

The influence of LEO cycling at 60 percent DOD on the end of discharge voltage for the 125 Ah noncatalyzed wall wick IPV nickel-hydrogen flight cells is shown in Fig. 17. All three of the noncatalyzed wall wick cells failed (cycles 9,588, 13,900, and 20,575). The failure was characterized by degradation of end of discharge voltage to 1.0 V. The cells did not fail due to an electrical short. The influence of cycling on the end of charge pressure for the noncatalyzed wall wick cells is shown in Fig. 18. The pressure for the three cells increased up to about cycle 2000 then decreased. The average pressure increase at cycle 2000 is about 9 percent higher than at the beginning of life.

The cycle life testing will continue until cell failure. A post-cycle teardown and failure analysis will be conducted to evaluate the cause of failure. This information will be used to affect further improvements.

BOILER PLATE CELL - For Testing Lightweight Nickel Electrodes - The cell cycled for 10,000 cycles, as shown in Fig. 19, before the test was terminated. The effect of cycling on the end of discharge voltage is shown in Fig. 20. An end-of-discharge voltage of about 1.175 V is observed for the first 1000 cycles. The average end-of-discharge voltage gradually dropped to about 1.060 V at 9000 cycles and remained constant until the end of the cycle test.

Final characterization testing will be conducted and will be reported later. Failure analysis will also be conducted to evaluate the cause for failures.CONCLUDING REMARKS

A breakthrough in the LEO cycle life of individual pressure vessel nickel-hydrogen battery cells was reported. The cycle life of boiler plate cells containing 26 percent KOH electrolyte was about 40,000 accelerated LEO cycles at 80 percent DOD compared to 3,500 cycles for cells containing 31 percent KOH. Results of the boiler plate cell tests have been validated at NWSC, Crane, Indiana. Forty-eight ampere-hour flight cells containing 26 and 31 percent KOH have undergone real time LEO cycle life testing at an 80 percent DOD, 10°C. The three cells containing 26 percent KOH failed on the average at cycle 19,500. The three cells containing 31 percent KOH failed on the average at cycle 6,400.

Validation testing of NASA Lewis 125 Ah advanced design IPV nickel-hydrogen flight cells is also being conducted at NWSC, Crane, Indiana under a NASA Lewis contract. This consists of characterization, storage, and cycle life testing. There was no capacity degradation after 52 days of storage with the cells in the discharged state, on open circuit, 0°C, and a hydrogen pressure of 14.5 psia. The catalyzed wall wick cells have been cycled for over 22,694 cycles with no cell failures in the continuing test. All three of the noncatalyzed wall wick cells failed (cycles 9,588, 13,900 and 20,575).

Cycle life test results of the Fibrex nickel electrode have demonstrated the feasibility of an improved nickel electrode giving a higher specific energy nickel-hydrogen cell. A nickel-hydrogen boiler plate cell using an 80 mil thick, 90 percent porous Fibrex nickel electrode has been cycled for 10,000 cycles at 40 percent DOD.

REFERENCES

1. L. Miller, "The Ni-H_2 Battery System: A Space Flight Application Summary," 1988 IECEC; *Proceedings of the Twenty-Third Intersociety Energy Conversion Engineering Conference*, Vol. 2, ASME, New York, 1988, pp. 489-492.

2. H. S. Lim, and S. A. Verzwyvelt, "KOH Concentration Effect on Cycle Life of Nickel-Hydrogen Cells, III. Cycle Life Test," *Journal of Power Sources*, Vol. 22, Mar.-Apr. 1988, pp. 213-220.

3. H. S. Lim, and S. A Verzwyvelt, "KOH Concentration Effect on the Cycle Life of Nickel-Hydrogen Cells, IV. Results of Failure Analysis," *Journal of Power Sources*, Vol. 29, Feb. 1990, pp. 503-519.

4. E. Adler, T. Duranti, P. Frisch, T. Jacewicz, H. Rogers, L. Samoss, S. Stadnick, and L. Tinker, "Nickel-Hydrogen Battery Advanced Development Program," AFWAL-TR-80-2044, Hughes Aircraft Company, 1980.

5. D. Warnock, "Life Test of 50 Ah NiH_2 Battery," The 1981 Goddard Space Flight Center Workshop, G. Halpert, ed., NASA CP-2217, 1982, pp. 487-500.

6. J. J. Smithrick, "Cycle Life Test and Failure Model of Nickel-Hydrogen Cells," IECEC '83: *Proceedings of the Eighteenth Intersociety Energy Conversion Engineering Conference*, Vol. 4, AIChE, New York, 1983, pp. 1535-1542.

7. D. H. Fritts, "Testing the Mechanical Characteristics of Sintered Nickel-Battery Plaque and Their Relationship to Nickel-Electrode Performance," *Journal of Power Sources*, Vol. 6, Apr. 1981, pp. 171-184.

8. D. F. Pickett, H. H. Rogers, L. A. Tinker, C. A. Bleser, J. M. Hill, and J. S. Meador, "Establishment of Parameters for Production of Long Life Nickel Oxide Electrodes for Nickel-Hydrogen Cells," Energy to the 21st Century; *Proceedings of the Fifteenth Intersociety Energy Conversion Engineering Conference*, Vol. 3, AIAA, New York, 1980, pp. 1918-1924.

9. V. C. Mueller, "Failure Analysis of Nickel Hydrogen Cell Subjected to Simulated Low Earth Orbit Cycling," The 1983 Goddard Space Flight Center Battery Workshop, D. Baer and G. W. Morrow, eds., NASA CP-2331, 1983, pp. 523-538.

10. K. M. Abbey, and D. L. Britton, "Electrolyte Management in Porous Battery Components - Static Measurements," NASA TM-83073, 1982.

11. J. J. Smithrick, "Initial Performance of Advanced Designs for IPV Nickel-Hydrogen Cells," *Power Sources 11: Research and Development in Non-Mechanical Electrical Power Sources*, L. J. Pearce, ed., International Power Sources Symposium Committee, Leatherhead, England, 1986, pp. 215-226 (Also, NASA TM-87282).

12. J. J. Smithrick, and S. W. Hall, "Effect of KOH Concentration on LEO Cycle Life of IPV Nickel-Hydrogen Flight Cells - An Update," *Proceedings of the 26th Intersociety Energy Conversion Engineering Conference*, IECEC '91, D. C. Black, ed.,Vol. 3, American Nuclear Society, 1991, pp. 276-281.

13. J. J. Smithrick, and S. W. Hall, "Effect of LEO Cycling on 125 Ah Advanced Design IPV Nickel-Hydrogen Flight Cells - An Update," *Proceedings of the 25th Intersociety Energy Conversion Engineering Conference*, IECEC '91, D. L. Black, ed., Vol. 3, American Nuclear Society, 1991, pp. 311-317.

14. D. F. Pickett, "Preparation of Nickel Electrodes," U. S. Patent 3,827,911, Aug. 1974.

15. J. J. Smithrick, M. A. Manzo, and O. Gonzalez-Sanabria, "Advance Designs for IPV Nickel-Hydrogen Cells," IECEC '84: Advanced Energy Systems - Their role in Our Future; *Proceedings of the Nineteenth Intersociety Energy Conversion Energy Conference*, Vol. 1 American Nuclear Society, New York, 1984, pp. 631-635 (Also, NASA TM-83643).

16. H. S. Lim, and S. A. Verzwyvelt, "Electrochemical Behavior of Heavily Cycled Nickel Electrodes in Ni H_2 Cells Containing Electrolytes of Various KOH Concentration," *Proceedings of the Symposium on Nickel Hydroxide Electrodes*, D. A. Corrigan, A. A. Zimmerman, eds., Electrochemical Society Proc., Vol. 90-4, Electrochemical Society, 1990, pp. 341-355.

17. O. D. Gonzalez-Sanabria, "Effect of NASA Advanced Designs on Thermal Behavior of Ni-H_2 Cells," 1988 IECEC; *Proceedings of the Twenty-Third Intersociety Energy Conversion Engineering Conference*, D. Y. Goswami, ed., Vol. 2, ASME, New York, 1988, pp. 453-456.

18. H. S. Lim, G. R. Zelter, T. T. Smithrick, and S. W. Hall,"Destructive Physical Analysis Results of Ni/H_2 Cells Cycled in LEO Regime," *Proceedings of the 26th Intersociety Energy Conversion Engineering Conference*, ECEC '91, D. L. Black, ed., Vol. 3, American Nuclear Society, 1991, pp. 304-310.

TABLE 1. - CAPACITY OF HUGHES FLIGHT CELLS CONTAINING 26 AND 31 PERCENT KOH ELECTROLYTE

Cell	Capacity,[a] A-hr	KOH concentration, percent
1	59.0	31
2	59.9	31
3	59.0	31
4	53.8	26
5	53.2	26
6	52.3	26

[a] Discharge at 1.4 C rate, 10 °C.

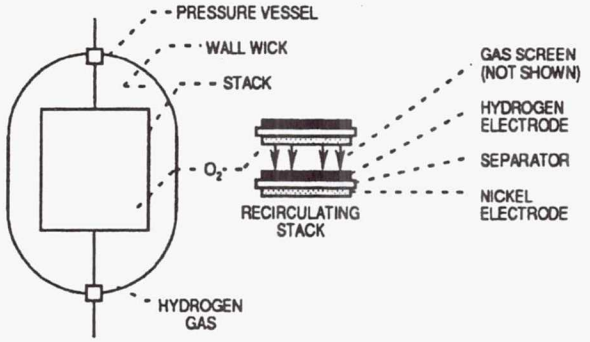

FIGURE 1 - ILLUSTRATION OF HUGHES RECIRCULATION STACK INDIVIDUAL PRESSURE VESSEL NICKEL-HYDROGEN CELL

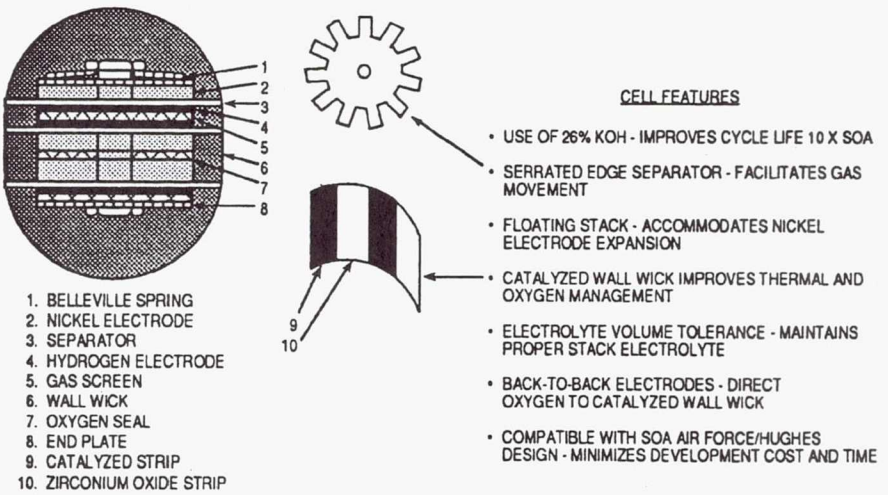

FIGURE 2 - NASA ADVANCED DESIGN IPV NICKEL-HYDROGEN CELL-CATALYZED WALL WICK

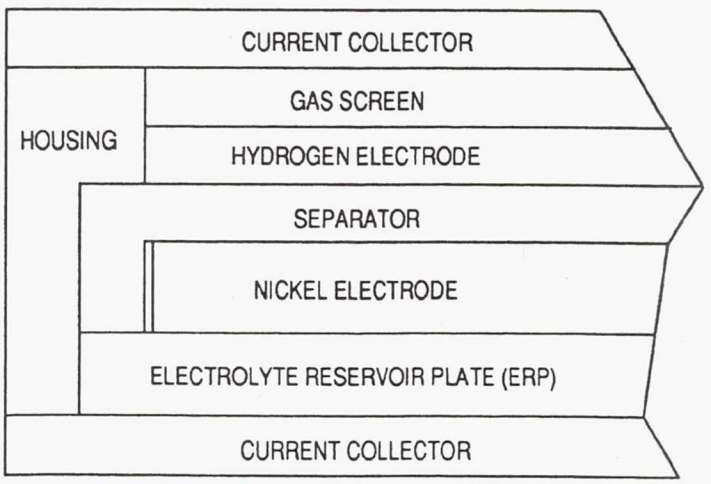

FIGURE 3 - CROSS-SECTIONAL UNIT OF THE NICKEL-HYDROGEN CELL

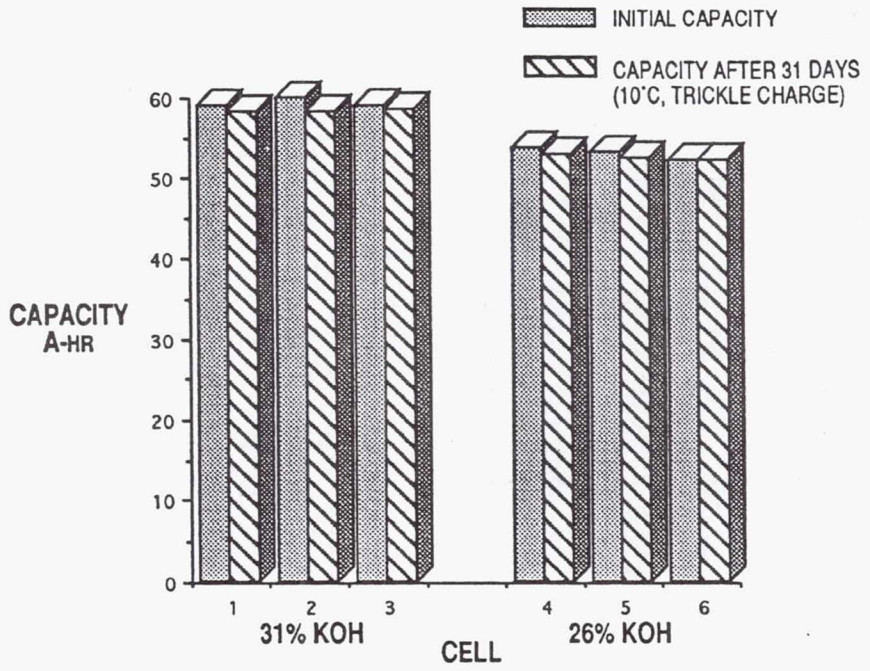

FIGURE 4 - EFFECT OF STORAGE ON CAPACITY OF 48 A-hr HUGHES IP Ni/H_2 FLIGHT CELLS.

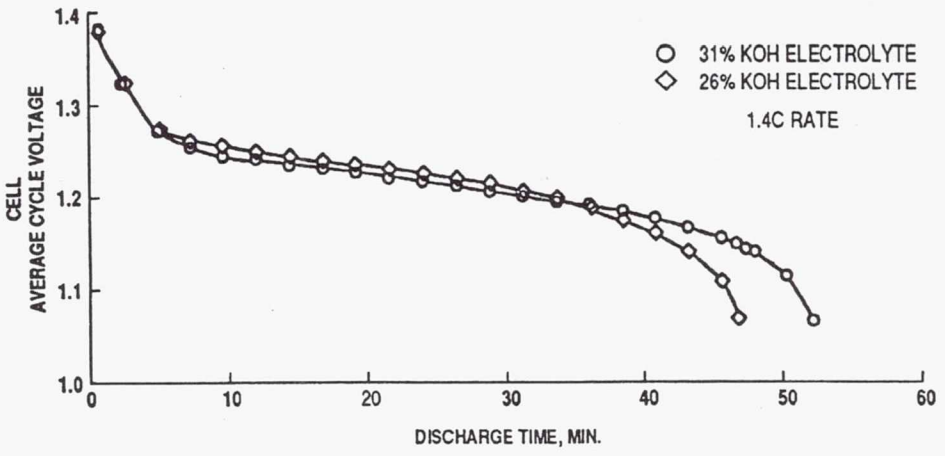

FIGURE 5 - COMPARISON OF HUGHES 49 A-hr IPV Ni/H_2 FLIGHT CELLS CONTAINING 26 PERCENT AND 31 PERCENT KOH ELECTROLYTE

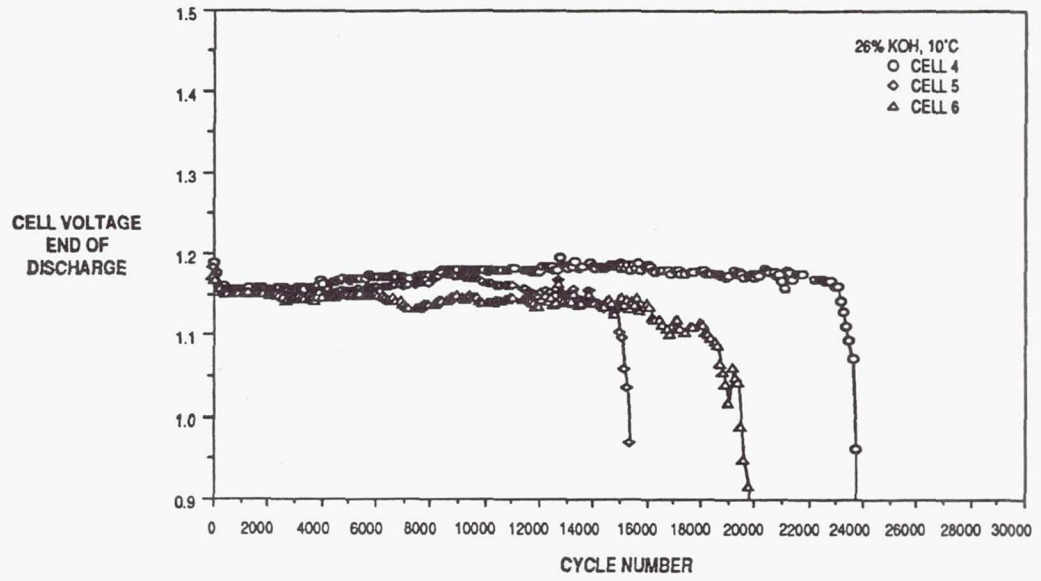

FIGURE 6 - EFFECT OF LEO CYCLING AT 80 PERCENT DOD ON 48 A-hr IPV HUGHES FLIGHT CELLS CONTAINING 26 PERCENT KOH ELECTROLYTE, 10°C.

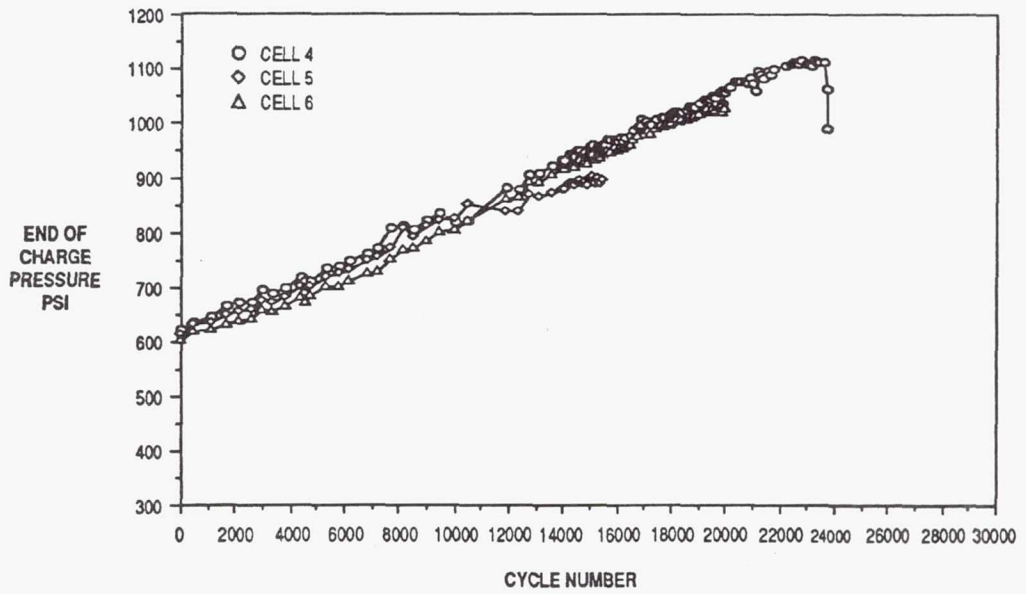

FIGURE 7 - EFFECT OF LEO CYCLING AT 80 PERCENT DOD ON 48 A-hr IPV HUGHES FLIGHT CELLS CONTAINING 26 PERCENT KOH.

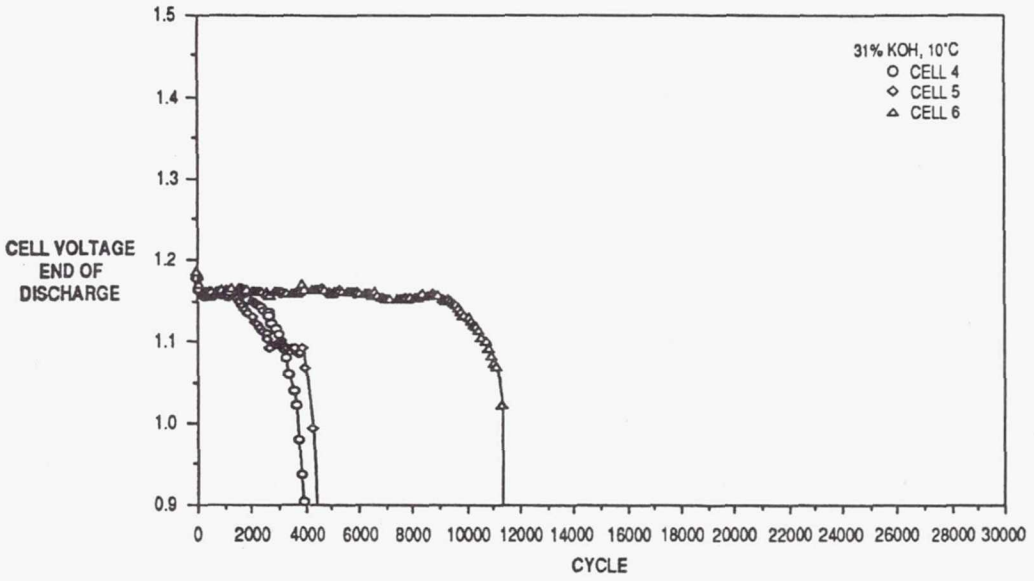

FIGURE 8 - EFFECT OF LEO CYCLING AT 80 PERCENT DOD ON HUGHES FLIGHT CELLS CONTAINING 31 PERCENT KOH ELECTROLYTE, 10°C.

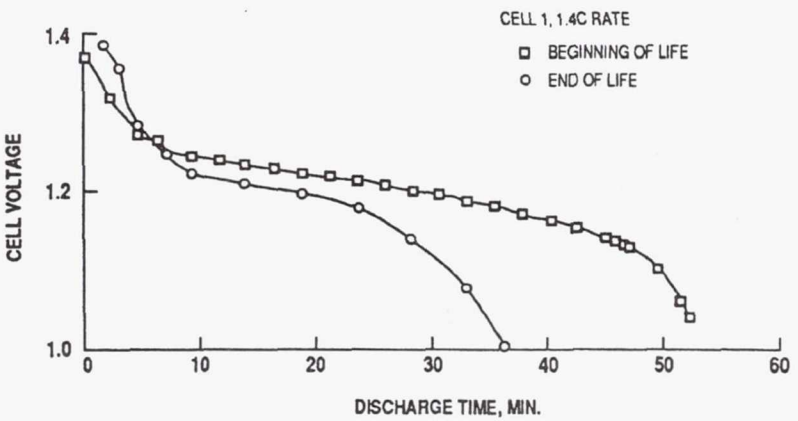

FIGURE 9 - COMPARISON OF HUGHES 48 A-hr IPV Ni/H_2 FLIGHT CELLS CONTAINING 31 PERCENT KOH ELECTROLYTE

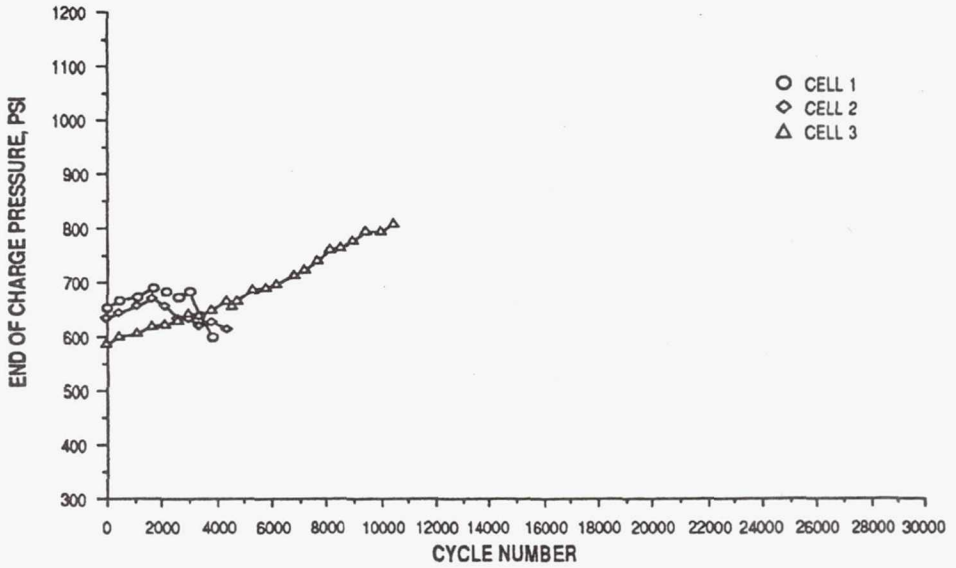

FIGURE 10 - EFFECT OF LEO CYCLING AT 80 PERCENT DOD ON HUGHES FLIGHT CELLS CONTAINING 31 PERCENT KOH.

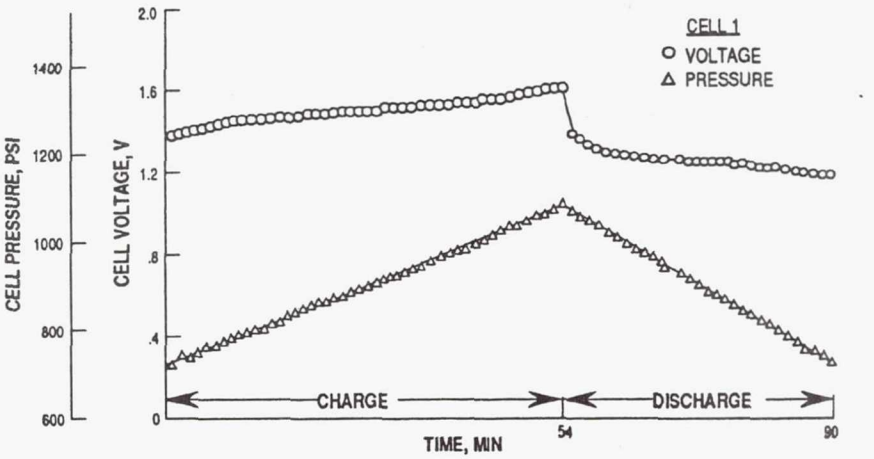

FIGURE 11 - CELL VOLTAGE AND PRESSURE DURING CHARGE AND DISCHARGE FOR A REPRESENTATIVE 125 A-hr ADVANCED CATALYZED WALLWICK IPV Ni/H $_2$ FLIGHT BATTERY CELL

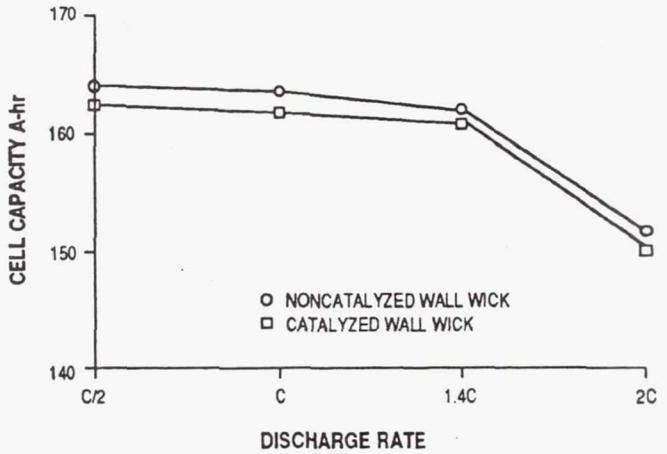

FIGURE 12 - COMPARISON OF EAGLE-PICHER 125 A-hr Ni/H $_2$ CELLS CATALYZED AND NONCATALYZED WALLWICK

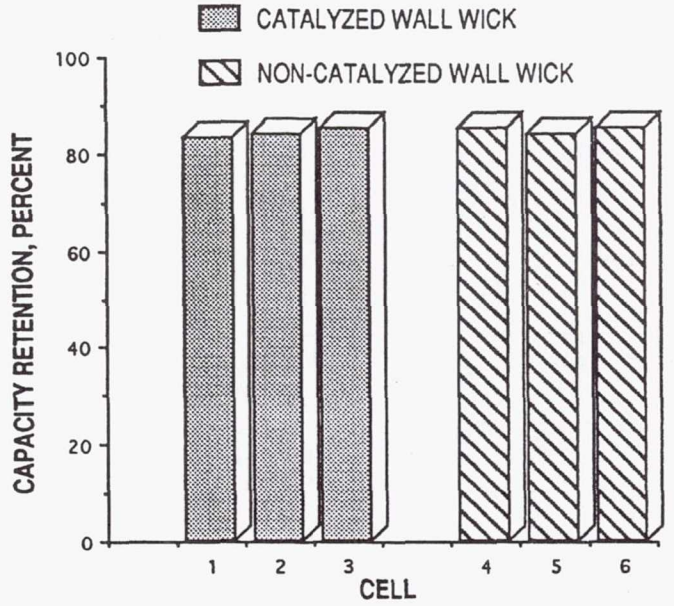

FIGURE 13 - CAPACITY RETENTION OF 125 A-hr EAGLE-PICHER ADVANCED IPV Ni/H_2 FLIGHT CELLS AFTER 72 hr OPEN CIRCUIT STAND

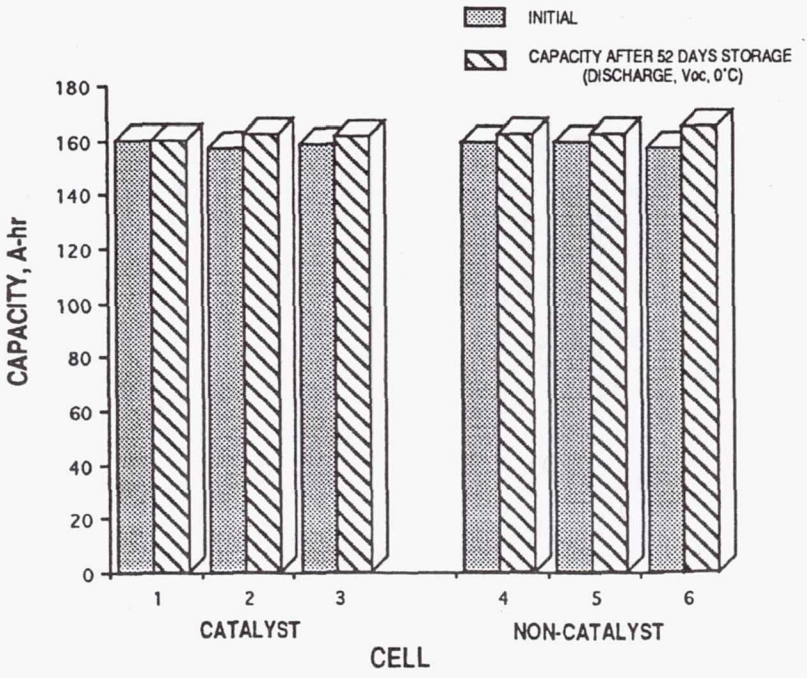

FIGURE 14 - EFFECT OF STORAGE ON CAPACITY OF 125 A-hr EAGLE-PICHER ADVANCED IPV Ni/H_2 FLIGHT CELLS, CATALYZED AND NONCATALIZED WALLWICK, 26 PERCENT KOH.

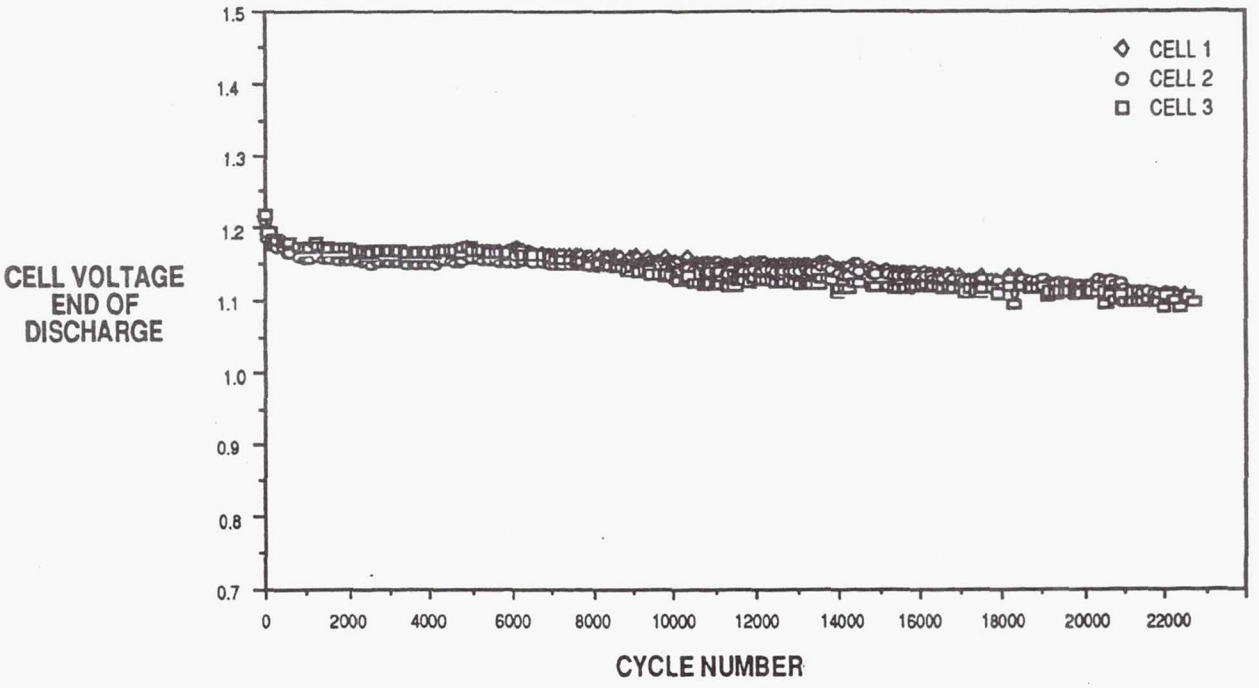

FIGURE 15 - EFFECT OF LEO CYCLING ON 125 A-hr NASA LEWIS ADVANCED CATALYZED WALLWICK IPV Ni/H_2 CELLS MANUFACTURED BY EAGLE-PICHER, 26 PERCENT KOH, 60 PERCENT DOD, 10°C.

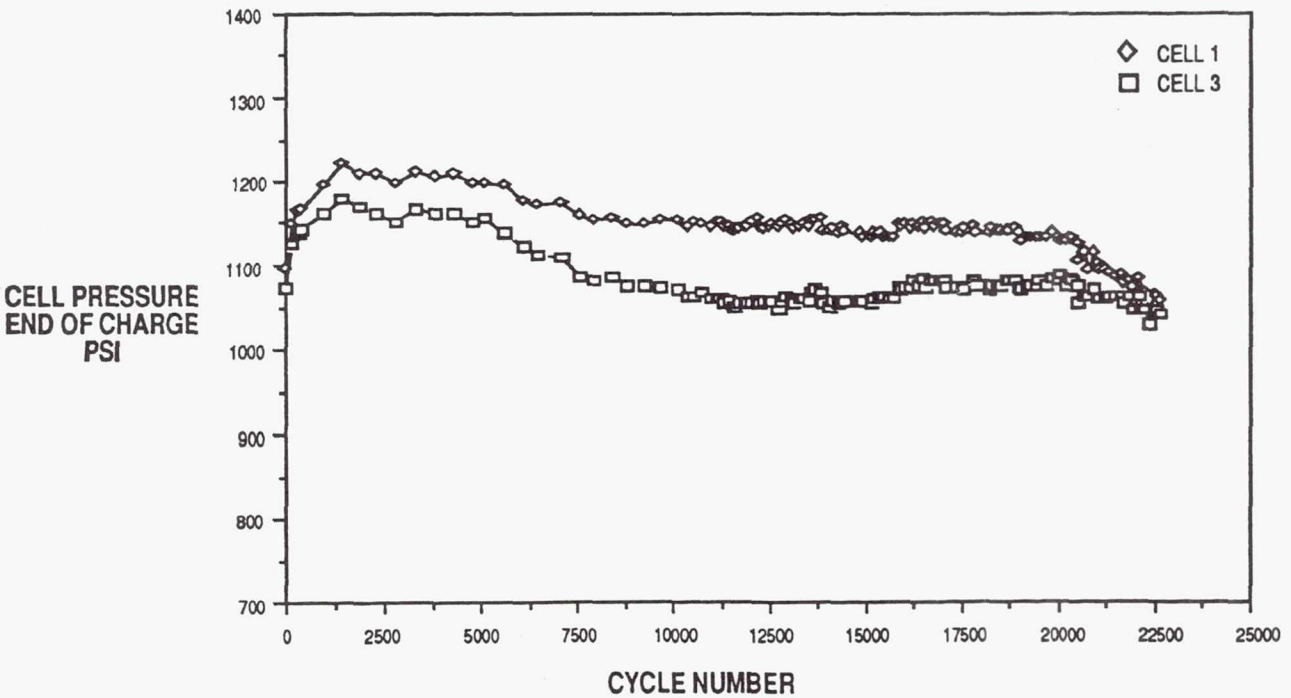

FIGURE 16 - EFFECT OF LEO CYCLING ON 125 A-hr NASA LEWIS ADVANCED CATALYZED WALLWICK IPV Ni/H_2 CELLS MANUFACTURED BY EAGLE-PICHER, 26 PERCENT KOH, 60 PERCENT DOD, 10°C.

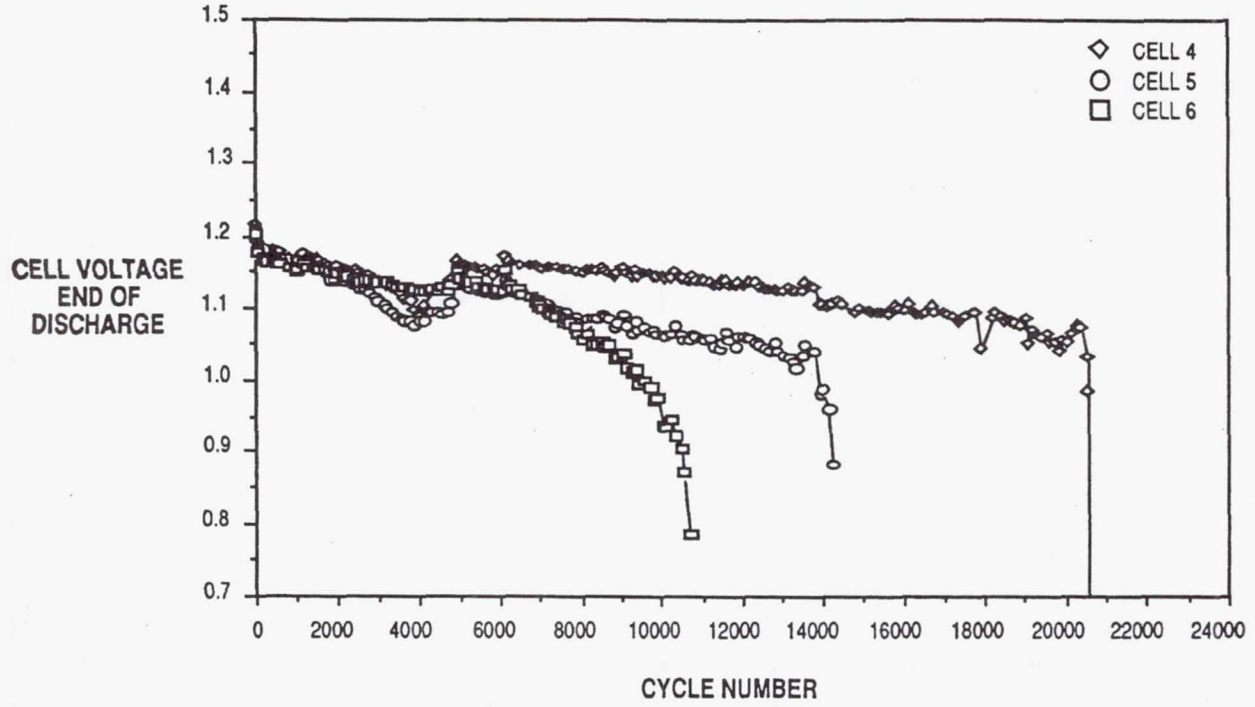

FIGURE 17 - EFFECT OF LEO CYCLING ON 125 A-hr NASA LEWIS ADVANCED NONCATALYZED WALLWICK IPV Ni/H_2 CELLS MANUFACTURED BY EAGLE-PICHER, 26 PERCENT KOH, 60 PERCENT DOD, 10°C.

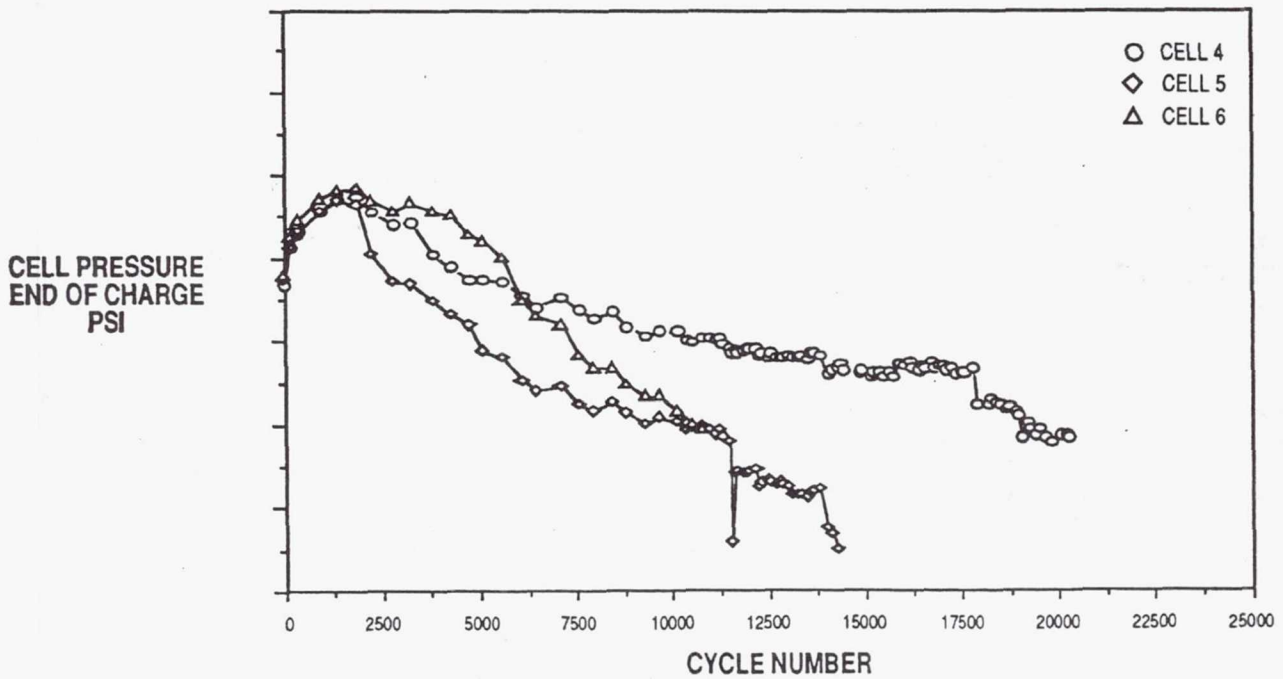

FIGURE 18 - EFFECT OF LEO CYCLING ON 125 A-hr NASA LEWIS ADVANCED NONCATALYZED WALLWICK IPV Ni/H_2 CELLS MANUFACTURED BY EAGLE-PICHER, 26 PERCENT KOH, 60 PERCENT DOD, 10°C.

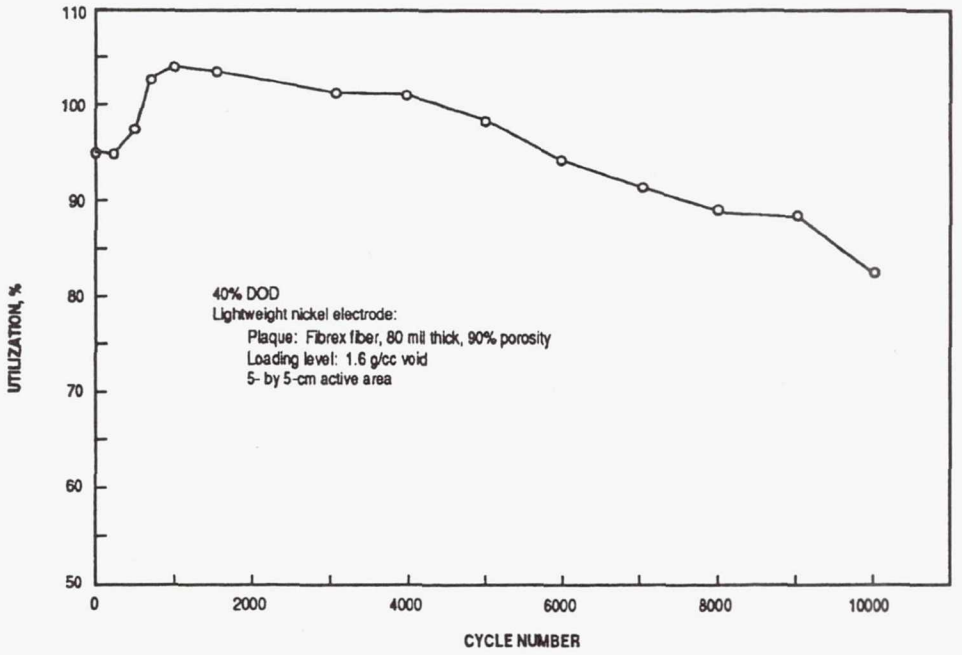

FIGURE 19 - UTILIZATION VERSUS CYCLE NUMBER OF A NICKEL-HYDROGEN CELL USING A FIBEREX NICKEL ELECTRODE.

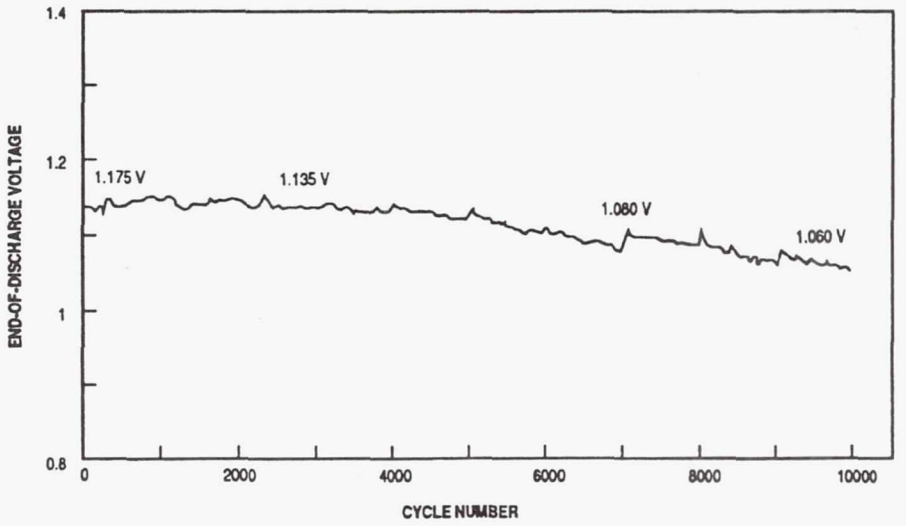

FIGURE 20 - END OF DISCHARGE VOLTAGE VERSUS NUMBER OF CYCLES FOR A NICKEL-HYDROGEN CELL USING A FIBEREX NICKEL ELECTRODE.

Section
Two

Fuel Cells

PRIMARY AND SECONDARY ELECTRICAL SPACE POWER BASED ON ADVANCED PEM SYSTEMS

N. E. Vanderborgh, J. C. Hedstrom and K. R. Stroh
Advanced Engineering Technology Group
Los Alamos National Laboratory
Los Alamos, New Mexico 87545

and

J. R. Huff
Ballard Power Corporation
Albuquerque, New Mexico 87109

INTRODUCTION

For new space ventures, power continues to be a pacing function for mission planning and experiment endurance. Although electrochemical power is a well demonstrated space power technology, current hardware limitations impact future mission viability. In order to document and augment electrochemical technology, a series of experiments for the National Aeronautics and Space Administration Lewis Research Center (NASA LeRC) are underway at the Los Alamos National Laboratory that define operational parameters on contemporary proton exchange membrane (PEM) hardware operating with hydrogen and oxygen reactants. Because of the high efficiency possible for water electrolysis, this hardware is also thought part of a secondary battery design built around stored reactants -- the so-called regenerative fuel cell. An overview of stack testing at Los Alamos, and of analyses related to regenerative fuel cell systems are provided in this paper.

Finally, this paper describes work looking at innovative concepts that remove complexity from stack hardware with the specific intent of higher system reliability. This new concept offers the potential for unprecedented electrochemical power system energy densities.

STACK TEST PROGRAM

Although contemporary designs are not space qualified, available PEM stacks are being tested to ascertain the utility of this fuel cell design for long term space power applications. Tests are conducted that operate multi-kilowatt stacks on hydrogen and oxygen. Experiments are run that explore individual cell voltages, the effects of reactant stoichiometry, thermal management, and water balances during stack operation. To date, two fuel cell stacks manufactured by Ballard Power Systems, Vancouver, B.C., have been evaluated: 1) a stack using DuPont Nafion^{TM} 117 electrolyte membranes; and 2) a similar stack formed using experimental polyperfluorosulfonic acid polymer membranes manufactured by Dow Chemical Company.

Fuel cell stack testing requires the establishment of a safe and regulated test environment. Under NASA sponsorship, Los Alamos designed and fabricated two test stations to obtain reliable test data. These test stations monitor inlet and outlet parameters, and accomplish a full mass and energy balance around the test. One test station utilizes a passive load bank to facilitate long-term, unattended testing under rather continuous conditions. The second utilizes a computer-controlled electronic load that permits programmed load changes. Because the objective of these tests is to provide data on stack life and performance decay

rates, long term testing is necessary. The tests are fully automated with a control computer that is able to diagnose faults and, if necessary, terminate a particular test.

The test configuration is shown schematically in Fig. 1. The experiment is designed to measure reactant flows, product flows, current and voltage, and heat flows. The determination of water production rates and locations helps in the evaluation of candidate membrane materials used to form PEM stacks. Electrochemical water production is frequently used to supply makeup water, making this diagnostic measurement difficult. Water flows were partitioned in the experimental design specifically to determine stack water balances.

Electrochemical water production occurs in the cathode compartment as the result of two processes, hydrogen oxidation and water generation as the result of electro-osmosis (transport of water from the anode to cathode membrane faces as the result of proton motion). Water transport occurs through motion of a hydrated proton, $H(H_2O)_n^+$. This type of transport is frequently termed "water drag." Water also moves from the wet cathode to the anode through the membrane controlled by membrane mass transfer rates.

The model predicts that appreciable fractions of water can be produced in the anode compartment, depending on the value selected for k_s and n, where k_s is a

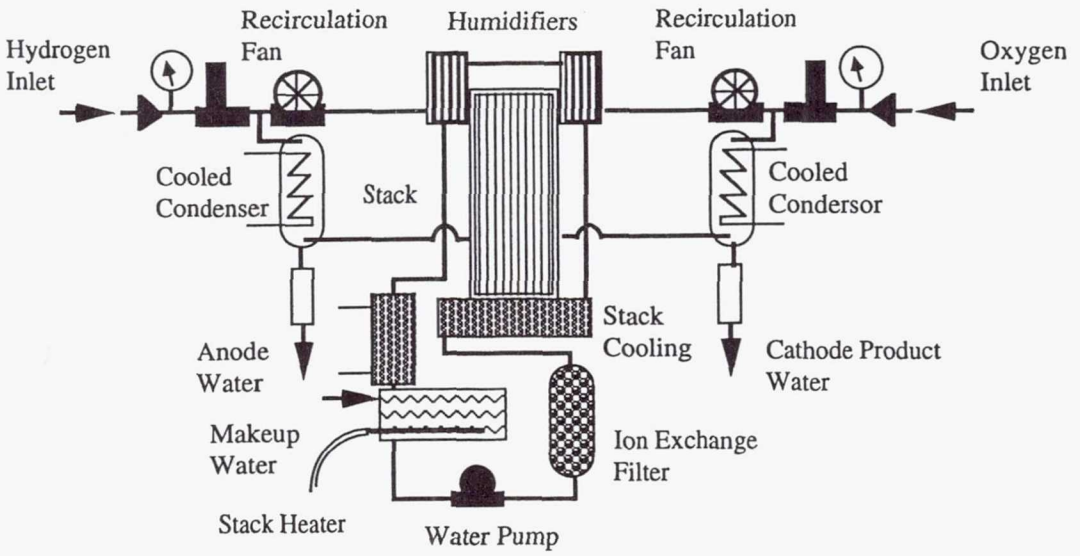

Fig. 1 Stack test schematic -- recirculation of both H_2 and O_2 and condensation of product water allows full measurement of mass and energy flows.

Stack Performance Models. An energy- and mass-balance computer model has been developed, assuming simple stack reactant and cooling flow geometry. The partitioning of the chemical hydrogen energy into heat and electrical energy is modeled. This fuel cell stack code also includes implicit terms for membrane water transport.

water mass transfer coefficient that contains both diffusive and convective terms, and n is the stoichiometry factor that describes the average proton hydration number. Model development is discussed in Refs. 1-5. Additional discussion, related to the data presented below, can be found in Ref. 1.

Stack Test Results. Early experiments showed relatively short stack lifetimes. The cause of failure was typically excess cross over, that is, excessive leakage anode to cathode resulting from one or more failed membranes. Ballard worked to correct these failures and supplied a series of modified stacks with improved membranes, electrodes, gaskets, and seals. A variety of stack clamping designs have been tested. Each time a stack was refitted to solve a known technical problem, the clock was set to zero and testing started on that new configuration. Initially failures occurred near 200 hours; the last stack tested, fitted with Nafion membranes, obtained a test duration of 1250 hours.

Likewise, ancillaries have also been improved during this test program. Initially recirculation pumps used a metal bellows design that typically lasted less than 24 hours. A whole series of recirculation pumps for both hydrogen and oxygen have been evaluated, and currently lifetimes in excess of 500 hours are predicted. The water circulation pump, used for thermal control, also now shows useful, long lifetime. These stack tests will continue until the 5,000 hour continuous operating goal is achieved.

To date, two improved 4-kW stacks have been tested -- the Ballard Mark V "Nafion" and "Dow" stacks. The Nafion stack tested has 46 single cells, using graphite bipolar plates. Each cell has an active area of 232.3 cm^2 (0.25 ft^2). The higher performance of the Dow membrane allows that stack to contain only 40 cells. The stacks are water cooled through the use of integrated cooling hardware. Cooling water also flows through the humidification section that forms one end of the stack.

Some representative data from these tests can be found in Table I. These data were obtained operating the stacks at a *constant current* of 125 amps resulting in a current density of 538 mA/cm^2 (500 amp/ft^2). Under these conditions, the average cell voltage for the Nafion stack was 0.752 V and was 0.799 V for the Dow stack. The apparent electrical efficiency (electrical energy/HHV fuel energy) was 50.7% for the Nafion stack and 54.1% for the Dow stack.

Measurement of voltage performance under various load conditions with time is straightforward and gave, in general, expected results. The successful partition of chemical energy into electrical energy and exhaust heat routinely showed internal and external leak rates were very low on the improved stacks. Additional stack testing and performance model details can be found in Refs. 1 and 6.

POWER SYSTEM DESIGN

The preceding sections described Los Alamos activities for NASA LeRC related to contemporary PEM fuel cell components. The following sections describe system analyses and conceptual design work related to complete fuel cell power systems. The first section describes a completed study of regenerative fuel cell systems configured with evolutionary hardware. The last sections present an innovative concept for PEM fuel cell configuration and power system integration that offers the potential for both higher reliability (through use of fewer active components and reduced complexity) and unprecedented energy density in an electrochemical power system.

Regenerative Systems. Los Alamos has completed a technology assessment and trade-off study of fuel cell and electrolyzer technologies suitable for use in a regenerative fuel cell (RFC) system for Project Pathfinder [Ref. 7, see also Refs. 8-10]. The major components of an RFC system can be seen in Fig. 2. The technology assessment provides the basis for selecting the most promising candidate fuel cell and electrolyzer technologies for the Pathfinder RFC energy storage system. The trade-off study identifies the general characteristics of a 25-kW, 20,000-h energy storage system utilizing the fuel cell and electrolyzer

technologies identified in the technology assessment phase. The resulting system incorporates PEM, metal-hardware fuel cell stacks, PEM electrolysis stacks, and compressed-gas reactant storage in filament-wound, lined-composite, high-performance tanks.

ment and system integration, there would be no difference between the space and terrestrial components. Total system considerations would also be very similar. Only later would development efforts become application specific.

TABLE I Energy Balances and Water Balances from Operating PEM Fuel Cell Stacks

Energy Balance

Membrane Type	Fuel Flow	Reject Heat	Stack Heat Loss	Anode Heat Loss	Cathode Heat Loss	Electrical Energy
Nafion	8532W (HHV)	3581W	187W	165W	284W	4327W
Dow	7395W (HHV)	3006W	160W	187W	287W	3997W

Water Balance

Membrane Type	Water In ("makeup")	Product Water (from H_2 flow)	Anode Water Flow	Cathode Water Flow
Nafion	252 g/h	1,935 g/h	181 g/h	2,027 g/h
Dow	345 g/h	1,674 g/h	453 g/h	1,633 g/h

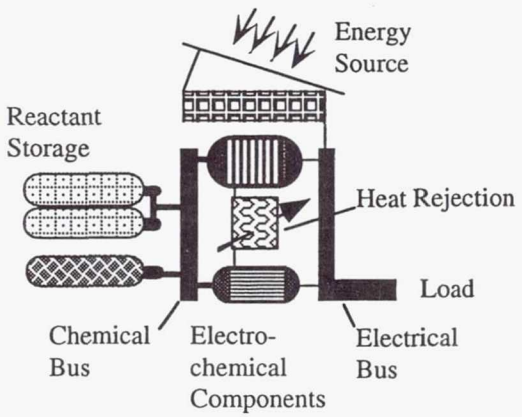

Fig. 2 Major components of a regenerative fuel cell (RFC) system.

During program deliberations, it became apparent that some terrestrial applications could profitably use an RFC system. In the initial stages of develop-

Simple, Modular PEM Systems. A space power system requires a weight- and volume-constrained, reliable and rugged power supply. Some applications have the benefit of low gravity (for example, on the lunar surface), but other applications must function in the microgravity of space. Demonstrated contemporary electrochemical systems are quite complex (especially in ancillary components contrasted to electrochemical components), making the high reliability requirements of future space missions quite challenging. However, new designs offer the potential to eliminate heavy bipolar plates and greatly simplify stack thermal management, thereby reducing system complexity. Moreover, such designs can, in concept, handle freeze-thaw cycles with little problem.

Given the basic concept of a proton exchange membrane (PEM) fuel cell op-

erating on hydrogen, we have developed a concept[1] that has the potential for exhibiting the necessary and desirable characteristics [Refs. 11 and 12]. Modularity permits both flexibility in mission planning and increasing overall reliability. Appropriate power system designs tend to integrate into human habitat modules, simplifying heat management in space environments.

The selection of compressed hydrogen storage in a composite pressure vessel presents the system designer with a sizable cylindrical section. In considering ways to optimize the packaging of an entire power system, a concept was developed that wraps the PEM fuel cell components around the exterior of the hydrogen tank. In this concept, the necessary flow fields, anode, membrane, and cathode are assembled in an annular configuration. This configuration is modular, and useful voltages can be obtained by electrically connecting the anode and cathode of adjacent modules in series. An efficient solid-state DC-DC converter raises the "stack" voltage to the desired system output voltage. Higher system powers can be obtained by incorporating additional annular PEM modules.

An individual module consists of an annular arrangement of PEM fuel cell components. From the inside out there are successive layers performing the function of the porous electrocatalytic anode, the proton exchange membrane, and the porous electrocatalytic cathode. Pressurized oxygen is recirculated over the exterior of the cathode providing the oxidant. Hydrogen is fed from the storage tank through a pressure regulator to a plenum feeding the anode flow field.

The fuel cell stack is assembled on the exterior of the hydrogen storage tank, which completely supports the annular fuel cell modules. As a result, the fuel cell components can be very thin, providing high performance, low weight, and ease of heat removal. System start-up can be rapid because the low mass of the cell allows the membrane and catalysts to rapidly attain the optimum operating temperature. The gas-diffusion portion of the electrodes is constructed from carbon felt embedded, if necessary, with a wire-screen conductor. An optimized membrane fabricated with integral thin-film catalyst layers is hot-pressed between the carbon felt electrodes to complete the cell. No clamping forces or associated hardware are required. We envision fabrication of two carbon-felt electrode sections on a continuous electrical conductor, where one electrode section becomes the anode of the "upstream" cell and the next electrode section becomes the cathode of the "downstream" cell. The continuous conductor electrically connects the anode and cathode of adjacent modules. (The transition must also maintain anode-to-anode and cathode-to-cathode electrical separation, continuity of the anode hydrogen flow field, and separation of the anode and cathode gas flows.) The interconnection concept can be see in Fig. 3.

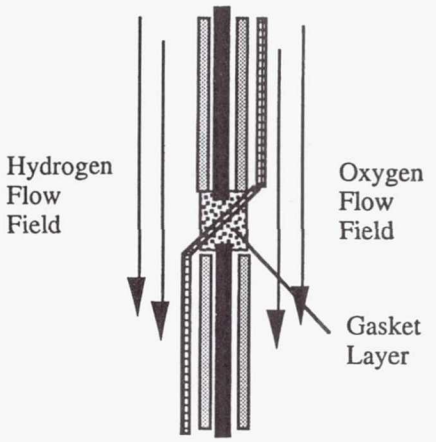

Cell Stacking Scheme

Fig. 3 Concept for interconnection of modular annular fuel cells.

The composite tank is wrapped with a non-conducting layer to prevent elec-

---

1 Work performed for the US Army's Belvoir Research, Development, and Engineering Center, Fort Belvoir, VA.

trical connection between the individual module anodes. This layer is fabricated from a low-density, high-porosity, open-cell polymer that acts as the anode flow field. An additional layer of the same material covers the exterior of the stack assembly, mechanically protecting the annular modules and preventing any exterior contact from shorting cathode-to-cathode, while allowing the free flow of oxygen, product water, and excess heat through the interconnected porosity.

The recirculating cathode oxygen flow serves to remove heat caused by fuel cell inefficiencies from the stack and to sweep product water from the system. Subsequent heat exchange from the recirculating cathode flow will condense the product water vapor to liquid where it can be collected and drained to the electrolyzer water source. (In the absence of gravity, centrifugal separation of the liquid water will be required.)

A close-fitting shroud encloses the system. This shroud channels the cathode flow, supports those components not directly mounted on the tank, and provides the pressure boundary for the fuel cell system. Some fraction of the waste heat will dissipate through the shroud. Ribs on the inside of the shroud contact and retain the porous layer covering the cathode. The use of composite material for the shroud could provide exceptional stiffness and strength with little weight impact.

A connecting boss on the upper end of the composite storage tank feeds the hydrogen pressure regulator. The porous annular anode flow field is connected to the pressure-regulated hydrogen supply by a plenum. Experimental results suggest that hydrogen humidification is not required if cell current densities are kept below about 500 mA/cm^2. A connecting boss on the bottom of the tank locates a safety valve and a valved fill port for refueling from the electrolyzer. Because water will slowly accumulate in the dead-end anode flow field, a periodic purge of a "sump" is required, with a corresponding valve and control circuit.

Safety considerations are expected to require the incorporation of hydrogen leak sensing and automatic shut-off of the high-pressure gas supply. Hydrogen sensors can be relatively simple and robust, consisting of a catalyst to enhance hydrogen oxidation and a thermocouple to sense that the exothermic reaction is occurring. This function does not significantly complicate the microprocessor control system.

Figure 4 displays the annular module PEM H_2-O_2 fuel cell concept. When integrated with an electrolyzer, the resulting configuration forms the reversible energy storage/generation portion of a regenerative power system.

Example System. To illustrate the concept, we have performed some scoping calculations on a 5-kW, 20,000 W-h system. To increase the power density, we have extended the design concept (described above and in Refs. 11 and 12) by "folding" the PEM membrane and electrode assemblies into two concentric cylinders. Here, one mono-layer of cells covers the hydrogen tank surface (as above), but then "crosses over" and folds back on itself with a continued mono-layer of cells lining the inside of the shroud/pressure boundary. The inner and outer PEM cells are arranged so that the cathodes face a common oxygen flow field.

For reactant storage at 3,000 psi, the resulting configuration has a shroud outer diameter of approximately 36.3 cm (14.3 in) and an overall length of about 133 cm (52.3 in). The corresponding oxygen tank has an outer diameter of 25.4 cm (10 in) and an overall length of 88.9 cm (35 in). The calculated weight of the tanks, reactants, fuel cell stack, shroud/pressure boundary and ducting is 28.7 kg (63.2 lb). Higher hydrogen storage pressure will decrease volume, but have little impact on overall weight. Including a rough estimate for the weight of those necessary components not included above, it appears that a primary (but refuelable) "battery" of this design could have an energy density (excluding

the heat rejection components) exceeding 500 W-h/kg (227 W-h/lb). Higher stored energy will increase the energy density, with the system energy density approaching that of the reactant storage subsystem. Figure 5 displays a cross-section through the example fuel cell module.

Direct radiators are large, therefore, and consequently heavy. In an application where living or equipment space must be conditioned, however, use of this "waste" energy for heating, with subsequent rejection of excess heat from the larger surface of the conditioned volume, may prove attractive.

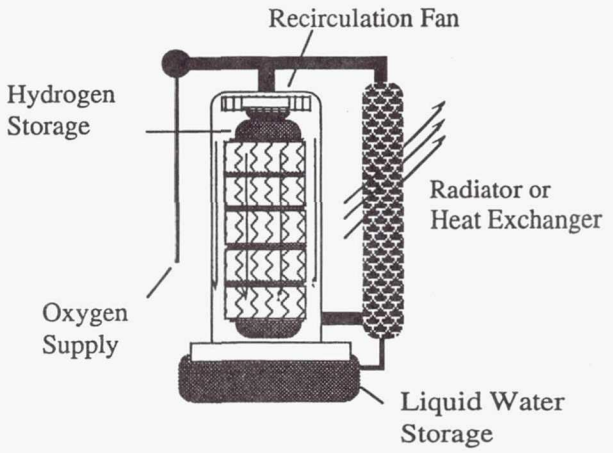

Fig. 4 Simple modular system concept using annular PEM fuel cells.

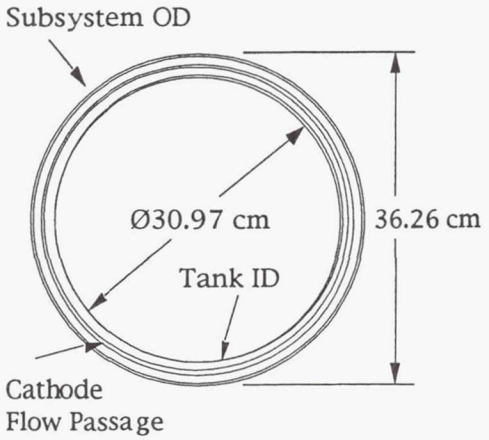

Fig. 5 Horizontal cross-section through example fuel cell system showing relative dimensions.

Heat rejection is a challenge for this technology because the optimum operating temperature of the fuel cell components is no more than about 90°C.

Regenerative System Integration. The concept and example above require additional functions and components to complete a regenerative system (see Fig. 2 and Ref. 7). Electrolysis could proceed at the reactant storage pressure in a separate electrochemical component, with a water pump raising the water from the storage reservoir to the electrolyzer pressure. Alternately, electrolysis could occur in a reversible fuel-cell/electrolyzer at the low fuel-cell operating pressure, with the product reactants subsequently pumped up to the required storage pressure. Each approach involves challenges with high pressure pumps and interfaces. Additional design work and trade-off studies are required to optimize the overall system in terms of reliability, weight, and volume.

Concept Summary. In summary, the series-integrated annular module PEM H_2-O_2 regenerative fuel cell system

consists of the following major components:

- A fuel cell subsystem consisting of several annular PEM modules, the anode and cathode flow-field layers, the anode feed plenum, and gasketing;
- A hydrogen delivery system consisting of a high-performance graphite-composite reinforced compressed-gas storage tank with a shut-off valve, pressure regulation, a safety valve, a valved fill port, and an anode-flow-field purge valve;
- An oxygen delivery system consisting of a high-performance graphite-composite reinforced compressed-gas storage tank with a shut-off valve, pressure regulation, a safety valve, a valved fill port, a humidifier, a recirculation fan, a heat exchanger with provision for product water collection, and a shroud/pressure boundary;
- An electrolyzer system consisting of a high-pressure electrolyzer with necessary pumps, valving, water storage, and photovoltaic array;
- An electronic package containing DC-DC power conditioning, sensors, and controls;
- Mechanical supports; and
- A heat rejection radiator or connection with an integrated thermal management system (for example, providing cabin heat).

We believe that the development of the annular modular configuration described above could lead to a system that exhibits the necessary and desirable characteristics for application to a variety of space or planetary missions. This same technology would certainly have broad uses in both the civilian and military sectors.

FUTURE WORK

As part of the ongoing effort, the Los Alamos National Laboratory will assist the NASA Lewis Research Center by conducting an electrochemical cell test program to provide critical life, reliability, and performance data currently lacking in the data base of PEM fuel cells and water electrolyzers. Los Alamos will provide technical support for fuel cell programs managed by NASA LeRC at the discretion of the NASA program manager. Los Alamos will also continue to develop, in collaboration with NASA, the single cell stand that was delivered to NASA LeRC during Fiscal Year 1992.

REFERENCES

1. Vanderborgh, N. E., Kimble, M. C., Huff, J. R., and Hedstrom, J. C., "PEM Fuel Cell Stack Heat and Mass Management," Proc. 27th Intersociety Energy Conversion Engineering Conference (IECEC), Vol. 3, pp. 407-411 (1992).

2. Nguyen, T., Hedstrom, J., and Vanderborgh, N., "Heat and Mass Transfer Design Issues in PEM Fuel Cell Hardware," Proc. American Institute of Chemical Engineers (AIChE) Meeting, San Francisco CA (November 1989).

3. Vanderborgh, N., Huff, J., and Hedstrom, J., "Heat and Mass Transfer Effects in PEM Fuel Cells," Proc. 24th Intersociety Energy Conversion Engineering Conference (IECEC), p. 1637 (1989).

4. Rieke, P., and Vanderborgh, N., "Temperature Dependence of Water Content and Proton Conductivity in Polyperfluorosulfonic Acid Membranes," J. Membrane Science, Vol. 32, pp. 313-328 (1987).

5. Nguyen, T., Guante, J., and Vanderborgh, N., "Ion Transport

Through Polyperfluorosulfonic Acid Membranes," Materials Research Society Fall Meeting, Boston, MA, (November 28-December 2, 1988).

6. Vanderborgh, N., Hedstrom, J., and Huff, J., "Thermal Management of Advanced Fuel Cell Power Systems," Proc. 25th Intersociety Energy Conversion Engineering Conference (IECEC), p. 149 (1990).

7. Huff J., Vanderborgh, N., and Hedstrom, J., "Technology Assessment and Trade-off Study of Fuel Cell and Electrolyzer Technologies for the Project Pathfinder Energy Storage System," Los Alamos National Laboratory LA-UR-90-3244 prepared for the National Aeronautics and Space Administration Lewis Research Center (May 1991).

8. Huff, J., Hedstrom, J., Vanderborgh, N., and Prokopius, P., "Regenerative Fuel Cell Systems for Project Pathfinder," Proc. European Space Power Conference, Madrid, Spain (October 2-6, 1989). Published by ESA Pub. Div., Noordwijk, Netherlands, pp. 217-219.

9. Vanderborgh, N., Hedstrom, J., and Huff, J., "Electrochemical Energy Storage Using PEM Systems," Proc. European Space Power Conference, Florence, Italy (September 1991).

10. Vanderborgh, N., Hedstrom, J., and Huff, J., "Advanced Space Power PEM Fuel Cell Systems," Proc. European Space Power Conference, Madrid, Spain (October 2-6, 1989). Published by ESA Pub. Div., Noordwijk, Netherlands.

11. Vanderborgh, N. E., and Stroh, K. R., "High Energy Density Stack Design," Los Alamos National Laboratory PATENT DISCLOSURE (December 11, 1992).

12. Vanderborgh, N. E., Stroh, K. R., and Meier, R., "Analysis of Fuel Cells, Reactant Delivery Systems, and System Integration for Individual Power Sources," Los Alamos National Laboratory LA-UR-93-345 Revised (January 1993).

PEM REGENERATIVE FUEL CELLS

Larry L. Swette, Anthony B. LaConti, Stephen A. McCatty
Giner, Inc.
14 Spring Street
Waltham, MA 02154-4497

ABSTRACT

This paper will update the progress in developing electrocatalyst systems and electrode structures primarily for the positive electrode of single-unit solid polymer proton exchange membrane (PEM) regenerative fuel cells. The work was done with DuPont Nafion 117 in complete fuel cells (40 cm^2 electrodes). The cells were operated alternately in fuel cell mode and electrolysis mode at 80°C. In fuel cell mode, humidified hydrogen and oxygen were supplied at 207 kPa (30 psi); in electrolysis mode, water was pumped over the positive electrode and the gases were evolved at ambient pressure. Cycling data will be presented for Pt-Ir catalysts and limited bifunctional data will be presented for Pt, Ir, Ru, Rh and $Na_xPt_3O_4$ catalysts as well as for electrode structure variations.

INTRODUCTION

In prior work [1, 2, 3], a large number of candidate bifunctional positive electrode catalysts were evaluated for chemical and electrochemical stability and for catalytic activity in 30% KOH at 80°C. As a result of this work, two potentially bifunctional catalyst systems were identified: 1) $Na_xPt_3O_4$ [4] and 2) metal/metal oxide combinations of Rh, Pt and Ir [3]. More recently the scope of the program was expanded to include development of bifunctional positive electrode catalysts for the regenerative PEM fuel cell, focusing on many of the same catalysts.

In order to alternate between oxygen reduction and oxygen evolution on the same electrode, in addition to bifunctional catalysis, it is necessary to have an electrode structure that can perform in both of these modes. Some of the effort on this program was directed to the development of such structures. The approach taken was to develop catalyst/binder compositions optimized separately at the particulate level for either oxygen reduction (more hydrophobic) or oxygen evolution (more hydrophilic) and then combine these at an optimal ratio in a single electrode, referred to as an "integrated dual-character" (IDC) electrode. In this approach the catalyst for each function can be the same material if it shows bifunctional activity (e.g., $Na_xPt_3O_4$), or two different monofunctional catalysts (e.g., Pt for O_2 reduction and IrO_2 for O_2 evolution). This approach, developed for the alkaline system, was extended to the PEMRFC by introducing a two-layer structure to achieve an appropriate interface to the more confined two-dimensional character of the proton exchange membrane.

EXPERIMENTAL

Catalyst Materials

Pt black, used in both the positive and negative electrode structures, was fuel cell grade material obtained from Engelhard Industries. Metal oxide catalysts were prepared by proprietary modifications of Adams-type fusions of the metal salts in a nitrate flux [5]; metal/metal oxide catalysts (Pt-MO_x) were prepared by co-fusion of the metal salts in a similar manner followed by electrochemical reduction of the PtO_2 to Pt, or were blends of separately prepared materials (Pt-$Na_xPt_3O_4$).

$Na_xPt_3O_4$ was typically prepared by firing mixtures of Na_2CO_3 and PtO_2 under oxygen at 650°C or higher for several hours. In most cases it was necessary to use a proprietary activation procedure to develop significant catalytic activity and acceptable conductivity.

The surface areas of all materials were determined by the BET nitrogen adsorption method using a Micromeritics Flowsorb II 2300 instrument. The electrical conductivities of materials were estimated by a 2-point method measuring the resistance of the powders under moderate compression [2]. The compositions of the metal oxides prepared by nitrate fusion were determined in earlier work by X-ray diffraction analysis. Iridium chloride fusions yield IrO_2, which becomes slightly oxygen deficient IrO_{2-x} ($x = \sim 0.05$) if electrochemically reduced. Rhodium chloride fusions yield RhO_2. The ruthenium salt fusions yield RuO_2, which also becomes oxygen deficient RuO_{2-x} ($x = \sim 0.1$) if electrochemically reduced. The $Na_xPt_3O_4$ preparations were also analyzed by XRD for chemical characterization and determination of phase purity. The sodium content in $Na_xPt_3O_4$ can be determined from the unit cell parameter, a_o:

$$x = (a_o - 5.59)/0.11$$

Recent preparations of $Na_xPt_3O_4$ have exhibited moderate surface areas and marginally acceptable conductivities without any post-synthesis treatment and have been tested in that form. Materials characterization data is summarized in **Table 1**.

PEM Regenerative Fuel Cell Testing

A rechargeable fuel cell requires 1) a negative electrode that is active for both H_2 oxidation and H_2 evolution and 2) a positive electrode that is active for both O_2 reduction and O_2 evolution. The general approach to achieve bifunctional electrode structures was to partially distribute the charge and discharge functions to separate catalyst layers of a composite electrode each of which is optimized primarily for one function. A hydrophilic PEM-bonded layer supports the gas evolution functions; for oxygen evolution the selected catalyst, at a loading of 1-3 mg/cm^2, was blended with 10-20 wt% of the ionomer and pressed onto the surface of the membrane. The gas-consumption discharge functions are supported by a separate more hydrophobic catalyst layer which was physically pressed against the PEM-bonded layer by the mechanical compression of the cell assembly.

Platinum is a good catalyst for the negative electrode reactions in both alkaline and acid electrolytes. We used the composite electrode structure for most of the PEM cell configurations. For the negative electrode the combination consisted of a platinum layer bonded directly to the PEM (optimized for hydrogen evolution) and a separate IDC electrode (optimized for hydrogen oxidation). The "free-standing" component of the composite electrode consisted of an IDC platinum composition bonded to wetproofed carbon paper.

The requirements for the positive electrode are more difficult to meet because of the scarcity of efficient bifunctional oxygen catalysts. In addition, a titanium current collector is required because carbon support materials are not stable under oxygen evolution conditions. Platinum is an excellent O_2-reduction catalyst for the fuel-cell mode, but is relatively poor for oxygen evolution. IrO_2 is an excellent O_2-evolution catalyst, but a poor O_2-reduction catalyst. For electrolysis cells it is mixed or alloyed with Pt to improve the conductivity of the IrO_2. The general approach was to use Pt black for the oxygen reduction function in the free-standing component and to incorporate the more favorable oxygen evolution catalyst in the PEM-bonded layer, with Pt added to improve conductivity. For baseline performance data we used Pt or Pt-IrO_2 as the oxygen electrode catalyst. Three baseline cell types were fabricated and tested: a Pt/Pt fuel cell (also tested as an electrolyzer), a Pt/Pt-IrO_2 electrolyzer, and several Pt/Pt-IrO_2 bifunctional cell configurations; subsequently, Pt/Pt-$Na_xPt_3O_4$ bifunctional cells of similar construction were also tested [6]. More recently, as the oxygen evolution catalyst, we have evaluated Pt-RuO_x, RuO_x-IrO_x and RhO_2, and we examined the performance of Pt-IrO_x and $Na_xPt_3O_4$ with repeated cycling.

The baseline Pt/Pt fuel cell and the experimental bifunctional cells were fabricated with a Nafion 117 PEM and utilized composite electrodes (catalyst layer bonded to the PEM plus a free-standing IDC electrode) on both sides. The baseline fuel cell and all of the experimental bifunctional cells had the same negative (H_2) electrode configuration. On the oxygen side, the PEM-bonded electrode was Pt, Pt-IrO_2, Pt-RuO_x, RuO_x-IrO_x, RhO_2 or Pt-$Na_xPt_3O_4$, and the free-standing electrode was Pt or Pt-$Na_xPt_3O_4$ on titanium mesh (Pt-plated). The baseline electrolysis cell had only the PEM-bonded electrode layers, optimized for gas evolution only (without ionomer

added). In electrolysis mode, the cells were run at ambient pressure with heated water pumped through the positive electrode chamber; in fuel-cell mode the gases were supplied at 207 kPa and the H_2 stream was humidified at 90-120°C. The majority of testing was done at a cell temperature of 80°C.

RESULTS

As described above, three different types of PEM cells were constructed and tested to establish a performance baseline for single-function cells (fuel cell or electrolyzer) and a bifunctional cell. Subsequently, bifunctional PEM cells with Pt-$Na_xPt_3O_4$ positive electrodes were fabricated and tested to determine the relative performance of this potential catalyst in acid electrolyte. More recently we have evaluated Pt-RuO_x, RhO_2 and RuO_x-IrO_x as the oxygen evolution components in bifunctional cells and investigated the performance of Pt-IrO_x and Pt-$Na_xPt_3O_4$ under limited cycling conditions.

Baseline Cells

Baseline Pt/Pt Fuel Cell. - In fuel-cell mode, this cell ran at 0.874 V at 100 mA/cm^2 and at 0.714 V at 500 mA/cm^2 at 80°C. As an electrolyzer, performance was poor, as expected, primarily because Pt is not a very good catalyst for O_2 evolution; 1.77 V at 100 mA/cm^2, 2.00 V at 500 mA/cm^2 at 80°C. This cell was provided with the same positive electrode structure as used in the bifunctional cells (an IDC platinum composition at a loading of 8-10 mg/cm^2 on a Ti current collector mesh) so that the electrolyzer performance of Pt could also be measured. More recently a non-reversible Pt/Pt cell, optimized for fuel cell operation, was built and tested. In this cell the anode and cathode were of the same composition and configuration; the PEM-bonded layers consisted of Pt at a loading of 1 mg/cm^2 with 10 wt% ionomer, and the free-standing electrodes consisted of an IDC composition of Pt at a loading of 4 mg/cm^2 on wetproofed carbon paper (Toray HO-30). The fuel cell performance of these two cells is compared in **Figure 1**. It can be seen that the cell optimized for fuel cell operation gave slightly better performance.

Baseline Pt/40Pt-60IrO_2 Electrolyzer. - This cell ran at 1.50 V at 100 mA/cm^2 and at 1.671 V at 500 mA/cm^2. This is fairly typical performance for a dedicated electrolyzer cell with Nafion and Pt/Pt-IrO_2 catalysts. This cell was not tested in fuel-cell mode. The performance is presented in **Figure 2** in comparison to the baseline Pt/Pt fuel cell and the baseline Pt/Pt-IrO_2 bifunctional cell.

Baseline Bifunctional Pt/Pt-IrO_2 Cell. - Several Pt/Pt-IrO_2 cells with varying IrO_2 contents and electrode structures were evaluated initially to optimize bifunctional performance [6]. A Pt/40Pt-60IrO_2 cell (#5 in **Tables 1 & 2**) cell exhibited the best performance in both modes. At 500 mA/cm^2, this cell ran at 1.587 V in electrolysis mode and at 0.723 V in fuel-cell (#5) mode. The comparable voltages for the baseline cells are 1.671 V for the electrolyzer and 0.714 V for the fuel cell. The performance is presented in **Figure 2** in comparison to the baseline Pt/Pt fuel cell and the baseline Pt/Pt-IrO_2 electrolyzer.

Catalyst Evaluation

Bifunctional Pt/Pt-$Na_xPt_3O_4$ Cells. - Two different bifunctional cells were constructed for the initial evaluation of $Na_xPt_3O_4$ as a component of the oxygen electrode catalyst. The first cell (#6, $Na_xPt_3O_4$ prep.#21, see Tables 1 & 2) used a two-layer oxygen catalyst structure bonded to the PEM consisting of very hydrophilic $Na_xPt_3O_4$ (10% ionomer) and a less hydrophilic Pt transition layer. The balance of the composite electrode was a free-standing IDC electrode consisting of a 33/67 mix of $Na_xPt_3O_4$ and Pt. This cell gave excellent fuel cell performance (0.74 V at 500 mA/cm^2), as shown in **Figure 2** and **Table 2**, better than the Pt/Pt cell (0.714 V) and the best Pt/40Pt-60IrO_2 cell (0.723 V). The cell performance in electrolysis mode was 1.697 V at 500 mA/cm^2, better than Pt/Pt (2.00 V), but not as good as the best Pt/40Pt-60IrO_2 cell (1.587 V).

The second $Na_xPt_3O_4$-containing bifunctional cell (#7, $Na_xPt_3O_4$ prep.#34A3) was constructed using a single layer of $Na_xPt_3O_4$ with 10% ionomer bonded to the PEM and the standard IDC Pt free-standing IDC electrode as the composite oxygen electrode. This cell showed reduced performance in both modes compared to

the first $Na_xPt_3O_4$ cell (**Figure 2** and **Table 2**). In the fuel-cell mode, the voltage at 500 mA/cm^2 was 0.657 V. In electrolysis mode, the voltage was 1.766 V at 500 mA/cm^2, which is still a significant improvement over a pure Pt/Pt cell. The differences in performance between these two cells may be partly due to differences in catalytic activity since the materials, although very similar in physical characteristics, are from two separate and somewhat different preparations (see **Table 1**); a larger part of the differences, however, may be attributed to the changes in electrode structure in Cell #7 resulting in a higher resistance interface.

Pt/Pt-IrO_2. - Cell #8 was an attempt to repeat the build of the baseline bifunctional Pt/Pt-IrO_2 cell (#5) but with two slight differences: slightly more ionomer in the PEM-bonded layer and the introduction of a thin Pt transition layer between the bonded layer and the free-standing electrode. The cell had somewhat higher resistance and did not perform quite as well as Cell #5; the performance curves are shown in **Figure 3.**

RuO_x-IrO_x was used as the PEM-bonded layer for oxygen evolution in Cell #9 and the Pt transition layer was included for comparison to Cell #8. The electrolysis performance was better than for Cell #8 but the fuel cell performance was not as good (see **Figure 3**). It is anticipated that a structural reconfiguration of the cell duplicating Cell #5 would significantly upgrade fuel cell performance with this catalyst.

Pt-RuO_x was used as the PEM-bonded layer for oxygen evolution in Cell #10 and the Pt transition layer was again included for comparison. The performance was quite similar to the performance observed for RuO_x-IrO_x (see **Figure 3**).

RhO_x was used as the PEM-bonded layer for oxygen evolution in Cell #11 but the Pt transition layer was eliminated. This material was difficult to work with because of the very high surface area and more development would be required for a fair evaluation. Two performance points are shown in Table 2, but the cell was not very stable in either mode.

Repetitive Cycling Tests

Cells #12 and #13 were attempts to reproduce the electrode structures and performance of the baseline bifunctional Pt/40Pt-60IrO_2 cell (#5) for the purpose of investigating tolerance to repetitive cycling. The first build (#12) had somewhat higher than typical internal resistance and showed lower performance than Cell #5 (**Table 2**). The cell was subjected to six charge/discharge cycles at 500 mA/cm^2, shown in **Figure 4**, after which it developed a leak and testing was terminated.

Cell #13 came somewhat closer in performance to Cell #5; in fuel cell mode it was not quite as good as Cell #5 but in electrolysis mode it was somewhat better (see **Table 2**). This build was subjected to fifteen charge/discharge cycles, at which point it also developed a leak. The performance at 500 mA/cm^2, shown in **Figure 5**, remained fairly constant for both modes of operation over the fifteen cycles.

Cells #14, #15 and #16 were attempts to fabricate bifunctional positive electrodes similar to that used in Cell #5 but based on $Na_xPt_3O_4$, also for the purpose of investigating tolerance to repetitive cycling. The first two builds (#14 & #15) did not give very stable performance and were not cycled (see **Table 2**). Cell #16 did not show any significant improvement in performance but was somewhat more stable (see **Figure 6**) and was subjected to five charge/discharge cycles. Neither the performance of Cell #5 nor the performance of the earlier $Na_xPt_3O_4$ build (#6) was reproduced, but the cyclic performance was stable and better than Pt alone.

CONCLUSIONS

Regenerative PEM fuel cells showing efficient bifunctional performance can be fabricated with traditional Pt and Pt-Ir catalysts if the electrode structures are properly designed.This investigation has also identified RuO_x as a catalyst with good potential for improving the oxygen evolution component of a bifunctional positive electrode. $Na_xPt_3O_4$ was identified in our earlier work as a catalyst with potential for bifunctional operation in

both alkaline and acid electrolytes; the current work has confirmed this with limited charge/discharge cycling but additional development will be required to achieve more reproducible catalyst properties and performance.

ACKNOWLEDGEMENTS

This phase of the work was supported by NASA Lewis Research Center under the direction of Dr. Patricia Loyselle on Contract No. NAS3-24635. We would also like to acknowledge the assistance of Prof. B.L. Chamberland of the University of Connecticut in the selection and identification of numerous materials tested in this program.

REFERENCES

1. L. Swette and J. Giner, J. of Power Sources, 22 (1988) 399-408.

2. L. Swette and N. Kackley, J. of Power Sources, 29 (1990) 423-436.

3. L. Swette, N. Kackley and S.A. McCatty, J. of Power Sources, 36 (1991) 323-339.

4. L. Swette and N. Kackley, "Bifunctional Alkaline Oxygen Electrodes," IECEC Conf. Proceedings, Boston, MA, Aug. 4-9, 1991.

5. R. Adams and R.L. Shriner, J. Am. Chem. Soc., 45 (1923) 2171-2179.

6. L. Swette, N.D. Kackley and A.B. LaConti, "Regenerative Fuel Cells," Presented at the 27th Intersociety Energy Conversion Engineering Conference, San Diego, CA, Aug. 3-7, 1992

TABLE 1

PEMRFC positive electrode: composition and characteristics of PEM-bonded layer

Cell #	Catalyst	Ratio (wt%)	Loading (mg/cm^2)	Ionomer (wt%)	Surface Area (m^2/g)
5	$Pt\text{-}IrO_x$	40-60	1	10	104
6	Pt overlay	33	1	0	28
	$Na_xPt_3O_4$ #21*	67	2	10	12
7	$Na_xPt_3O_4$ #34A3*	100	2	10	7
8	$Pt\text{-}IrO_x$	40-60	1	15	117
9	$RuO\text{-}IrO_x$	50-50	2	25	114
10	$Pt\text{-}RuO_x$	40-60	1	15	69
11	RhO_2	100	1	18	224
12	$Pt\text{-}IrO_x$	40-60	1	10	117
13	$Pt\text{-}IrO_x$	40-60	1	10	117
14	Pt black +	33	1	10	29
	$Na_xPt_3O_4$ #41*	67	2	10	18
15	Pt black +	33	1	10	29
	$Na_xPt_3O_4$ #43*	67	2	10	35
16	Pt black +	33	1	10	29
	$Na_xPt_3O_4$ #43*	67	2	10	35

* $Na_xPt_3O_4$ Characteristics

Prep No.	Surface Area (m^2/g)	Conductivity ($ohm\text{-}cm^{-1}$)	Unit Cell Parameter	Na_x-value
#21	12	33	5.671(3)	0.74
#34A3	7	30	5.674(1)	0.76 ("activated")
#41	18	0.3	5.675(3)	0.77
#43	35	3.4	5.688(1)	0.89

TABLE 2

Cell voltage in fuel-cell and electrolysis modes for baseline cells and bifunctional PEM cells. 80°C, electrolysis at ambient pressure, fuel cell at 207 kPa.

Cell Performance in --->	Electrolysis Mode		Fuel-Cell Mode	
Positive Electrode Red./Evol. Cat.	**100 mA/cm² (V)**	**500 mA/cm² (V)**	**100 mA/cm² (V)**	**500 mA/cm² (V)**
Baseline Fuel Cells				
Pt/Pt (reversible)	1.770	2.000	0.874	0.714
Pt/Pt (fuel cell)	Not Tested	Not Tested	0.901	0.733
Baseline Electrolyzer				
Pt/40Pt-60IrO_2	1.500	1.671	Not Tested	Not Tested
Bifunctional Cells				
#5 Pt/40Pt-60IrO_2	1.456	1.587	0.901	0.723
#6 Pt/$Na_xPt_3O_4$-Pt	1.545	1.697	0.903	0.740
#7 Pt/$Na_xPt_3O_4$-Pt	1.621	1.766	0.839	0.657
#8 Pt/40Pt-60IrO_x	1.477	1.624	0.888	0.704
#9 Pt/50RuO_x-50IrO_x	1.406	1.627	0.778	0.565
#10 Pt/40Pt-60RuO_x	1.417	1.589	0.784	0.566
#11 Pt/RhO_2	----	1.675	----	0.460
#12 Pt/40Pt-60IrO_x	1.489	1.620	0.858	0.640
#13 Pt/40Pt-60IrO_x	1.455	1.550	0.870	0.714
#14 Pt/33Pt-67$Na_xPt_3O_4$	----	1.873	0.873	0.698
#15 Pt/33Pt-67$Na_xPt_3O_4$	1.599	1.797	0.866	0.704
#16 Pt/33Pt-67$Na_xPt_3O_4$	1.618	1.799	0.838	0.597

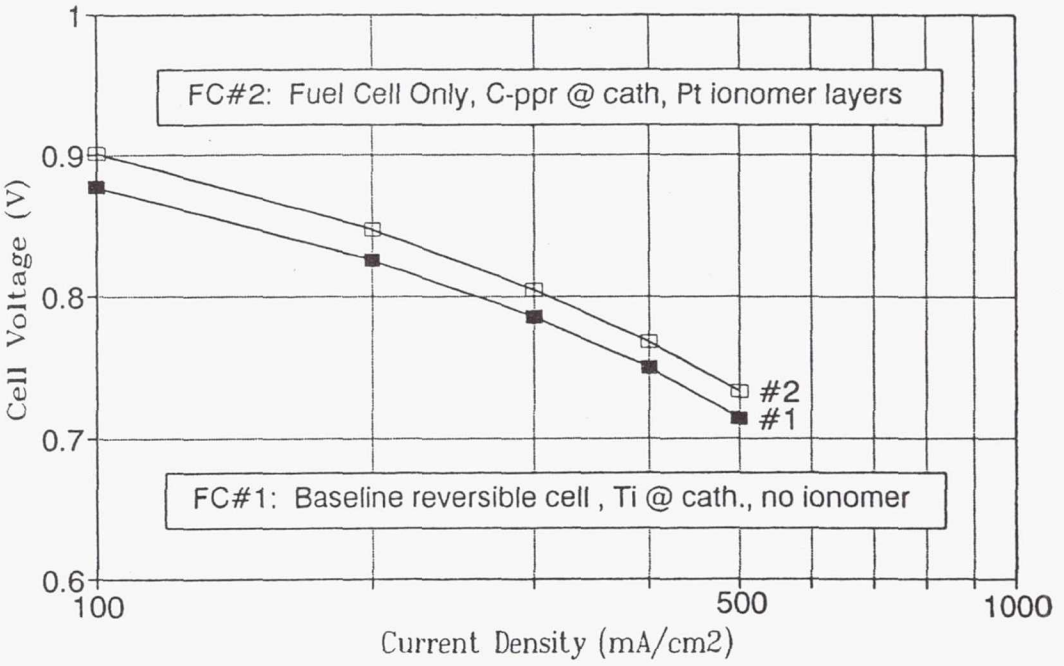

Fig. 1.—PEM Pt/Pt fuel cell performance (fuel cell mode only; 80°C, 30 psi).

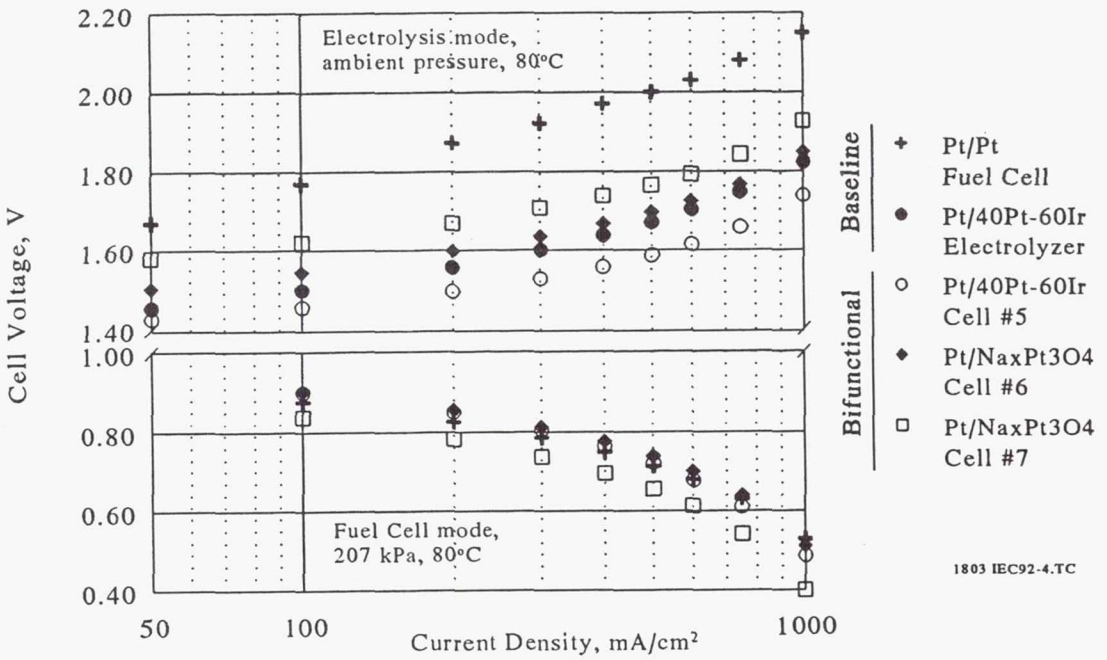

Fig. 2.—Performance of bifunctional $Pt/Na_xPt_3O_4$ PEM cells.

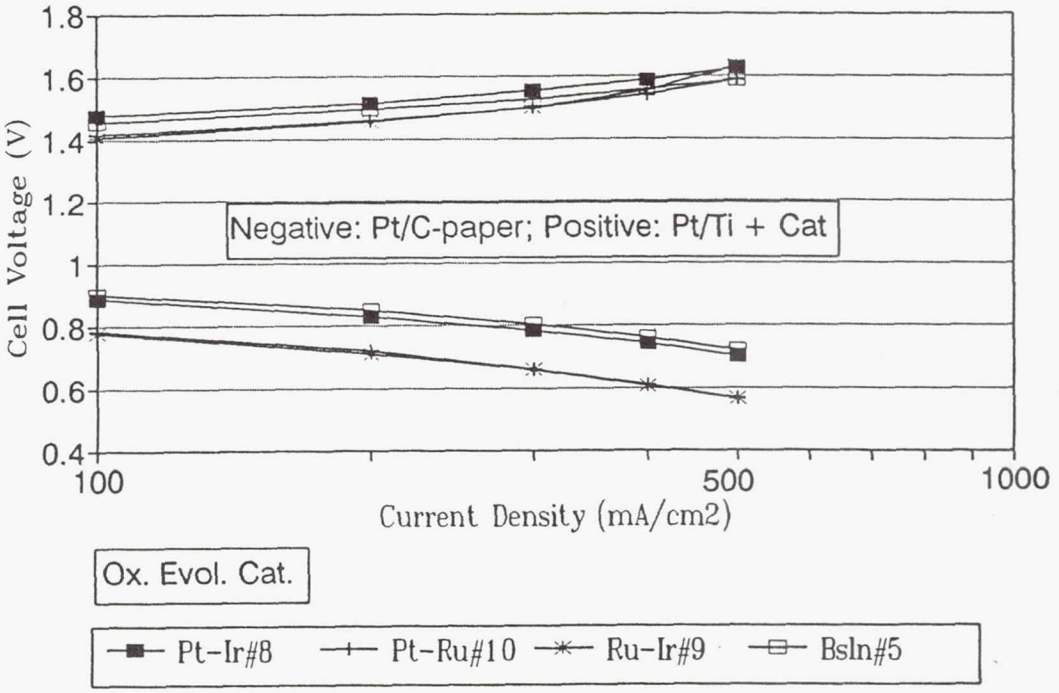

Fig. 3.—Bifunctional oxygen catalyst evaluation (Nafion 117, 80°C, 30 psi).

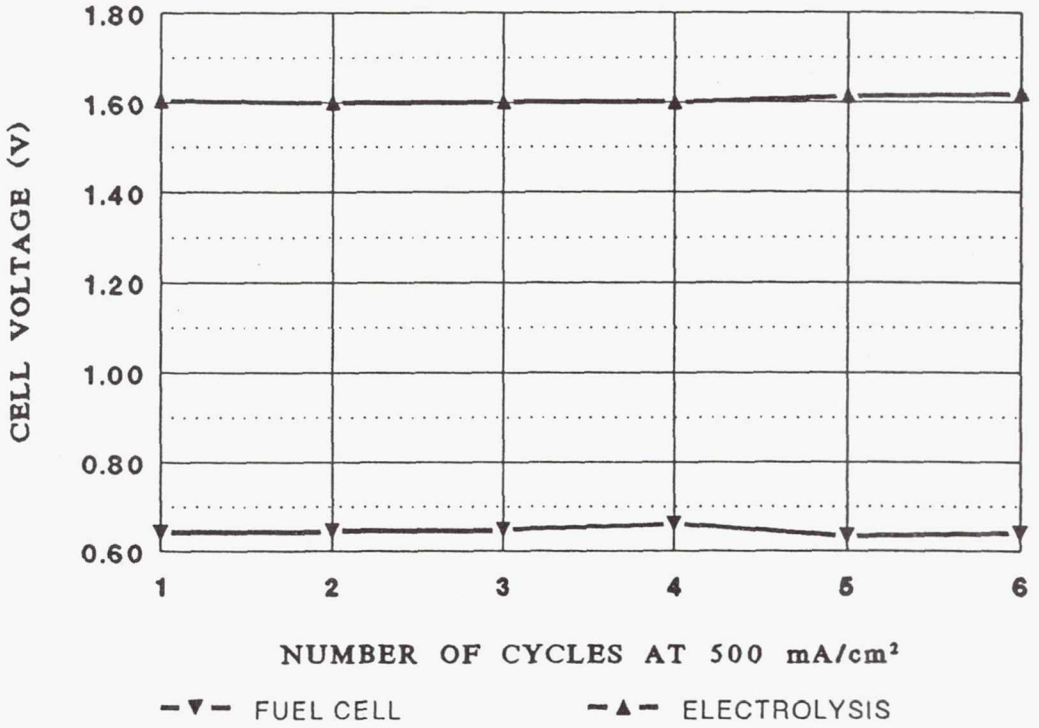

Fig. 4.—Cyclic performance of Cell #12 (Pt/Pt-IrO_x, 80°C).

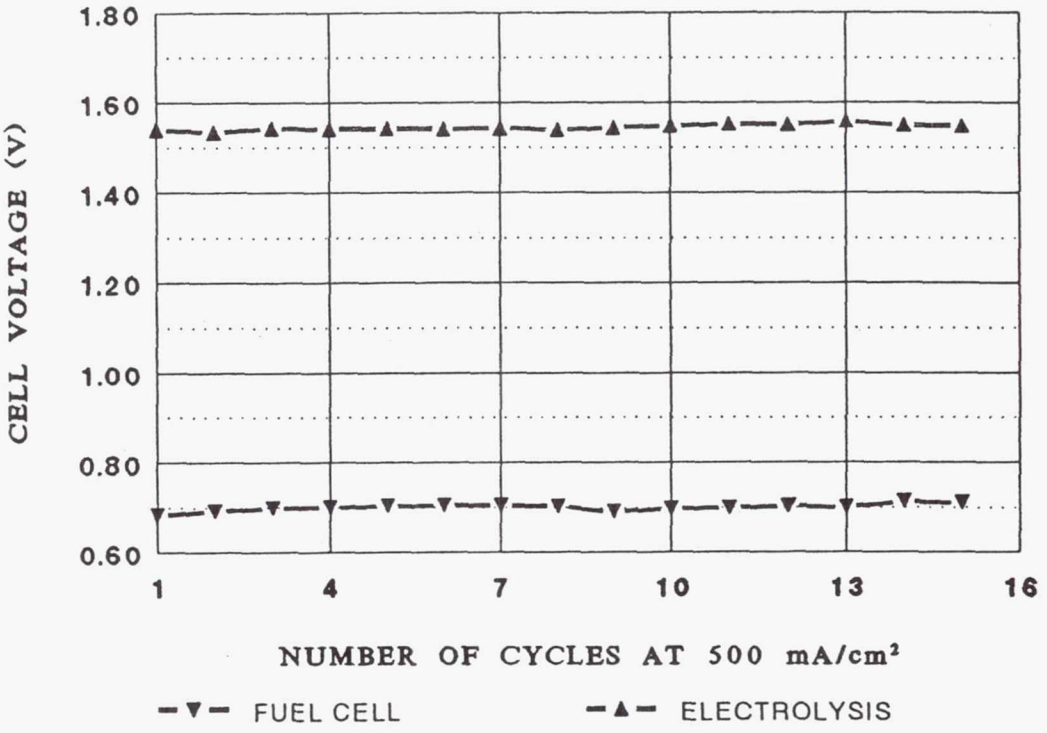

Fig. 5.—Cyclic performance of Cell #13 (Pt/Pt-IrO_x, 80°C).

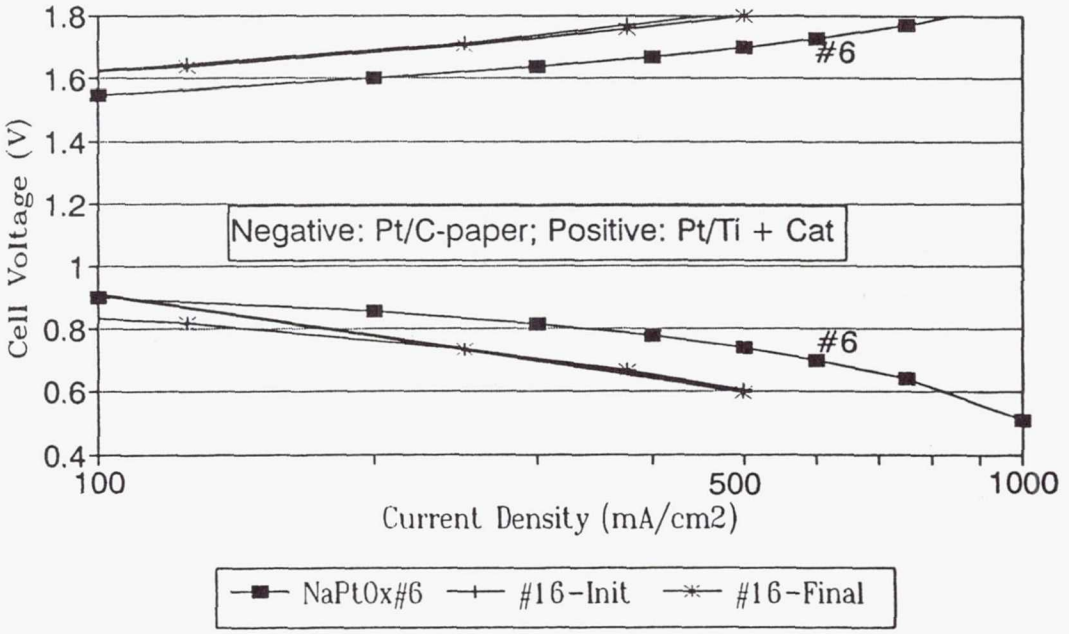

Fig. 6.—Cell #16 before and after five cycles (Nafion 117, 80°C, 30 psi).

HIGH POWER DENSITY PROTON EXCHANGE MEMBRANE FUEL CELLS

Oliver J. Murphy, G. Duncan Hitchens and David J. Manko

Lynntech, Inc.
7610 Eastmark Drive, Suite 105
College Station, Texas 77840

ABSTRACT

Proton exchange membrane (PEM) fuel cells use a perfluorosulfonic acid solid polymer film as an electrolyte which simplifies water and electrolyte management. Their thin electrolyte layers give efficient systems of low weight, and their materials of construction show extremely long laboratory lifetimes. Their high reliability and their suitability for use in a microgravity environment makes them particularly attractive as a substitute for batteries in satellites utilizing high-power, high energy-density electrochemical energy storage systems. In this investigation, the Dow experimental PEM (XUS–13204.10) and unsupported high platinum loading electrodes yielded very high power densities, of the order of 2.5 W cm^{-2}. A platinum black loading of 5 mg per cm^2 was found to be optimum. On extending the three-dimensional reaction zone of fuel cell electrodes by impregnating solid polymer electrolyte into the electrode structures, Nafion was found to give better performance than the Dow experimental PEM. The depth of penetration of the solid polymer electrolyte into electrode structures was 50–70% of the thickness of the platinum-catalyzed active layer. However, the degree of platinum utilization was only 16.6% and the roughness factor of a typical electrode was 274.

INTRODUCTION

There is increasing interest in the development of fuel cell systems as power sources in space, on land and for marine applications [1-3]. Since fuel cells bring about the direct conversion of stored chemical energy to electrical energy without the intermediate generation of thermal energy, they are not limited by the Carnot cycle, unlike heat engines [4]. Thus, energy conversion efficiencies for fuel cell systems (45%–65%) are generally a factor of 2 higher than those for heat engines, e.g., diesel generators. Although considerable advances have been made in fuel cell systems over the past three decades [5,6], they are still considered as an emerging technology. However, for manned spacecraft applications (Gemini, Apollo and Space Shuttle Orbiter), relatively small (1 kW–12 kW) and highly reliable fuel cell power plants have been fabricated and used successfully. Similarly, for terrestrial electrical power generation, relatively large systems (40 kW–11 MW) have been built and demonstrated to be viable candidates for commercial power generation [7].

Traditionally, satellite energy storage has been provided by nickel-cadmium batteries and, more recently, by rechargeable nickel-hydrogen batteries [8], where the primary power source is solar photovoltaic panels. However, with increasing satellite applications, and the associated growing demand for electrical energy storage, in particular, for systems having high peak power outputs, has led to a search for alternatives to rechargeable aqueous-based battery systems [8]. Operating conditions in respect to the charge regime and cycle life of satellite power sources have become much more demanding, in particular, for long-lived, low earth orbit (LEO) satellites in equatorial orbit [9]. For such an application, the number of cycles required of an electrochemical energy storage system is 5,840 per year, or over 50,000 for a ten-year satellite lifetime. This

extremely high cycle life has led to the consideration of lightweight, efficient, high power density, regenerative fuel cells for such satellite applications [8,10].

High power densities, and high energy conversion efficiencies, are a prerequisite for the development of lightweight, small-volume and low-cost fuel cell systems having high specific energies (Wh/kg) and high energy densities (Wh/l). At present, the only fuel cell systems that have the capability of achieving high power densities (> 1 W cm^{-2}) are the proton exchange membrane (PEM) and the alkaline fuel cell (AFC) systems [11,12]. Of these, the PEM system is the leading candidate fuel cell-based power source for demanding satellite applications. The attractiveness of this fuel cell system stems from a number of advantageous characteristics that it possesses, compared to AFC systems. These include: (i) low-temperature operation; (ii) cold start-up capability; (iii) negligible electrolyte management problems, since it uses a proton exchange polymer membrane as an electrolyte; (iv) infinite life on open-circuit stand; (v) higher reliability; (vi) can tolerate high reactant gas pressure differentials across the PEM electrolyte layer, and (vii) ease of thermal and fluid management. Because of the attainment of high power density and high energy conversion efficiency, together with the CO_2-rejecting nature of the strongly acidic PEM electrolyte layer, this fuel cell system readily satisfies the requirement of a dual-use fuel cell technology, e.g., as the power source for electric vehicles where air, rather than oxygen, is used as the oxidant feed gas.

Research and development areas presently being addressed by many research groups, in order to make PEM fuel cells cost-competitive and more effective in meeting various mission requirements, involve optimizing the structure, chemical composition and configuration of fuel cell components [13-17]. These include: (i) electrode structures (platinum-based catalyst loadings and thicknesses of gas diffusion and active layers) [13,18]; (ii) PEM electrolyte material (thickness, conductivity, stability and mechanical characteristics) [11,13,17]; (iii) preparation of membrane and electrode (M&E) assemblies (hot-pressed membranes and gas diffusion electrodes, cast active layers on membranes in physical contact with gas diffusion electrodes and electrodeposited noble metal catalysts in the outer layers of PEM-impregnated gas diffusion electrodes) [13,15,19]; (iv) lightweight, readily mass produced, bipolar plates, cell frames and gasket materials [20], and (v) thermal and water management [16].

In the present investigation, various proton exchange membrane materials, together with unsupported, high platinum loading electrodes (1–10 mg Pt cm^2), were used as the basic cell components for carrying out performance evaluations in 5 cm^2 active area single-cell test fixtures. To increase the utilization of expensive platinum electrocatalysts, electrode structures were impregnated with a solubilized form of various proton exchange membrane materials. Membrane and electrode assemblies were prepared by a proprietary hot-pressing procedure. Humidified oxygen and hydrogen gases at various pressures were used as reactants. Performance characteristics (V-i curves) were recorded at various cell operating conditions (temperature and reactant gas pressures). Using representative M&E assemblies, a cyclic voltammetric technique was used to measure the degree of platinum catalyst utilization in porous gas diffusion electrodes. Also, energy dispersive spectroscopy (EDS) was applied to the cross-sections of tested M&E assemblies, in order to determine the thickness of active electrode layers and the depth of penetration of solubilized PEM material into electrode structures.

EXPERIMENTAL

Electrodes And Proton Exchange Membranes

High surface area, pure platinum black electrocatalyst materials were used for both the hydrogen and oxygen electrodes. The geometric area of each electrode was 5 cm^2. Commercially available (Johnson-Matthey, Inc.) fuel cell gas diffusion electrodes, fabricated using unsupported platinum black (surface area of 35–50 $m^2\ g^{-1}$), with platinum loadings of either 1, 2.5, 5 or 10 mg cm^{-2} were used.

Three proton exchange membrane materials, two from Du Pont and one from Dow Chemical Company, were investigated. Of these, only Nafion® 117 from Du Pont is commercially available. The others, Nafion® 115 and the Dow experimental membrane (XUS-13204.10) were made available in small quantities for experimental purposes. The acid membranes consist of a thin film of perfluorinated sulfonic acid polymer material that possesses good chemical and thermal stabilities [21,22]. The structural formula for these cation exchange membranes is given in Figure 1. Both Nafion® 117 and Nafion® 115 have equivalent weights of 1100 and thicknesses in the dry state of 175 μm and 125 μm, respectively. The Dow experimental membrane has an equivalent weight of approximately 800, a thickness in the dry state of 125 μm and a conductivity of approximately 0.12 $\Omega^{-1}\ cm^{-1}$, as measured with an AC bridge [23].

Before being used, PEM materials were washed in various solutions to remove trace organic and inorganic contaminants. The purification procedure involved boiling the proton exchange membranes in a 10 vol % aqueous H_2O_2 (30 vol %) solution for one hour, followed by boiling for one hour in pure water and subsequently boiling for a second hour in a fresh sample of pure water. Membranes were then removed and boiled for one hour in 0.5 M H_2SO_4, followed by boiling for one hour each in two different samples of pure water. On completing the purification procedure, membrane specimens were stored in the last sample of washwater at room temperature prior to use.

A 5 wt % Nafion solution in a mixture of lower aliphatic alcohols and 10% water was obtained from Aldrich Chemical Company. Portions of this solution (or a similar in-house prepared solution of the Dow PEM material) were brush-coated onto the catalyzed surfaces of fuel cell electrodes. On allowing the first coat to dry in air for a few minutes, a second coat was then applied in a similar fashion. Afterward, the PEM-impregnated electrodes were placed in an oven at 80°C and allowed to dry for 45 minutes in an air atmosphere. From the difference in weight before and after impregnation, PEM loadings (approximately 0.6 mg cm^{-2}) within the catalyzed electrode structures were determined.

PEM-impregnated electrodes were bonded onto both sides of purified proton exchange membranes, using a proprietary hot-pressing procedure. Pressed M&E's were immediately removed from the hot press and mounted in a test fuel cell fixture.

Single Cell Test Fuel Cells

Test fuel cell fixtures were fabricated using machined graphite blocks, having rib-channel patterns on one side, which facilitated the distribution of humidified gases to the porous gas diffusion electrodes, as well as providing current collection from the electrodes. The active cell area, represented by the rib-channel patterns, was 5 cm^2. A membrane and electrode (M&E) assembly, which is the principal component of a cell, was obtained on pressing porous electrode materials onto both sides of a proton exchange membrane, using a proprietary method. Teflon-coated fiberglass gasket materials, placed on both sides of the membrane, provided sealing on

bolting the cell components together. Copper endplates enabled test cell fixtures to be bolted together, and electrical cartridge heaters inserted into the walls of the copper plates allowed various operating cell temperatures to be selected.

After allowing 24 hours to condition a new M&E assembly in a test fuel cell fixture under predetermined gas pressures (usually 0 psi H_2 and 0 psi O_2) and a temperature of 50°C, the performance characteristics of a cell were determined. This involved placing an electronic load, set to operate in the constant load mode, between the terminals of a cell. Performance characteristics (V-i curves) were then recorded at various operating conditions of a cell (temperature and pressure). On completing performance characterizations for some of the test cells, the oxygen gas inlet was removed from the cathode compartment and replaced by an inert gas, e.g., argon. The cathode compartment was then purged overnight with argon, and cyclic voltammetric profiles for the oxygen electrode were subsequently recorded at a scan rate of 50 mV s^{-1} between the potential limits of hydrogen and oxygen gas evolution at a cell temperature of 50°C with hydrogen gas at 1 atm flowing over the anode and reference electrodes, and argon gas at a pressure of 1 atm flowing over the cathode. The latter profiles were recorded using an EG&G PAR Instruments model 362 scanning potentiostat, in conjunction with a Yokogawa model 3025 X-Y recorder.

Test Station Hardware

Fuel cell test stations used in this investigation had: (i) microprocessor control of hydrogen and oxygen gas temperatures entering the fuel cell; (ii) control of gas pressures from atmospheric to 200 psi; (iii) flow meters for the control and measurement of gas flow rates; (iv) electronic loads with a maximum capability of 300 W, and (v) a data acquisition system, with appropriate interfacing for the automated collection and processing of data. An important component of each test station was an attached temperature-controlled environment chamber that housed the test fuel cell fixture and the hydrogen and oxygen gas humidification vessels. The temperature of the controlled environment chamber could be raised or lowered on activating an electrical heating pad placed at the bottom of the chamber. Appropriate electrical connections to components within the chamber were made by isolated electrical feedthroughs, mounted on the walls of the chamber.

RESULTS AND DISCUSSION

Nature Of PEM Electrolyte Material On The Performance Of M&E Assemblies

Since ohmic overpotentials are largely determined by the thickness and by the conductivity of proton exchange membranes, the performance of M&E assemblies using membrane materials thinner than Nafion® 117 (e.g., Nafion® 115) and alternative membranes having the same thickness as Nafion® 115 but at least a factor of 2 higher in conductivity (e.g., Dow experimental membrane, XUS-13204.10) were evaluated. The more highly conducting Dow PEM also possesses better water retention characteristics than Nafion®.

Using unsupported high platinum loading electrodes (5 mg Pt per cm^2) and segments of Nafion 117®, Nafion® 115 and the Dow experimental membrane, M&E assemblies were prepared. V-i profiles for the resulting assemblies, tested at a fuel cell temperature of 95°C with H_2/O_2 reactant gas pressures of 30 psi/40 psi, are presented in Figure 2. A considerable improvement in PEM fuel cell performance was obtained on using the Dow experimental proton exchange membrane, as compared with Nafion® proton exchange membranes.

In the absence of mass transport overpotentials, and taking the hydrogen oxidation reaction to be kinetically fast, the three V-i profiles presented in Figure 2 may be expressed by [24,25]:

$$V = V_0 - b \log i - R_i i \quad (1)$$

where

$$V_0 = V_r + b \log i_0 \quad (2)$$

V_r is the thermodynamic reversible potential for the fuel cell reaction, i_0 and b are the exchange current density and Tafel slope for the oxygen reduction reaction and R_i is the differential resistance of the cell. When activation overpotential (primarily due to the oxygen reduction reaction) and ohmic overpotential are the major sources of power loss, the data points corresponding to these regions in the V-i profiles can be fitted to Equation [1], and the parameters V_0, b and R_i extracted using the method of least squares fit. Excellent agreement between the experimental data points and simulated V-i profiles from the curve fitting was obtained up to current densities where mass transport effects became noticeable. The values of V_0, b and R_i for the three M&E assemblies, represented by the V-i profiles presented in Figure 2, are summarized in Table 1.

The values for V_0, which correspond to the cell potential at a current density of 1 mA cm^{-2}, are similar for the three M&E assemblies. The values for the Tafel slope, b, are close to those reported by other investigators [26]. The interesting result from the table is given by the values for R_i, which decrease in an expected manner on taking into account the physico-chemical characteristics of the Nafion® and Dow membrane materials [23,27]. Based on these values of R_i, the exceptionally good performance obtained from the M&E assembly containing the Dow membrane can be readily understood in terms of low ohmic overpotentials.

The value of 0.075 Ω cm^2 for the M&E assembly containing the Dow membrane consists of the resistance across the membrane itself and contact resistances between other components in the test fuel cell fixture. In the absence of a Dow PEM, the contact resistances for the identical fuel cell fixture, and similar electrodes were measured at 95°C and yielded a value of 0.032 Ω cm^2. Thus, the resistance across the PEM itself was 0.043 Ω cm^2. On taking the reported value for the specific resistance of the Dow PEM, 8 Ω cm [23] and the actual measured thickness (45 μm) of the Dow PEM in the hot-pressed M&E assembly yields a membrane resistance of 0.036 Ω cm^2. Thus, using the developed proprietary hot-pressing procedure for the preparation of M&E assemblies, ohmic losses across M&E assemblies approach their theoretically limiting values.

V-i profiles for an M&E assembly (Dow PEM and unsupported, high platinum loading electrodes—5 mg Pt per cm^2), fabricated using the proprietary hot pressing procedure and tested using a fuel cell temperature of 95°C and H_2/O_2 gas pressures of 30 psi/40 psi, 60 psi/70 psi and 160 psi/160 psi, are presented in Figure 3. As expected, increasing gas pressures gave rise to better fuel cell performance due to the effect of pressure on electrochemical reaction rates.

Variations of power density with cell potential and with current density for this M&E assembly tested at a fuel cell temperature of 95°C with H_2/O_2 gas pressures of 160 psi/160 psi, using both humidified and dry oxygen gas are presented in Figure 4(a) and 4(b), respectively. It can be seen from the figure that the fuel cell performed surprisingly well on dry oxygen gas and may be able to function satisfactorily in this manner, at least for short periods of time, e.g., under

pulse power conditions. More importantly, it is apparent from the data presented in Figure 4 that extremely high power densities of the order of 2.5 W cm^{-2} were obtained at a cell potential of 0.48 V and a current density of 5.1 A cm^{-2}.

Impact Of Electrode Structure On The Performance Of M&E Assemblies

To maximize electrocatalyst utilization in PEM fuel cells, previous researchers [26,28] impregnated catalyzed electrode structures with solubilized Nafion® PEM material. This treatment was found to enhance the three-dimensional nature of the active catalyzed layers of fuel cell electrodes and was observed to give rise to a reduction in activation and mass transport overpotentials [13,25,26]. Because of the improved fuel cell performance obtained on using the Dow experimental PEM as the solid electrolyte film, it was decided to investigate if further improvements in fuel cell performance could be obtained if solubilized Dow membrane solution was impregnated into the catalyzed electrode layers instead of the Nafion® solution. Thus, M&E assemblies were fabricated using the Dow experimental PEM as electrolyte and unsupported, high platinum loading electrodes (5 mg Pt per cm^{-2}). However, for one M&E assembly, the electrodes were impregnated with the commercially available Nafion® solution, while the second M&E assembly was constructed using identical electrodes but impregnated with in-house-prepared Dow membrane solution [29,30].

V-i profiles for the two similar M&E assemblies tested using a fuel cell temperature of 95°C and H_2/O_2 gas pressures of 100 psi/100 psi are presented in Figure 5. It can be seen from the figure that the Nafion®-impregnated electrodes gave better performance than the corresponding Dow-impregnated electrodes. This was also observed from data derived from other similar M&E assemblies. This unexpected result may be due to the fact that the lower equivalent weight of the Dow experimental membrane with its associated higher sulfonic acid group content, giving rise to increased water retention in the membrane, brings about flooding within the electrode structures, which impedes the access of reactant gases to platinum catalyst sites. However, the higher – CF_2 – content of Nafion® compared to the Dow PEM (cf., Fig.1) facilitates a greater solubility of dissolved oxygen in the Nafion® impregnated PEM electrolyte material [31]. The higher localized concentration of dissolved oxygen at platinum particle/PEM electrolyte interfaces within electrode structures can support higher oxygen reduction reaction rates accounting for the trend observed. Hence, while the characteristics of the Dow PEM are most suitable when it is used as the proton exchange membrane itself, they may not be as appropriate as Nafion® for impregnation within electrode structures. Thus, it seems that the best combination for an optimized M&E assembly is the use of the Dow experimental PEM as the electrolyte layer and dissolved Nafion® as the electrolyte material to be used for impregnating catalyzed electrodes, so as to increase the three-dimensional character of fuel cell electrodes.

On operating PEM fuel cells at high power densities, most of the electrochemical reactions, giving rise to high cell currents, will occur near the front surface of the catalyzed electrodes. A simple analysis of electrode pore models shows that high IR drops within the length of pores dictates that most of the current is localized in the outer catalyzed layers of electrodes. Hence, to achieve high power densities, it is advantageous to localize a large fraction of the electrocatalyst material in the outer layers of fuel cell electrodes. Therefore, platinum electrocatalyst loading would be expected to have a significant effect on the performance of PEM fuel cells.

To investigate the effect of platinum electrocatalyst loading on PEM fuel cell performance, a number of M&E assemblies were fabricated using the Dow experimental PEM and Nafion®-

impregnated, unsupported platinum electrodes with loadings of 1, 2.5, 5 or 10 mg Pt per cm^2. V-i profiles for the resulting assemblies, tested using a fuel cell temperature of 95°C and H_2/O_2 gas pressures of 100 psi/100 psi, are presented in Figure 6. Fuel cell performance was observed to increase with increasing platinum catalyst loading, reaching a maximum at a loading of 5 mg Pt per cm^2. This can be more clearly seen in the variation of power density with cell potential and with current density, shown in Figure 7, for these assemblies. The dependence of maximum power density on platinum catalyst loading was in the order:

$$5 \text{ mg cm}^{-2} > 10 \text{ mg cm}^{-2} > 2.5 \text{ mg cm}^{-2} > 1 \text{ mg cm}^{-2}.$$

Relatively thick platinum-catalyzed active layers, as found in electrodes having a Pt loading of 10 mg per cm^2, may impede the access of dissolved PEM material into the electrode structures or introduce mass transport overpotentials, which hinder high fuel cell performance. The behavior of the M&E assembly with the highest Pt loading electrodes at high current densities [cf., Fig. 6] supports these conclusions.

In the case of unsupported, high surface area platinum black catalyzed electrodes, active layer thicknesses corresponding to a platinum loading of 5 mg per cm^2 are optimum for PEM fuel cells yielding the highest performance. For aerospace applications where high performance and reliability are of the highest priority, the cost associated with the platinum, approximately $200 per kW at a current density of 1A cm^{-2} [19], can be justified. However, for terrestrial applications, e.g., fuel cell power sources for electric vehicles, this cost figure is too high and carbon-supported, low platinum loading electrodes will have to be used.

Scanning Electron Microscopy And Energy Dispersive Spectroscopy Of M&E Assemblies

Scanning electron micrographs (SEM's) at various magnifications of the cross-section of an M&E assembly, fabricated using Nafion®-impregnated, unsupported, high platinum loading electrodes (5 mg Pt per cm^2) and the Dow experimental proton exchange membrane (XUS–13204.10) are presented in Figure 8. The fibers in the weaves of the carbon cloth backing can be readily seen in Figure 8(a). The bonding between the membrane and the electrocatalyst layers appears to be excellent, and no degradation was observed after completing a short-duration lifetime test (240 hours). The cross-section of the M&E assembly, shown in the SEM given in Figure 8(b), is centered on the interface between the proton exchange membrane and the catalyzed layers of one electrode. Some of the locations along the cross-section, where energy dispersive spectroscopy (EDS) elemental analyses were performed, are numbered on the micrograph. Exposure of the electron beam spot on the proton exchange membrane during EDS data collection brought about decomposition of the PEM polymer material [cf., Fig. 8(b)].

The three key layers of the M&E assembly, namely, the gas diffusion layer, the active platinum-catalyzed layer and the PEM electrolyte film, were analyzed using EDS. Representative energy dispersive spectrographs for each of these layers are presented in Figure 9. The gas diffusion layer [cf., Fig. 9(a)] shows high-intensity elemental carbon and fluorine signals, arising from the Teflon-bonded, high surface area carbon powder material used in fabricating this layer. The weak elemental platinum signal observed is probably due to carryover of platinum particles from the active layer on slicing the M&E assembly. The spectrograph for the active platinum electrocatalyst layer [cf., Fig. 9(b)] is dominated by a high-intensity elemental platinum signal, as expected. Also, in this figure, weak signals from carbon and fluorine (associated with Teflon bonding of the platinum electrocatalyst particles) and sulphur are to be noted; the latter is probably

associated with Nafion® impregnated into the active platinum-catalyzed layer. In the spectrograph derived from the PEM electrolyte film [cf., Fig. 9(c)], high-intensity signals were obtained, corresponding to carbon, fluorine and sulphur. This is in agreement with a proton exchange membrane consisting of a perfluorosulfonic acid polymer material. No elemental platinum dissolved into the membrane during fuel cell operation, as evidenced by the lack of a platinum signal.

Elemental peak height ratios as a function of distance across the cross-section of the M&E assembly, shown in the electron micrograph presented in Figure 8(b), are given in Figure 10. The profile derived from the Pt/C elemental peak height ratios shows that the thickness of the platinum-catalyzed active layer is approximately 15–20 μm. Examination of the profiles associated with S/C and F/C elemental peak height ratios, given in Figure 10, demonstrate that the impregnated Nafion® does not penetrate the entire thickness of the unsupported platinum-catalyzed active layer. A rough estimate of the Nafion® penetration depth is of the order of 50–70% of the thickness of the platinum-catalyzed active layer. This depth of penetration of solubilized Nafion® into the platinum-catalyzed active layer is likely to be sufficient for PEM fuel cell operation at high power densities (cf., Figs. 3 and 4). However, for high energy conversion efficiencies at lower current densities, new methods which facilitate greater penetration of solubilized Nafion® into active catalyzed layers need to be developed.

Electrocatalyst Utilizations And Roughness Factors For Unsupported, High Platinum Loading Fuel Cell Electrodes

The charge associated with the formation of a hydrogen monolayer or the removal of a monolayer of oxide film, measured using the cyclic voltammetric technique, was used to estimate the degree of platinum utilization and the roughness factor of unsupported, high platinum loading (5 mg Pt per cm^2) fuel cell electrodes. Cyclic voltammetric profiles recorded for Nafion®-impregnated, unsupported platinum black electrodes in test fuel cell fixtures are given in Figure 11. The voltammetric profiles are similar to those obtained for smooth platinum in aqueous acid solutions [32]. The poorly resolved hydrogen adsorption and desorption regions, the double layer region and the oxide film formation and reduction regions are easily discernible. From the voltammetric charge associated with either the monolayer oxide film reduction peak or the adsorbed hydrogen monolayer region, information can be derived concerning the electrochemically active surface area and the degree of platinum electrocatalyst utilization under typical fuel cell operating conditions. The relevant data is presented in Table 2.

It can be seen from the table that satisfactory agreement between the adsorbed hydrogen monolayer charge and the oxide film reduction charge was obtained. From the known platinum catalyst loading (5 mg Pt per cm^2) and assuming spherical platinum particles, 85 Å in diameter, a maximum electrochemically active surface area was estimated. For the unsupported, high platinum loading, oxygen electrode, comparison of the calculated and experimentally determined electrochemically active areas or adsorbed hydrogen charges indicate that the degree of platinum utilization was only 16.6% and that the roughness factor for this electrode was 274. Clearly, either some of the surface of the platinum particles are not in contact with the Nafion®-impregnated electrolyte material or not all of the surface is electrochemically active. The non-electrochemical EDS technique tends to overestimate the thickness of the platinum-catalyzed layer taking part in electrochemical reactions. Further investigations are necessary to resolve this issue.

CONCLUSIONS

1. To obtain high power densities in PEM fuel cells, activation, ohmic and mass transport overpotentials were minimized by the use of optimized M&E assemblies.

2. The Dow experimental PEM (XUS–13204.10) gave much superior performance than Nafion PEM materials, which are manufactured by Du Pont.

3. Extremely high power densities of the order of 2.5 W cm^{-2} were obtained at a cell potential of 0.48 V and a current density of 5.1 A cm^{-2} on using the Dow PEM and unsupported, high platinum loading electrodes (5 mg Pt per cm^2).

4. Electrode structure factors, e.g., nature of the three-dimensional active catalyzed layer, electrocatalyst loading, etc., had a significant effect on PEM fuel cell performance, that is, in obtaining high power densities.

5. Elevated reactant gas pressures and fuel cell temperatures considerably enhanced fuel cell performance.

6. There was no evidence of deterioration or degradation in any of the tested M&E assemblies or other fuel cell components after completing fuel cell performance evaluations.

ACKNOWLEDGMENT

Proton exchange membrane fuel cell research and development work performed at Lynntech, Inc. is supported by the U.S. Air Force (Contract No.: FO4611-90-C-0095) and by the U.S. Navy (Contract No.: N00024-91-C-4067). This support is gratefully acknowledged.

REFERENCES

1. M. Warshay and P. Prokopius, J. Power Sources, 29 (1990) 193.

2. R. A. Lemons, J. Power Sources, 29 (1990) 251.

3. W. H. Kumm, J. Power Sources, 29 (1990) 169.

4. J. O'M. Bockris and S. Srinivasan, "Fuel Cells: Their Electrochemistry," McGraw-Hill, New York (1969).

5. S. S. Penner, Energy: The International Journal, 11 (1986) 1-229.

6. A. J. Appleby and F. R. Foulkes, "Fuel Cell Handbook," Van Nostrand Reinhold, New York (1989).

7. J. J. Hirschenhofer, Mech. Eng., Sept. 1992, p. 82.

8. G. Halpert and A. Attia, in: "Proc. 24th IECEC," ed., W. D. Jackson, IEEE, 345 East 47th Street, New York, NY 10017, Vol. 3, p. 1429 (1989).

9. H. S. Lim and S. A. Verzwyvelt, J. Power Sources, 22 (1988) 213.

10. A. J. Appleby, J. Power sources, 22 (1988) 377.

11. K. Prater, J. Power Sources, 29 (1990) 239.

12. S. Srinivasan, J. Electrochem. Soc., 136 (1989) 41C.

13. S. Srinivasan, O. A. Velev, A. Parthasarathy, D. J. Manko and A. J. Appleby, J. Power Sources, 36 (1991) 299.

14. D. S. Watkins, K. W. Dircks and D. G. Epp, U.S. Patent 4,988,583, Jan. 29, 1991.

15. M. S. Wilson and S. Gottesfeld, J. Electrochem. Soc., 139 (1992) L28.

16. A. P. Meyer, in: "Proc. 24th IECEC," ed., W. D. Jackson, IEEE, 345 East 47th Street, New York, NY 10017, Vol. 3, p. 1619 (1989).

17. K. Straber, Ber. Bunsenges. Phys. Chem., 94 (1990) 1000.

18. M. S. Wilson and S. Gottesfeld, J. Appl. Electrochem., 22 (1992) 1.

19. E. J. Taylor, E. B. Anderson and N. R. K. Vilambi, J. Electrochem. Soc., 139 (1992) L45.

20. S. M. Misiaszek, "Low Pressure Air Breathing Fuel Cell Stack Development," Paper on Fuel Cell Developments at Energy Partners, West Palm Beach, FL 33407, Dec. 1992.

21. A. Eisenberg and H. L. Yeager, eds., "Perfluorinated Ionomer Membranes," ACS Symp. Series, No. 180 (1982).

22. U.S. Patent No. 4,417,969 (1983), assigned to Dow Chemical Company.

23. G. A. Eisman, Extended Abstract, "Int. Seminar on Fuel Cell Technology and Applications," Netherlands, Oct. 26-29, 1987, p. 287.

24. M. Ratcliff, F. L. Posey, D. K. Johnson and H. L. Chum, J. Electrochem. Soc., 132 (1985) 577.

25. S. Srinivasan, E. A. Ticianelli, C. R. Derouin and A. Redondo, J. Power Sources, 22 (1988) 359.

26. E. A. Ticianelli, C. R. Derouin and S. Srinivasan, J. Electroanal. Chem., 251 (1988) 275.

27. R. S. Yeo and H. L. Yeager, in: "Modern Aspects of Electrochemistry," eds., B. E. Conway, R. E. White, and J. O'M. Bockris, Plenum Press, New York (1985), Vol. 16, pp. 437-504.

28. I. D. Raistrick, U.S. Patent 4,876,115 (Oct. 1989).

29. M. N. Szentirmay, L. F. Campbell and C. R. Martin, Anal. Chem., 58 (1986) 661.

30. R. B. Moore and C. R. Martin, Anal. Chem., 58 (1986) 2569.

31. S. Srinivasan, Personal communication, March 1993.

32. L. D. Burke and M. B. C. Roche, J. Electroanal. Chem., 164 (1984) 315.

TABLE 1. VALUES OF V_0, b AND R_i FOR M&E ASSEMBLIES CONTAINING EITHER NAFION® 117, NAFION® 115 OR THE DOW MEMBRANE (XUS–13204.10) AS POLYMER ELECTROLYTE

Polymer Electrolyte	Reactants	Reactant Pressures (psi)	Fuel Cell Temp. (°C)	V_0 (V)	b (V decade^{-1})	R_i (Ω cm^2)
Nafion 117	H_2/O_2	30/40	95	1.012	0.052	0.208
Nafion 115	H_2/O_2	30/40	95	0.995	0.044	0.176
Dow Membrane	H_2/O_2	30/40	95	1.013	0.053	0.075

TABLE 2. ROUGHNESS FACTOR AND DEGREE OF PLATINUM UTILIZATION FOR NAFION-IMPREGNATED UNSUPPORTED HIGH SURFACE AREA PLATINUM BLACK-BASED FUEL CELL ELECTRODE

	NAFION-IMPREGNATED ELECTRODE*
Experimentally determined adsorbed hydrogen charge, $Q_{H,exptl.}$	288 mC
Experimentally determined oxide film reduction charge, $Q_{O,exptl.}$	566 mC
Experimentally determined electrochemically active surface area, E_{SA}, from $Q_{H,exptl.}$ (assuming 210 μC cm^{-2})	1,371 cm^2
Calculated real surface area (assuming 85 Angstroms diameter Pt particles)	8,250 cm^2
Geometric surface area, G_{SA}	5 cm^2
Surface roughness factor [ratio of experimentally determined electrochemically active surface area (E_{SA}) to geometric surface area (G_{SA})]	274
Calculated adsorbed hydrogen charge, $Q_{H,calc.}$ (assuming 85 Angstroms diameter Pt particles)	1,733 mC
Degree of electrocatalyst utilization, $Q_{H,exptl.}/Q_{H,calc.}$	16.6%

*Unsupported high surface area platinum black-based electrode with a platinum loading of 5 mg per cm^2.

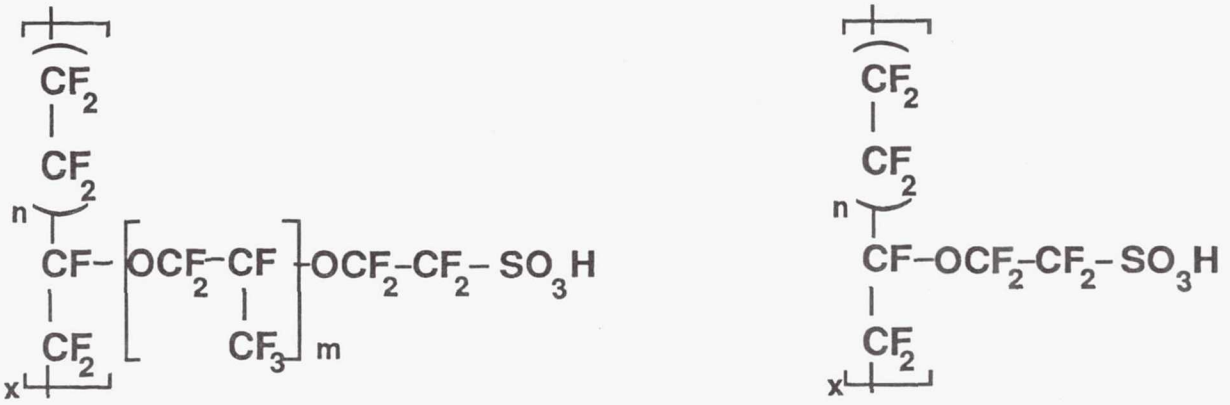

Structure of Du Pont's Nafion
n=6.6 and m =1

Structure of Dow Experimental
Membrane n = 3.6-10

FIGURE 1. Structural formula for proton exchange membranes.

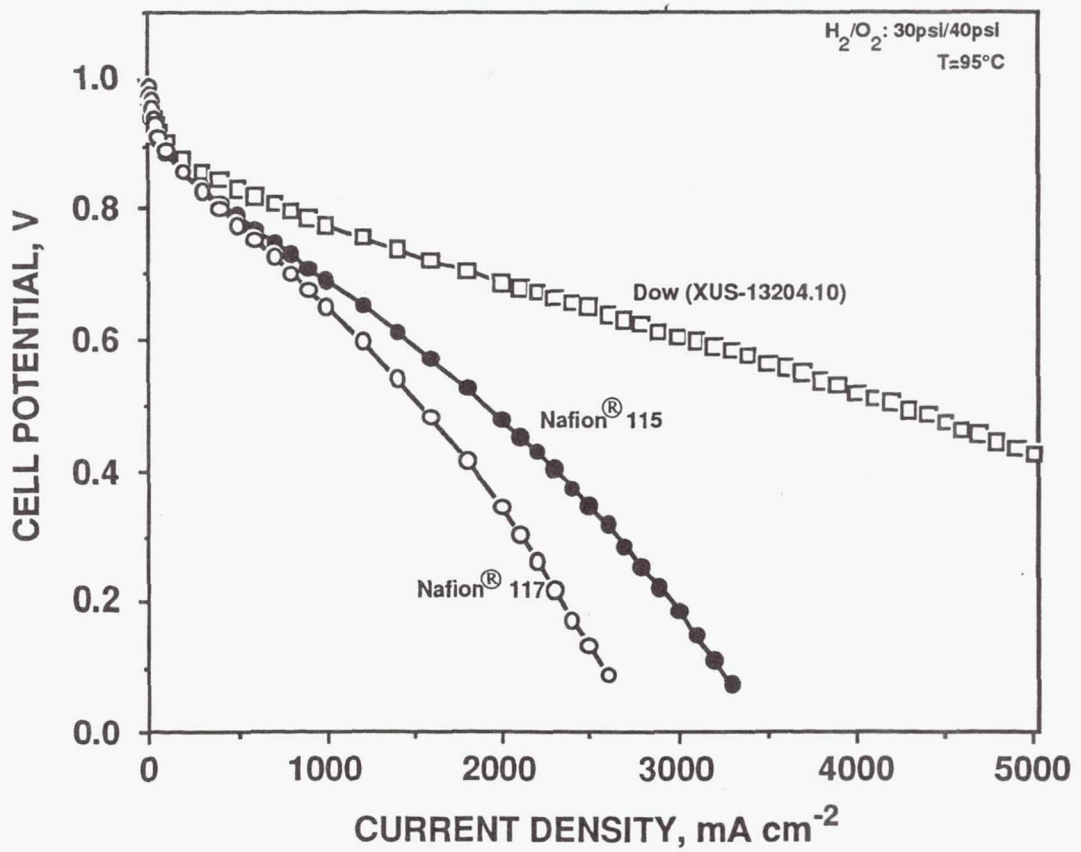

FIGURE 2. Fuel cell potential-current density profiles for M&E assemblies containing Nafion® 117, Nafion® 115 and the Dow PEM.

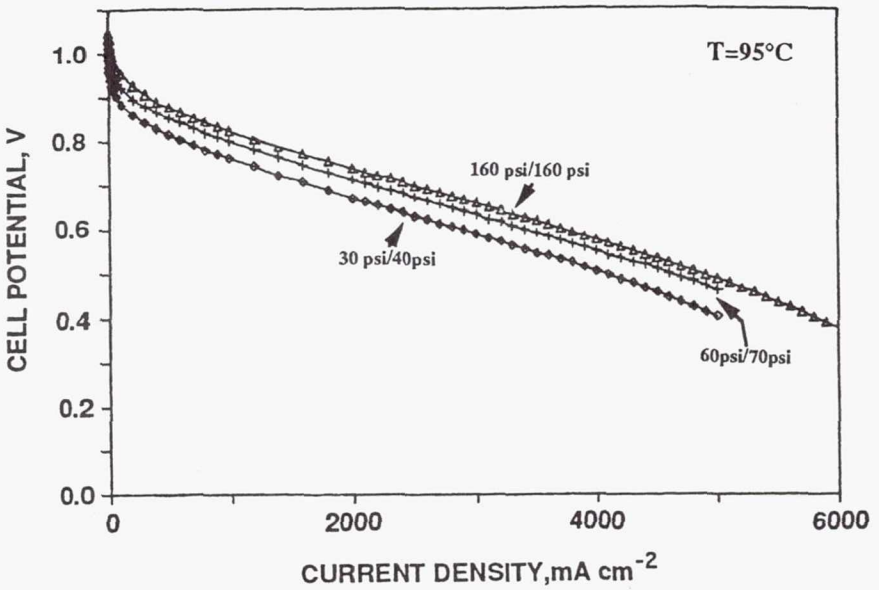

FIGURE 3. Fuel cell potential current density profiles for a Dow PEM-based M&E assembly tested at various H_2/O_2 gas pressures.

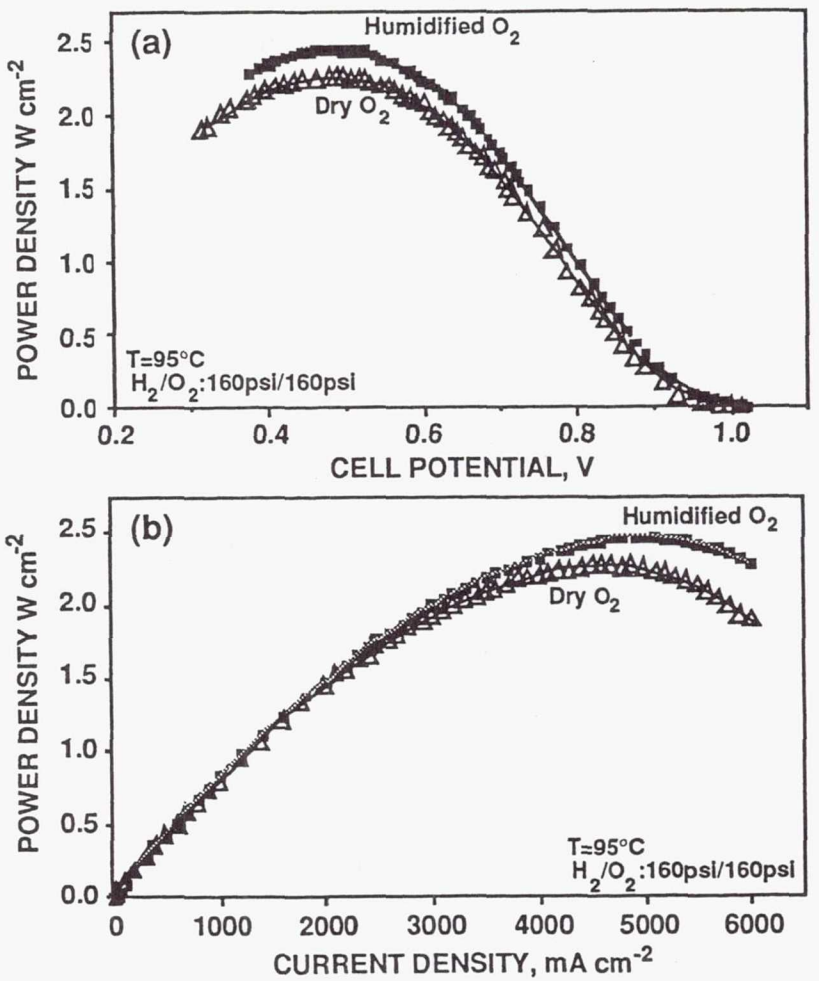

FIGURE 4. Variation of power density: (a) with cell potential and (b) with current density for a PEM fuel cell supplied with humidified H_2 gas and humidified or dry O_2 gas.

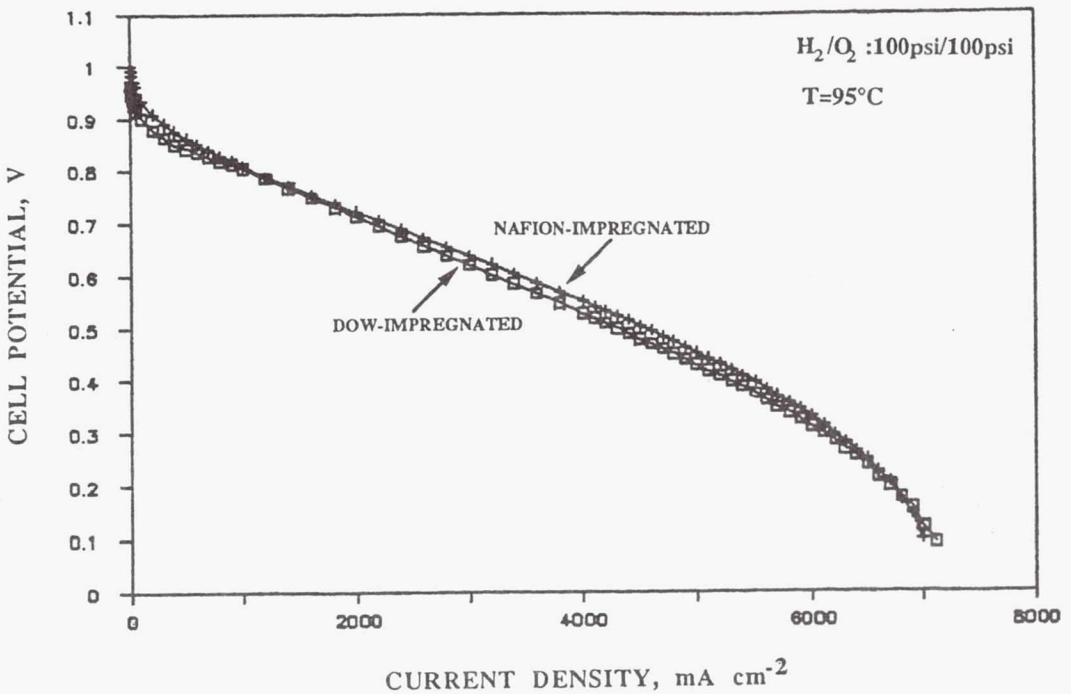

FIGURE 5. Fuel cell potential-current density profiles for M&E assemblies containing Nafion-impregnated or Dow-impregnated high platinum loading electrodes.

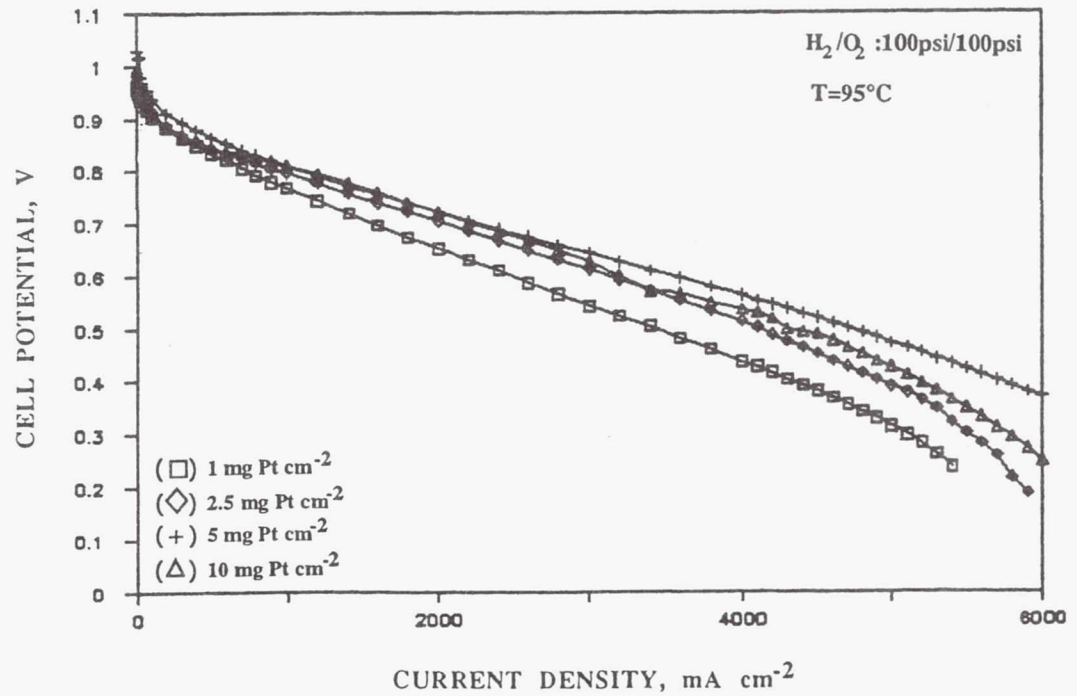

FIGURE 6. Fuel cell potential-current density profiles for M&E assemblies containing high platinum loading electrodes.

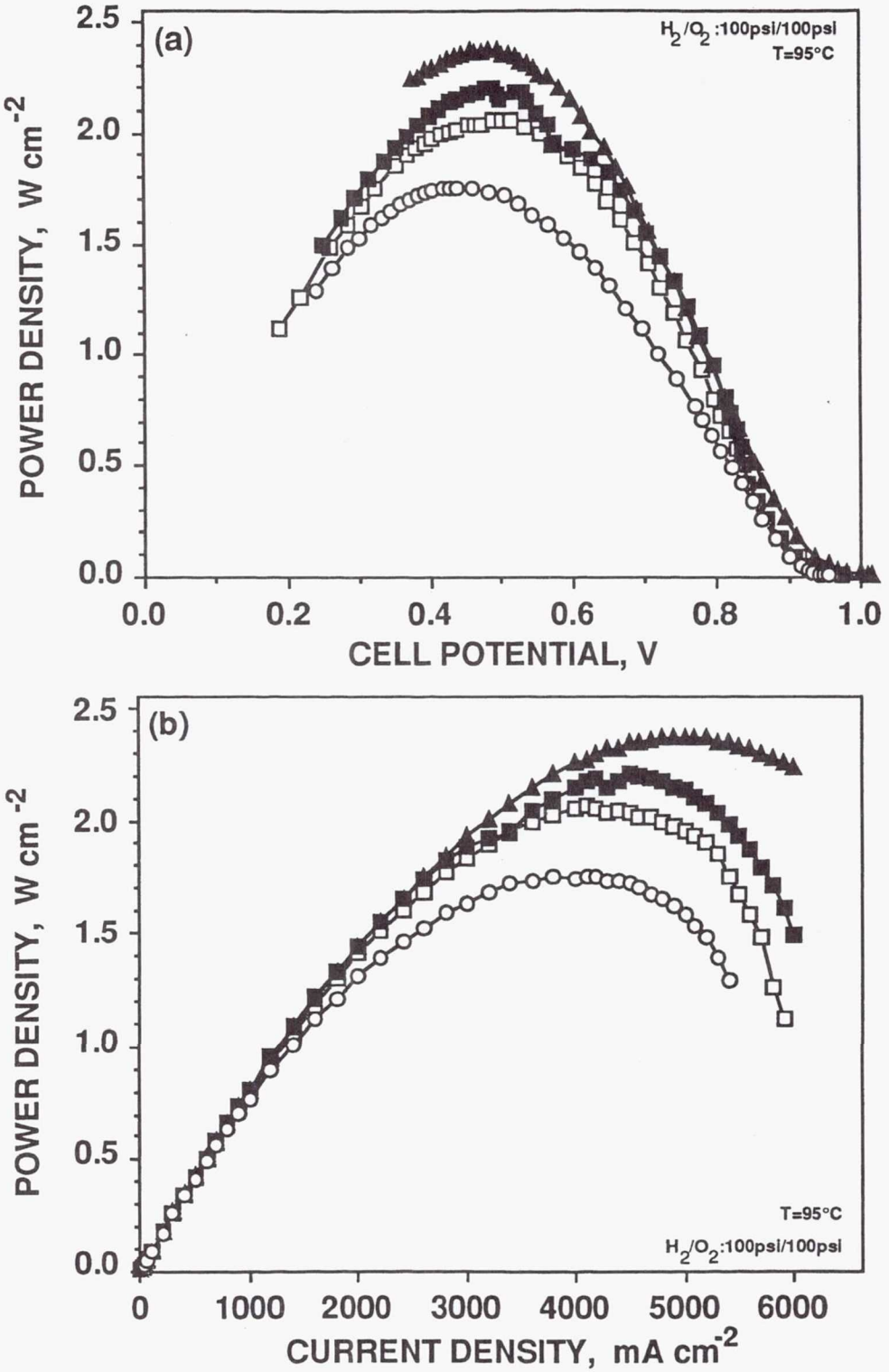

FIGURE 7. Variation of power density: (a) with cell potential and (b) with current density for a PEM fuel cell supplied with humidified H_2 and O_2 gases. M&E assemblies consisted of the Dow experimental membrane and unsupported high platinum loading electrodes:(○)1 mg Pt cm^{-2} ;(□) 2.5 mg Pt cm^{-2};(▲) 5 mg Pt cm^{-2}; and, (■)10 mg Pt cm^{-2}.

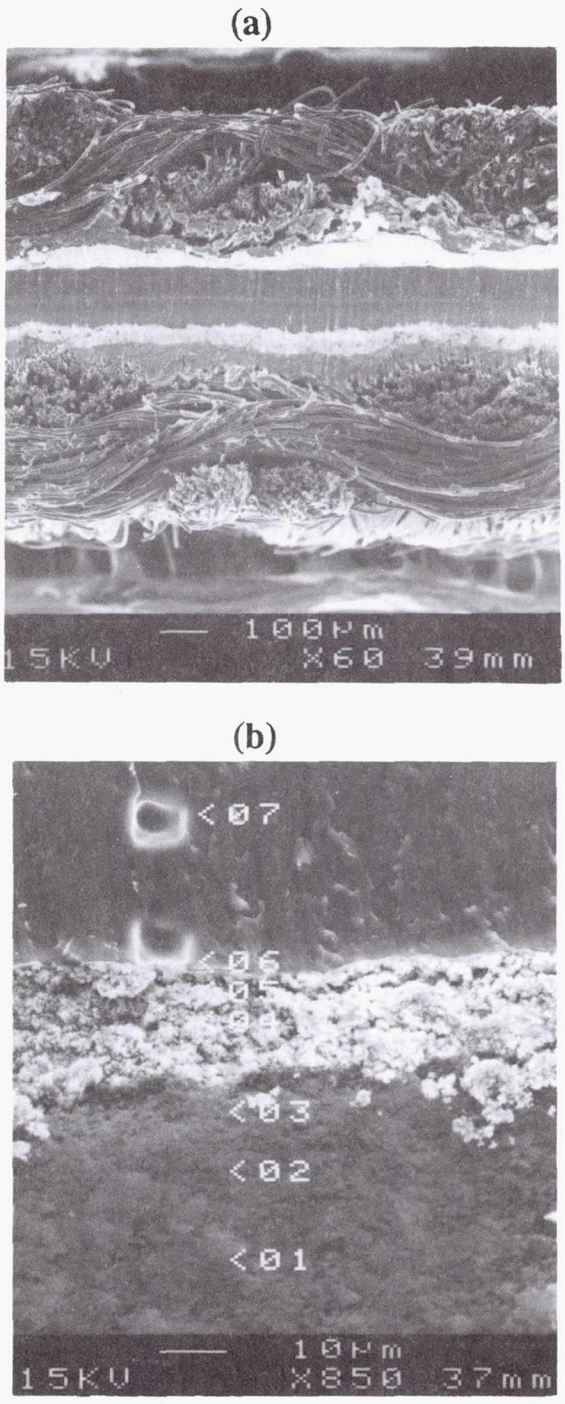

FIGURE 8. Scanning electron micrographs of the cross-section of an M&E assembly fabricated using Nafion-impregnated unsupported high platinum loading electrodes and Dow experimental PEM.

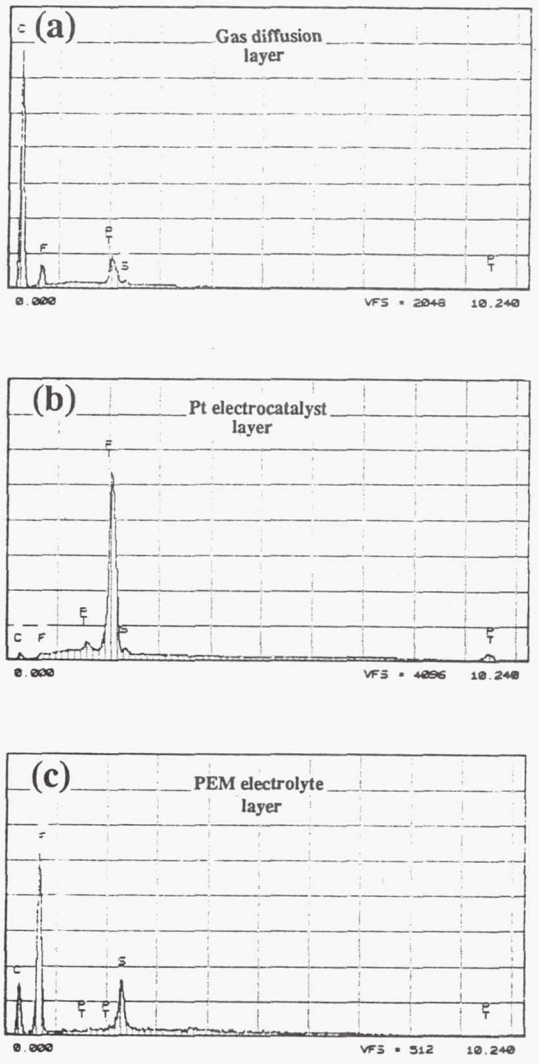

FIGURE 9. Energy dispersive spectrographs taken at three different locations along the cross-section of an M&E assembly fabricated using unsupported high platinum loading electrodes and Dow experimental membranes.

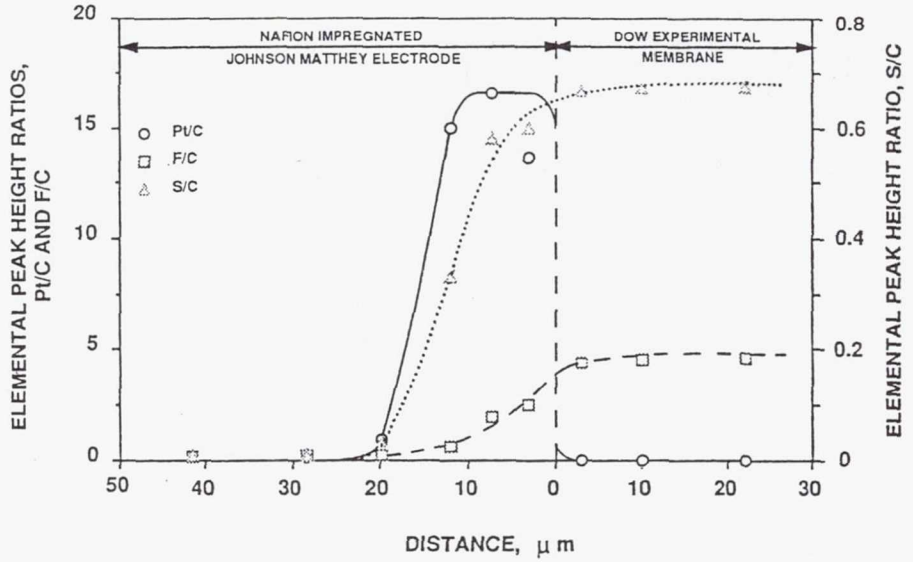

FIGURE 10. Elemental peak height ratios as a function of distance along the cross-section of an M&E assembly fabricated using unsupported high platinum loading electrodes and Dow experimental PEM.

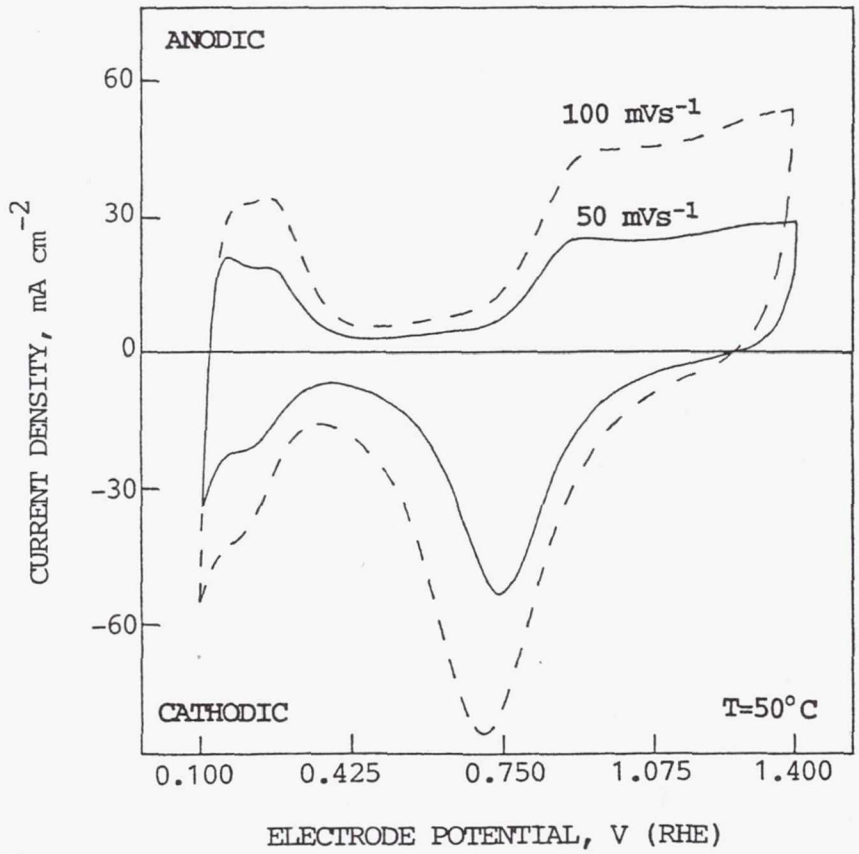

FIGURE 11. Cyclic voltammograms for an M&E assembly fabricated using Nafion-impregnated unsupported high platinum loading electrodes (5 mg Pt per cm^2) and Nafion 117 PEM.

THE ELECTROLYTE CHALLENGE FOR A DIRECT METHANOL-AIR POLYMER ELECTROLYTE FUEL CELL OPERATING AT TEMPERATURES UP TO 200 °C

Robert Savinell, Ernest Yeager, Donald Tryk, Uziel Landau, Jesse Wainright
Dominic Gervasio, Boris Cahan, Morton Litt, Charles Rogers and Daniel Scherson
Case Center for Electrochemical Sciences
Case Western Reserve University
Cleveland, OH 44106

ABSTRACT

Novel polymer electrolytes are being evaluated for use in a direct methanol-air fuel cell operating at temperatures in excess of 100 °C. The evaluation includes tests of thermal stability, ionic conductivity and vapor transport characteristics. The preliminary results obtained to date indicate that a high temperature polymer electrolyte fuel cell is feasible. For example, Nafion 117 when equilibrated with phosphoric acid has a conductivity of at least 0.4 $\Omega^{-1}cm^{-1}$ at temperatures up to 200 °C in the presence of 400 torr of water vapor and methanol vapor cross over equivalent to 1 mA/cm^2 under a one atmosphere methanol pressure differential at 135 °C. Novel polymers are also showing similar encouraging results. The flexibility to modify and optimize the properties by custom synthesis of these novel polymers presents an exciting opportunity to develop an efficient and compact methanol fuel cell.

INTRODUCTION

The direct methanol-air fuel cell is a very promising system for a wide spectrum of applications where high efficiency and light weight are required. Methanol is attractive for fuel cell use for a number of reasons; it is more convenient to store and handle than hydrogen or ammonia, and it offers a relatively high energy density. The direct methanol fuel cell is favored over the indirect (reformed methanol) system since the direct oxidation of methanol offers the promise of greater efficiency and simplicity with lower weight and lower cost resulting from the elimination of the fuel reformer. Present direct methanol-air fuel cell configurations are severely limited by the lack of sufficiently active catalysts for the methanol anode, and to a lesser extent, the oxygen cathode. In addition, current methanol-air fuel cells are hindered by the cross-over of methanol from the anode to the cathode, which results in a loss of efficiency via chemical reaction of the fuel with oxygen and depolarization of the cathode.

The use of solid polymer electrolytes offers new opportunities to overcome the catalyst stability and activity problems, provided the polymers are stable and retain reasonable ionic conductivity at temperatures approaching 200 °C. The use of a polymer electrolyte membrane (PEM) at 200 °C should allow for the identification of effective catalysts which lack sufficient activity at the lower temperatures typical of conventional PEM fuel cells or that are significantly deactivated by the adsorption of phosphate in high temperature phosphoric acid fuel cells. The higher temperatures will increase the catalytic activity substantially, while depressing the self-poisoning effects associated with strongly adsorbed intermediates. The polymer should have other properties such as high oxygen solubility and low electrolyte adsorption which will promote better electrode performance. In addition, the use of a polymer electrolyte as opposed to a liquid electrolyte should result in extended fuel cell life due to the elimination of electrolyte movement within the electrodes, i.e. electrode flooding. A DARPA sponsored project is in progress at CWRU with the objective of developing highly efficient methanol-air polymer electrolyte fuel cells. This research is focused on 1) developing new ion-conducting polymers capable of operation at 200 °C, 2) more active and stable electrocatalysts for methanol oxidation, 3) high performance electrocatalysts for oxygen reduction that are tolerant of methanol and its oxidation products, 4) optimized electrode structures and 5) new high area electrocatalyst supports with greater oxidative stability than the traditional carbon.

This paper will focus on recent results obtained with several promising solid polymer electrolytes. In particular, the electrolytes are being evaluated with respect to three criteria; 1) thermal stability, 2) proton conductivity, and 3) transport of methanol, oxygen, water and carbon dioxide. These evaluations are being carried out under temperatures and environments (humidity level, oxidizing or reducing conditions) that are indicative of the anode and cathode conditions in an operating fuel cell.

RATIONALE OF APPROACH

The present commercially available sulfonic acid ionomers (e.g. Nafion 117, Dow 560, see Figure 1) depend on water to solvate the protons generated by the ionization of the sulfonic acid groups. When the polymers are subjected to temperatures above 100 ^{o}C at one atmosphere pressure, water is lost, including the water solvating the hydronium ions. The membrane shrinks and conductivity is lost. The use of a pressurized system can extend the useful temperature range, but at the expense of overall system efficiency. For an operating temperature of 200 ^{o}C, the pressure required is too high to be practical. It has been shown that the ionization of trifluoro methane sulfonic acid (CF_3SO_3H) can be produced by the addition of phosphoric acid to yield $P(OH)_4^+$ and $CF_3SO_3^-$ [1]. A similar effect occurs with the equilibration of sulfonic acid ionomers in concentrated phosphoric acid. The phosphoric acid acts as a Bronsted base, ionizing the strong sulfonic acid groups and solvating the proton in the same manner as water. However, due to the relatively low vapor pressure/high boiling point of phosphoric acid, it would not be expected that ionization and solvation would be lost at temperature above 100 ^{o}C. The use of phosphoric acid has the disadvantage that H_3PO_4 or its dissociation products are strongly adsorbed on Pt based catalysts, resulting in a loss of catalytic efficiency.

The equilibration of Nafion with phosphoric acid is one example of the focus of the polymer synthesis effort within the DARPA direct methanol fuel cell project. The goal of the synthesis effort is to produce a polymer that is stable at high temperatures, with a superacid functionality for conductivity and enhanced catalytic activity, also containing an immobilized Bronsted base. One possibility is that the immobilization of the base could be accomplished by bonding the base onto the polymer backbone. It may also be possible to synthesize a polymer in which water is strongly hydrogen bonded, which would reduce the activity of the water and allow water to be retained at temperatures above 100 ^{o}C.

Researchers at Clemson University are currently developing perfluorosulfonimide polymers analogous to Nafion. Examples of some of the polymers currently under study are given in Figure 1a,b. One of the advantages of the sulfonimide functionality is that much greater flexibility in the design of the polymer is possible. For example, the side chain length can be varied and one or more functional groups can be included in the side chain. In this manner a wide range of ion exchange capacities can be obtained, and the domain structure of the polymer can be varied to provide optimized conductivity and vapor barrier properties. In addition, preliminary samples of these materials have been shown to be soluble in dimethylformamide (DMF) and are readily cast into films. This behavior is in distinct contrast to Nafion, which is only solublized with considerable effort.

Researchers at University of Iowa are currently developing perfluorophosphonic acid polymers as shown in Figure 1c. It is expected that these polymers will have excellent thermal stability, will be melt formable and will have good conductivity resulting from the two ionizable protons on each side chain. In addition, it is expected that this material will strongly hydrogen bond to water to provide high temperature conductivity without the need for a low vapor pressure solvent such as phosphoric acid. Since the functional groups are part of the polymer chain, they should be sufficiently sterically hindered to prevent adsorption onto active catalyst sites. In addition, it may be possible to make co- or ter- polymers of these materials with the perfluorosulfonimide polymers described above.

A third synthesis effort is underway at CWRU to produce films of polybenzimidazole (PBI) which have been doped with a strong acid such as sulfuric acid and then reacted at high temperature to produce a polymer with the acid anion bound to the phenyl ring on the polybenzimidazole. The protons are ionized by the basic nitrogen atoms in the benzimidazole rings as shown in Figure 1d. Polybenzimidazoles are known to have excellent oxidative and thermal stability, and should be further stabilized by the reaction with acid. Proton hopping between basic sites should provide ionic conductivity

and the barrier properties of these films should be better than that of Nafion since the benzimidazoles will be a single phase material, unlike the nonpolar fluorocarbon/polar ionic biphasic nature of Nafion.

EXPERIMENTAL

Preparation of Polymer Electrolytes

Nafion 117 (acid form) membranes were obtained from duPont and hydrated by immersion in boiling water for four hours. Following hydration, the samples were either left in distilled water until use or were equilibrated with phosphoric acid. The phosphoric acid equilibration consisted of immersion in 85% H_3PO_4 at 150 ^oC for 12 hours. Following equilibration the samples were left in phosphoric acid until use.

Polybenzimidazole was purchased from Celanese. Films were cast from a solution of the polymer in dimethylacetamide using a Gardner knife. The films were then doped by immersion in 8M sulfuric acid for 16 hours.

The perfluorosulfonimide membranes were prepared by Dr. D. DesMarteau and co-workers at Clemson University. The details of the polymer synthesis have been given elsewhere [2]. These membranes were hydrated and equilibrated with phosphoric acid using the same procedure as was used for the Nafion 117 samples. The results discussed below are for the difunctional polymer (acid form) shown in Figure 1b. The ion exchange capacity of this material was 0.66 mg H/g.

Four Probe Conductivity Measurements

The conductivity measurements were made with a four probe apparatus constructed at CWRU. In this apparatus two Pt foil electrodes are clamped to the ends of a 3 cm (L) x 0.5 cm(W) sample. These electrodes are used to pass current through the sample. The magnitude and frequency of the applied current were controlled using a PAR 173 potentiostat/galvanostat and a Wavetek 186 signal generator. Two platinum wires (0.5 mm dia.) spaced 1 cm apart, were used to measure the voltage drop in the center of the sample. Voltage measurements were made at three or more current levels to ensure that the (i,v) behavior was ohmic. The current was applied at two different frequencies, 100 and 1000 Hz. No frequency dependence was observed. The entire apparatus was contained within a sealed stainless steel vessel, which was placed inside an oven and connected to a gas manifold system so that the temperature, pressure and composition of the gas phase in contact with the sample could be controlled. Measurements as a function of water partial pressure above 100 ^oC were performed by partially evacuating the cell and then injecting sufficient liquid water via a septum to yield the desired water partial pressure.

Vapor Permeability Measurements

The vapor permeability measurements were made using a technique based on ASTM D-1434. In this experiment the membrane separates two thermostated chambers. In one chamber (the retentate) a constant partial pressure (typically 15 psi) of the gas of interest is maintained. As the gas permeates across the membrane the pressure in the second chamber (the permeate) is monitored. Both chambers contain an equal background pressure of an inert gas. Assuming that the pressure in the second chamber is small compared to that in the first chamber, the pressure rise is linear with respect to time and can be directly related to a pseudo-steady-state flux of gas across the membrane. In our apparatus the membrane area was π cm^2, and the volume of the second chamber, including the internal volume of the pressure gauge, was 10 cm^3. A stainless steel screen was used to support the membrane on the low pressure side. An MKS Baratron pressure gauge was used to measure the pressure independent of gas composition to within one torr. A Hewlett Packard 7090A recording plotter was used to record the pressure as a function of time. The same apparatus was also used to measure methanol fluxes in pervaporation. In the pervaporation experiment, one side of the membrane was contacted with pure, liquid methanol, while the

permeate cell on the other side of the membrane was initially evacuated. Following evacuation, the permeate cell volume was sealed. As methanol permeates across the membrane, it evaporates upon reaching the permeate volume. By measuring the pressure rise in the permeate volume, the methanol flux can be determined as in the vapor phase permeability experiments. In order to prevent methanol from condensing, the pressure in the permeate volume was never allowed to exceed the vapor pressure of methanol at the temperature used.

RESULTS AND DISCUSSION

Conductivity

The conductivity as a function of temperature for phosphoric acid equilibrated Nafion 117 (Nafion/H_3PO_4) in three different environments is shown in Figure 2. The curves labeled 'Dry' (pure N_2) and '370 torr H_2O/400 torr N_2' are self explanatory. The third curve, labeled 'H2O/MeOH/N2' is for a vapor phase with a water partial pressure of 350 torr, a methanol partial pressure of 350 torr and a nitrogen partial pressure of 100 torr, i.e., conditions similar to what might be found at the anode of the fuel cell. From these curves it can be seen that the presence of water in the atmosphere significantly increases the conductivity, and that the presence of water and methanol together increases the conductivity still further. These results suggest that even above 100 °C, the conductivity is dependent on the solubility of water in the membrane. Since the water solubility in Nafion is enhanced by the presence of methanol [3], if the conductivity depends on the water content of the membrane, a higher conductivity would be expected with methanol present, which is what was observed. The decrease in conductivity at higher temperatures suggests that the water content decreases with increasing temperature.

The conductivity results for the Clemson sulfonimide polymer 'B' (shown in Figure 1b) equilibrated with phosphoric acid are presented in Figure 3 (Vs. temperature at 400 torr water partial pressure) and Figure 4 (Vs. water partial pressure at 125 °C). For comparison purposes the conductivity of Nafion /H_3PO_4 under similar conditions is also shown. Although the reproducibility of the data for the sulfonimide samples is not good, the results are promising with conductivities significantly higher than Nafion being observed in some samples. The poor reproducibility may be the result of the sample equilibration procedure, which was the same as that used for the Nafion samples and resulted in highly swollen films. It may be possible to optimize the equilibration procedure for the sulfonimide material, to yield more reproducible results.

The conductivity results for the highly doped polybenzimidazole material are shown in Figure 5, as a function of temperature with a water partial pressure of 400 torr. The Nafion 117/H_3PO_4 results under the same conditions are again given for comparison. This sample contained approximately 250 mol% H_2SO_4, i.e., about 2.5 H_2SO_4 molecules to each repeat unit. With this doping level, the conductivity approaches that of Nafion, being about 50% lower at temperatures above 160 °C.

The best conductivity results to date are summarized in Table 1 for films at 170 °C and ca. 400 torr water partial pressure in terms of conductivity and voltage drop for a fuel cell operating at 100 mA/cm^2. For comparison literature values are given for 96% phosphoric acid at 170 °C and water equilibrated Nafion at 80 °C. While the conductivities obtained in this work are far below that of liquid phosphoric acid, they are very comparable to that of Nafion under traditional low temperature conditions.

Permeability

The permeability of oxygen through a Nafion 117 film equilibrated with phosphoric acid, Nafion equilibrated with water, a sulfonimide 'B' film equilibrated with water, and a PBI film doped with H_2SO_4 was measured using the closed volume technique. The results are summarized in Table 2a. The current density column represents the current density equivalent to the flux across the membrane with a one atmosphere pressure differential as a driving force. The equivalent current density was calculated as $i = nFN$ where $n = 4$ for the oxygen reduction reaction, F is Faraday's constant and N is the flux. For comparison, literature values for oxygen permeation in phosphoric acid and in Nafion (water equilibrated

and dry) are also given. There is reasonably good agreement between our result for water equilibrated Nafion and the literature value shown, indicating that our apparatus appears to be functioning properly. The permeability of oxygen in the phosphoric acid equilibrated Nafion at temperatures above 100 ^{o}C is similar to that in water equilibrated Nafion at 80 ^{o}C. This result indicates that the performance of the cathode should not be hindered by poor oxygen transport to the electrode surface, which, as shown in the table, is a limitation of liquid phosphoric acid. The sulfonimide 'B' material is orders of magnitude more permeable to oxygen, most likely due to the fact that it was swelled greatly by the equilibration process. As indicated above, a different swelling procedure may be necessary to obtain optimal results with the sulfonimide polymers. The lowest oxygen permeability was obtained with the polybenzimidazole material, which was expected to show good barrier properties.

The permeability of methanol vapor through Nafion 117 films equilibrated with phosphoric acid and equilibrated with water was also measured. These results are summarized in Table 2b. The equivalent current density was calculated as shown above, but taking n = 6 for methanol oxidation. The results show that the permeability of methanol through the phosphoric acid equilibrated Nafion films at temperatures above 100 ^{o}C is significantly lower than through water equilibrated Nafion at 85 ^{o}C. From this preliminary result it appears that methanol crossover to the cathode will be less of a problem for a fuel cell operating at the higher temperatures under consideration. Since the diffusion coefficient might be expected to rise with temperature, the lower permeability is probably the result of a lower solubility for methanol in Nafion at the higher temperatures. A lower rate of methanol crossover should result in higher efficiency and a lower probability of cathode depolarization by methanol.

The results from the pervaporation experiments are given in Table 2c in terms of equivalent current density. A literature value for methanol pervaporation through Nafion 125 is also given for comparison. The pervaporation results are in relatively good agreement with the literature value cited. The agreement gives added confidence to our beliefs that our permeation apparatus and experimental procedures are producing valid results. These results show much higher permeation fluxes for the case where the membrane is contacted by liquid methanol as opposed to the permeation when methanol vapor is in contact with the membrane. Thus the methanol crossover through phosphoric acid equilibrated Nafion at temperatures above 100 ^{o}C may be considerably smaller than would be expected based on conditions where liquid methanol is in contact with a Nafion membrane.

Thermal Stability

The thermal stability of the sulfonimide 'B' polymer was investigated using Differential Scanning Calorimetry (DSC) as shown in Figure 6. An endothermic process starting at about 150 ^{o}C can be seen, corresponding to the loss of water from the membrane. The thermal decomposition of the polymer can be seen at temperatures above 320 ^{o}C. This result shows that under these conditions (N_2 atmosphere, heating at 10 ^{o}C/min) the polymer is stable in the temperature range of interest.

Thermogravimetric Analysis (TGA) has been used to study the thermal stability of polybenzimidazole and to follow the reaction between PBI film and sulfuric acid. In Figure 7a the TGA scan for an undoped PBI film in nitrogen is shown. The heating rate was 10 ^{o}C/min. The PBI film lost water at about 80 ^{o}C and underwent thermal degradation at 550 ^{o}C. The TGA of PBI doped with approximately 20 mol% sulfuric acid is shown in Figure 7b. This result shows a loss of water at 100 ^{o}C and also showed two further weight losses starting at 330 ^{o}C and 415 ^{o}C. The first loss at 330 ^{o}C is attributed to the reaction of the acid with PBI to generate sulfonic acid groups while the second loss is probably due to loss of SO_2 or SO_3 from the polymer. The weight loss due to thermal degradation has been shifted to 600 ^{o}C, which indicates that the reaction with the sorbed acid improved the thermal stability of the film.

CONCLUDING REMARKS

A research program is in progress at CWRU/Clemson University/University of Iowa aimed at developing a highly efficient methanol-air polymer electrolyte fuel cell capable of operation at temperatures up to 200 °C. Preliminary results obtained to date indicate that the electrolyte requirements needed to realize this goal can be met. In particular, three novel polymer electrolytes have shown stability and sufficient ionic conductivity at the elevated temperatures envisioned.

ACKNOWLEDGMENTS

This work was supported under a University Research Initiative Grant from the Defense Advanced Research Projects Agency, ONR contract # NOOO14-92-J-1848. The authors acknowledge the collaboration of Professor D. DesMarteau of Clemson University and Professor D. Burton of the University of Iowa.

REFERENCES

1. E. Yeager, M. Razaq, D. Gervasio, A. Razaq and D. Tryk, in "Structural Effects in Electrocatalysis and Oxygen Electrochemistry", Proceedings Volume #92-11, The Electrochemistry Society, Pennington NJ, p. 440, 1992.

2. K. Sung and D. D. DesMarteau, *Polym. Preprints*, **33(2)**, 168, 1992.

3. S. Kato, K. Nagahama, H. Noritomi and H. Asai, *J. Membrane Sci.*, **72**, 31 (1992)

4. T. Springer, T. Zawodzinski and S. Gottesfeld, *J. Electrochem. Soc.*, **138**, 2334, 1991

5. D. Linden, "Handbook of Batteries of Fuel Cells", McGraw Hill, New York, 1984.

6. K. Klinedinst, J. Bett, J. Macdonald and P. Stonehart, *J. Electroanal. Interface. Chem.*, **57**, 281, 1974.

7. T. Sakai, H. Takenada, N. Wakabayashi, Y. Kawami and E. Torikai, *J. Electrochem. Soc.*, **132**, 1328, 1985.

Table 1
MEMBRANE CONDUCTIVITY

Membrane / Electrolyte	Conditions	Conductivity / $ohm^{-1}cm^{-1}$	Voltage loss at 100 mA/cm^2	Reference
Nafion 117 / H_2O	80 °C, Saturated H_2O Vapor	0.08	25 mV	4
96 % H_3PO_4	170 °C	0.64	< 5 mV	5
Nafion 117 / H_3PO_4	170 °C, 400 torr H_2O	0.04	50 mV	this work
Clemson U. B / H_3PO_4	170 °C, 400 torr H_2O	0.05 - 0.10	20 - 40 mV	this work
PBI / H_2SO_4	170 °C, 400 torr H_2O	0.02	100 mV	this work

Table 2a
OXYGEN PERMEABILITY

Membrane/Electrolyte	Temperature / °C	Current Density / mA/cm^2	Reference
95% H_3PO_4	120	0.04	6
95% H_3PO_4	150	0.08	6
Nafion 117 /35 % H_2O	80	0.46	7
Nafion 117 / dry	80	0.06	7
PBI / H_2SO_4	80	0.08	this work
Nafion 117 / H_2O	80	0.6 - 0.8	this work
Clemson B / H_2O	76	20 - 47	this work
Nafion 117 / H_3PO_4	123	0.35 - 0.45	this work
Nafion 117 / H_3PO_4	150	0.25 - 0.67	this work

Table 2b
METHANOL PERMEABILITY

Membrane	Temperature / ^{o}C	Current Density / mA/cm^2
Nafion 117 / H_2O	85	2.9 - 3.3
PBI / H_2SO_4	85	3.1
Nafion 117 / H_3PO_4	135	0.5, 0.5, 0.4 (3 samples)
Nafion 117 / H_3PO_4	140	0.9
Nafion 117 / H_3PO_4	155	1.1

Table 2c
METHANOL PERVAPORATION

Membrane	Temperature / ^{o}C	Current Density / mA/cm^2	Reference
Nafion 117 / H_2O	25	10 - 18 27 - 30 16 (3 samples)	this work
Nafion 117 / H_2O	50	52 388 (2 samples)	this work
Nafion 125 / H_2O / $(CH_3)_3NH^+$	50	290	3

Figure 1
Example Structures of Polymer Electrolytes

a. Perfluorosulfonimide (monofunctional)

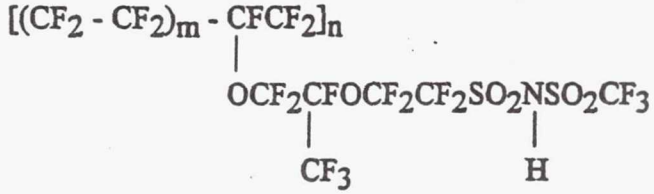

b. Perfluorosulfonimide (difunctional)

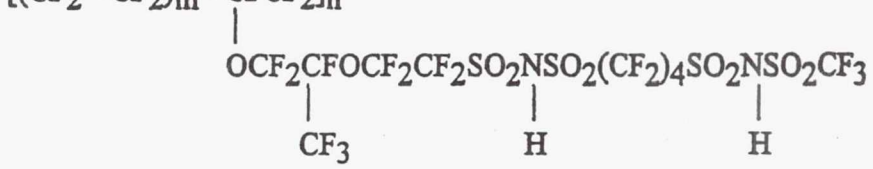

c. Perfluorophosphonic acid

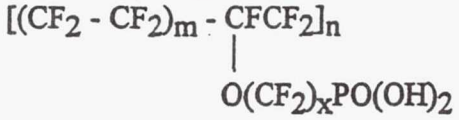

d. Polybenizimidazole (reacted with sulfuric acid)

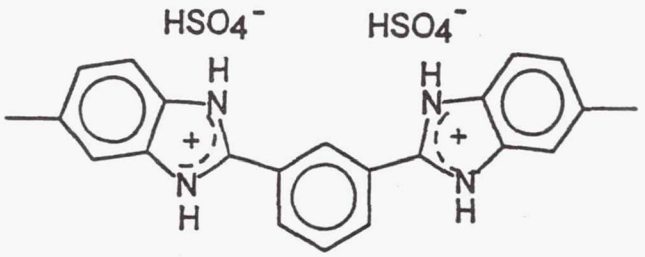

e. duPont Nafion

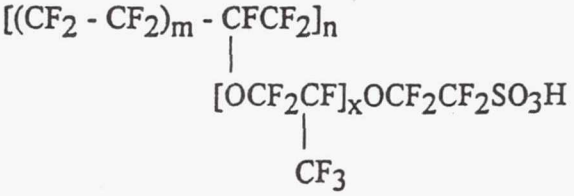

f. Dow

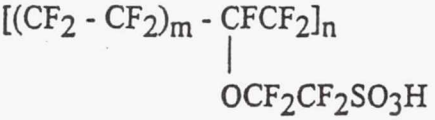

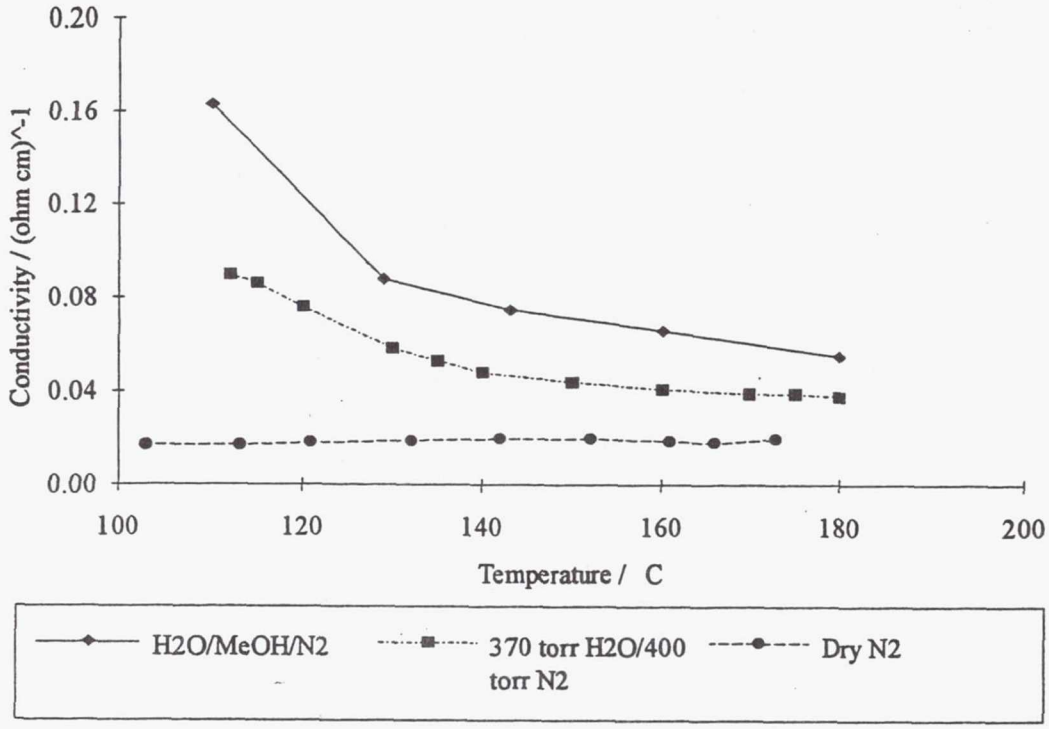

Figure 2 Nafion 117/H_3PO_4 Conductivity in different environments.

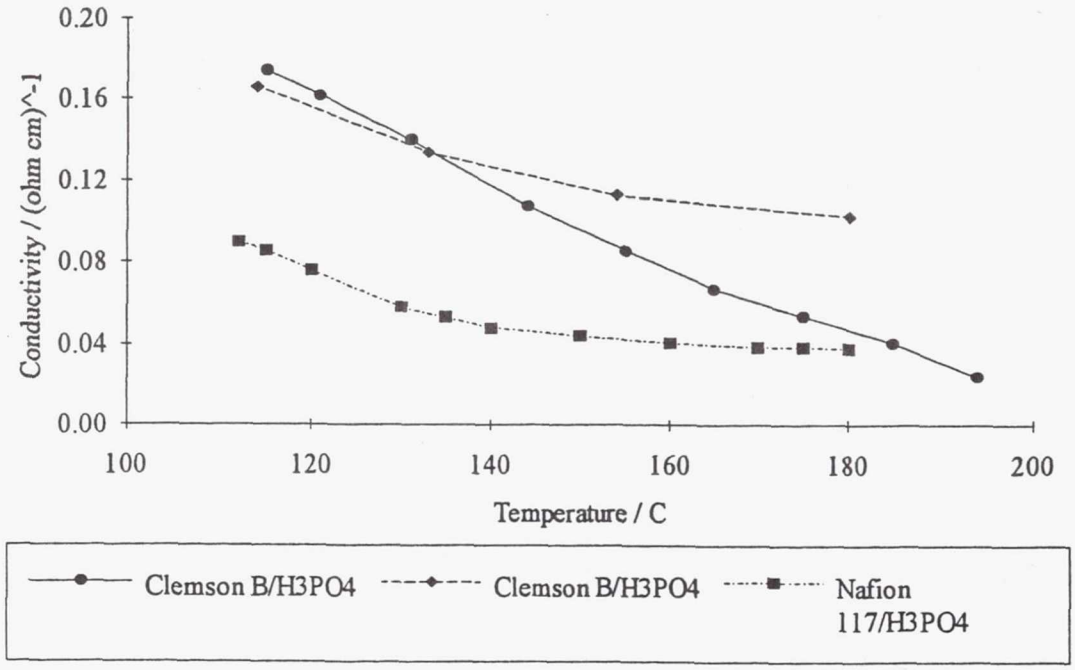

Figure 3 Conductivity vs Temperature at 400 torr water partial pressure.

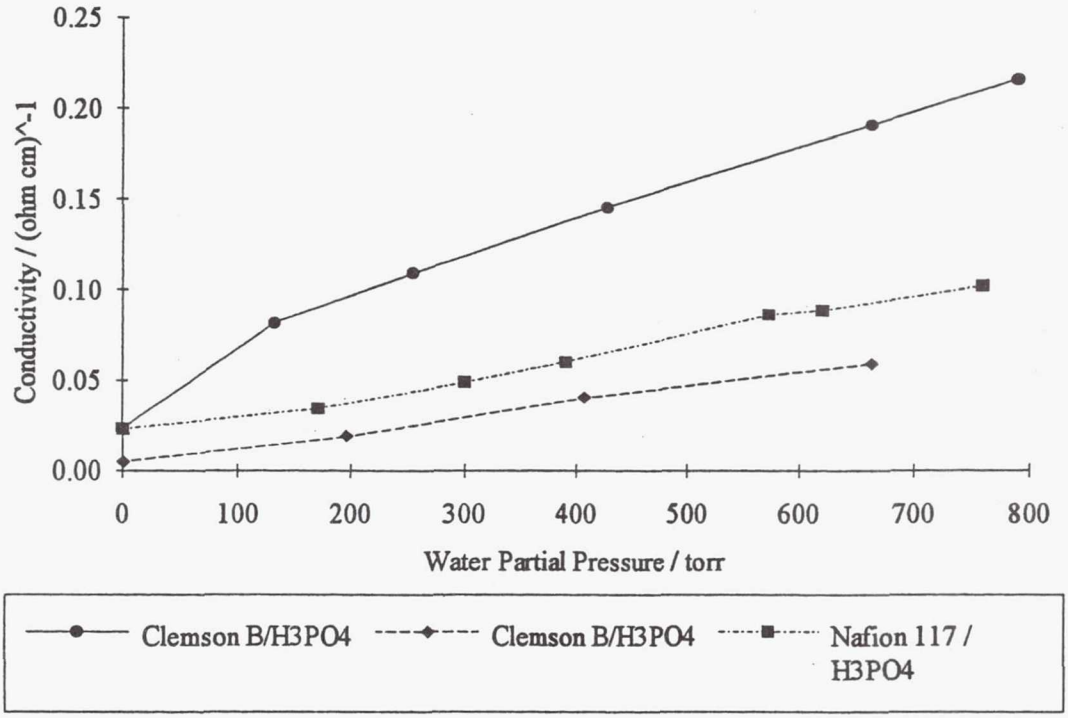

Figure 4 Conductivity vs Water Partial Pressure at ca . 125 °C.

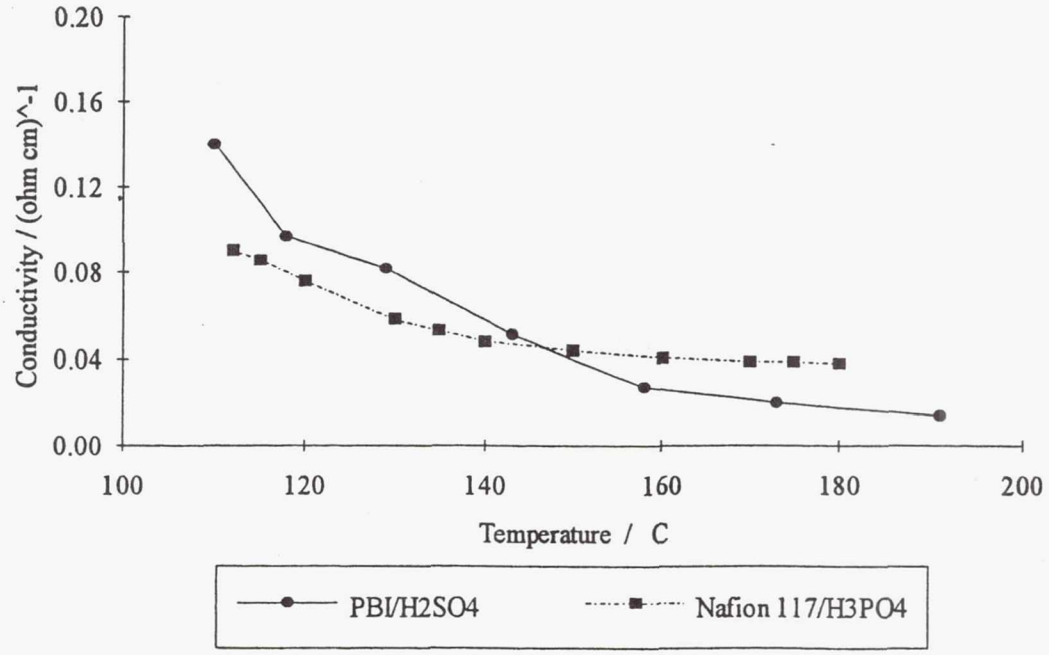

Figure 5 Polybenzimidazole Conductivity, 400 torr water partial pressure.

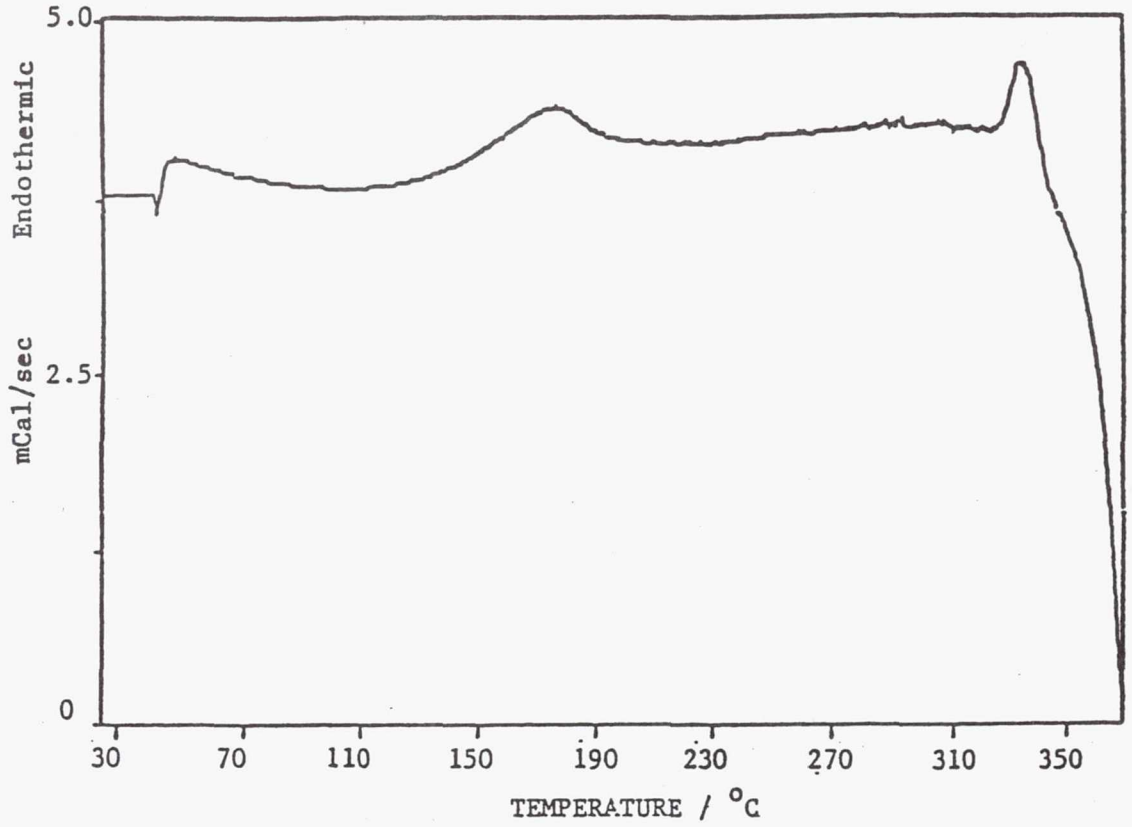

Figure 6 DSC of sulfonimide polymer 'B'.

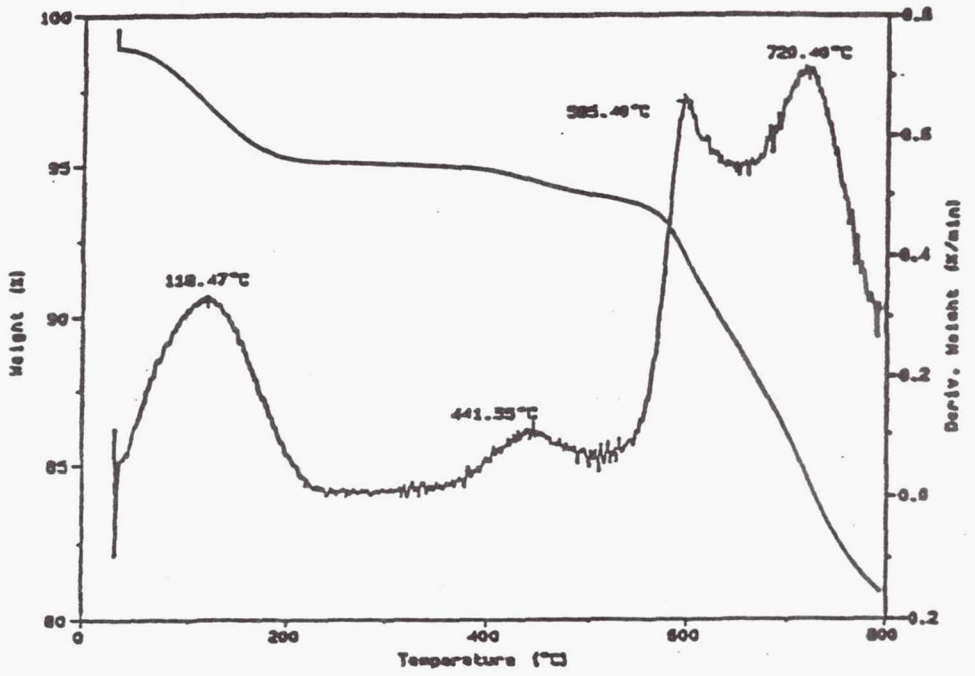

Figure 7a TGA of undoped PBI polymer.

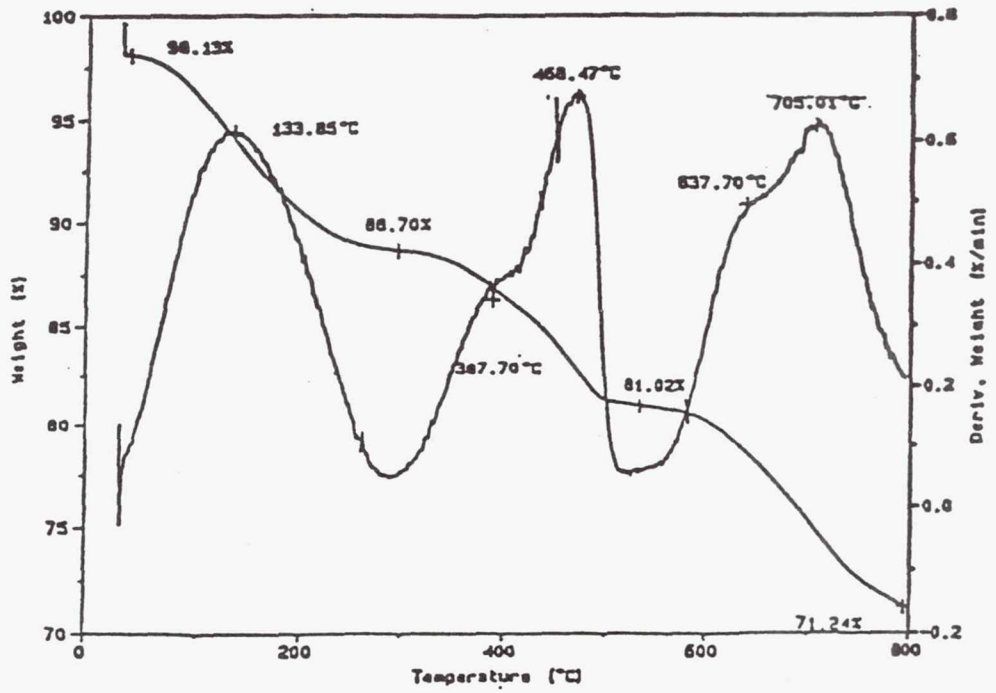

Figure 7b TGA of Sulfuric acid doped PBI polymer.

ADVANCES IN DIRECT OXIDATION METHANOL FUEL CELLS

S. Surampudi, S.R. Narayanan, E. Vamos, H. Frank and G. Halpert
Jet Propulsion Laboratory
California Institute of Technology
Pasadena, CA 91109

A. LaConti and J. Kosek
Giner, Inc.
Waltham, MA 02154-9147

G.K. Surya Prakash and G.A. Olah
University of Southern California
Los Angeles, CA 90089-1661

ABSTRACT

Fuel cells that can operate directly on fuels such as methanol are attractive for low to medium power applications in view of their low weight and volume relative to other power sources. A liquid feed direct methanol fuel cell has been developed based on a proton exchange membrane electrolyte and Pt/Ru and Pt catalyzed fuel and air/O_2 electrodes respectively. The cell has been shown to deliver significant power outputs at temperatures of 60 to 90° C. The cell voltage is near 0.5 V at 300 mA/cm^2 current density and an operating temperature of 90° C. A deterrent to performance appears to be methanol crossover through the membrane to the oxygen electrode. Further improvements in performance appear possible by minimizing the methanol crossover rate.

INTRODUCTION

Direct oxidation methanol fuel cells (DMFC) are attractive for several defense and transportation applications in view of their lower weight and volume compared to indirect fuel cells [1,2]. The weight and volume advantages of direct oxidation fuel cells are due to the fact that they do not require any fuel processing equipment. Elimination of the fuel processor also results in simpler design and operation, higher reliability, less maintenance, and lower capital and operating costs. Further, direct oxidation fuel cells are projected to have rapid and multiple start up capabilities, and the ability to easily follow varying loads.

Under a task sponsored by the Defense Research Projects Agency (DARPA), JPL, USC, and Giner, Inc. are engaged in the development of direct methanol fuel cells for future defense applications. A near term objective of the program is to identify advanced catalysts and electrolytes and demonstrate the DMFC technology at the cell level. This paper describes the progress made to date on this effort.

ASSESSMENT OF CATALYSTS FOR THE OXIDATION OF METHANOL

Anodic oxidation behavior of methanol was investigated in half cells using both supported and unsupported catalysts at a loading of 0.5 mg/cm^2. In these experiments 0.5 M sulfuric acid was used

as the electrolyte along with 0.001 M perflurooctane sulfonic acid, and the fuel concentration was 1.0 M. These half cell experiments were carried out at 45°. Anodic oxidation characteristics of CH_3OH at various unsupported (Pt-Sn and Pt-Ru) and supported catalysts (Pt, Pt-Sn and Pt-Ru) are given in Figures 1 and 2. It can be seen from these results that Pt-Ru is the most promising among the state-of-the-art Pt based catalysts for the oxidation of methanol. This observation is in agreement with the results reported in the literature [3,4]. All further studies were carried out using Pt-Ru catalyst.

Improved kinetics of methanol oxidation on Pt-Ru catalyst were observed with an increase in temperature, catalyst loading and methanol concentration. Figure 3 reveals a significant reduction of polarization as the temperature is raised from 25 to 60° C. Throughout the current density range of 1 to 100 mA/cm^2 the polarization is reduced almost 100 mV by this temperature increase. Figure 4 gives the results of the catalyst loading studies. Results show that the increase from 1 to 5 mg/cm^2 resulted in the reduction of almost 100 mV polarization throughout the current density range from 1 to 100 mA/cm^2. Increasing the methanol concentration also resulted in lower anodic polarization for the oxidation of methanol (Figure 5).

EVALUATION OF ELECTROLYTES FOR THE OXIDATION OF METHANOL

Liquid Electrolytes

Boron trifluoride dihydrate, triflic acid, perfluoroethane sulfonic acid and perflurooctane sulfonic acid (C_8 acid) were evaluated as candidate electrolytes for the oxidation of methanol. Experiments were carried out in half cells using activated Pt-Ru gas diffusion electrodes obtained from commercial sources. Pt-Ru electrodes were found to be unstable and dissolve in boron trifluoride dihydrate electrolyte. Hence no further experiments ere carried out with this electrolyte. Anodic oxidation characteristics of methanol in the other three electrolytes are given in Figure 6. Some of the important findings of this study are: a) anodic oxidation of methanol in triflic acid is comparable to its oxidation is sulfuric acid, b) perfluroethanesulfonic acid was found to be unattractive for the oxidation of methanol, and c) marginally improved oxidation behavior was observed with perflurooctanesulfonic acid electrolyte.

Solid Polymer Electrolytes

Nafion, a polymer electrolyte membrane (PEM), is an attractive alternate to the liquid electrolytes for liquid feed methanol cells for several reasons including: a) simplified design, b) simplified assembly and operation, c) lower corrosion, and d) minimization or elimination of shunt currents. The material has been used quite successfully in gas feed hydrogen/oxygen fuel cells.

For these reasons, Nafion was evaluated as an electrolyte in a liquid feed half cell. A methanol-water mixture only (without acid) was introduced to the fuel compartment. Nafion 117 (Du Pont) was used, and the anode catalyst was a supported Pt-Ru type that was bonded directly to the Nafion. Figure 7 compares performance of this cell with the Nafion electrolyte to the previously employed sulfuric acid electrolyte. Hence, Nafion was selected as the candidate electrolyte in all further studies.

CELL DESIGN

Design Optimization

Two cell design options were considered for direct oxidation methanol fuel cells including: a) gas or vapor feed design and b) liquid feed design. Initial considerations indicated that gas feed design is preferable in that it could employ existing fuel cell type gas diffusion electrodes. Furthermore, the gas feed design could operate at the higher temperatures that were anticipated to be necessary for high performance. Subsequent deliberations considered the fact that the liquid feed design would not require a vaporizer and would therefore be much simpler in design and operation. The other potential advantages of liquid-feed design are: a) elimination of complex water and thermal management systems, b) multiple use capability of the methanol-water as the fuel, for humidification purposes and as an efficient stack coolant, and c) significantly lower system size and weight. This cell design does not suffer from the disadvantages of prior liquid-feed cell designs which employed liquid electrolytes. The use of PEM eliminates the problem of troublesome shunt currents and also eliminates problems associated with corrosion of cell components. Tests have shown that the PEM does not degrade with operation and is suitable for continuous operation. Fuel catalysts were found to exhibit improved performance with the solid electrolyte membrane. On this basis JPL began development of liquid feed type direct methanol fuel cells.

Schematic Diagram of Liquid Feed Direct Methanol Fuel Cells

Figure 7 give a schematic diagram of the complete laboratory type liquid feed methanol system employing the membrane electrolyte. The MEA (membrane-electrode assembly) consists of a layer of Nafion electrolyte 7 mil thick with fuel and air/O_2 electrodes bonded to either side. Electrode dimensions are 2 inch by 2 inch by approximately 10 mil thick. The MEA is positioned between the machined portion of two graphite blocks. The machined area on each block is a rectangular pattern with open channels (designated as the flow field) to allow flow of liquid or gas across the electrode surfaces. Inlet and outlet ports communicate with the flow fields via holes drilled into the carbon blocks and equipped with threaded fittings at the sides of the blocks. Stainless steel support plates, with the same overall length and width as the carbon plates, are located on the back surface of the plates. The stainless steel plates as well as the carbon blocks are drilled in their outer perimeter to accommodate bolts that are used to compress the assembly for sealing and to provide electrical contact between the electrode and un-recessed area of the flow field.

The methanol solution is introduced into the fuel compartment of the cell via a pump and then returned to a fuel storage reservoir as shown in Figure 8. The end product, carbon dioxide, is entrapped in the exit fuel line and released in the storage reservoir. Pressurized air or O_2 is introduced to the air compartment of the cell and vented without circulation. Heaters are located on the outside surface of the cell to control sell temperature. Finally, the cell is equipped with a small closed end hole to accommodate an internal thermocouple.

PERFORMANCE OF LIQUID FEED DIRECT METHANOL FUEL CELLS

Effect of Temperature

Voltage-current characteristics of the liquid feed direct methanol fuel cell were measured over a range of temperatures with 2 M methanol as fuel and pure O_2 as oxidant. Results are given in Figure 9 in terms of operating cell potential versus current density. Each point represents an

essentially steady state voltage that was achieved after about 5 minutes of continuous operation at the indicated current density. Inspection of Figure 8 reveals a marked increase in performance with increase in temperature over the range of 30° C to 90° C. For example, at a potential of 0.55 V, the current density outputs are 10, 45, and 140 mA/cm^2 at temperatures of 30, 60, and 95° C respectively. Similarly, at a potential of 0.50 V, the current density outputs are 20, 110, and 260 mA/cm^2 at 30, 60 and 95° C. The trend of increased output with increase in temperature is in accord with that exhibited by other fuel cells. The increased output at higher temperatures is attributed to a combination of factors consisting of a reduction of cell ohmic resistance, activation polarization, and concentration polarization.

Effect of Methanol Concentration

The effect of methanol concentration on the cell performance was also determined. Three separate runs were carried out at 60° C each with a different fuel concentration of 0.5 M, 2.0 M, and 4.0 M methanol. The effect of fuel concentration on overall cell performance is given in Figure 10 in terms of voltage-current characteristics. Inspection of these results shown that a higher operating current densities, higher cell voltage is obtained with 2 M methanol while somewhat lower outputs are obtained with both the higher concentration, 4 M methanol, and the lower concentration, 0.5 M methanol. At lower current densities 0.5 M methanol was found to provide higher cell operating voltage than 2.0 M methanol. On this basis there appears to be an optimum concentration for operation for different current densities. The optimum may be between 0.5 M and 2 M methanol. The lower performance of the cell at fuel concentrations less than 0.5 M is probably due to the concentration polarization effects. The poor performance of the cell at higher methanol concentrations was found to be due to the fuel crossover phenomenon. Support for the proposed impact of crossover at high concentrations was shown in half cell studies on the oxygen electrode. It was found that the O_2 electrode performance is significantly lowered at higher methanol concentrations [5]. For example, the O_2 electrode potential dropped more than 100 mV at 100 mA/cm^2 as methanol concentration was increased from 2 to 4 M methanol. This finding emphasizes the need to minimize the crossover rate to improve performance of the O_2 electrode and hence the overall cell performance.

Fuel Utilization Studies

In order to examine fuel utilization, a cell was set up and run continuously at constant current with a finite amount, 200 ml of 1.0 M methanol solution in the circulation tank, without replenishment of the methanol. Initially the current was set at 1.875 A (75 mA/cm^2), and the cell temperature was held at 80°. Results are given in Figure 11 in terms of cell voltage versus percent utilization of the fuel. The utilization was taken as output amp-hrs/theoretical amp-hrs (from the amount of methanol and its electrochemical equivalent). Inspection of this figure reveals that voltage drops sharply at 75 mA/cm^2 when utilization approaches 60%. The sharp drop in voltage at this point is believed to be associated with concentration polarization of the fuel electrode that is, in turn, due to an inadequate supply of methanol to the electrode. The methanol supply is, in turn, limited by the low methanol concentration at this point (near 0.5 M or less). The phenomenon is consistent with prior half cell studies that revealed the onset of high polarization when methanol concentration declines below this level.

PROBLEMS AND ISSUES

Performance of the liquid feed methanol fuel cells is already attractive for some applications and is approaching the levels required for electric vehicle propulsion. With some improvements in

electrical performance, efficiency and cost, this system can indeed be considered a serious candidate for electric vehicle applications. These improvements can be achieved by developing high performance anode catalysts, new membranes with reduced methanol permeability, methanol insensitive cathode catalysts, and low cost materials (non-Pt based catalysts, membranes, bipolar plate materials, etc.).

CONCLUSIONS

Some of the major finding of the study are:

1) Pt/Ru catalyzed electrodes are well suited for oxidation of methanol.

2) Performance of Pt/Ru catalyzed carbon electrodes increases with increased temperatures (25 to 60° C), increased fuel concentration, (0.5 to 2 M methanol) and increased catalyst loading (0.5 to 5 mg/cm^2).

3) A new liquid feed DMFC has been developed based on a proton exchange membrane electrolyte, Pt/Ru catalyzed fuel electrode, and Pt catalyzed air/O_2 electrodes.

4) The new cell can deliver significant outputs in excess of 250 mA/cm^2 at potentials near 0.5 V at moderate temperatures (less than 190° F).

ACKNOWLEDGEMENT

The work described here was carried out at the Jet Propulsion Laboratory, California Institute of Technology, in a program sponsored by ARPA under contract with the National Aeronautics and Space Administration.

REFERENCES

1) S.D. Fritts and R.K. Sen, *Assessment of Methanol Electro-Oxidation for Direct Methanol-Air Fuel Cells*, DOE Report PNL-6077 (1988).

2) S. Surampudi, S.R. Narayanan, E. Vamos, H. Frank and G. Halpert, *Proceedings of the Eighth Annual Battery Conference on Applications and Advances*, Long Beach, CA (January 1993).

3) M.M.P. Jansen and J. Moolhuysen, *Electrochim. Acta, 21*, 869 (1976).

4) M. Watanabe, M. Uchida and S. Moto, *J. Electroanal. Chem., 229*, 395 (1987).

5) S.R. Narayanan, E. Vamos, S. Surampudi, H. Frank and G. Halpert, *Extended Abstracts of the Fall 1993 Meeting of the Electrochemical Society*, in press.

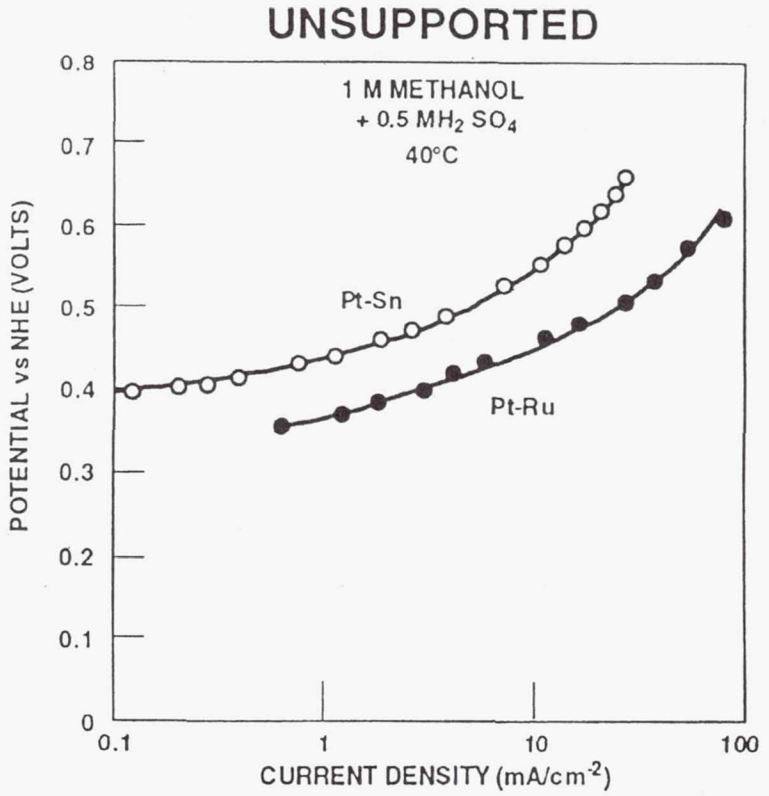

Figure 1. Evaluation of Unsupported Catalysts for Methanol Oxidation.

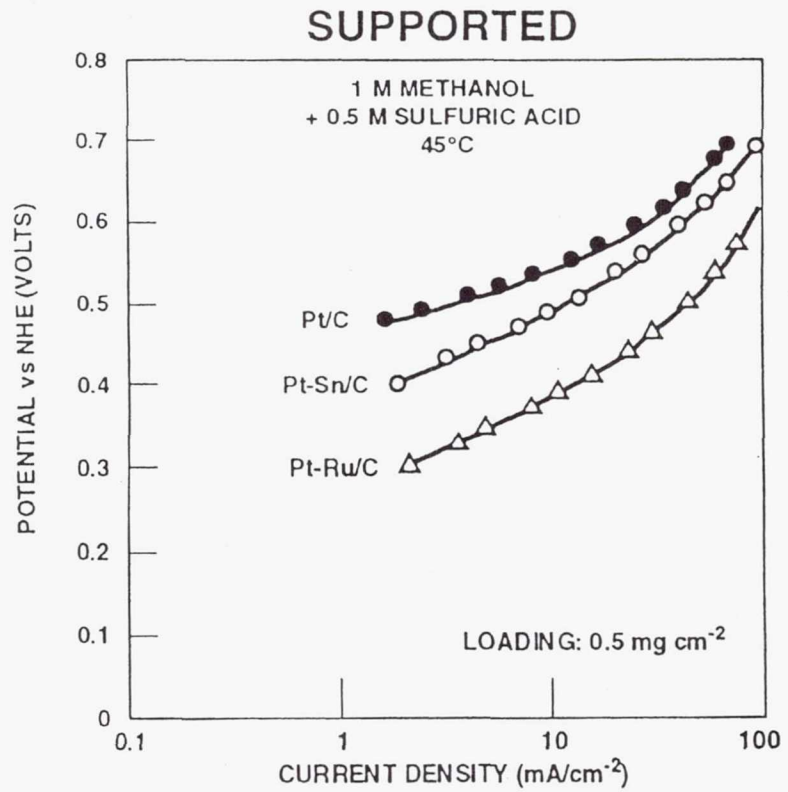

Figure 2. Evaluation of Supported Catalysts for Methanol Oxidation.

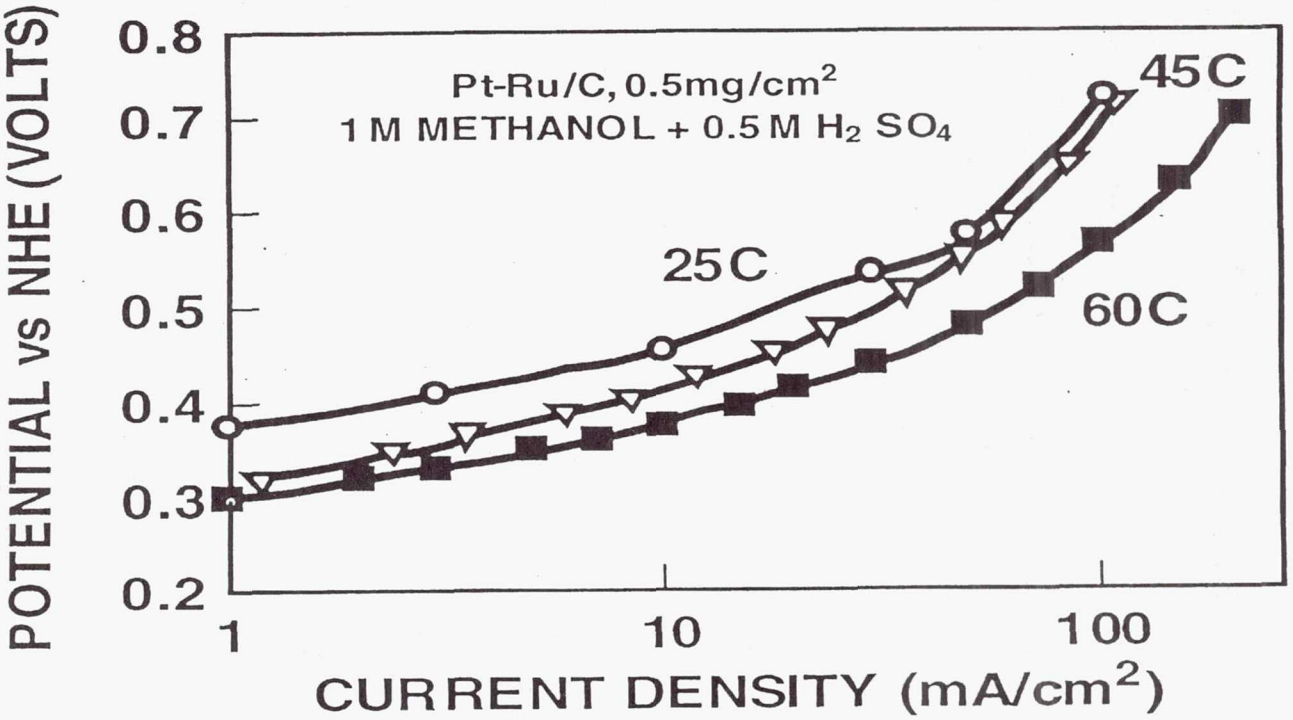

Figure 3. Effect of Temperature on Performance of Pt/Ru Electrodes.

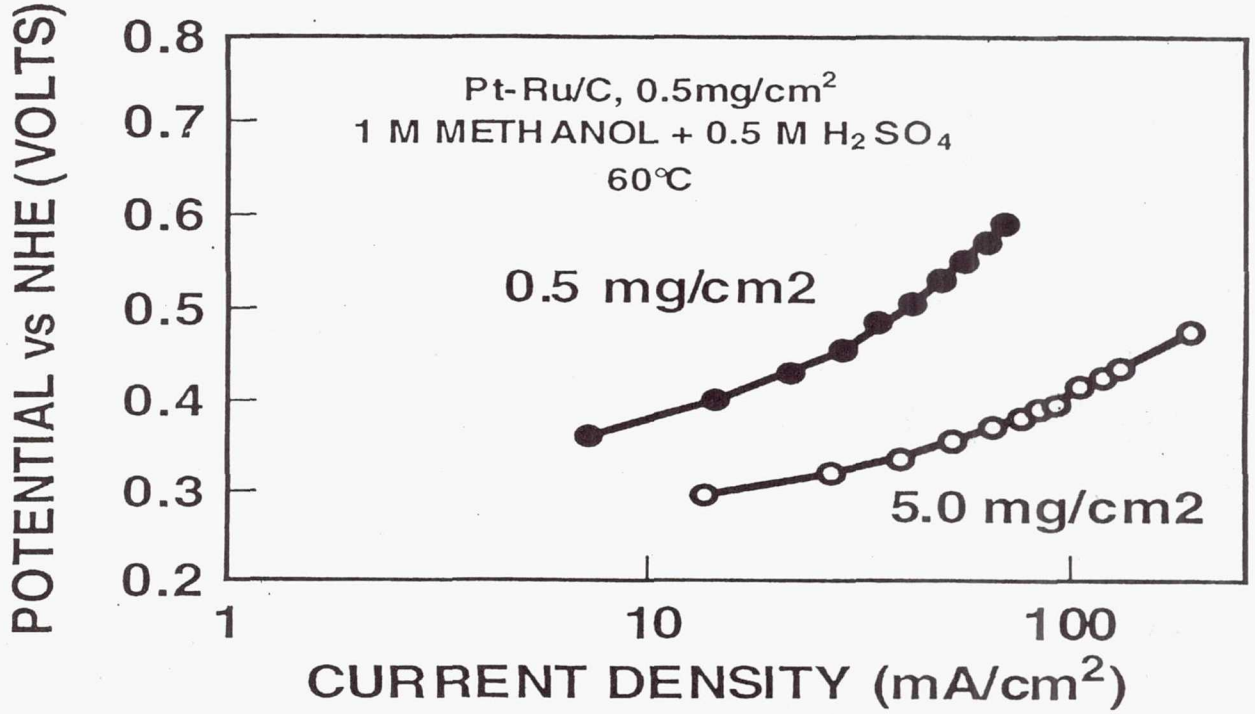

Figure 4. Effect of Catalyst Loading on Performance of Pt/Ru Electrodes.

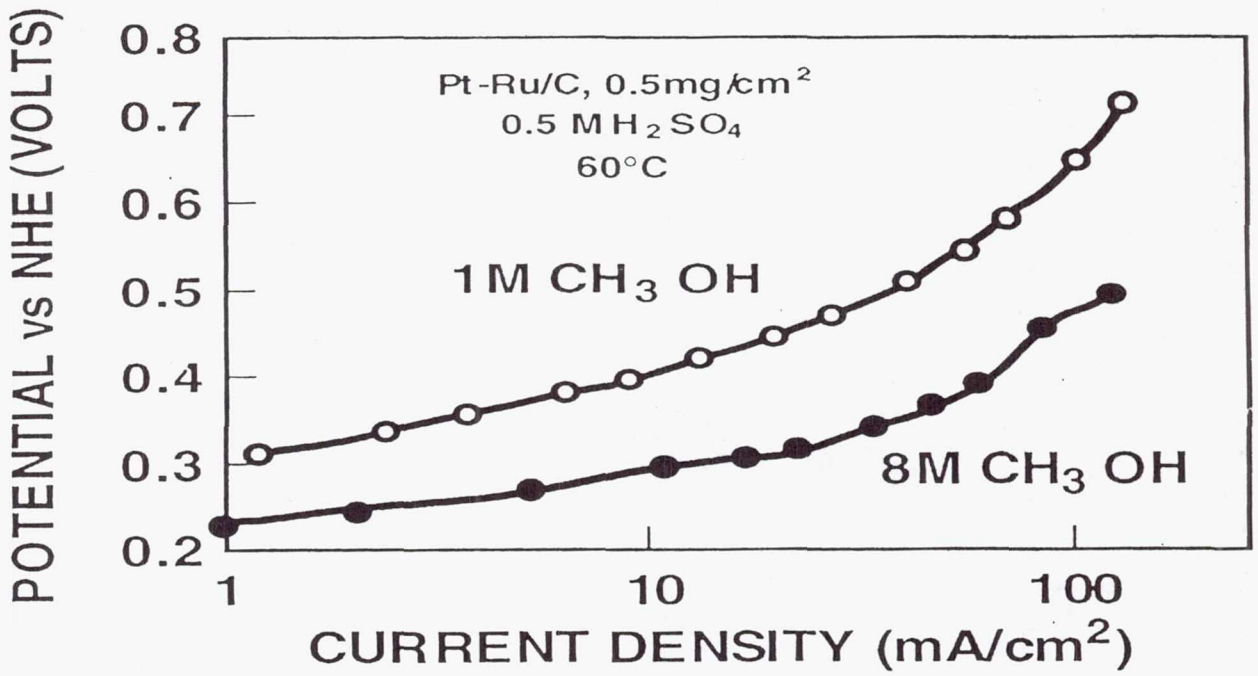

Figure 5 Effect of Fuel Concentration on Performance of Pt/Ru Electrodes.

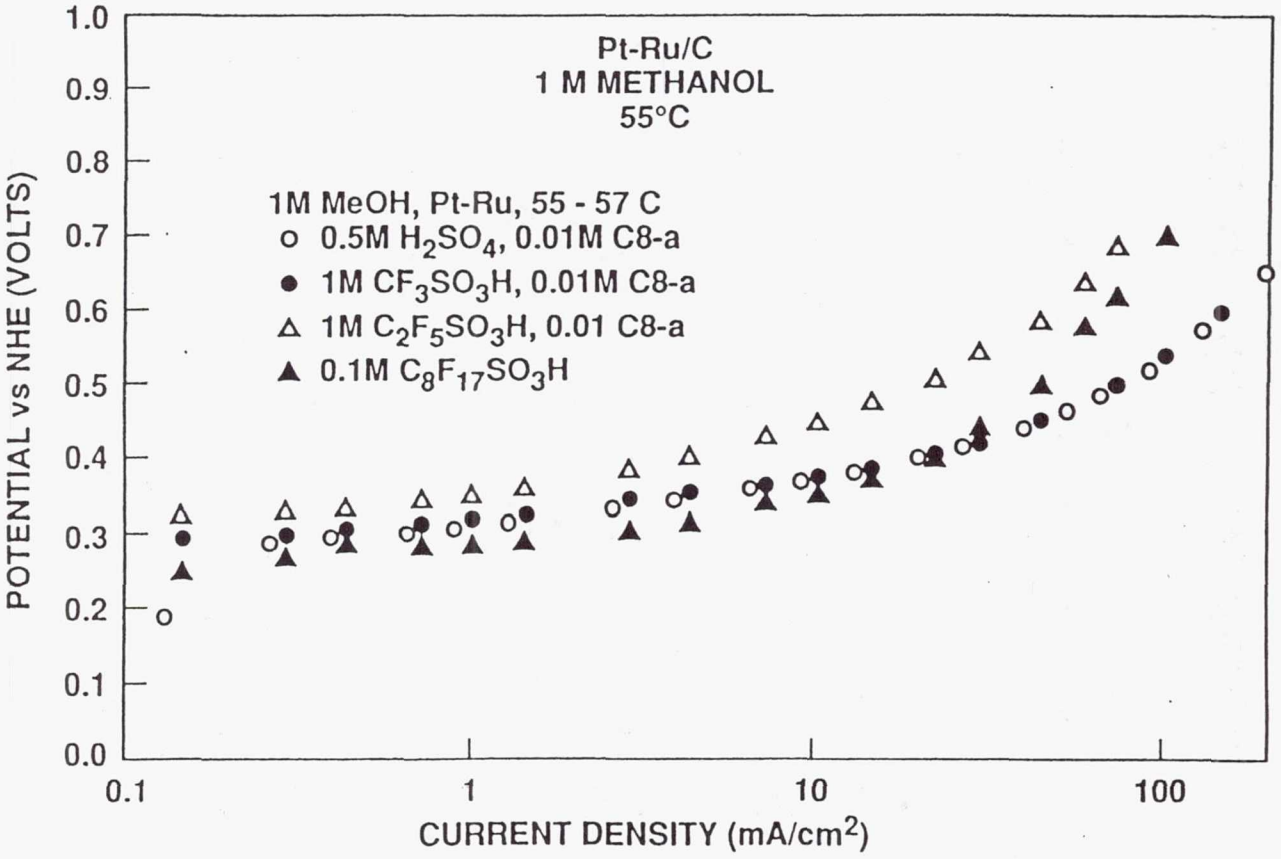

Figure 6. Anodic Oxidation of Methanol in Various Electrolytes.

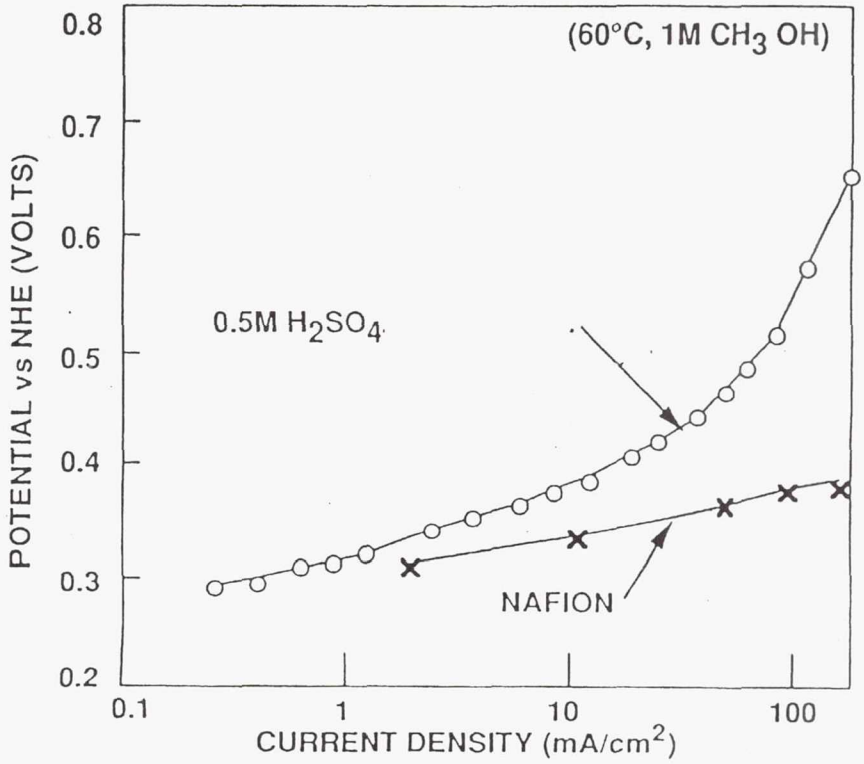

- IMPROVE FUEL OXIDATION CHARACTERISTICS WITH NAFION

Figure 7. Evaluation of Electrolytes for Anodic Oxidation of CH_3OH.

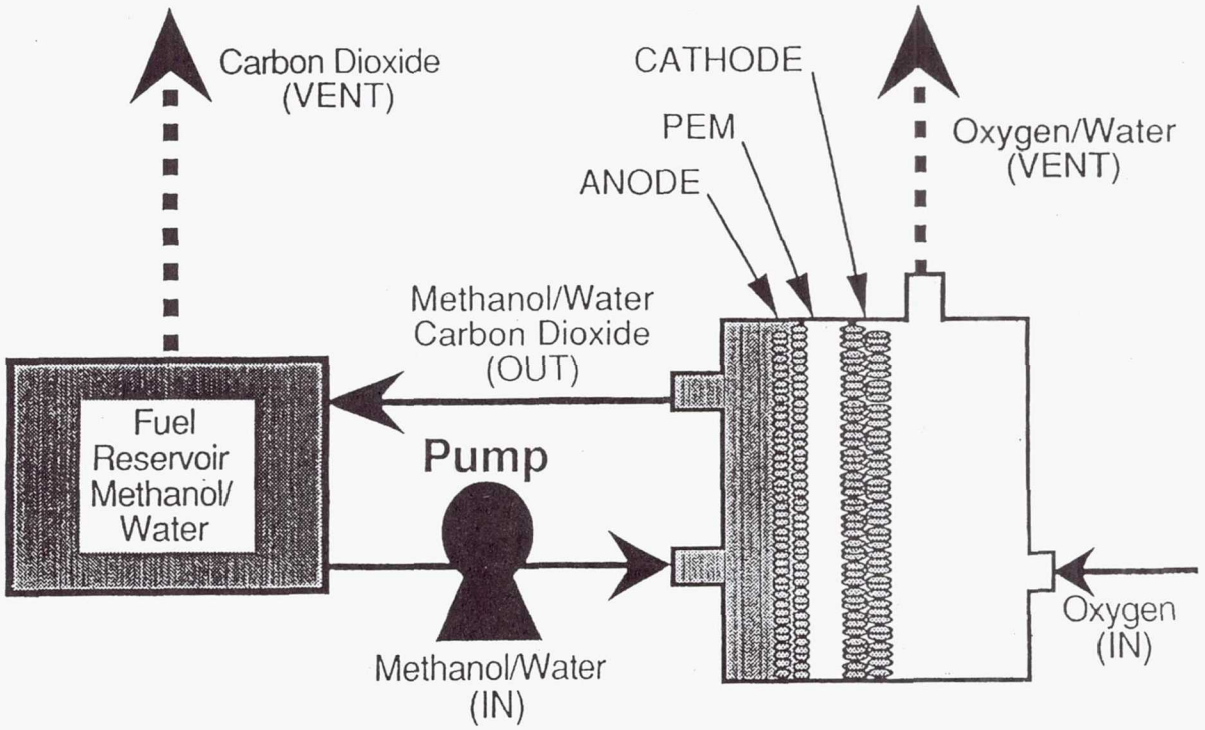

Figure 8. Diagram of JPL Liquid Feed Direct Methanol Fuel Cell.

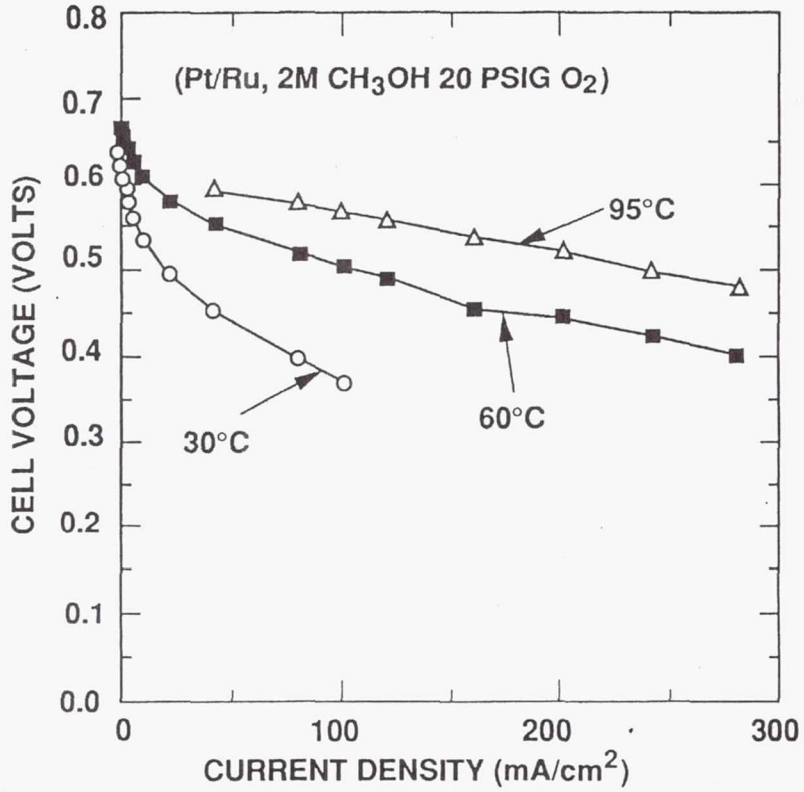

Figure 9. Effect of Temperature on Cell Performance.

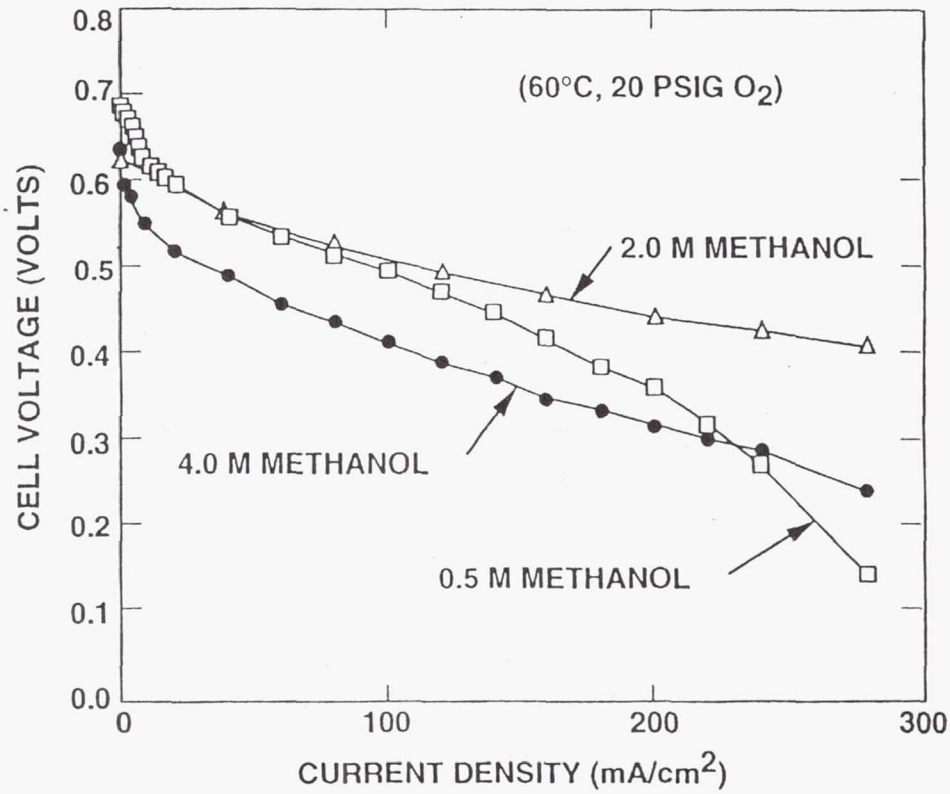

Figure 10. Effect of Fuel Concentration on Cell Performance.

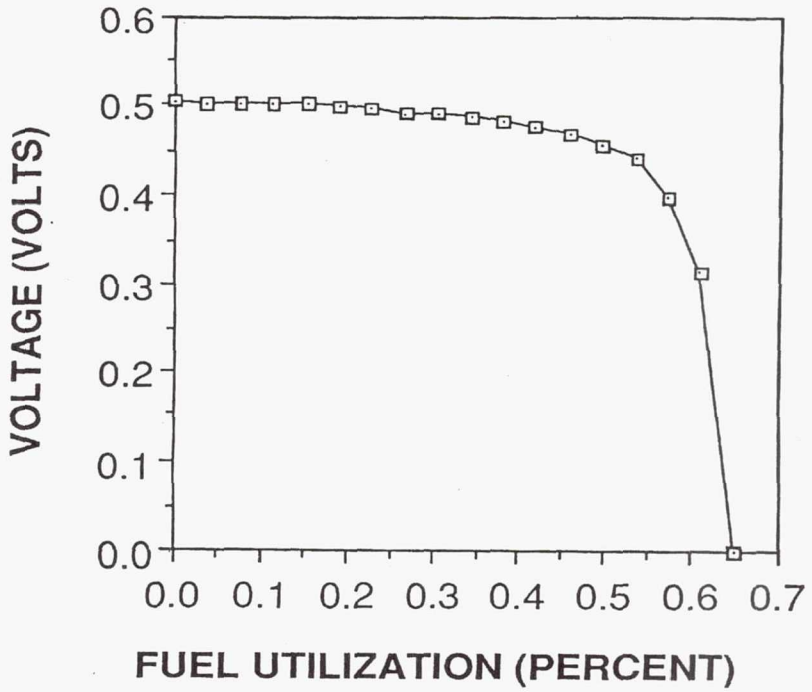

Figure 11. Voltage vs Fuel Utilization Curve.
Current Density, 62° C. 20 PSIG Oxygen.
1 M Methanol Initial Concentration,
75 mA/cm^2

RECENT ADVANCES IN SPE® WATER ELECTROLYZER

James F. McElroy
HAMILTON STANDARD DIVISION
UNITED TECHNOLOGIES CORPORATION
WINDSOR LOCKS, CONNECTICUT 06096-1010

ABSTRACT

A new cell structure has been introduced into the SPE Water Electrolyzer which has improved overall characteristics significantly. Weight, reliability, and efficiency are the characteristics that are improved the most, with volume having a second order improvement. This paper discusses the capabilities of the new cell structure and the impact it would have in various space applications.

INTRODUCTION

In recent years, high pressure water electrolysis has been considered for several space applications. These space applications include the generation of high pressure hydrogen and oxygen for space station reboost propulsion, the generation of high pressure hydrogen and oxygen for lunar base energy storage, and the generation of high pressure oxygen for on-orbit space suit oxygen supply recharge. The technical approach taken with the SPE Water Electrolyzer has been to use the previously developed nuclear submarine SPE Electrolyzer design while reducing mass wherever possible. Because the basic nuclear submarine SPE Electrolyzer cell design is limited to approximately 400 psi differential pressures overboard and across the cell, the stack of cells must be pressure balanced in a nitrogen-filled dome when operating above 400 psi. This results in significant mass and system complexity.

Within the last two years, a new SPE Water Electrolyzer cell structure has been developed. This cell structure, which has a lower mass than the 400 psi design, requires no pressure-balanced dome when operating at elevated pressures (i.e., up to several thousand psi). This cell structure is configured to permit the hydrogen and oxygen compartments to operate at differential pressures equivalent to the maximum system pressure and, finally, this cell structure results in lower cell voltage (i.e., higher efficiency).

BACKGROUND

SPE Water Electrolysis Technology Overview

The heart of the SPE Water Electrolyzer is the electrolysis cell which consists of an ion exchange membrane with Teflon® bonded, finely divided metal electrodes. Figure 1 shows this arrangement along with the water electrolysis reactions. Since the fixed acid ion exchange membrane has neither a traditional bubble point nor free electrolyte, operating pressures and hydrogen-oxygen differentials are limited only by the surrounding structures. This affords a significant safety factor in maintaining positive separation of the hydrogen and oxygen products.

The introduction of the perfluorocarbon cation exchange membrane in the late 1960s enabled the development of the SPE Electrolyzer. In prior years, water electrolyzers made with existing ion exchange membranes had useful lifetimes of only a few hundred hours. With the use of perfluorocarbon ion exchange membranes, the SPE Water Electrolyzer cell life has been demonstrated to be in excess of 14 years and projected to over 30 years depend,ing on operating conditions.

In most practical applications, a number of cells are stacked in a filter press arrangement with as many as 100 cells electrically connected in series while the fluids are passed through the cells in parallel. Without any free electrolyte, the parallel fluid flows can be conducted without fear of shunt currents inducing stray water electrolysis and its potentially deleterious result of product gas mixing. The purity of the product gases from SPE Water Electrolyzers is typically greater than 99.99%.

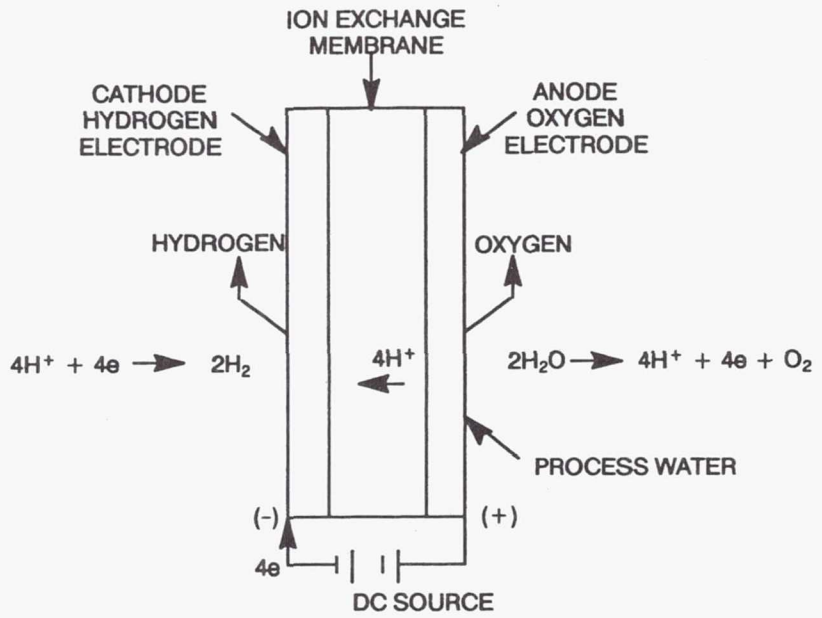

Fig. 1. - SPE Water Electrolyzer Reactions

Nuclear Submarine Oxygen Generators

The cell structures, developed during the 1970s for nuclear submarine oxygen generation, have a capability of operating continuously at up to 400 psi. Limited by stack compression and cell frame strength, pressures higher than 400 psi are obtained by placing the entire stack within a pressure vessel. Figure 2 shows a pair of 100 cell stacks, for 3000 psi operation, with their pressure vessel domes removed. The thick lower end plates form one end of the pressure vessels.

The nuclear submarine SPE Oxygen Generator cell structure is also limited to about 400 psi differential pressure between oxygen and hydrogen. The significance of this design limit is that a moderately complex pressure control system is employed at 3000 psi. The pressure control system maintains oxygen and hydrogen pressures within 400 psi even during a power loss depressurization.

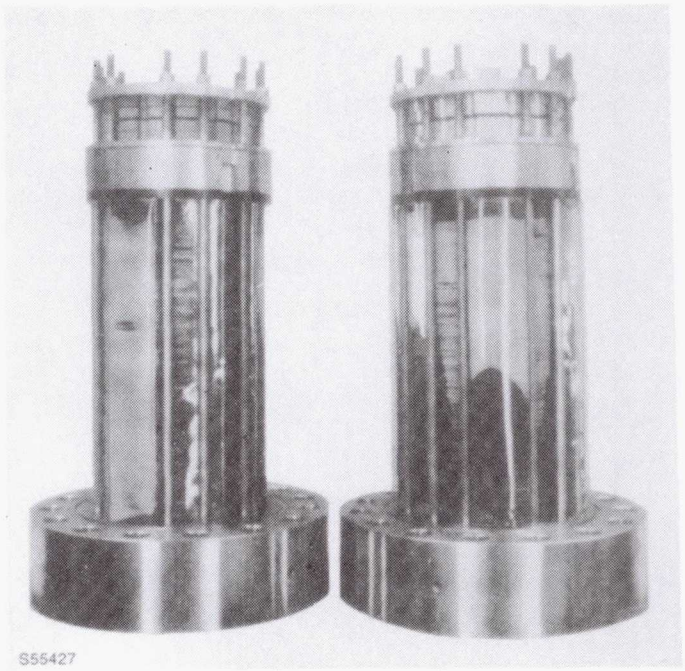

Fig. 2. - 225 SCFH U.S. Navy SPE Oxygen Generator Modules

Space Station SPE Propellant Generator Demonstrator

Under contract to NASA/JSC, a 3000-psi hydrogen-oxygen generator based on the Naval 0.23 ft^2 SPE Water Electrolyzer cell configuration was designed and delivered. The purpose was to demonstrate the feasibility of producing 3000 psi hydrogen and oxygen on orbit for periodic rocket motor firing to maintain Space Station Freedom orbital altitude.

To reduce the mass and decrease the volume, as compared to the U.S. Navy design, several configuration changes were made to the supporting pressure vessel and fluid manifold. The resultant SPE propellant generator demonstrator is significantly smaller and lighter. In the SPE propellant generator demonstrator, the pressure vessel is two torispherical domes opposed on either side of a central fluid plate. This configuration, with a rating of 4 pounds of water electrolyzed per hour, is shown in Figure 3. The dimensions of the SPE propellant generator demonstrator are 13 inches across the domes and 13 inches in diameter at the dome flanges. The total weight of the cell stack for space station propulsion is 193 lbs.

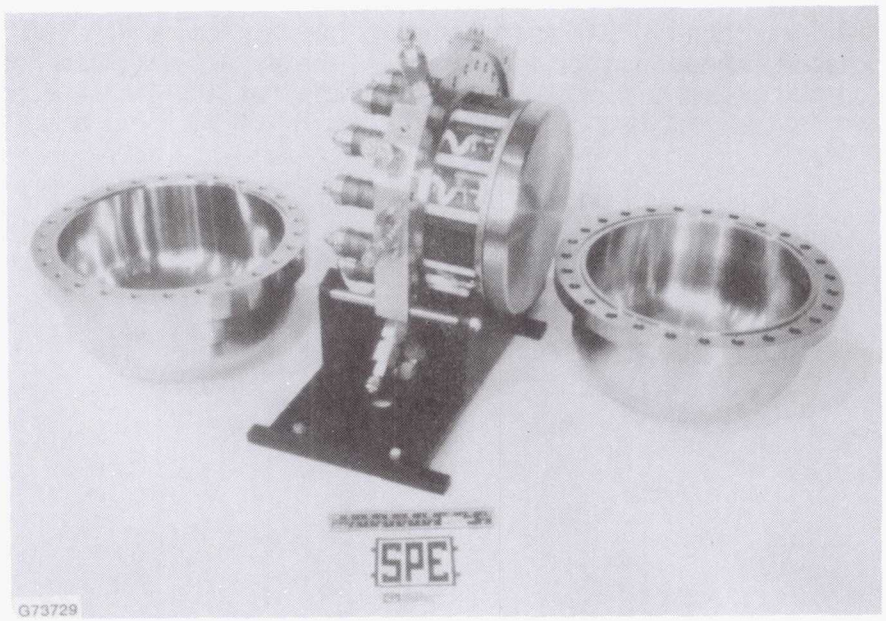

Fig. 3. - SPE Propellant Generator, Domes Removed

Although the weight of the pressure vessel for the SPE Propellant Generator is significantly reduced from the nuclear submarine SPE Oxygen Generator pressure vessel, the system complexity remains the same. Figure 4 describes the SPE Propellant Generator system fluid schematic. As shown on Figure 4, the pressure vessel is charged with nitrogen gas. This gas is increased slowly while the system comes to pressure so as to prohibit any differential pressure from exceeding 400 psi. Both the product hydrogen and product oxygen are pressure regulated using the pressure vessel nitrogen as a reference. An elaborate array of regulators, valves and relief valves is required in each of the three gas systems to prevent any unsafe condition (i.e., no two simultaneous and independent failures will produce a safety hazard). Since the cells are only designed for 400 psi differential pressure, no two failures in the pressure control system can allow pressure differentials to exceed 400 psi.

THE NEW SPE CELL STRUCTURE

In order to further reduce weight and simplify the high pressure SPE Electrolyzer system pressure controls, a new SPE cell structure has been developed. This new cell structure requires no pressure vessel enclosure in order to operate at elevated pressures. Demonstrated characteristics of this new cell structure include:

- Leak free at greater than 3000 psi internal pressure
- Leak free at greater than 3000 psi oxygen chamber to hydrogen chamber differential pressure
- Pressure capability demonstrated with advanced thin membranes
- Over 30,000 operating cell hours demonstrated at 2000 psi differential pressure

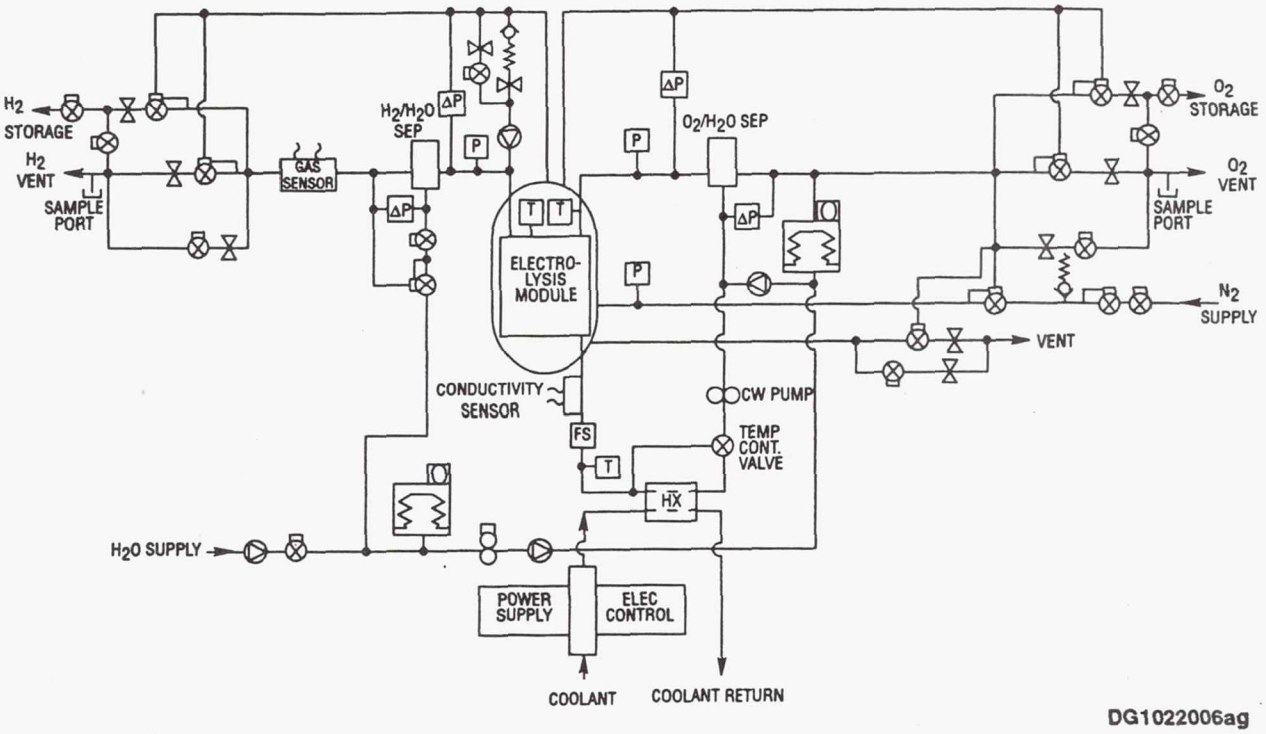

Fig. 4. - SPE Propellant Generator System Fluid Schematic

- Over 4000 operating hours on a single unit at 2000 psi differential pressure
- Three cell stack operated at 2000 psi differential pressure.

The basic construction materials for the new SPE cell structure are the same as used in the nuclear submarine SPE Oxygen Generator system. Therefore, from a materials compatibility viewpoint, the maturity of over 10 million SPE cell hours in nuclear submarine applications is maintained.

As previously mentioned, the weight of the domed stack in the Space Station SPE Propellant Generator Demonstrator is 193 lbs. In using the new SPE cell structure the stack weight for the same total active cell area would be 30 lbs. A minor volume improvement is also obtained by elimination of the pressure vessel and a reduction of the cell spacing from seven cells per inch in the nuclear submarine design to 10 cells per inch in the new structure.

The new SPE cell structure produces improved electrolyzer efficiency by significantly reducing internal component electrical resistance in the non-0membrane components. Further, ionic conductivity is improved since the new SPE cell structure is compatible with new high performance thin membranes whereas the SPE nuclear submarine electrolyzer cell structure is not. Figure 5 displays the performance improvement obtained with the new SPE cell structure.

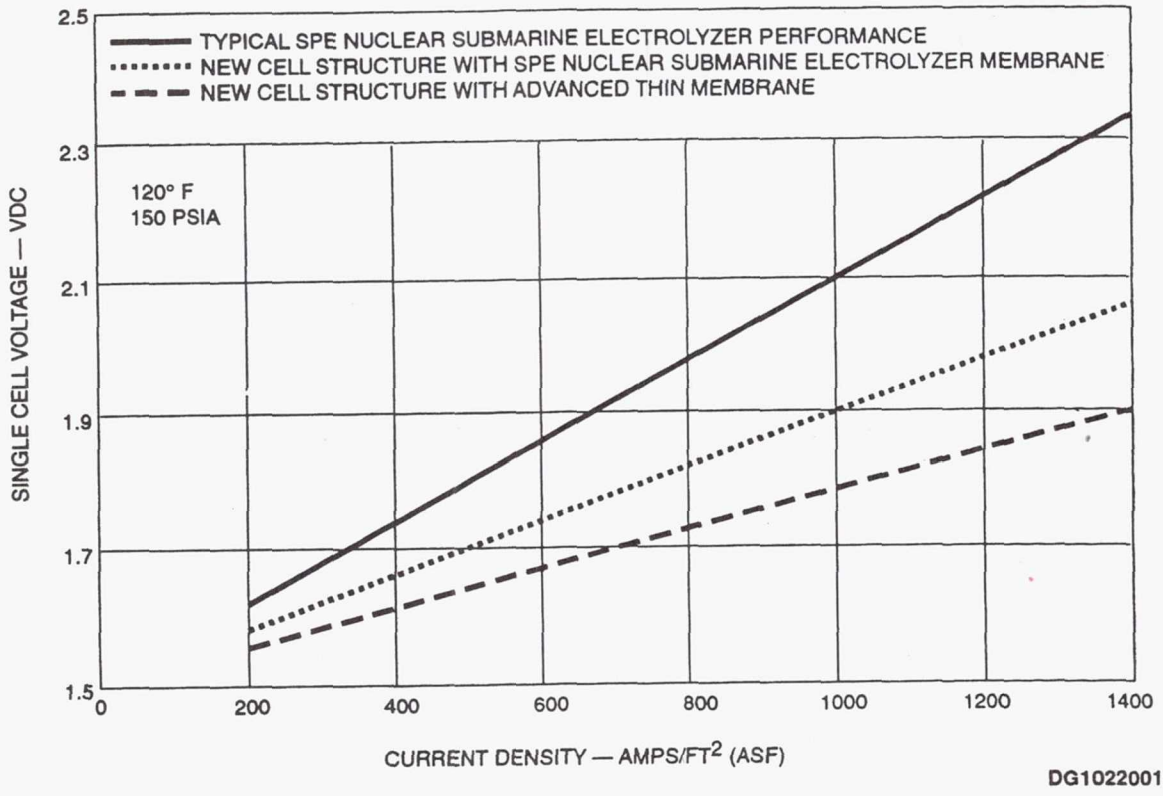

Fig. 5. - Single Cell Electrolyzer Performance

SYSTEMS IMPACT FROM THE NEW SPE CELL STRUCTURE

Apart from the aforementioned weight reductions from the new SPE cell structure, the simplification and reliability improvement in resultant systems is dramatic. In the case of the Space Station SPE Propellant Generator, the nitrogen subsystem would be altogether eliminated as would the array of regulators, valves and relief valves intended to maintain differential pressures below 400 psi. A high pressure SPE Electrolyzer fluid schematic incorporating the characteristics of the new cell structure is shown in Figure 6. This figure depicts the required SPE Electrolyzer fluid schematic when it is desired to deliver both gaseous products at high pressure (i.e., high pressure hydrogen and oxygen for reboost propulsion or lunar base energy storage). This Figure 6 fluid schematic can be compared with the previously displayed Figure 4 to obtain a full appreciation of the components eliminated by virtue of using the new SPE cell structure.

Further simplification and reliability improvements and weight reductions are obtained if only one of the product gases is desired to be delivered at high pressure. In the nuclear submarine SPE Oxygen Generator cell design both product gases are produced at high pressure when only the oxygen is required to be at 3000 psi. The hydrogen, having been produced at about 3000 psi, is simply regulated down to its desired pressure level. The new SPE cell structure allows each product gas to be generated at its own desired pressure level.

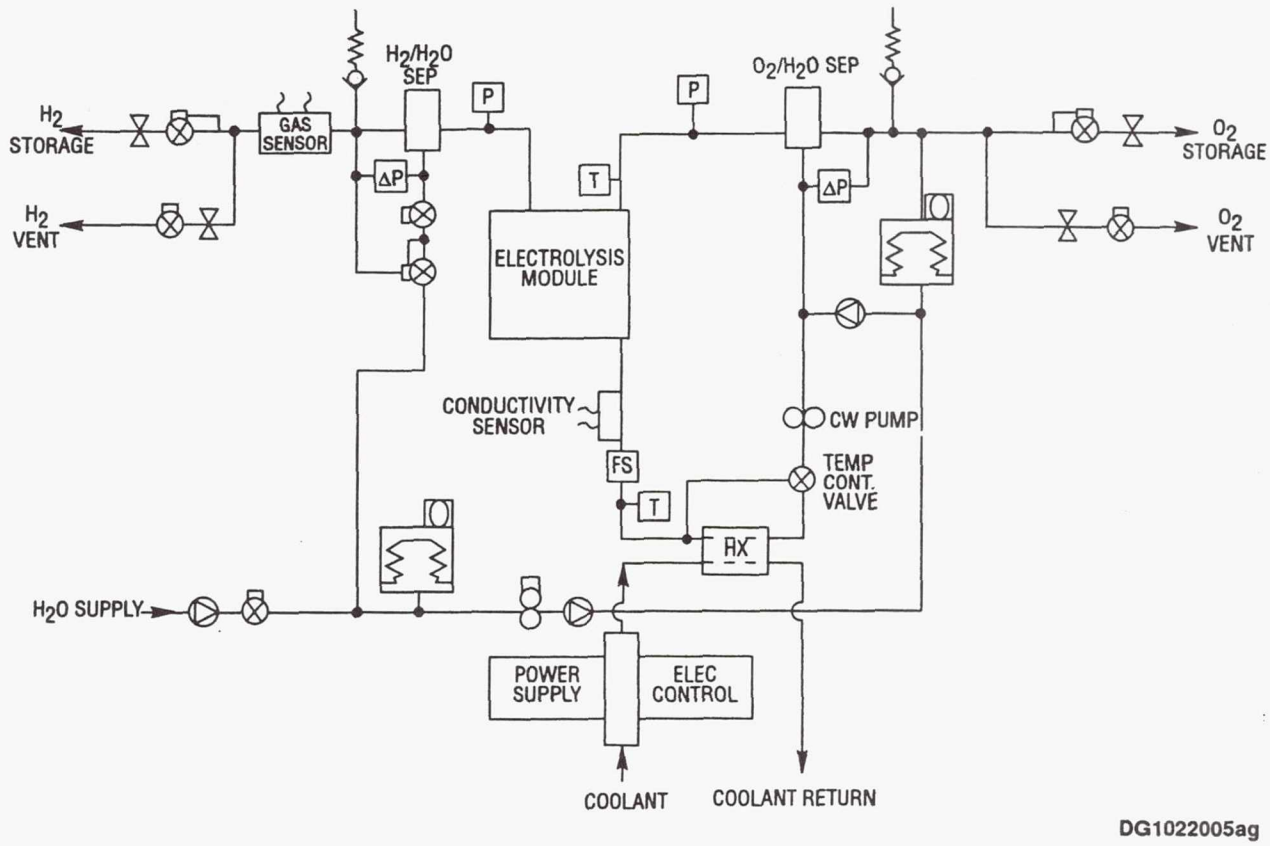

Fig. 6 - High Pressure SPE Electrolyzer Fluid Schematic with the New Cell Structure

A lunar soil or material processing facility could require high pressure hydrogen from water electrolysis while the product oxygen was discharged to ambient for local metabolic purposes. Such an electrolyzer with the new SPE cell structure is shown on Figure 7. The further improvements in this configuration include:

- The high pressure water feed pump is eliminated.
- Oxygen pressure regulation components are eliminated.
- Remaining oxygen system components can be designed for ambient pressure operation at a significantly reduced weight.
- Additionally, the high pressure hydrogen/ambient pressure oxygen configuration is more efficient due to reduced diffusion and the oxygen pressure Nernst effect.

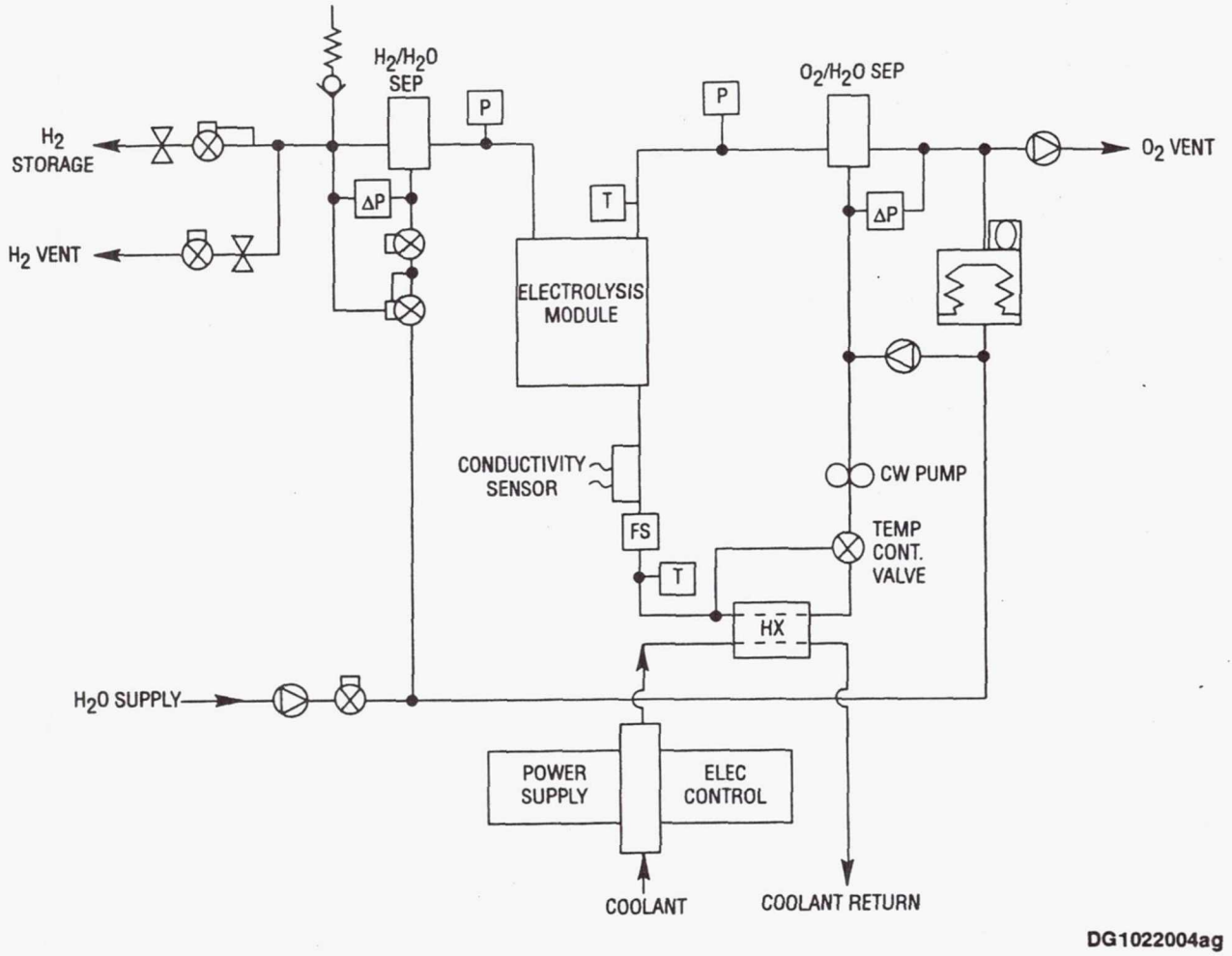

Fig. 7. - High Pressure Hydrogen SPE Electrolyzer Fluid Schematic with the New Cell Structure

The last possible configuration with the new SPE cell structure is an electrolyzer producing high pressure oxygen and ambient pressure or low pressure hydrogen. Such a configuration could be used to recharge spacesuit oxygen supplies while on orbit. Figure 8 shows the fluid schematic for high pressure oxygen and low pressure hydrogen. In this arrangement process water is introduced into the SPE Electrolyzer through the hydrogen chambers of each cell. Because water must diffuse through the cell membranes to the oxygen anodes before the molecule is split into oxygen gas, electrons and protons, current densities are limited to a maximum of 500 amperes per square foot. However, the very major advantage is the elimination of almost all of the high pressure components.

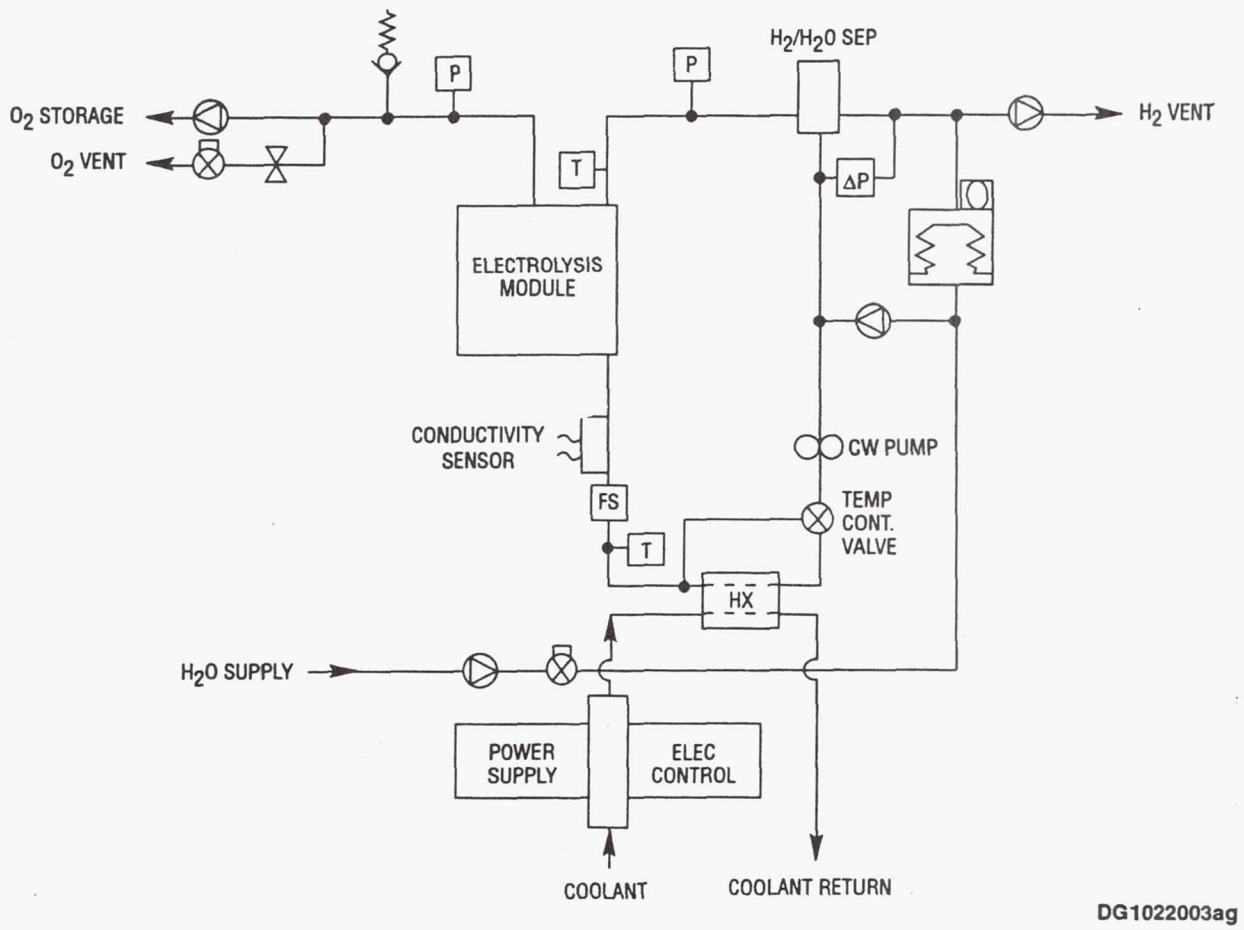

Fig. 8. - High Pressure Oxygen SPE Electrolyzer Fluid Schematic with the New Cell Structure

SUMMARY

The recently developed new SPE cell structure has allowed a much greater range of capabilities in the SPE Electrolyzer product than with prior designs. Depending on the application, it is expected that the simpler system will result in reliability improvements by at least a doubling of MTBF; system weight reductions up to 50%; an improved efficiency or a doubling of current density at a constant efficiency; and last but not least, system costs significantly reduced.

Section
Three

Advanced Concepts for Space Power

HIGH ENERGY DENSITY ALUMINUM-OXYGEN CELL

E. J. Rudd and D. W. Gibbons
ELTECH Research Corporation
Fairport Harbor, OH 44077

ABSTRACT

An alternative to a secondary battery as the power source for vehicle propulsion is a fuel cell, an example of which is the metal-air cell using metals such as aluminum, zinc, or iron. Aluminum is a particularly attractive candidate, having high energy and power densities, being environmentally acceptable and having a large, established industrial base for production and distribution.

An aluminum-oxygen system is currently under development for a UUV test vehicle and recent work has focussed upon low corrosion aluminum alloys, and an electrolyte management system for processing the by-products of the energy-producing reactions.

This paper summarizes the progress made in both areas. Anode materials capable of providing high utilization factors over current densities ranging from 5 to 150 mA/cm^2 have been identified, such materials being essential to realize mission life for the UUV. With respect to the electrolyte management system, a filter/precipitator unit has been successfully operated for over 250 hours in a large scale, half-cell system.

INTRODUCTION

An alternative to a secondary battery as the power source in a vehicle is a fuel cell. It has been shown that metals such as aluminum, zinc, lithium and iron may be used as a "fuel" in the fuel cell or metal-air battery. Aluminum is a particularly attractive candidate. The metal has both high energy and power densities, it is environmentally acceptable (as are the products of the cell reaction), it is easy to handle and has a large, industrial base for production and distribution.

The chemistry that is involved in the aluminum-air cell is shown by the following equations:

$$\text{Overall Cell Reaction: } Al + KOH + 3/4\ O_2 + 3/2\ H_2O \rightarrow KAl(OH)_4 \quad (1)$$

$$\text{Anode Reaction: } Al + KOH + 3OH^- \rightarrow KAl(OH)_4 + 3e^- \quad (1a)$$

$$\text{Cathode Reaction: } 3/4\ O_2 + 3/2\ H_2O + 3e^- \rightarrow 3OH^- \quad (1b)$$

$$\text{Corrosion Reaction: } Al + KOH + 3H_2O \rightarrow 3/2\ H_2\uparrow + KAl(OH)_4 \quad (2)$$

$$\text{Crystallization Reaction: } KAl(OH)_4 \rightarrow KOH + Al(OH)_3\downarrow \quad (3)$$

In operation, aluminum is dissolved (Equation 1) forming a soluble aluminate species and consuming the alkali metal hydroxide in the electrolyte. A corrosion reaction also occurs in the aqueous electrolyte, again forming the soluble aluminate together with hydrogen gas (Equation 2). This corrosion reaction is a coulombic inefficiency and, therefore, must be minimized. As the battery operates, the conductivity of the electrolyte decreases until precipitation or crystallization of aluminum trihydroxide occurs (Equation 3) , replenishing "free" hydroxide. Thus a "steady state" condition may be achieved with respect to electrolyte composition and conductivity, at which time the electrolyte will contain crystals of aluminum trihydroxide. As will be discussed later, controlling the electrolyte composition is very important.

The reaction at the cathode is the electroreduction of oxygen, which can only be sustained at practical rates by using a gas diffusion electrode. A three-phase boundary between the catalyst, electrolyte and reactant oxygen

must be established and this demands a unique electrode structure. It is known that the presence of carbon dioxide in the air feed stream to the cathode can lead to loss of performance, due probably to precipitation of alkali metal carbonates within the structure of the electrode. Therefore, the battery system must include a method to reduce the levels of carbon dioxide in the air feed steam, or ideally to remove it entirely. For a power source in an underwater vehicle, the fuel is necessarily oxygen, probably cryogenic oxygen, and removal of carbon dioxide is not required.

Aluminum cannot be electrodeposited from aqueous solutions, so that the aluminum-air battery is not a true secondary battery. The anode must be replaced mechanically, requiring novel features in the cell design, but offering relatively rapid refuelability.

The aluminum-air battery is, therefore, a multi-component system (Figure 1) and programs to develop this technology have necessarily focussed upon:

1. The Electrodes
2. The Electrolyte Management System, i.e., the separation of crystals of aluminum trihydroxide from the electrolyte and control of the composition and conductivity of that electrolyte
3. Cell Design to allow replacement of the anode material
4. The Auxiliary System, including a heat exchange unit, safe handling and/or disposal of hydrogen gas and control of carbon dioxide in the air feedstream

This paper will provide a brief review and summarize the recent progress made in the first two areas, the electrodes and the Electrolyte Management System.

THE ELECTRODES

Development of Aluminum Alloys

Aluminum reacts rapidly and irreversibly with oxygen to form a strongly-adhering oxide film, which largely determines the electrochemical behavior in aqueous electrolytes. Macdonald [1] has described aluminum as a passive metal, which displays an active-to-passive transition, a passive region and transpassive dissolution. The current-potential relationship can be represented schematically as in Figure 2 and a superior battery anode should, therefore, exhibit the following characteristics:

1. A very negative activation potential, (E_{CRIT})
2. High discharge currents at potentials only slightly anodic to the activation potential, i.e., a low value for the slope b,
3. A low corrosion current, (I_{CORR}), which remains low or decreases at the more anodic potentials required for dissolution.

Modification of the behavior of the oxide layer through the formation of alloys of aluminum has been extensively explored [2-6]. The incorporation of small concentrations of metals such as magnesium, calcium, zinc, gallium, indium, thallium, lead, mercury, and zinc, usually in combinations as ternary or quaternary alloys, has been effective in achieving activation (high rates of dissolution) and inhibition of corrosion.

The presence of certain impurities in the aluminum can markedly affect the electrochemical behavior. For example, the corrosion rate is particularly sensitive to the concentration of iron in the metal. Using manganese as an alloying element has been shown to reduce the rate of corrosion of primary aluminum (99.9% purity), which contains high levels of iron [7]. Typically alloy fabrication has used metal of higher purity, e.g., 99.995% and 99.999%.

The transition from fabrication at the laboratory-scale (bookmold ingots of weight approximately 3-5 lbs.) to the pilot-scale (150-250 lb. ingots) is not always readily achieved. The electrochemical performance of the large ingot material can be variable and often is inferior to that of the bookmold material. That the fabrication "practice" and thermomechanical processing is important is illustrated by the data presented as Table 1 [8]. This shows the electrochemical performance of an indium-manganese-magnesium alloy, prepared as a 150 lb. ingot by direct chill casting and processed in sections to give different grain structures and microstructures (Figure 3). For example, using the process IC, i.e., cooling slowly from the solutionizing temperature and only cold-working (cold-rolling) the alloy, will lead to an unrecrystallized structure with some precipitation of the alloying elements.

In the recent program to develop a power source for an unmanned underwater vehicle [9], emphasis has been upon mission life or the range achieved by the vehicle. It was then essential to identify an alloy with a low rate of corrosion in order to maximize the utilization of the metal fuel. An added advantage was that the hydrogen gas handling requirements within the system are minimized. The polarization characteristics remained important, as well as realizing a uniform, "smooth" surface as dissolution proceeded.

The electrochemical characteristics of three candidate alloys are presented as Table 2, showing the dependence of the anode potential and corrosion current density upon the external load. The percent utilization realized with these alloys is presented as Table 3, together with data for pure aluminum and earlier alloy materials. The target levels of performance are also shown in the table and are based upon a corrosion current density of 5 mA/cm^2 or less over the operating range of current densities.

The alloy materials were fabricated as large ingots by conventional industry practice, although the data shown as Table 2 was obtained in laboratory-scale cells. Alloy ERC-4 is clearly superior, meeting utilization requirements while maintaining acceptable polarization behavior. Alloys ERC-2 and ERC-3 closely approached the utilization targets but the former material showed poor physical characteristics during dissolution/corrosion due to intergranular attack. This was particularly serious in the full-scale single cell studies.

Development of Air Cathodes

The air cathode used in the recent programs to develop the aluminum-air or aluminum-oxygen battery as the power source in (a) an electric vehicle [8], and (b) an unmanned, underwater vehicle [9] is a high performance, two layer structure. The development of air cathode technology, involving ELTECH Research Corporation and Case Western Reserve University, has been described elsewhere [8,10] and has led to the present electrode, which is a laminate of

(a) an active layer, containing the catalyst (cobalt tetramethoxyphenylporphryn) absorbed onto a graphitized carbon black, pyrolyzed and coated with a perfluorinated ionomer,

(b) a gas supply layer, which is a mixture of the graphitized carbon black and teflon, and

(c) two nickel meshes, one on the gas side for mechanical support and the second on the electrolyte side for current distribution or collection.

This type of electrode has shown excellent extended performance under both constant current operation (Figure 4) and cyclic operation (Figure 5).

For use in the unmanned, underwater vehicle, it is necessary that the transport of oxygen gas through the electrode into the electrolyte be prevented, or at least minimized. A porous barrier layer was added, bonded to the nickel mesh and surface of the active layer. During operation the pores of this layer readily fill with electrolyte, providing an effective barrier to the transport of oxygen gas into the electrolyte.

The performance of the modified electrode, over the range of current densities of interest, is shown as Table 4.

THE ELECTROLYTE MANAGEMENT SYSTEM

Development of the Filter/Crystallizer

The Al/Air battery may operate in two basic modes, batch or steady state, depending on how one desires to treat the aluminate species generated in reactions 1 and 2. In the batch mode, fresh electrolyte is charged into the system and operation continues until the level of dissolved aluminate reaches saturation. This situation corresponds to an end of charge condition; no solids are formed during batch operation. Conversely, a near constant electrolyte composition can be maintained in the steady state mode by promoting the crystallization of the aluminate species into an insoluble hydroxide called hydrargillite, $Al(OH)_3$ (equation 3). During the cell refueling operation, the electrolyte tank is emptied and the $Al(OH)_3$ crystals may be sent to a Hall-Heroult cell for processing back into aluminum.

The performance of a batch operation battery is electrolyte volume limited and off-board facilities to process the supersaturated solutions of potassium aluminate would be required. Steady state operation produces a battery with greater capacity and a more constant voltage profile versus time for a given load. By promoting the crystallization of $Al(OH)_3$ and generating KOH, the energy capacity of the battery is significantly enhanced for a given electrolyte tank volume. This fact is illustrated in Figure 6 for a 200 liter electrolyte tank where battery capacity is plotted versus packing factor (P_f). The packing factor is a convenient way of representing filter/crystallizer performance. It may be defined as

$$P_f = \frac{V_E + V_C}{V_C}$$

where V_E is the electrolyte volume and V_C is the volume of crystals. A packing factor of 1 corresponds to a solid mass of $Al(OH)_3$ with no entrained electrolyte. A value of 2 in the figure means that the electrolyte tank is full of a dense, paste-like slurry at the end of mission, but only 100 liters of that mass is actually $Al(OH)_3$ crystals.

Solomon Zaromb and R. A. Foust, Jr. first described operation of Al/Air batteries with electrolyte regeneration by precipitation of $Al(OH)_3$ in 1962 [11,12]. Since then a variety of crystallizer/separator techniques have been attempted to control the electrolyte aluminate concentration as indicated in Table 5 [13-17]. With the exception of the filtration techniques, all of these methods have been rejected for propulsion applications because of weight, volume, and/or energy considerations.

Previous studies have shown that optimization of Al/O_2 energy and power density requires an electrolyte management system [18,19]. ELTECH's patented filter/crystallizer unit [20] maintains system simplicity, since only a filter and two additional valves are required. Mission duration is increased by continuously regenerating potassium hydroxide for subsequent reaction at the anode and storing cell discharge products compactly as a crystalline hydroxide species, $Al(OH)_3$. Continuous crystallization maintains a high and nearly constant electrolyte conductivity; therefore, stack voltage remains steady throughout the discharge cycle. As the stack is discharged, a crystal cake forms and gradually increases in thickness with a subsequent increase in pressure drop across the filter. When the pressure drop reaches a predetermined level, the cake is pulsed off the filter by backflushing (flow reversal) to settle in the bottom of the tank.

Filter/Crystallizer Operation

Test equipment utilized to investigate behavior of the filter/crystallizer is shown in Figure 7. Total hydroxide concentration is kept constant by water addition and backflush cycles are produced by 2-way solenoid "backflush valves." Figure 8 displays the results of a filter test for a power load of 40.3 Amps. This experiment was run in conjunction with an aluminum half cell driven by a power supply in which H_2 was evolved at the nickel counter-electrode. Electrolyte conductivity was continuously monitored by a Foxboro model 872 conductivity meter with an electrodeless sensor, 871EC.

Backflushes occurred at 5 psi or 202 Ah, whichever came first and, in the figure, a hollow circle indicates a backflush. A software bug prevented the system from backflushing properly for the first 20 hours. Operation began again at 40 hours after the necessary software modifications were made. Despite the system upsets the filter performed well for more than 250 hours, maintaining the conductivity between 300 and 400 mS/cm. Filter lifetime depends primarily on three factors:

1) the anode alloy,
2) the filter material, and
3) the backflush algorithm

ALUMINUM-OXYGEN SINGLE CELL PERFORMANCE

Full-scale aluminum-oxygen cells (with an active electrode area of 690 cm^2) have been integrated with the filter/crystallizer unit for a series of studies. The cell featured a fixed anode with backside temperature control and a modified AE100 cathode to minimize electrolyte leakage and oxygen gas blowthrough. The anode alloy, ERC-4, was manufactured from high purity aluminum as a 150 lb. ingot using conventional practice and thermomechanical processing. The experimental apparatus is that used in the filter/crystallizer studies (Figure 7), but incorporates the Al/O_2 single cell. The process streams were all maintained at 50°C with an oxygen gas flowrate of 1.75x stoichiometry. The unreacted oxygen was recycled to the cell using a peristaltic pump.

This single cell was operated at a constant current density of 50 mA/cm^2, drawing more than 5,000 amp-hours, during which time the cell voltage declined from 1.43 volts to 1.3 volts (see Figure 9). This decline in the cell voltage may be attributed to the increasing interelectrode gap in this particular (fixed electrode) cell design. A movable anode prevents this ohmic voltage loss and is essential to achieve the required high energy density. The data shown represents an energy yield of 3.9 kilowatt-hours/kilogram aluminum, which is significantly better than that obtained with earlier aluminum alloys.

Polarization data was recorded periodically and is presented as Figure 10 at two time and conductivity intervals. The fact that the data obtained approaches the target performance for a single cell is most promising, since, as stated above, the cell uses fixed anodes. The large decrease in cell voltage observed from open circuit to 25 mA/cm^2 is a consequence of the irreversibility of both the aluminum anode and the oxygen cathode reactions. At higher current densities the slope of the polarization curve decreases markedly, the voltage presumably being dominated by the concentration and ohmic overpotentials in the cell.

CONCLUSIONS

A brief review of the aluminum-oxygen cell and related technology has been presented. Two areas of this technology, considered to be critical to successful application in vehicular propulsion systems, were identified. Firstly, the fabrication of high performance aluminum alloys was demonstrated, using conventional industry practice. The alloys provided the required utilization targets for the aluminum fuel in operation in a vehicle. Secondly, an effective electrolyte management system has been developed, providing the necessary control of composition and conductivity of the electrolyte as well as removing the solid by-products of the energy-producing reactions. These developments led to the integration of a single, full-size aluminum-oxygen cell with the filter/precipitator unit to give over 5,000 ampere-hours of operation, with an overall energy density of 3.9 kilowatt-hours/kilogram aluminum.

ACKNOWLEDGEMENTS

A substantial part of this work was performed under the auspices of the Defense Advanced Research Projects Agency, Contract Number MDA-972-91-C-0040.

REFERENCES

1. *"Development and Evaluation of Anode Alloys for Aluminum-Air Batteries,"* Final Report to Lawrence Livermore National Laboratory from ELTECH Research Corporation, Contract Number 1806205, Section VIIIB, November 1987.

2. J. T. Reding and J. J. Newport, Materials Production, 5, 15 (1966).

3. T. Sakano, K. Toda, and M. Hanoda, Materials Production, 5, 45 (1966).

4. *"The Metallurgy and Electrochemistry of the Aluminum Anode,"* a report from the Fontana Corrosion Center for ELTECH Research Corporation, May 1984.

5. *"The Behavior of Aluminum in Aqueous Solutions,"* a report to the Norwegian Defense Research Establishment by T. Valand, NRDE-PUBL-81/1003, 1981.

6. *"Aluminum-Air Battery Development,"* Final Report to Lawrence Livermore National Laboratory from ELTECH Research Corporation, Contract Number 1806205, Sections VIIIC, VIIID, and X, November 1987.

7. *"Effect of Manganese Additions on the Performance of Aluminum Anode Alloys,"* a progress report to Lawrence Livermore National Laboratory by D. H. Scott, UCRL-15473, May 1982.

8. *"Development of Aluminum-Air Batteries for Application in Electric Vehicles,"* Final Report to Sandia National Laboratories from ELTECH Research Corporation, Contract Number SAND 91-7066, December 1990.

9. *"An Aluminum-Air Fuel Cell Power System for an Undersea Vehicle (UUV),"* Defense Advanced Research Projects Agency, Contract Number MDA-972-91-C-0040, July 1991.

10. *"Status of the Aluminum-Air Battery Technology,"* Proceedings of the Workshop on Structure Effects in Electrocatalysis and Oxygen Electrochemistry, Volume 92-11, Published by the Electrochemical Society, Inc., NJ (1992).

11. S. Zaromb, *"The Use and Behavior of Aluminum Anodes in Alkaline Primary Batteries,"* J. Electrochem. Soc., 109, 1125, (1962).

12. S. Zaromb and R. A. Foust, Jr., *"Feasibility of Electrolyte Regeneration in Aluminum Batteries,"* J. Electrochem. Soc., 109, 1191, (1962).

13. A. Maimoni, *"Lamella Settlers: Material Balances and Clarification Rates,"* Lawrence Livermore National Laboratory, UCRL-95924, 1987.

14. A. Maimoni, *"Crystallization of Aluminum Hydroxide in the Aluminum-Air Battery: Literature Review, Crystallizer Design and Results of Integrated Systems Tests,"* Lawrence Livermore National Laboratory, UCRL-53843, March 1988.

15. A. Maimoni, *"Aluminum-Air Battery Crystallizer,"* Lawrence Livermore National Laboratory, UCRL-95923, January 1987.

16. T. G. Swansiger and C. Misra, *"Development and Demonstration of Process and Components for the Control of Aluminum Air Battery Electrolyte Composition Through the Precipitation of Aluminum Trihydroxide,"* Alcoa Labs, Final Report under Subcontract No. 5724709, available as UCRL-15503, (1982).

17. M. Balasko, R. J. Adler, R. V. Edwards, and S. B. Adler, *"Initial Studies of Particle Trapping in Impeller Fluidizers,"* AIChE Symposium Series, 83, 112, (1987).

18. D. W. Gibbons, M. J. Niksa, and S. Sinsabaugh, *"Aluminum/Oxygen Fuel Cell with Continuous Electrolyte Management,"* Unmanned Systems, 9, 38, (1991).

19. A. Maimoni and J. F. Cooper, *"Development of the Aluminum-Air Battery for an Electric Vehicle,"* Energy Technology Review, Lawrence Livermore National laboratory, p. 9, April 1988.

20. R. J. Coin, C. W. Brown Jr., and J. M. Noscal, *"Metal-Hydroxide Crystallizer and Filter,"* U.S. Patent 4,994,332, (1991).

TABLE 1

Electrochemical behavior of an InMgMn alloy - effects of thermomechanical processing

	Open Circuit		100 mA/cm²		200 mA/cm²		300 mA/cm²		400 mA/cm²	
	Potl	Corr	Potl	Corr	Potl	Corr	Potl	Corr	Potl	Corr
From Process 1A*	-1.72	51.0	-1.70	35.0	-1.71	70.0	-1.66	58.5	-1.60	65.0
From Process 1B*	-1.77	38.1	-1.74	69.0	-1.56	20.0	-1.41	22.0	-1.27	10.0
From Process 1C*	-1.75	27.7	-1.67	31.9	-1.50	20.6	-1.38	17.5	-1.25	14.0
From Process 2*	-1.76	30.4	-1.71	41.0	-1.69	47.4	-1.65	58.0	-1.60	60.9

Electrolyte: 5M KOH, 60°C
Potential: Volts vs. Hg/HgO reference electrode
Corrosion: Expressed as a current density, mA/cm²
*as in Figure 3

TABLE 2

Electrochemical performance of selected alloys

	at 7 mA/cm²		at 25 mA/cm²		at 75 mA/cm²		at 125mA/cm²		at 175 mA/cm²	
	Potl	Corr	Potl	Corr	Potl	Corr	Potl	Corr	Potl	Corr
ERC-2	-1.78	4.8	-1.62	2.4	-1.47	2.7	-1.42	2.25	-1.39	1.25
ERC-3	-1.77	3.5	-1.71	1.3	-1.63	0.5	-1.35	2.0	-	-
ERC-4	-1.76	3.0	-1.58	0.2	-1.57	0.1	-1.52	0.8	-1.49	0.1

Electrolyte: 4M KOH containing 1.5M dissolved aluminum, 50°C
Electrode Area: 6.45 cm²
Potential: Volts vs. Hg/HgO reference electrode
Corrosion: Expressed as a current density, mA/cm²

TABLE 3

Corrosion characteristics of selected aluminum alloys

	% Utilization* at			
	5 mA/cm²	50 mA/cm²	100 mA/cm²	200 mA/cm²
High Purity Aluminum	0.05	31	54	76
ERC-1	12.5	56	71	81
Alcan BDW	19	72	83	92
ERC-2	43	94	97	98
ERC-3	59	98	98	-
ERC-4	62.5	~99	~99	~100
Performance Target	>50	>91	>95	>97.5

Electrolyte: 4M KOH containing 1.5M dissolved aluminum
Temperature: 50°C

*% Utilization = $\frac{\text{Faradaic Dissolution Current (load)}}{\text{Faradaic Dissolution Current + Corrosion Current}}$ %

TABLE 4

Electrochemical performance of the modified cathode

	Cathode Potential* (volts) vs. Hg/HgO at				
	Open Circuit	25 mA/cm²	50 mA/cm²	100 mA/cm²	200 mA/cm²
After 27 hours at 50 mA/cm²	+0.06	-0.07	-0.1	-0.13	-0.19
After 313 hours at 50 mA/cm²	+0.06	-0.06	-0.09	-0.12	-0.18
After 1000 hours at 50 mA/cm²	+0.07	-0.07	-0.09	-0.13	-0.21

Electrolyte: 4M KOH at 60°C
Gas: Oxygen, dry
Electrode Area: 14 cm²
*Corrected for IR contributions

TABLE 5

Alternative Solids Separation Techniques

- Gravity Settler
- Lamella Settler
- Hydrocyclone
- Centrifuge
- Wound Cartridge Filter
- Cross Flow Filter
- Helipump Impeller Fluidizer
- Poulos Separator

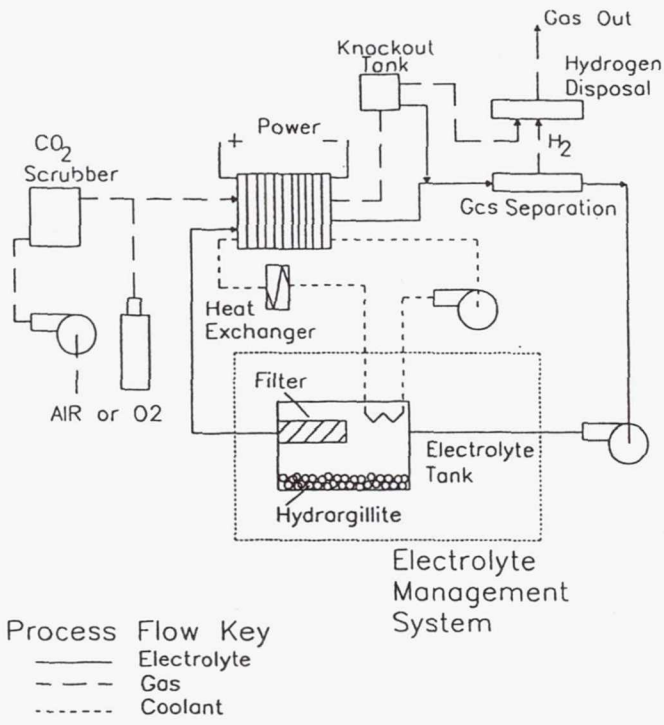

Fig. 1. -- Schematic Representation of the Aluminum-Oxygen cell system.

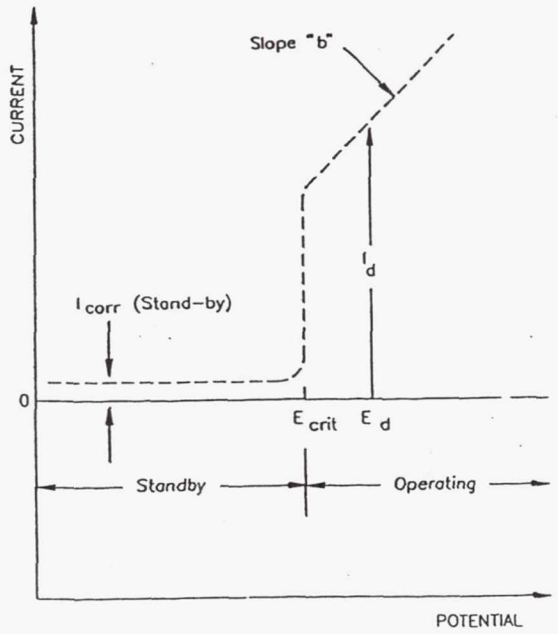

Fig. 2. -- Schematic representation of the current-potential relationship for aluminum in alkaline solutions.

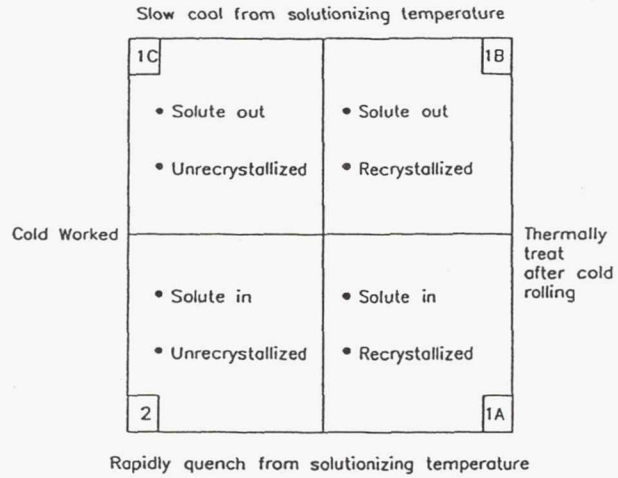

Fig. 3. -- Matrix to show the four types of structures resulting from the processing variations.

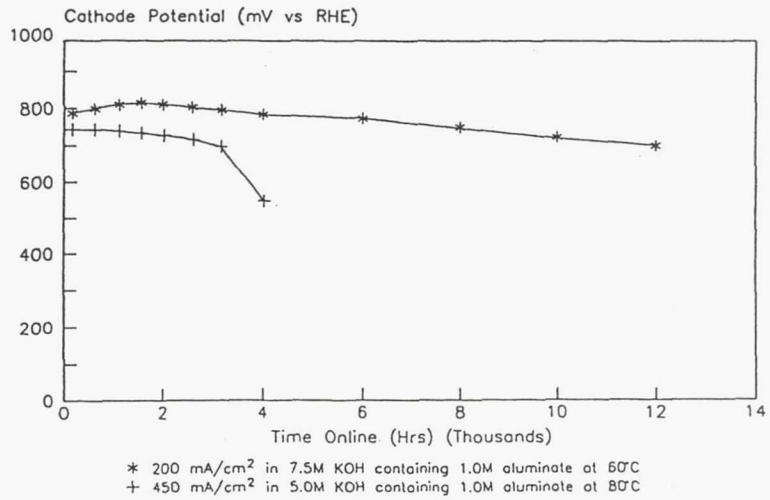

Fig. 4. -- Performance of polymer-modified air cathodes - constant current operation.

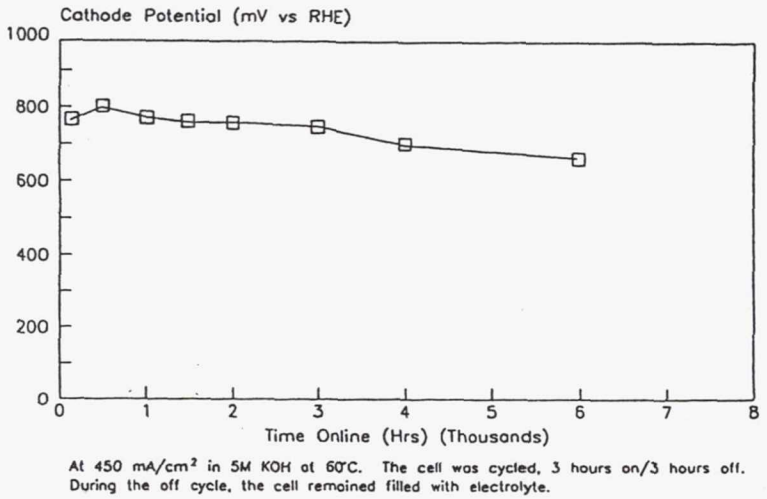

Fig. 5. -- Performance of polymer-modified air cathodes - cyclic operation.

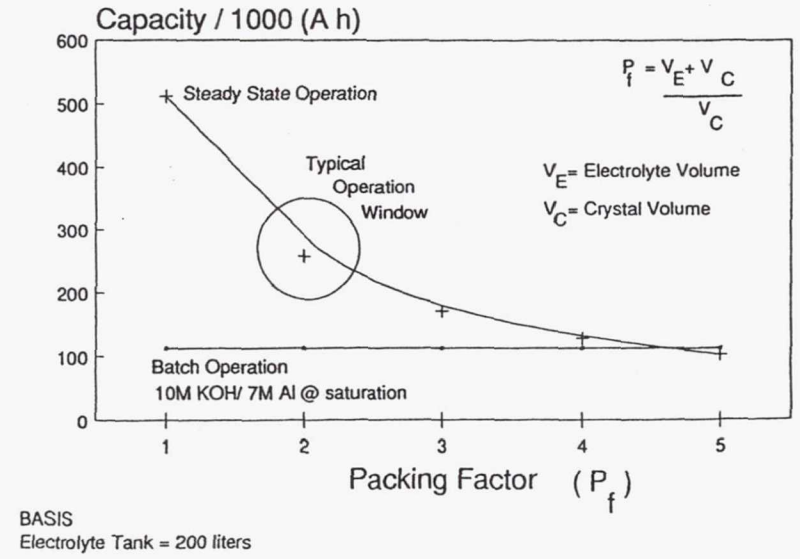

Fig. 6. -- Capacity for a given electrolyte volume.

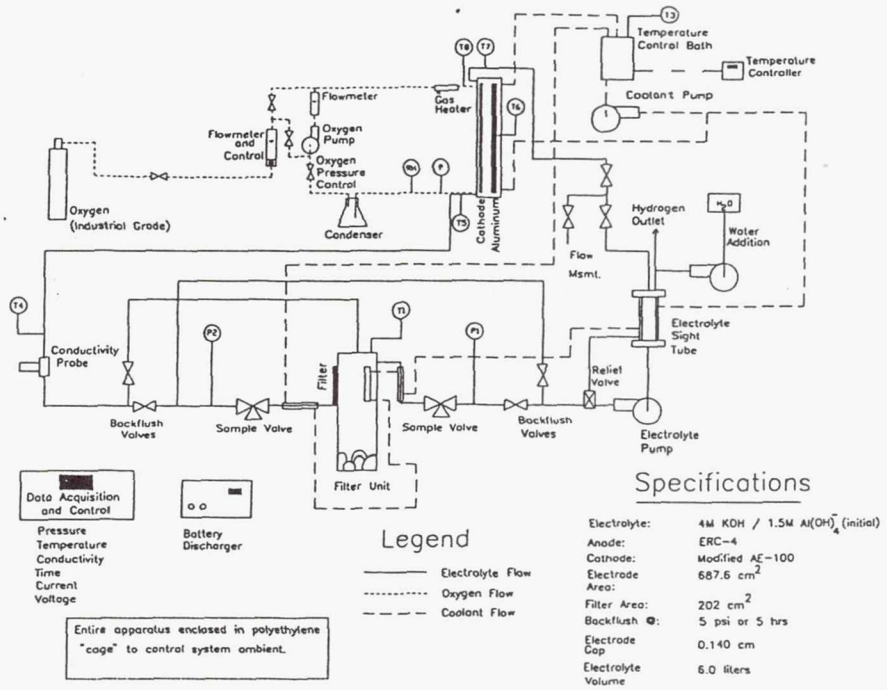

Fig. 7.-- Al/O_2 single cell test apparatus.

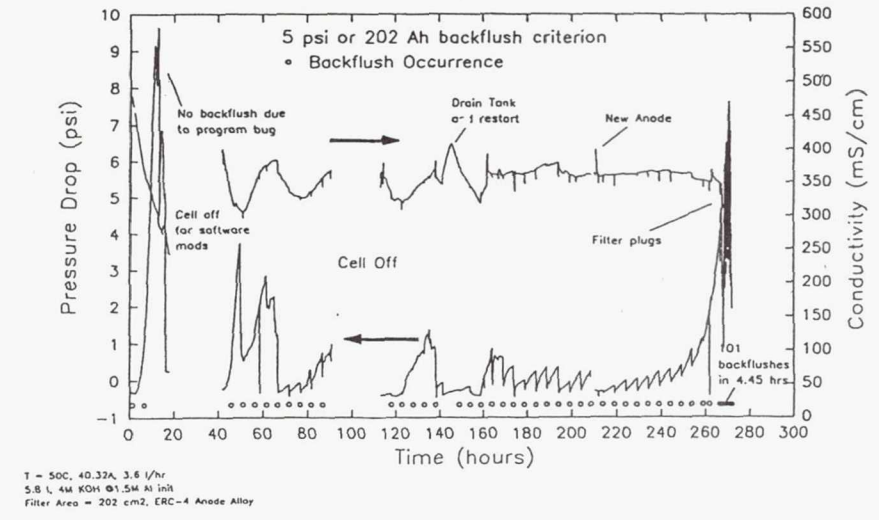

Fig. 8. -- Filter/crystallizer test.

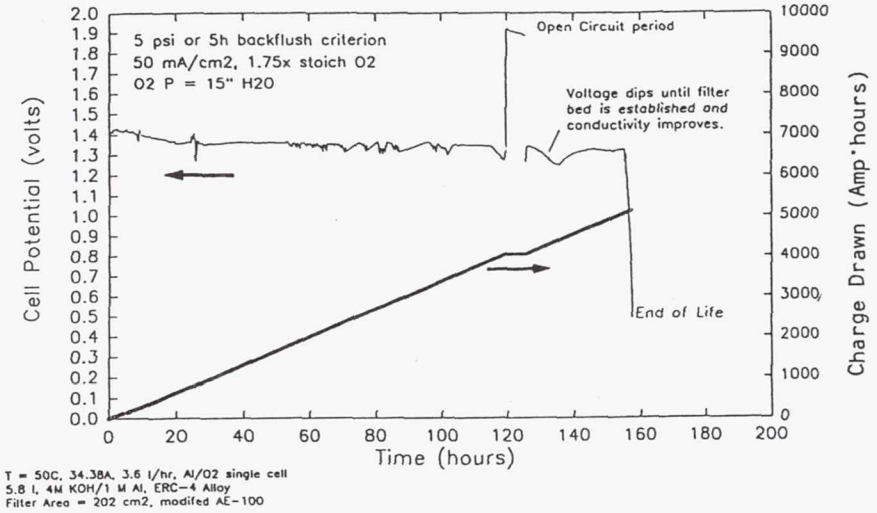

Fig. 9. -- Al/O_2 single cell test.

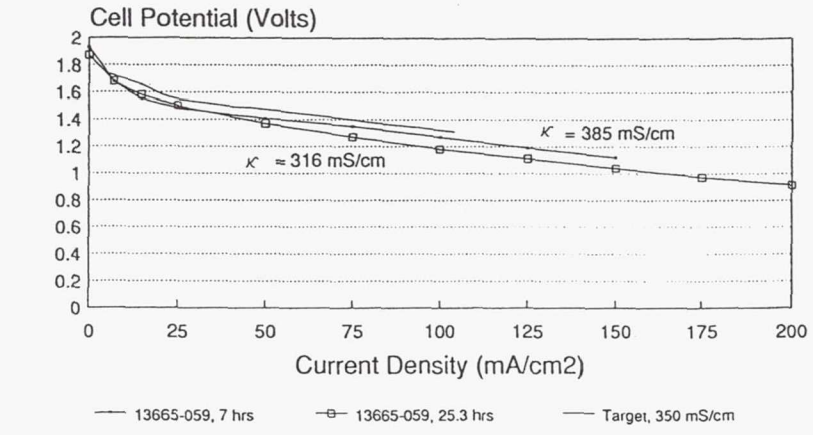

Fig. 10. -- Full scale Al/O_2 single cell results polarizations during mean power test.

COMPOSITE FIBER STRUCTURES FOR CATALYSTS AND ELECTRODES

Christopher J. Marrion, Donald R. Cahela, Soonho Ahn
and Bruce J. Tatarchuk

Department of Chemical Engineering
and the Space Power Institute
Auburn University, Alabama 36849

ABSTRACT

We have recently envisioned a process wherein fibers of various metals in the 0.5 to 15 micron diameter range are slurried in concert with cellulose fibers and various other materials in the form of particulates and/or fibers. The resulting slurry is cast via a wet-lay process into a sheet and dried to produce a free-standing sheet of "composite paper." When the "preform" sheet is sintered in hydrogen, the bulk of the cellulose is removed with the secondary fibers and/or particulates being entrapped by the sinter-locked network provided by the metal fibers. The resulting material is unique, in that it allows the intimate contacting and combination of heretofore mutually exclusive materials and properties. Moreover, due to the ease of paper manufacture and processing, the resulting materials are relatively inexpensive and can be fabricated into a wide range of three-dimensional structures. Also, because cellulose is both a binder and a pore-former, structures combining high levels of active surface area and high void volume (i.e., low pressure drop) can be prepared as free-standing flow through monoliths.

INTRODUCTION

Electrode structures and catalysts which function at a steady-state conversion level must simultaneously accommodate a number of physical processes including, among others: surface and interface kinetics and selectivity, heat transport, mass transport, thermal and/or electrical conduction, corrosion and sintering/deactivation. To beneficially accomplish these

physical processes electrode/catalyst designers must consider a number of individual design factors including void volume, specific surface areas of both catalytic/electrocatalytic materials and supports, micro- and macroporosity, mechanical stability, cost, safety and the addition of various additives and binders to promote wetability, hydrophobicity, reactant contacting and interfacial mass transport.

Many of the high surface area electrodes in use today are fabricated from particulate-based materials which are retained onto a screen/collector my means of various organic and polymeric binders (e.g., PTFE). Due to the packing constraints provided by these particulates and binders, free-standing electrode structures are only available in a limited range of flexibilities, void volumes and macroporosities. The resulting effectiveness factors and Thiele moduli often preclude the effective utilization of high surface area catalysts/electrocatalysts because of intra-electrode heat and mass transport limitations.

The focus of this effort is to utilize fibrous precursors as building blocks for enhanced electrode and catalyst structures. As shown in Figure 1, there are a number of inherent benefits derived from using these materials in electrically conductive and/or high surface area structures. Furthermore, the high aspect ratio possessed by fibers allows fabrication of free-standing structures of higher void volume and less resistance to both heat and mass transport. The process described herein also utilizes the sinter-attachment of micronic metal fibers to provide necessary mechanical contacting and stability. This feature eliminates the a priori use of void-filling binders unless they are critically required for other chemical reasons.

EXPERIMENTAL

Details of paper preform fabrication, sintering conditions, optimization considerations, choice of materials and other electrode preparation techniques may be found in references [1-7].

FABRICATION OF MONOLITHIC STRUCTURES

Due to the ease of paper processing and handling, preform sheets may be corrugated and rolled or layered so as to create flow channels for low transport resistance and high accessibility of the constituents (see Figure 2). Preform sheets may also be layered prior to sintering so as to create thicker electrodes/catalysts which can readily accommodate graded porosities and graded compositions depending upon the number and type of sheets which are stacked. Preform sheets incorporating ceramic fibers and cellulose may also be layered into a stack so as to integrally incorporate an electrolyte separator.

Metallic fibers in the preform permit these materials to be sintered to various current collectors and metallic surfaces as shown in Figures 3-5. With respect to the structures shown in Figures 3-5, cyclic voltammetry and other electrochemical techniques generally demonstrate excellent mechanical and electrical connectivity between micronic metal fibers, high surface area activated carbon fibers and the various substrates depicted. The only exception being the interior of a tube. Upon sintering and cellulose removal, there is a net shrinkage of the preform causing it to adhere quite tightly to the exterior of a curved surface, whereas there is a net recession away from the interior surface. This problem has been addressed by pre-sintering to a metallic mesh followed by attachment to the interior. The geometries shown in Figures 3-5 appear to meet many of the requirements necessary for incorporating fibrous materials into real devices while permitting electrical conduction as well as appropriate heat and mass transport.

INCLUSION OF CERAMICS, REFRACTORIES AND CATALYSTS: CONCOMITANT IMPACT ON VOID VOLUME

When high surface area and electrically conductive electrodes/catalysts are desired it is possible to incorporate activated carbon fibers from a variety of sources into the preform

along with appropriate metal fibers. Activated carbon fibers provide free-standing structures with up to 98% void volume. Such void volumes are beneficial for promoting mass transport, however, volumetric reactivity and energy density density are often sacrificed. This is especially the case for an electrochemical structure, where the void volume must be filled with the mass of a relatively low conductivity electrolyte. In these instances, the electrode/catalyst designer often requires a lower void structure and it is beneficial to use particulate based materials along with metallic fibers. Particulates allow more dense packing and are available in a broad selection of physical properties at reduced costs compared to fibers.

To address the above noted design consideration, Figures 6-9 demonstrate the feasibility of retaining catalytic/electrocatalytic particulates at various loading and compaction levels, approaching ca. 20% void volume. The high aspect ratio of the metallic fibers permits them to provide a "binding" function at a fraction of the corresponding weight or volume required for an organic or particulate binder. Metallic fibers also impart superior electrical and thermal conduction. Moreover, intraelectrode potential drops and ohmic losses are minimized and there is an opportunity to use electrocatalytic materials and supports often considered too resistive for practical cell designs. As demonstrated in these Figures, loadings as high as 6:1, particulate:metal fiber, are readily obtained. Compaction and void volume are controlled by mechanical pressure before, after or during sintering, as well as the amount of cellulose added to the preform. The aspect ratio and geometry of the fibers and particulates also impact upon the void volume.

ADDITION OF PRECIOUS METALS

Figure 10 provides selective chemisorption data and O_2-H_2 titration data for a stainless steel-activated carbon fiber electrocatalyst following addition of platinum. Impregnation is via an incipient-wetness technique with the liquid exterior to the carbon fibers removed by wicking into an appropriate blotter. High dispersions are obtained provided

the platinum is added after metal fiber sintering. Noncorrosive impregnation solutions must also be used to avoid attack on the stainless steel fibers.

TRANSPORT RESISTANCE VERSUS CATALYTIC ACTIVITY

Figure 11 provides polarization curves for oxygen reduction in a KOH half-cell, details of which are described elsewhere [8]. The salient feature of this plot is that a stainless steel-carbon fiber composite electrode (without Pt) can outperform a Pt-containing commercial electrocatalyst at higher current densities. Since the slopes of the polarization curves shown in Figure 11 are proportional to the lumped resistance, it appears that the nascent reactivity and easy accessibility of the activated carbon in the composite fiber electrode permit it to operate with a reduced mass transport limitation. Further details of this study, and an impedance analysis of the various resistance terms, are described elsewhere [8].

CONCLUSIONS

Mixed fibrous materials can be prepared from dissimilar materials to achieve physical properties which are often considered to be mutually exclusive using other means or materials. The enabling attribute/requirement is the entrapment of one or more components within the sinter-bonded matrix of the other component. Unique variations of specific surface area, void volume, macroporosity, etc., are obtained. Particulate materials may also be incorporated into these structures as well as active electrocatalysts. The ease of paper-making and paper processing/reprocessing permits ready fabrication of various monoliths and integrated structures at relatively low cost.

The nature of this fabrication approach, and the physical attributes of the resulting materials, permit the electrode/catalyst designer to accommodate heat transfer, mass

transfer, ohmic losses, interfacial kinetics and interphase contacting in a manner not previously available.

ACKNOWLEDGEMENTS

The authors wish to thank the following sponsors for support of various portions of the work described herein. SDIO/TNI via DNA001-85-C-0183, SDIO/TNI via DNA001-90-C-0127, U.S. Army - DAAL039260205-2, and the Exxon Foundation.

REFERENCES

1. D. Kohler, J. Zabasajja, A. Krishnagopalan, and B.J. Tatarchuk, J. Electrochem. Soc., 137 (1), 136 (1990)

2. D. Kohler, J. Zabasajja, F. Rose, and B.J. Tatarchuk, J. Electrochem. Soc., 137 (6), 1750 (1990)

3. B.J. Tatarchuk, M.F. Rose, A. Krishnagopalan, J.N. Zabasajja, and D. Kohler, U.S. Patent 5,080,963

4. B.J. Tatarchuk, U.S. Patent 5,096,663

5. B.J. Tatarchuk, M.F. Rose, A. Krishnagopalan, U.S. Patent 5,102,745

6. D.A. Kohler, M.S. Thesis, Auburn University (1989)

7. C.Y. Wu, M.S. Thesis, Auburn University (1991)

8. S. Ahn, Ph.D. Dissertation, Auburn University (1992)

Figure 1

Preparation and Design Rationale

Technical Approach: Attributes of the Composite Electrode

Central Theme: New materials from high aspect ratio precursors

Benefits:

- Thin fibers are more accessible to gases and electrolytes,
- Thin fibrous electrodes can be prepared with adjustable porosities and void volumes to enhance inter- and intra-electrode transport while accommodating required precipitation of chemical products at the cathode (viz., battery applications),
- Thin fibers can form interlocked networks of dissimilar and normally incompatible materials (i.e., metals, ceramics, carbons, etc.),
- Thin fibers provide very high surface to volume ratios yet are still self-supporting,
- Thin fibers can provide "averaged" material properties which are normally thought to be mutually exclusive (i.e., high surface area and high electrical conductivity, thermal and electrical conductivities, thermal expansion factors, etc.),
- Interlocked networks of thin fibers bonded to metallic backings provide flexible electrodes structures which can be readily assembled into devices even when one of the components is relatively brittle,
- Sintered fiber networks do not require pressure, are clog resistant, and possess higher inherent conductivities than powder systems.

Fabrication of Electrode and Catalyst Monoliths

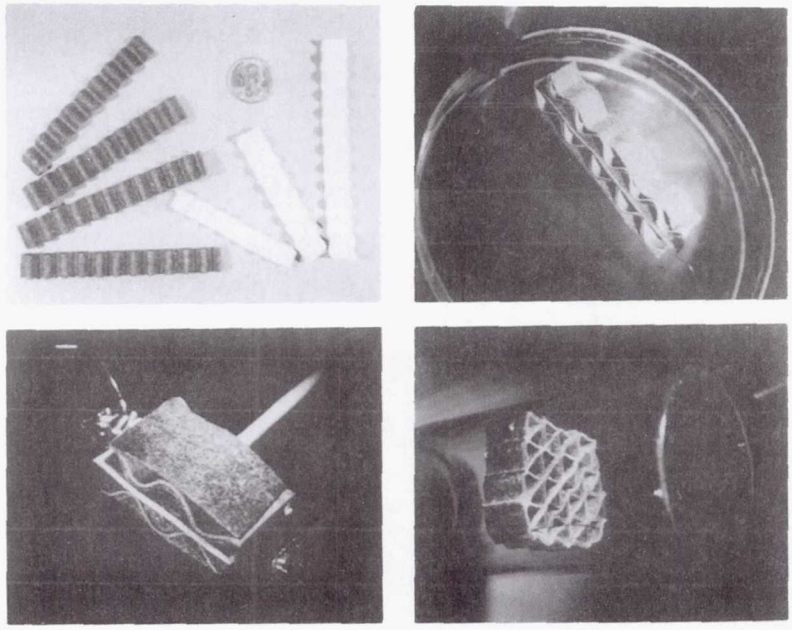

Figure 2

Figure 3

Composite Fiber Electrodes and Catalysts in Various Geometries

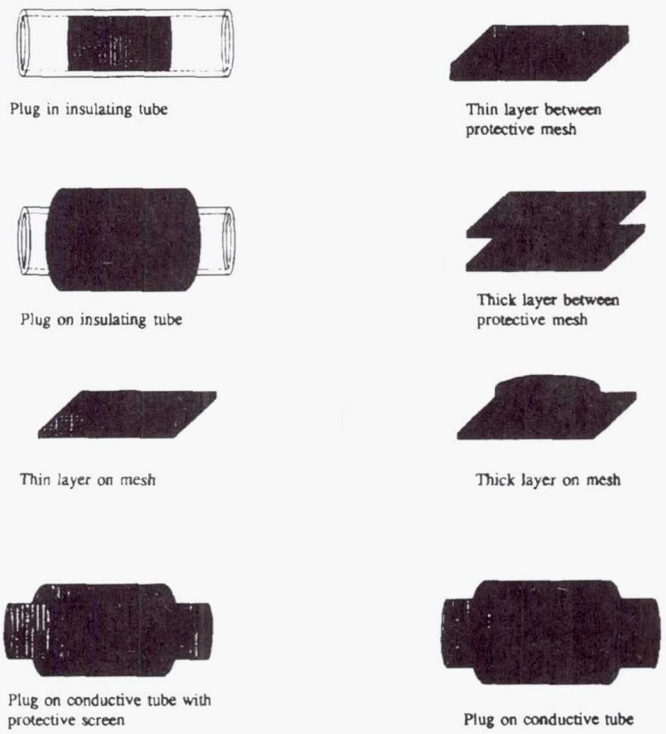

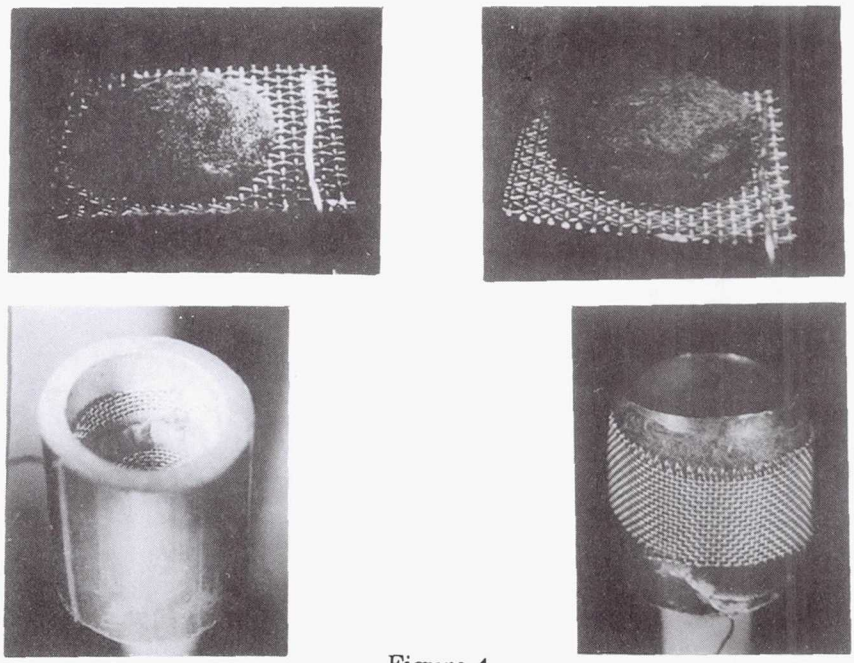

Figure 4

Composite Fiber Electrodes and Catalysts in Various Geometries

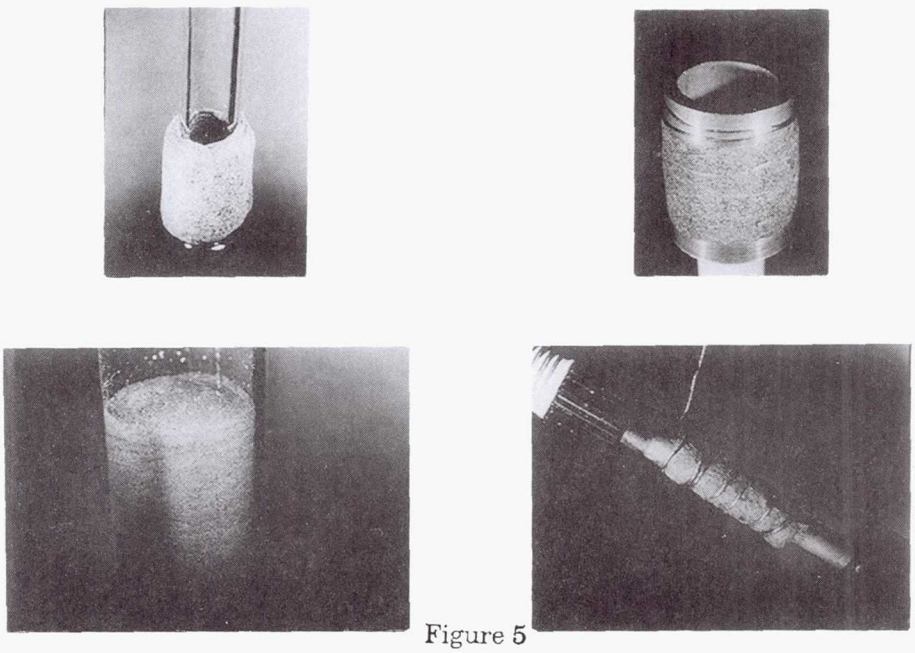

Figure 5

Fibrous Catalyst/Electrode Incorporating Carbonaceous Particulate

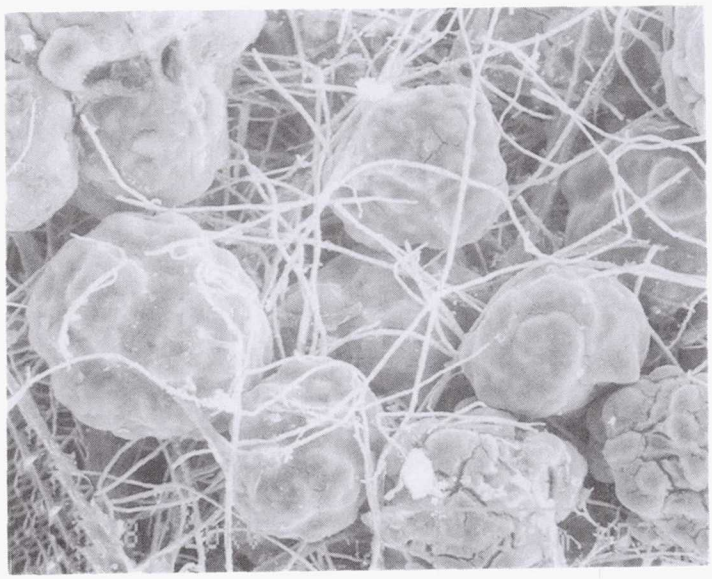

6 g Particulate : 1 g Steel Fiber

Figure 6

Fibrous Catalyst/Electrode Incorporating Carbonaceous Particulate

Particulate (@ 150 m^2/g) : 2 µm Stainless Steel

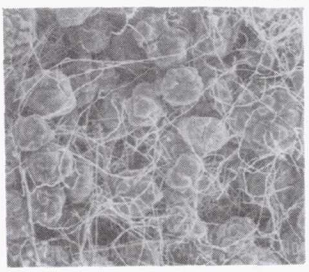

Sintered 6:1 Product

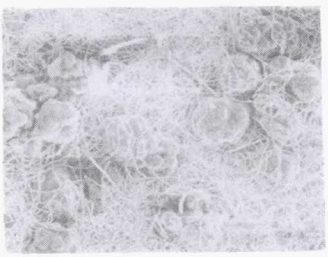

Preform @ 6:1 Loading

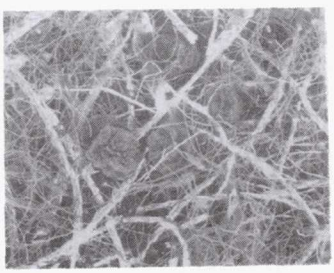

Preform 1:1 Loading

Figure 7

Stainless Steel Fibrous Network Incorporating Spray - Dried Ceramic

6 g Ceramic : 1 g Steel Fibers

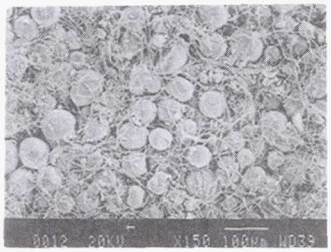

Preform After Densification/Sintering

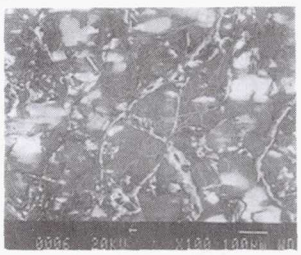

Preform Prior To Sintering

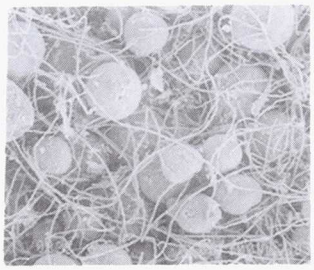

Preform After Sintering

Preform Prior To Sintering

Figure 8

Stainless Steel Fibrous Network Incorporating Spray - Dried Ceramic

6 g Ceramic : 1 g Steel Fibers

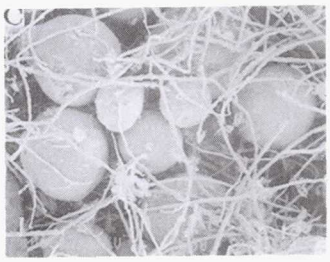

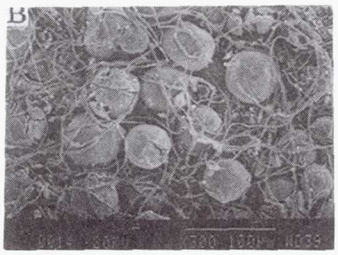

A. Extended Densification

B. Intermediate Densification

C. Minor Densification

Figure 9

Figure 10
Chemisorption and Titration
Electrodes Impregnated with Pt After Sintering

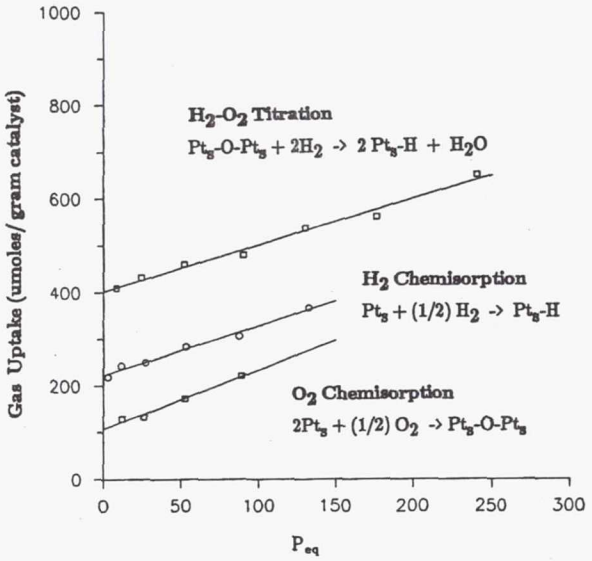

Catalyst	Impreg. Method	Metal Precursor	H_2 Uptake	Dispersion	Particle Size
13.6% Pt/C	Soaking/ Blotting	$(NH_3)_4Pt(NO_3)_2$	225 umoles	0.65	1.7 nm

Figure 11
O_2 Reduction in KOH Half - Cells

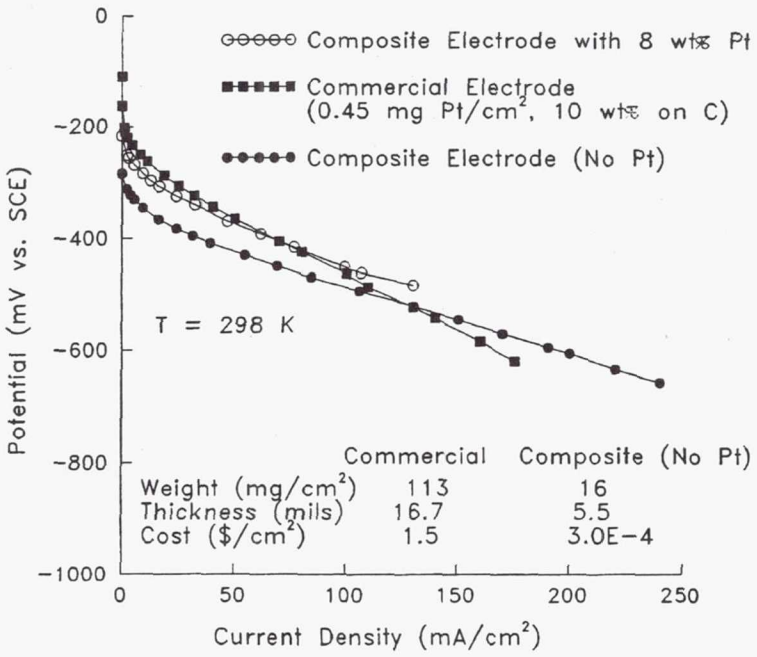

LIMITING FACTORS FOR CARBON BASED CHEMICAL DOUBLE LAYER CAPACITORS

M. Frank Rose, C. Johnson, T. Owens and B. Stevens
Space Power Institute
231 Leach Center
Auburn University
Auburn, Al 36849

ABSTRACT

The Chemical Double Layer (CDL) capacitor improves the energy storage density dramatically when compared with conventional electrolytic capacitors. When compared to batteries, the CDL Capacitor is much less energy dense, however the power density is orders of magnitude better. As a result, CDL-battery combinations present an interesting pulse power system with many potential applications. Due to the nature of the CDL, it is inherently a low voltage device. The applications of the CDL can be tailored to auxiliary energy and burst mode storages which require fast charge/discharge cycles. Typical of the applications envisioned are power system backup, directed energy weapons concepts, electric automobiles, and electric actuators. In this paper, we will discuss some of the general characteristics of carbon-based CDL technology, describing the structure, performance parameters, and methods of construction. Further, analytical and experimental results which define the state of the art are presented and described in terms of impact on applications.

INTRODUCTION

The major electrical energy storage systems of use in pulsed applications are capacitors, batteries and inductors. The application of inductive storage, except for short storage times, is dominated by the need for cryogens and superconducting material. Consequently, the intermediate storage needs have been almost totally dominated by batteries and capacitors or some combination of the two. Although the battery has high energy density, it suffers from low power density and a limited number of charge-discharge cycles. The highest energy density, low voltage capacitors to date have been the electrolytic capacitors. While high power density is possible, the units are polarity sensitive and in the high power versions, must be conditioned to maintain a fully functioning unit. It is used extensively for voltage smoothing in power systems. The Chemical Double Layer (CDL) capacitors, using aqueous electrolytes, have power densities much better than electrolytics and at least an order of magnitude better than the best conventional batteries.

In 1887, Helmholtz discovered that the interface between a conductor and a liquid electrolyte formed a layer capable of storing charge. For strong electrolytes, this layer [1] is estimated to be only a few angstroms thick. Due to the fact that there are materials with surface areas of a thousand square meters per gram, it is possible to engineer practical capacitors with the surface area, interface thickness ratio on the order of the inverse of the permittivity of free space. This results in capacitors with a capacitance greater than 1 farad in a volume on the order of a "dime". This technology was first pursued to practice by SOHIO [2] and NEC[3], and there are a considerable number of units commercially available for low voltage, high impedance applications. These units usually employ a rare-earth oxide or some form of carbon as the large surface area materials. There are a number of electrolytes, both aqueous and organic, available for use in these capacitors. The ultimate choice is governed by the application. In general, use of the organic electrolytes increases energy storage density at the expense of internal resistance.

There are numerous potential applications for the CDL technology. To date, they are used for memory backup, and as short-term backup power supplies. They are currently being investigated for such applications as electric vehicle acceleration and electromagnetic actuation. The restrictive number of applications is due in part to the need for pressure to reduce the equivalent series resistance to low values. While easy to achieve in a laboratory prototype, it is difficult to produce a commercial product with a pressurizing system. Further, due to the differences in pore geometry, the capacitance is very much a function of frequency which tends to make application at DC or less than 60 hz the primary region of operation. For high energy/power density applications, the ultimate device would possess the energy storage characteristics of a battery and the power characteristics of a capacitor. The CDL technology is a step in the right direction. During the past 5 years, there have been significant technological advances which tend to extend the range of applications by engineering out the need for pressure to obtain low internal resistance and by optimizing the pore geometry for a particular application. In that sense, they are "designer" devices which can be custom tailored to a particular task. The limits of CDL technology using carbon as the large surface area material have been explored extensively at the Space Power Institute. The remainder of this paper will present some of our results.

CAPACITOR STRUCTURE

Double Layer Capacitor Geometry

Figure 1a is a schematic drawing of a practical embodiment of the CDL technology utilizing carbon as the large surface area material. The carbon beds and membrane are soaked in a suitable electrolyte such as dilute solutions of sulfuric acid or potassium hydroxide. For powder beds, a seal is necessary to hold the powder in place, confine the electrolyte and serve as a confining medium when the finished product is placed under pressure to increase the contact area between individual particles in the compact. The end plates are chosen for compatibility with the electrolyte and as thin as possible. The porous membranes are suitable plastics which can be obtained in a variety of thicknesses and porosities. The rough equivalent electrically is that of two capacitors connected in series with the interconnect being the distributed electrolyte which ensures contact with the double layer. On the "other side of the capacitor", electrical contact is made through the individual carbon grains to the metallic end plates. It is obvious that the resistance of this path is greatly determined by the surface contact area between the individual grains and the position of any given grain within the bed. As a result, it is necessary to add considerable pressure to this geometry to reduce the internal resistance to a value which is acceptable. For potassium hydroxide electrolyte, 0.0025 cm nickel is chosen for the end plates and 0.0025 cm Nafion separators are used in laboratory cells. The thickness of the carbon bed is varied up to several millimeters as needed.

Figure 1b illustrates a capacitor structure which greatly reduces the need for pressure to produce a low equivalent series resistance. The active area in the capacitor is now made up of sinter locked fine metal fibers with diameters of a few microns interspersed throughout the bed of large surface area material. This unique composite can be made with high uniformity using standard paper making technology and has been described in detail elsewhere [4]. To further enhance conductivity, the metal fibers are also sinter locked to the metallic end plate which is of the same material as the fibers. The metal fibers drastically reduce the resistance associated with the carbon bed by providing larger metallic surface area for the individual grains or fibers of carbon to contact electrically. Capacitors made in this fashion show little or no pressure dependence of the equivalent series resistance.

Double Layer

It is very difficult to directly probe the interface between the metallic conductor and an electrolyte interface. There are a number of theoretical models [5] [6] whose only means of verification is the ability to predict macroscopic measurements such as capacitance and the charge storage associated with the double layer. The key parameters of interest for the double layer as an energy storage media are the value of the relative dielectric constant associated with the region in which the charge is stored, the thickness of the layer and the voltage at which the layer fails. These parameters are functions of the electrolyte species, and its concentration. Rose [1] has used a modified version of the Guoy-Chapman theory to calculate the thickness of the double layer as a function of concentration for strong aqueous electrolytes such as sulfuric acid and potassium hydroxide. This model shows that the storage layer decreases with electrolyte concentration to molecular dimensions which is consistent with the assumption that the energy storage media is essentially a single layer of molecules of the solvent. For aqueous electrolytes, this dimension is that of the water molecule and is on the order of angstroms. Fundamental studies by Bockris [6] indicate that the relative dielectric constant of this layer is on the order of 10. From an engineering perspective, the practical limit to voltage standoff occurs when the potential needed to dissociate the water is exceeded. That value is about 1.2 volts per cell. Substitution of these estimates of the critical parameters into the expression for capacitance indicates that it should be possible to build capacitors with capacitance on the order of 20-50 farads per real square centimeter of surface area. This is in general consistent with experimental results.

Large Surface Area Materials

Materials such as the activated carbons are highly fractionated with enormous surface area as a result of the structure pores. The large surface area materials most often used in the double layer capacitor technologies are the rare earth oxides and carbons such as "carbon black". In general, the carbons have the highest surface areas. It is possible to purchase commercially available materials which have surface areas greater than 2000 m^2/gm. Surface area of this magnitude is only achievable with a highly porous structure with average pore dimensions of a few angstroms in diameter. Activated carbon purchased from the American Norit Company, Inc. specifies that the surface area is about 1500 m^2/gm with a mean pore dimension of 22 angstroms. Clearly, pores with dimensions on the order of twice the double layer thickness or less cannot be used to store charge. As a result, much of the surface area is not accessible in any finished device. Further, it is necessary for the electrolyte to penetrate the pore in order that a conducting path be available to the external circuit. Consequently, the resistance from each micro-pore to the external circuit is dependent upon its size and position within the carbon bed. Clearly a trade off exists between the surface area and the pore dimensions for a particular application. Figure 2 is an approximate circuit diagram for a CDL. Starting at the top of the figure, the external resistance R_{ext} is associated with the external circuit, load, diagnostics, etc, and is under the control of the experimenter. Since the total capacitance of the array is the sum of the capacitance of billions of tiny pores, of differing values, in parallel, it is instructive to examine how the array is structured at least qualitatively. Since there is mirror symmetry in the unit, it is sufficient to examine the electrical pathways only to the membrane. For a given pore, there is the resistance associated with the current carrying path through the metallic end plate/metallic fibers and through the fiber/grains of carbon. In a porous bed with many fibers/grains tightly packed, there are a number of current carrying paths of various resistances possible from any given pore. The value of the resistance associated with that path is a function of the packing parameters, pressure, resistivity of the bed material, resistivity of the metallic end plates,and position within the bed. The Helmholtz double layer discussed above represents the "dielectric" or energy storage media in the usual sense. Passing through the double layer, the conducting electrolyte in the pore constitutes the other conducting electrode. The specific resistance of a pore will be a function of the diameter and length of the pore and has been designated as R_p. In similar fashion, the electrolyte is distributed

throughout the interstices of the bed forming multiple pathways to the porous membrane. The resistance R_{memb} is a function of the porosity of the membrane and is readily determined by experiment to be essentially the percent porosity times the resistivity of the electrolyte. Note that each pore is connected to its neighbor by shunt resistances which are functions of the resistivities of the constituents. The net result is that charge can be redistributed during and after a discharge event which has not totally depleted the stored energy. While a nuisance, this is not particularly of concern for most of the applications being considered today.

Electrolytes

Numerous electrolytes have been used for chemical double layer capacitor construction. The most common of the aqueous electrolytes are sulfuric acid and potassium hydroxide. The most desirable characteristic of these electrolytes are their low resistivity. Since they are aqueous based, it is necessary to operate each cell of the capacitor at a voltage less than 1.2 volts. Further, these electrolytes are corrosive, which places restrictions on the use of materials for long life devices. By contrast, organic electrolytes such as propylene carbonate with lithium and ammonium salts have electrical resistivities at least an order of magnitude greater than that of aqueous electrolytes. Organic electrolytes have been operated at voltages as high as 3.5 volts in practical devices. Since the energy storage density is proportional to the square of the charge voltage, it would appear that organic electrolytes would be desirable. Many commercial devices now employ organic electrolytes. However, the internal resistance of the finished capacitor is usually 10's of ohms. This high value of internal resistance limits application.

OPERATING CELL CHARACTERISTICS

In our laboratory, we have concentrated exclusively on the use of aqueous electrolytes and carbon materials for the large surface area . Our reasoning for these choices are the ready availability of cheap, well characterized materials which need no exotic processing to manufacture. The general model for a capacitor is that of a pure capacitance shunted by the Equivalent Parallel Resistance (EPR) and in series with the Equivalent Series Resistance(ESR). Figure 3 shows the pressure dependence of the ESR for a series of cells areas from 2 - 5 cm^2 and with various thicknesses. In general, the ESR decreases rapidly with pressure for all thicknesses investigated. There is almost an order of magnitude variation of the ESR for the capacitors made from packed powder beds. For many applications, it is desirable to reduce the ESR to an absolute minimum. While it is easy to apply pressure to small devices, it is far more difficult when large storage capacitors are desired. As was discussed earlier, the physical mechanism responsible for the decrease in ESR with pressure is the increase in contact area between individual grains in the bed and a reduction of the path through the electrolyte as the bed is compacted. To first order, the effect is independent of powder bed thickness and shows the same relative decrease with pressure. The horizontal line in Figure 3 is the data taken for a composite electrode made from 2 millimeter large surface area carbon fibers roughly 10 microns in diameter mixed with 2 mm nickel fibers with a diameter of 2 microns. The mix ratio was 2:1 by mass. Cellulose was added and the mix converted to a paper sheet using standard paper making equipment. Selective annealing in a hydrogen atmosphere reduced the cellulose and produced a sinter bond to the nickel backing plate and between fibers. Figure 4 is a electron micrograph of a typical sintered structure. The larger fibers in the picture are the carbon fibers. Note that the smaller metallic fibers are effectively bonded and contact the large fibers at many points along their length. In this way, extremely good contact between the metal end plates, the carbon fibers and the metal fibers are maintained with little or no pressure dependence of the ESR.

Since all of the elements of the CDL have resistivities which are functions of temperature, packed powder bed capacitors were made and operated from about 6 ^{o}C to 24 ^{o}C. The results are

shown in Figure 5. The ESR, over the range measured, changed by about 30% and is almost totally due to the change in resistivity of the electrolyte and the thermal contraction of the grains which reduces the contact area. The change in the electrolyte is the dominant term and accounts for roughly 80 % of the observed changes. Higher temperature behavior has not been investigated within the program. These data do point clearly to the fact that application of these devices in a situation with large temperature extremes will require environmental control. It is obvious that the lower limit to operating temperature is the point at which the electrolyte freezes. Practical consideration of the ESR requirements will certainly limit the temperature variation for the electrolyte to a few degrees about some design point. Since the ratio of the load impedance to the ESR determines the available usable energy, it would appear advantageous to operate the CDL at higher temperature for low impedance loads. Chemical double layer capacitors are "designer devices" which can be custom tailored to a particular application and temperature of operation is a variable which can be exploited.

Of equal interest is the Equivalent Parallel Resistance (EPR). In general, single cell capacitances of farads are readily attainable. An EPR of a kilohm allows storage time constants on the order of thousands of seconds. In general that is sufficient for many applications. However, applications demanding long-term storage may require trickle charging to maintain the requisite energy. Clever design of a device might result in the losses through internal currents sufficient to maintain the temperature at the most desirable operating point if operating in a cold environment. The nature of the EPR is not clearly understood. It appears to be influenced by the "purity" of the material in so far as that dependence might be mirrored by manufacturing processes. Adsorbed material on the surface of the carbon and impurities in the electrolyte could provide sufficient conduction through the double layer to account for the experimental observations. Figure 6 is a bar chart which shows the EPR for devices made from several carbon powders. All units were comparable in size and operated at room temperature. While the carbons had differing surface areas and pore size distributions, they were made by differing processes. While indicative of residual from processing, we were not able to verify that conclusion. If the EPR were a conduction process as described above, there should also be a strong correlation with temperature. Figure 7 illustrates the same temperature dependence as was observed in the EPR, clearly pointing to conduction through the electrolyte as the mechanism determining the EPR.

Over the range of temperatures investigated and for a constant pressure of 20 kg/cm^2, there was no temperature dependence of the capacitance. Since the beds investigated were tightly packed powder, after a minimum pressure, there was sufficient contact that almost all of the material was accessed for capacitance. Figure 8 illustrates the pressure dependence of the capacitance for two cells of the same area but of differing thicknesses. These cells were not made from the same carbon and the beds may not have been packed to the same density. Therefore, the capacitance does not appear to scale linearly with thickness as would be expected. The purpose of this graph, is to show that the pressure dependence of the capacitance is weak and not a factor in the design of powder bed CDL capacitors. Similar results are observed for the composite electrodes. Figure 9 is a plot of the capacitance for a number of cells of differing thickness, made from the same material, while trying to maintain the construction parameters identical. Packed powder bed are difficult to make uniformly. Intuitively, the capacitance should scale linearly with thickness. To within the accuracy of our measurements, linear scaling is observed but the slope is less than expected. The difficulty may be in the ability to accurately produce thick beds with equivalent packing density.

DISCUSSION

There are two options for practical application. A single device can be constructed uniquely in one unit for a particular application. In that case, the desired voltage can be met by a bipolar

stack of the requisite number of unit cells C_u. In order to achieve the desired value of the internal resistance, ESR and EPR, and total capacitance, the area and thickness of the cell can be adjusted to arrive at suitable parameters. Depending upon the application, design by this procedure may result in more energy than is optimum for the load. Referring to Figure 3, it is possible to construct single cells which allow "short circuit" currents as high as 5-10 A/cm^2 For a given area, the ESR and the C_u scale linearly with thickness of the active bed. This procedure results in the highest energy/power density by optimizing the packaging. More generally, a "standard" module made up of a number of unit cells can be built and any energy storage unit made up of the requisite number of standard modules in series/parallel arrays. Again, depending upon the load, it may not be possible to optimize all parameters of the storage unit simultaneously.

There is a wide variety of materials and techniques available for utilization in CDL technology. The current laboratory state-of-the-art is about 6 j/gm for aqueous electrolytes with the capacitive elements made from composite electrodes. For non-aqueous electrolytes, the energy density is at least double that amount. For internal resistance, the best ESR values for aqueous electrolytes is on the order of 0.1 ohm/cm^2 of active cell. The thickness of the cell for these values is 0.002-0.003 cm. Simple bipolar stacks from the carbon powder bed technology have been constructed to evaluate sealing and any engineering problems which might occur as large numbers are stacked for higher voltage operation. Up to 50 cells have been made and little or no problems encountered. The largest of these experimental units operated at 50 volts and stored 1200 joules. The energy density was greater than 3j/g even though no care was taken to minimize the materials used in the construction. The unit was tested periodically for several months with little or no degradation.

Further advancements in this technology must rely on engineering of the pore structure to maximize the surface area available while simultaneously maximizing the pore diameter. It is probable that factors of 2 or more improvement can be realized by a concerted effort.

ACKNOWLEDGEMENT

This work was supported by the Strategic Defense Initiative Organization's Office of Innovative Science and Technology (SDIO/TN) through contract number DNA001-91-C-0127 with the Defense Nuclear Agency.

REFERENCES

1. M. F. Rose, Proc. 33rd International Power Sources Symposium, The Electrochemical Society Inc., June 13 - 16, 1988, Cherry Hill, NJ.

2. D. L. Boos, H. A. Adams, T. H. Hacha, and J. E. Metcalfe, Proc 21st Electronics Components Conference, 1971

3. K. Sanada and M. Hosokawa, NEC Research and Development, 55, p. 21 - 28, 1979

4. D. Kohler, J. Zabasajja, A. Krishnagopalan, and B. Tatarchuk, J. Electrochem. Soc., Vol. 137, No. 1, 1990

5. I. L. Cooper and J. A. Harrison, Electrochemical Acta, 29, No. 8, 1984

6. J. O'M. Bockris, Materials Science and Engineering, 53, 1982

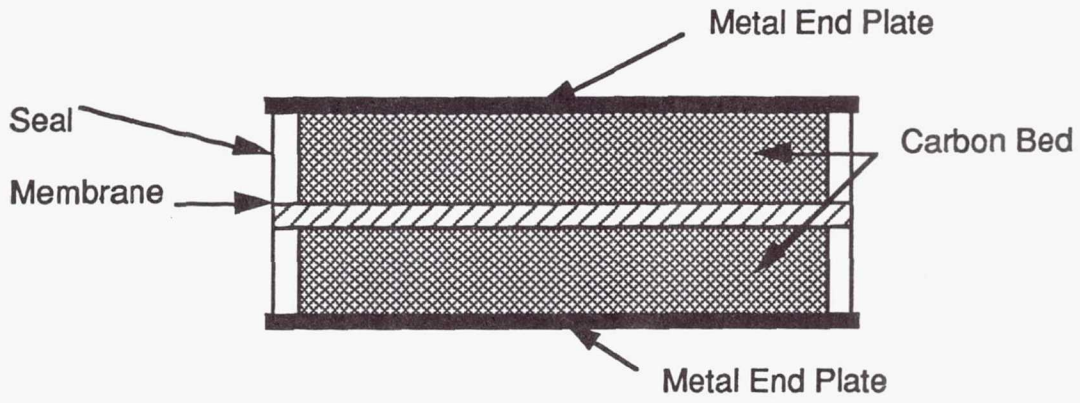

Figure 1a. Schematic drawing of a packed carbon powder bed Chemical Double Layer (CDL) capacitor

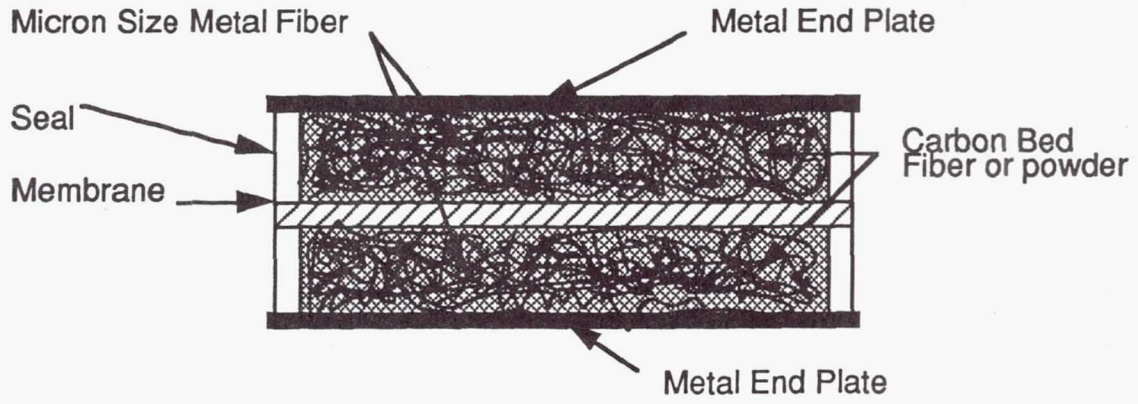

Figure 1b. Schematic drawing of a Chemical Double Layer (CDL) capacitor using a composite electrode structure.

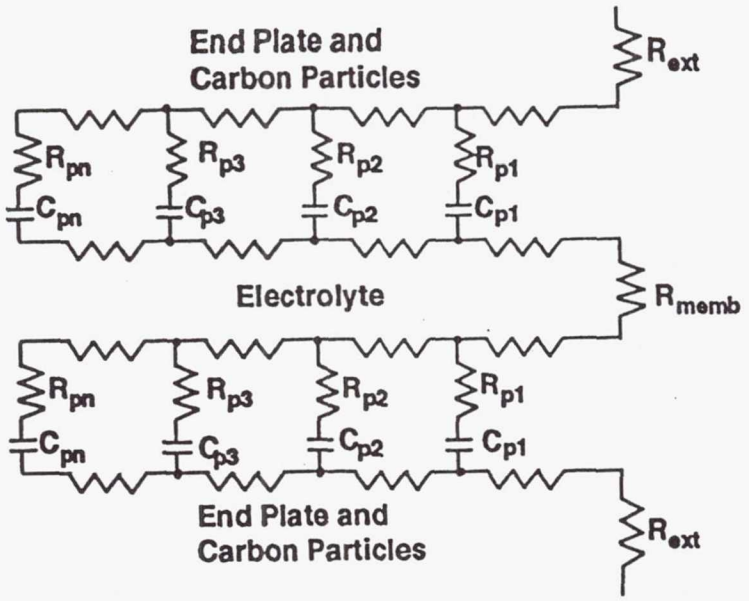

Figure 2. Approximate schematic for a Chemical Double Layer (CDL) capacitor.

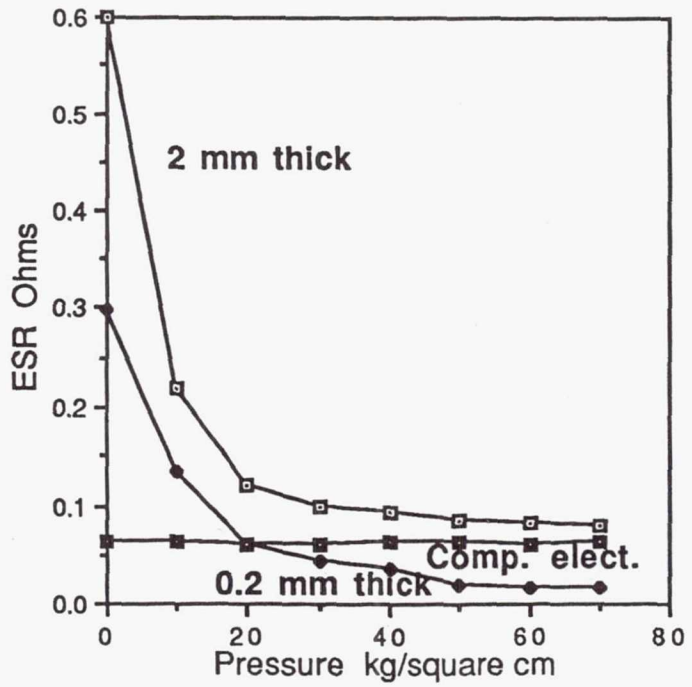

Figure 3. Pressure dependence of the Equivalent Series Resistance (ESR) for powder and composite electrode structures.

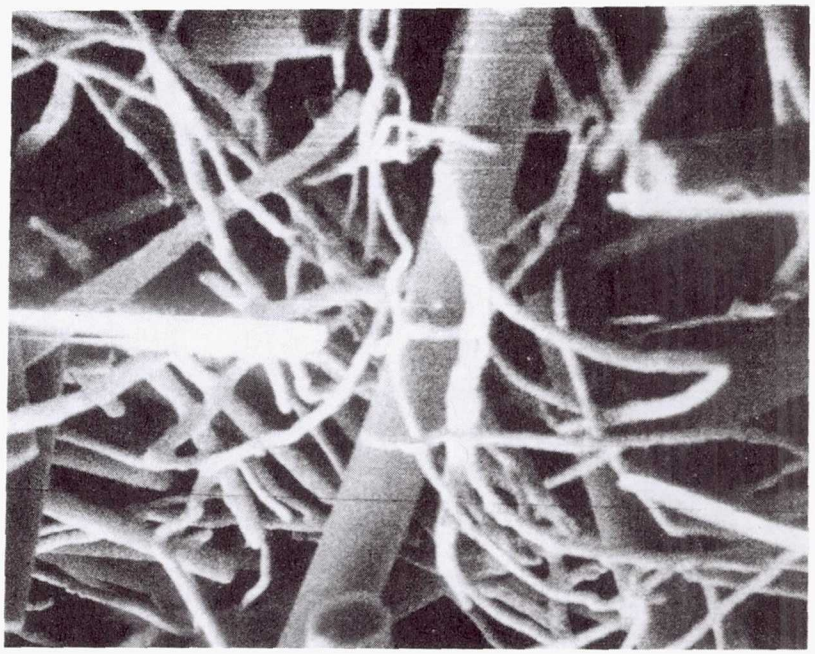

Figure 4. Electron micrograph of composite electrode structure showing large carbon fibers and smaller sinter-locked metal fibers.

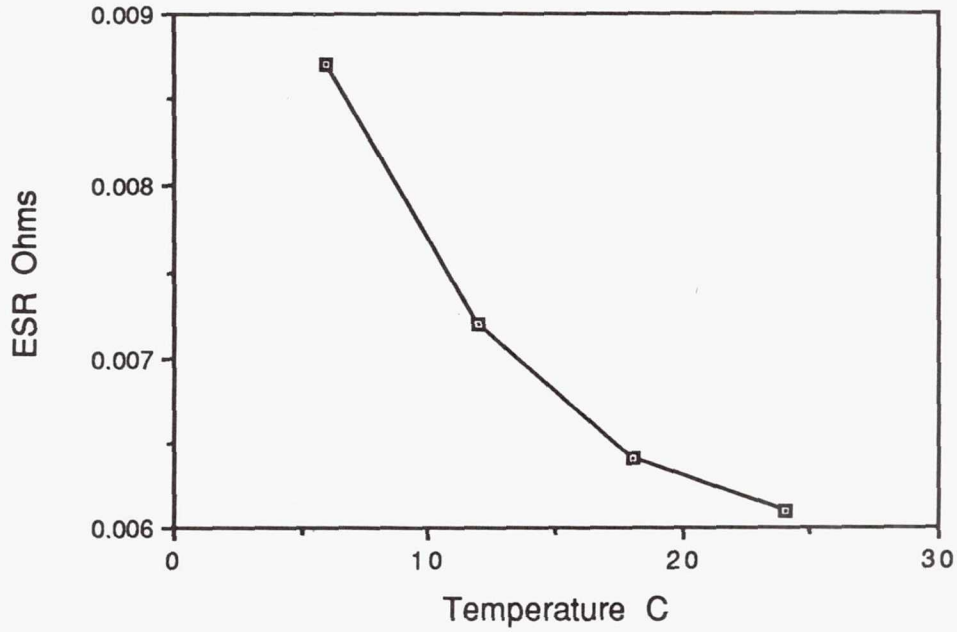

Figure 5. Temperature dependence for the Equivalent Series Resistance(ESR) for a packed carbon bed capacitor using H_2SO_4 electrolyte.

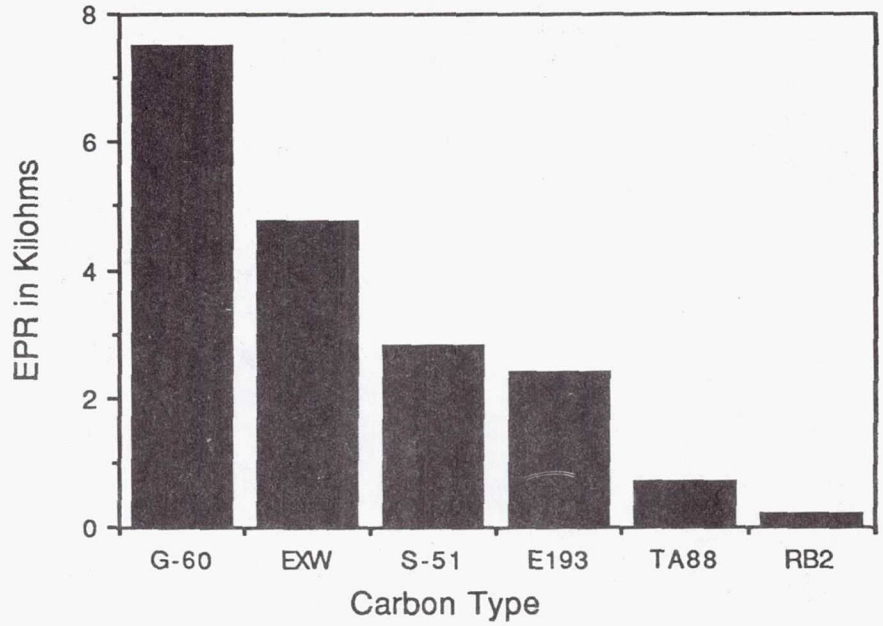

Figure 6. Equivalent Parallel Resistance (EPR) for cells made with packed carbon beds using carbon powder from several commercial sources.

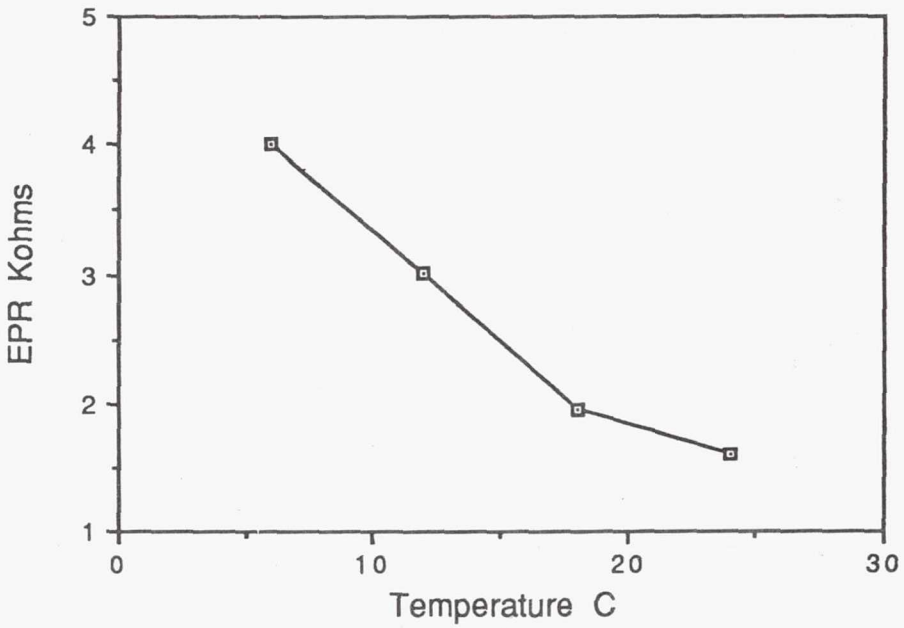

Figure 7. Equivalent Parallel Resistance (EPR) as a function of temperature for a packed carbon bed device.

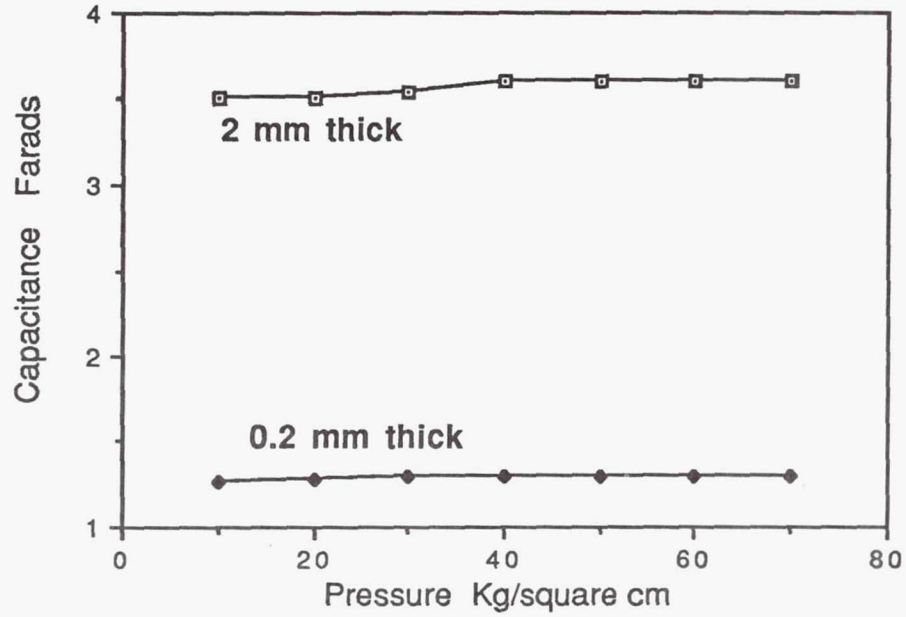

Figure 8. Pressure dependance of the capacitance of a packed carbon bed CDL for two bed thicknesses.

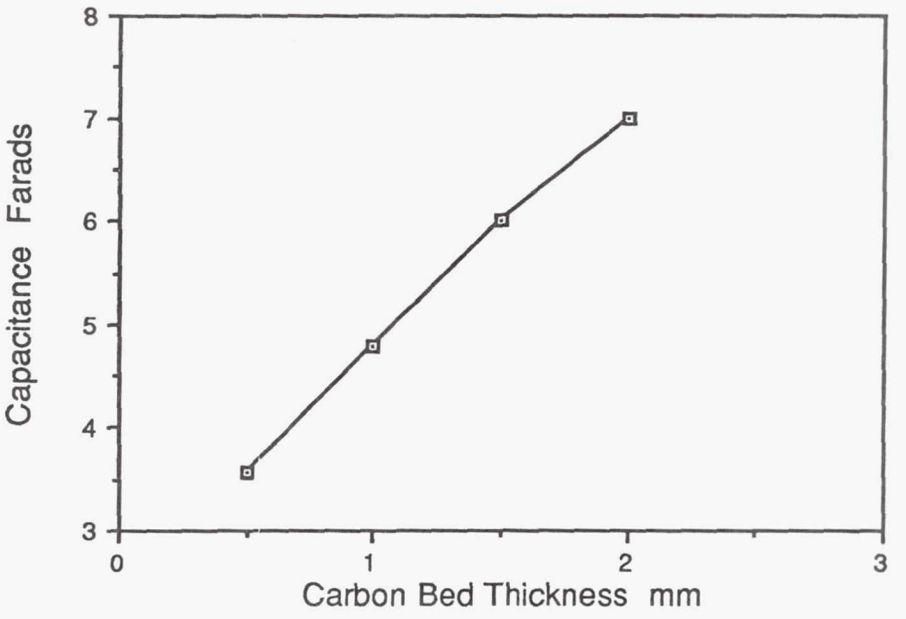

Figure 9. Unit cell capacitance as a function of the thickness of the packed powder bed.

A HIGH PERFORMANCE H_2-Cl_2 FUEL CELL FOR SPACE POWER APPLICATIONS

Everett B. Anderson,* E. Jennings Taylor,** Gerald Wilemski, and Alan Gelb
PSI Technology Company
A Division of Physical Sciences Inc.
20 New England Business Center
Andover, MA 01810

INTRODUCTION

NASA has numerous airborne/spaceborne applications for which high power and energy density power sources are needed. The proton exchange membrane fuel cell (PEMFC) is an attractive candidate for such a power source. PEMFC's offer many advantages for airborne/spaceborne applications. They have high power and energy densities, convert fuel to electrical power with high efficiency at both part and full load, and can rapidly startup and shutdown. In addition, PEMFC's are lightweight and operate silently.

A significant impediment to the attainment of very high power and energy densities by PEMFC's is their current exclusive reliance on oxygen as the oxidant. Conventional PEMFC's oxidize hydrogen at the anode and reduce oxygen at the cathode. The electrode kinetics of oxygen reduction are known to be highly irreversible, incurring large overpotential losses. In addition, the modest open circuit potential of 1.2V for the H_2-O_2 fuel cell is unattainable due to mixed potential effects at the oxygen electrode. Because of the high overpotential losses, cells using H_2 and O_2 are capable of achieving high current densities only at very low cell voltages, greatly curtailing their power output. Based on experimental work at PSI Technology Company (PSIT) on chlorine reduction in a gas diffusion electrode, we believe significant increases in both the energy and power densities of PEMFC systems can be achieved by employing chlorine as an alternative oxidant.

BACKGROUND

A hydrogen/chlorine fuel cell reacts hydrogen and chlorine to form hydrogen chloride. A schematic of a proposed system is shown in Fig. 1. Hydrogen gas is oxidized at the anode to produce protons which are transported across the cation exchange membrane. Chlorine gas is reduced at the cathode to produce chloride ions. Depending on the application duty cycle and lifetime requirements either a captive or flowing electrolyte may be used.

The net cell reaction is $1/2\ H_2 + 1/2\ Cl_2 \rightarrow HCl$. The standard cell potential for this reaction is 1.36V at 25°C. In an actual fuel cell the operating voltage is lower due to polarization and ohmic losses. Consequently, the power output is lower than the theoretical power output. Nonetheless, both the oxidation of hydrogen and the reduction of chlorine are known to be relatively non-polarizable electrochemical reactions and capable of high cell voltages at high current densities.

We can support this statement for chlorine reduction with our own measurements using the rotating disc electrode (RDE) technique [1] to determine mass transport parameters and mass transport corrected kinetic and mechanistic information about chlorine reduction. We have used the RDE technique to obtain the exchange current density for chlorine reduction on platinum in 7M HCl at 25°C [2] from a mass transport corrected Tafel plot. We calculated an exchange current density of about 10^{-1} mA/cm^2. This value is approximately eight orders of magnitude greater than the exchange current density for oxygen reduction on platinum (10^{-9} mA/cm^2).

---

*Author to whom correspondence should be addressed.

**Current Address: Farachem Technology, Inc., 300 East Auburn Ave., Springfield, OH 45505.

Relatively little research has been reported on hydrogen chlorine fuel cells. Recent research has focused on hydrogen/chlorine regenerative fuel cells for load leveling applications [3-7]. The regenerative fuel cell application, although related, is quite different from the H_2-Cl_2 fuel cell discussed here. In the regenerative fuel cell the chlorine electrode acts in both the consuming (cathodic) and generating (anodic) modes, while the system referred to in this paper needs to be optimized for the chlorine consuming mode only.

In the H_2-Cl_2 regenerative fuel cell, the hydrogen catalyst is attached to a Nafion™ cation exchange membrane to prevent chloride ion from poisoning the platinum electrocatalyst. Halide ions, in general, and chloride, in particular, have been shown to alter the adsorption isotherms of hydrogen on platinum [8, 9]. The chlorine reactant is dissolved in the electrolyte and is oxidized at a flow-by electrode during the electrolysis (charge) mode and is reduced at a flow-by electrode during the fuel cell (discharge) mode. However, mass transport limitations at the flow-by electrode decreases the cathode performance and limit the power output during discharge.

For a H_2-Cl_2 fuel cell for NASA, we suggest the use of gas diffusion electrodes analogous to those used in H_2-O_2 proton exchange membrane fuel cells for power generation. Besides the PSIT work reported in this paper, there is only one report of the use of a chlorine consuming gas diffusion electrode [10], for the chlorination of various organics. However, due to limitations of the organic anode reaction, performance at the chlorine gas diffusion electrode could not be abstracted. Even so, the mass transport limitations at a chlorine gas diffusion electrode should be considerably less than at flow-by or flow-through electrodes [11].

RESEARCH AT PSIT

PSIT is developing H_2-Cl_2 fuel cells for application to chlor-alkali technology. These fuel cells are intended for widespread commercial use, hence, capital cost considerations are paramount. Furthermore, high current densities are neither anticipated nor required. Consequently, our current efforts are concerned with developing low-cost, low-loading electrocatalysts.

Under a DOE Phase II SBIR Program (Contract No. DE-AC02-86ER80366), PSIT developed a hydrogen/chlorine fuel cell technology to reduce the power requirements and increase the system efficiency of brine electrolysis in the chlor-alkali industry. In this program, PSIT determined 1) the kinetics of chlorine reduction on several catalysts; 2) the actual polarization behavior of a chlorine gas diffusion electrode; 3) the conductivity of a commercially available membrane in the environment of interest to our system; and 4) the conductivity of HCl as a function of concentration. Using these data we projected very favorable polarization behavior for our H_2-Cl_2 fuel cell. In addition, we engaged in chlorine gas diffusion electrode development and constructed a laboratory scale process development unit (PDU) for the H_2-Cl_2 fuel cell.

The subject of this paper differs from that of our current developmental efforts in the need to develop electrodes and fuel cells capable of very high current densities at moderate voltages. The NASA application requires much higher performance electrodes. PSIT is highly familiar with the basic design issues and believes in the feasibility of employing high-loading, Cl_2 and chloride-tolerant H_2 electrodes capable of high current densities with low overpotential losses. Next, we will summarize our efforts in the areas of chlorine gas diffusion electrode development and chloride-tolerant electrodes for H_2 oxidation.

We have measured current-potential curves for Cl_2 reduction at 23°C in 3M HCl on a number of different electrocatalysts in a gas diffusion electrode configuration. These electrocatalysts included: 1) high surface area (HSA) carbon black (Ketjen EC300J, Akzo Chemie); 2) heat treated HSA carbon black (Graphitized Ketjen); 3) low-loading (0.5 mgPt/cm^2) carbon-supported Pt; and 4) high surface area lead ruthenate mixed metal oxide. The polarization behavior of these materials is shown in Fig. 2. The best Cl_2 reduction performance was observed for the supported platinum electrocatalyst. These results indicate extremely low polarization behavior (70 mV at 1 A/cm^2) for the supported platinum electrode compared to that of O_2, which does not even register a current under similar conditions. The measured rest potential of 1.29V shows a mixed potential loss of only 70 mV from the equilibrium value of 1.36V, a loss that is also

much smaller than that suffered by oxygen electrodes. These results are obtained on what is almost certainly a far from optimal electrode structure and are highly encouraging. They form the basis for the conservative power and energy density estimates discussed below.

Chloride ions poison platinum, greatly reducing its effectiveness as an electrocatalyst for hydrogen oxidation. If unchecked, chloride ion poisoning could preclude the attainment of high power and energy densities in the H_2-Cl_2 fuel cell. In work at PSIT, we have demonstrated that smooth platinum's tolerance of chloride ion was improved by coating the platinum with a thin film of Nafion. Recently, we developed a method to impregnate a carbon-supported Pt gas diffusion electrode structure with Nafion and coat the individual Pt particles in order to utilize the Nafion's ability to protect platinum from the chloride ion. The method involves soaking the electrode in a Nafion solution for different times to vary the loading of Nafion in the electrode. In Fig. 3. we present the results of electrochemical Pt surface area measurements on electrodes treated with Nafion for 30s and 12 hr. These are compared with results for untreated electrodes that were presoaked in a water/alcohol solution for 30s and 12 hr, respectively, to facilitate wetting upon immersion in the chloride test solutions.

No effect of chloride was seen with any electrode until the 0.1M chloride concentration. At this value, the standard anode presoaked for 12 hr suffered a 47% reduction in surface area, from 112 to 59 m^2/g. The comparable Nafion coated anode demonstrated no loss of surface area at the same concentration. The coating of the anode with Nafion, therefore, had a positive effect on the chloride tolerance. The other electrodes also showed no effect at this concentration. The surface area of the lightly coated anode approached that of the heavily coated anode, suggesting improved chloride tolerance for the lightly coated anode as well. Any effect of chloride at 0.1M on the untreated anode presoaked for 30s was probably lost due to incomplete wetting of the electrode.

At 1M chloride ion concentration, the surface area of both untreated anodes decreased, while the Nafion coated anodes exhibited little change. This behavior in 1M HCl clearly demonstrated successful protection of the platinum by coating with Nafion. The total surface area lost for the coated anode was less than 15% compared to a loss of surface area for the uncoated anode of greater than 75%.

H_2-Cl_2 PEMFC SYSTEM PERFORMANCE

To examine the relative merits of the H_2-Cl_2 PEMFC system compared to the H_2-O_2 PEMFC system, we estimated the power and energy densities of these two systems over a wide range of mission lifetimes. The results shown in Fig. 4 indicate that the H_2-Cl_2 PEMFC will significantly outperform the H_2-O_2 PEMFC. For mission lifetimes of 1 min, 1 hr, and 10 hr, we conservatively estimate the energy and power densities of the H_2-Cl_2 PEMFC system to be, respectively, 20 Wh/kg and 1200 W/kg at 0.73V, 152 Wh/kg and 152 W/kg at 1.12V and 199 Wh/kg and 20 W/kg at 1.26V. These values are, respectively, 2, 1.5, and 1.33 times greater than the corresponding values optimistically estimated for an H_2-O_2 PEMFC system based on state-of-the-art performance recently reported by Ballard Power Systems (BPS) [12]. For lifetimes greater than 10 hr, the energy and power densities of the H_2-Cl_2 system asymptotically approach 1.3 times those of the H_2-O_2 system. It is significant that, according to Appleby [13], the energy density figure of 152 Wh/kg (and greater) for the 1 hr mission (or longer) "exceeds the energy available from any known secondary battery, including sodium-sulfur." Also note that the energy density of the H_2-Cl_2 system exceeds 110 Wh/kg (50 Wh/lb) for all mission lifetimes longer than 15 min.

The estimates shown in Fig. 4 are based on the following assumptions: The fuel cell stack contains 50 cells of 232 cm^2 (0.25 ft^2) each and weighs 45 kg as suggested by BPS [12]. The assumed mass significantly affects the estimates only for mission lifetimes less than 1 hr; for longer missions the mass of reactants and storage tanks predominates. The latter masses were taken from an Air Products catalog and are 0.112 kg/mol for Cl_2, 0.190 kg/mol for O_2, and 0.206 kg/mol for H_2. With these assumptions, the mass to power ratio M (kg/kW) for each system can be written as

$$M(H_2\text{-}Cl_2) = 45/P + 5.93t/V \quad (1)$$

$$M(H_2\text{-}O_2) = 45/P + 5.62t/V \quad (2)$$

where t is the mission lifetime in hours, V is the cell potential in volts, and, P is the stack power in kilowatts.

The current (I) - potential (V) behavior of a single cell is adequately represented by a linear relation: $V = V^o(1\text{-}0.5I/I_p)$, where V^o is the rest potential and I_p is the current at which the peak cell power is obtained. For the BPS H_2-O_2 cell at 102°C and 5.8 atm, V^o is 0.985Vand I_p is 1250A. With these measured values, the linear current-potential relation actually overpredicts cell performance and thus provides optimistic power estimates for the H_2-O_2 system. For the H_2-Cl_2 cell, we have V^o= 1.34V (our measured room temperature value of 1.29V plus 50 mV Nernst gain for operating at 6 atm) and a projected value for I_p of 1943A based on 80 mV loss at 232A (we measured 70 mV at 1 A/cm^2). Since this initial chlorine electrode is unlikely to be optimal, these performance predictions should be conservative. Operation at higher temperature with an improved chlorine electrode is certain to give better performance.

It is important to note that since the mass of reactants and storage tanks increases with length of mission, the optimal power and energy densities for a given mission lifetime will occur at a lower current and higher potential than those at the peak power point for the cell. In Fig. 5, the optimum cell potential and total stack power are plotted versus mission lifetime. It is noteworthy that for each mission lifetime, the H_2-Cl_2 system achieves optimal power and energy density at a voltage higher than that of the H_2-O_2 system. Since the kg/kW due to the reactants and storage tanks varies inversely with the voltage, the advantage of having an electrochemical system with an intrinsically and significantly higher potential at each current is very apparent.

The significantly larger power and energy densities of the H_2-Cl_2 system are the result of its larger open circuit potential and chlorine reduction kinetics that are much more reversible than those of oxygen. The theoretical open circuit potential of a hydrogen-chlorine cell is about 160 mV higher than that of hydrogen-oxygen. Moreover, our rest potential measurements indicate a mixed potential loss of only 70 mV, much smaller than for oxygen. Both of these factors combine to provide significantly higher cell voltages. Furthermore, the exchange current density for Cl_2 reduction on smooth Pt is about eight orders of magnitude greater than that of O_2, and our measurements show much smaller overpotential losses at high current densities for Cl_2 than for O_2. A H_2-Cl_2 PEMFC therefore appears capable of achieving very high power and energy densities thereby overcoming a severe limitation of oxygen based cells. Finally, the extremely rapid H_2 oxidation and Cl_2 reduction kinetics combined with the large freezing point depressions of concentrated HCl should give the H_2-Cl_2 PEMFC significant cold start capability.

CONCLUSIONS

The H_2-Cl_2 PEM fuel cell has the potential to be a versatile and reliable high performance power source for NASA applications. We have shown that the development of a H_2-Cl_2 PEM fuel cell could yield a system with power and energy densities inherently greater than currently available in H_2-O_2 fuel cells. These devices would be valuable power sources for airborne/spaceborne high power applications. The cells would be highly efficient at both partial and full load, be capable of very rapid startup and shutdown, be lightweight and silent, and should have significant cold-start capability. The critical enabling technologies for this system are the development of high performance, long-lived chlorine gas diffusion electrodes and chloride-tolerant hydrogen anodes. Based on experimental work at PSIT, we believe that the achievement of these higher energy and power densities are feasible with this type of fuel cell configuration.

REFERENCES

1. Pleskov, Y.V. and Filinovskii, V.Y. (1976), The Rotating Disc Electrode, Consultants Bureau, New York.

2. Taylor, E.J., Moniz, G., and Gelb, A., (1987), PSI-2007/TR-650.

3. Yeo, R.S., McBreen, J. Tseung, A.C.C., Srinivasan, S., McElroy (1980), "An Electrochemically Regenerative Hydrogen-Chlorine Energy Storage System: Electrode Kinetics and Cell Performance," J. Applied Electrochemistry, 10, 393-404.

4. Chin, D.T., Yeo, R.S., McBreen, J. and Srinivasan, S. (1979), J. Electrochem. Soc., 126, 713.

5. Yeo, R.S. and McBreen, J. (1979), "Transport Properties of Nafion Membranes in Electrochemically Regenerative Hydrogen/Halogen Cells," J. Electrochem. Soc. 126, 1682.

6. Gileadi, E., Srinivasan, S., Salzano, F.J., Braun, C., Beautrere, A., Gottesfeld, S., Nuttal, L.J., and Laconti, A.B. (1977/78), J. Power Sources, 2, 191.

7. Balko, E.N. (1981), J. Applied Electrochemistry, 11, 91.

8. Breiter, M.W. (1963), "Voltammetric Study of Halide ion Adsorption on Platinum in Perchloric Acid Solutions," Electrochem. Acta, 8, 925-35.

9. Bagotzky, V.S., Vassilyev, Y.B., Weber, J., Pirtskhalava, J.N. (1970), "Adsorption of Ions on Smooth Platinum Electrodes," Electroanal. Chem. Interfac. Electrochem., 27, 31-46.

10. Langer, S.A. and Yurchak, S. (1970), "Electrogenerative Chlorination," J. Electrochem. Soc., 117(4), 510.

11. Srinivasan, S. (1986), private communication.

12. Watkins, D., Dircks, K., and Epp, D. (1988), "Canadian Solid Polymer Fuel Cell Development," Fuel Cell Seminar 1988, Program and Abstracts, p.350.

13. Appleby, A.J. (1987), "Regenerative Fuel Cells For Space Applications," Space Electrochemical Research and Technology (SERT), NASA Conference Publication 2484 (NASA Scientific and Technical Information Office).

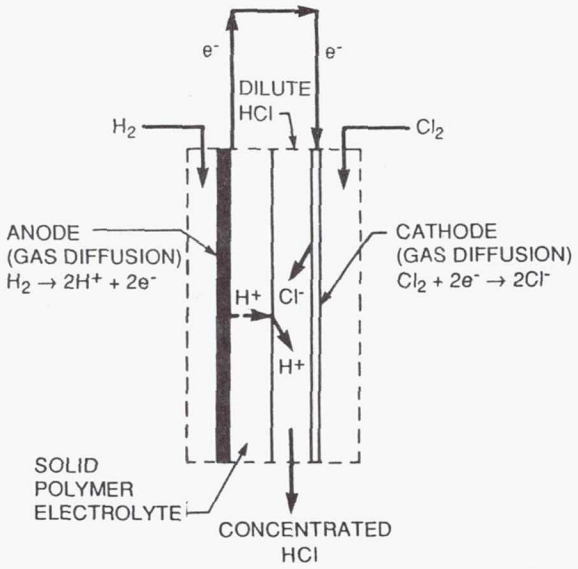

Fig. 1.–Schematic of H_2-Cl_2 Fuel Cell Using a Gas Diffusion Cl_2 Electrode with a Flowing Electrolyte. A captive electrolyte system for short-term applications is also an option.

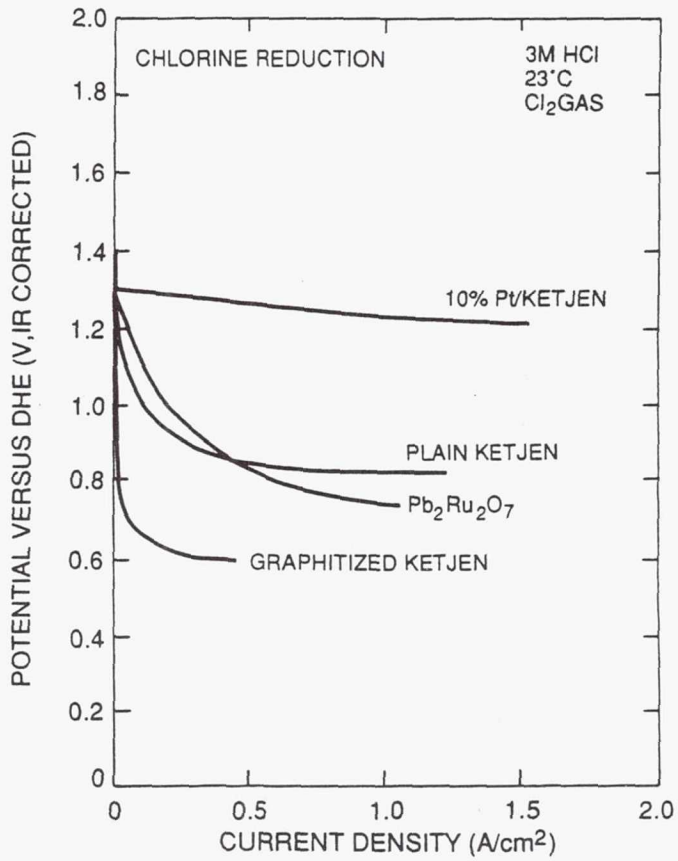

Fig. 2.–Chlorine Reduction Polarization Data in 3M HCl at 23°C with (a) 10% Pt/Ketjen, (b) Plain Ketjen, (c) Graphitized Ketjen and (d) lead-ruthenium oxide. Maximum current density here is determined by IR drop of the half-cell, not by electrode behavior.

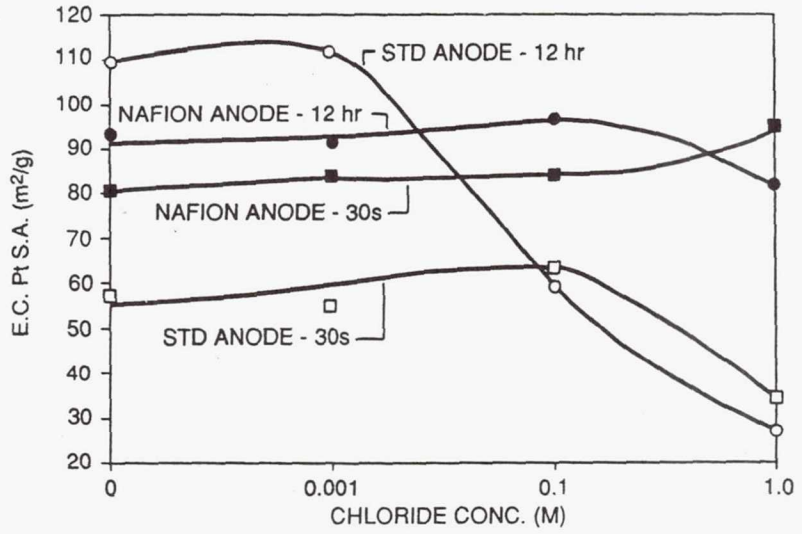

Fig. 3.–Results of Chloride Tolerance Study of Uncoated and Nafion Coated Standard Platinum Anodes

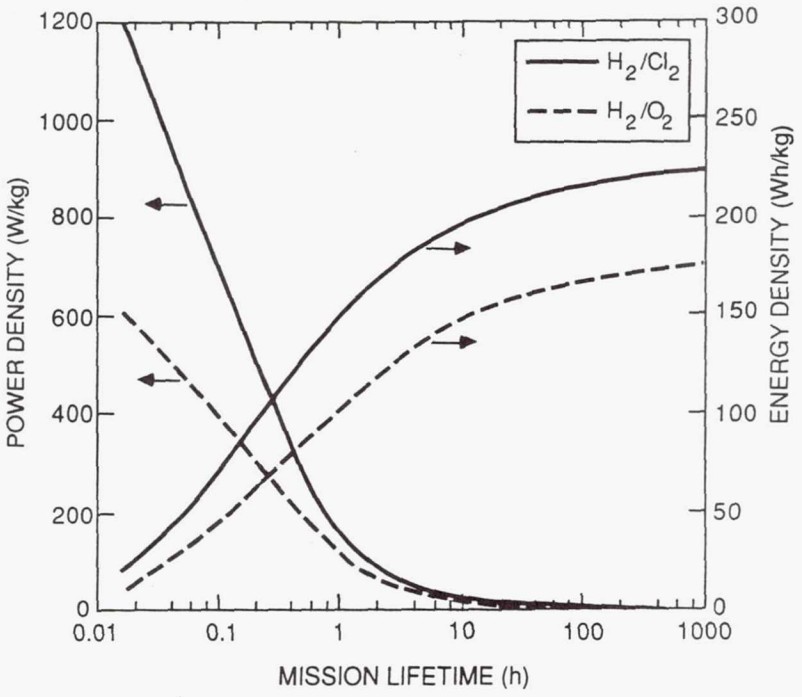

Fig. 4.–Estimated Optimum Power and Energy Densities Versus Mission Lifetime for PEMFC Systems

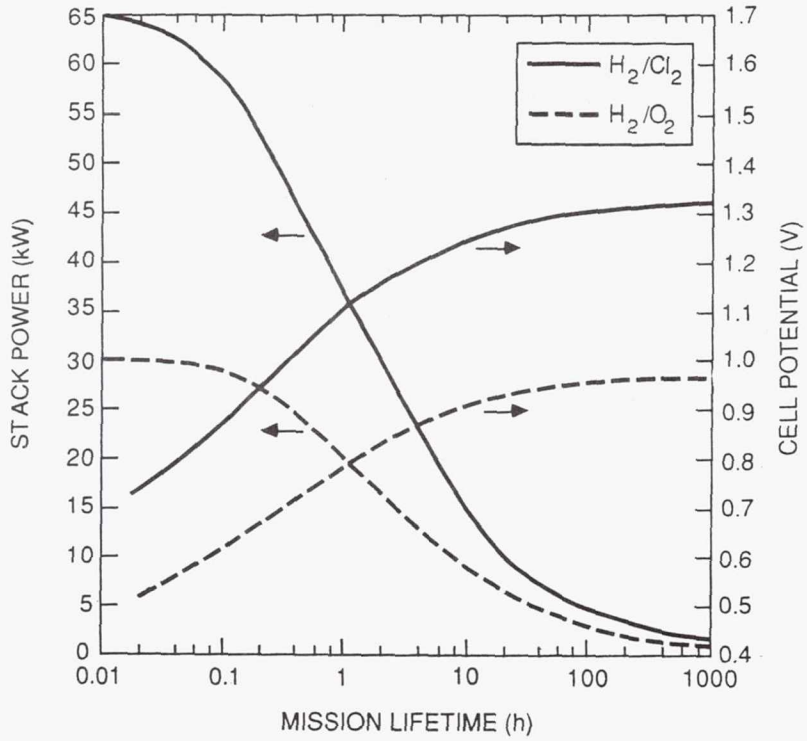

Fig. 5.–Estimated Optimum Cell Voltage and Stack Power Versus Mission Lifetimes for PEMFC System

HAIRY CARBON ELECTRODES STUDIED BY CYCLIC VOLTAMMETRY AND BATTERY DISCHARGE TESTING

Deborah D. L. Chung and Xiaoping Shui
Composite Materials Research Laboratory, State University of New York at Buffalo
Buffalo, NY 14260-4400

Christine A. Frysz
Technology Division, Wilson Greatbatch, Ltd.
10,000 Wehrle Drive, Clarence, NY 14031

ABSTRACT

Hairy carbon is a new material developed by growing submicron carbon filaments on conventional carbon substrates. Typical substrate materials include carbon black, graphite powder, carbon fibers and glassy carbon. A catalyst is used to initiate hair growth with carbonaceous gases serving as the carbon source. To study the electrochemical behavior of hairy carbons, cyclic voltammetry (CV) and discharge testing were conducted. In both cases, hairy carbon results surpassed those of the substrate material alone.

INTRODUCTION

Because carbon and graphite exhibit an advantageous blend of chemical, electrical, mechanical and thermal properties, they are very often considered for electrochemical applications. Chemically, carbon and graphite offer good corrosion resistance, are available in high purity and readily form intercalation products. Not only are they good electrical conductors, but they also exhibit high thermal conductivity and low thermal expansion. Carbon and graphite are lightweight, easily handled, and are also available in a variety of physical structures including carbon fibers, submicron carbon filaments, carbon blacks and graphite powders. The battery electrode is among the electrochemical applications requiring the characteristics just described.

Military, space and commercial applications continue to become more and more demanding. Today's technological strides require that batteries be compact but capable of providing higher energy and power density while still maintaining long shelf life and good discharge characteristics. Continued advancement in carbon and graphite technology can contribute toward achieving these goals by providing improvements to the characteristics that most influence performance.

Hairy carbon, a new material comprising tiny carbon filaments grown on conventional carbon substrates, have been developed. The hairs on the carbon are submicron filaments with diameters ranging between 0.05 μm and 0.2 μm. Figures 1a and b are scanning electron photomicrographs of hairy carbon grown on carbon black. Two different magnifications of the same sample are displayed. At the lower magnification, Figure 1a, a small portion of a hairy carbon black cluster is shown. The submicron nature of the hairs can very easily be seen at the higher magnification presented in Figure 1b.

Hairy carbons are not to be confused with conventional carbon fibers or carbon filaments as developed by Tibbetts and coworkers at General Motors.[1-3] Whereas hairy carbon is catalytically grown from carbonaceous gases, carbon fibers are typically prepared either from a pitch material or from a polymer precursor such as polyacrylonitrile. In contrast to hairy carbon, carbon fibers have diameters of the order of 10 μm. Carbon filaments, like hairy carbon, are submicron in nature (typical diameters of 0.2 μm) and are also catalytically grown from carbonaceous source gases, but carbon filaments are very long and tend to cling to each other as does cotton wool. Consequently, dispersion and mixing are very difficult. Since hairy carbons can be produced on particulate carbon substrates, the particulate nature of the finished product is preserved. Dispersion and mixing, therefore, remain very easy. An added advantage is that the length of the 'hair' can be easily controlled gearing the finished product toward the intended application. In fact, the hairs can be so short that they resemble nodules.

Carbon filaments, like hairy carbon, can be grown using carbon monoxide or many different hydrocarbons as the source.[4-10] Methane and other aliphatics, olefins, and aromatics have all been shown to produce carbon filaments when exposed to appropriate catalysts. The presence of gases which can gasify carbon (hydrogen, water, carbon dioxide) reduces the driving force and lowers the rate of filament growth, ultimately stopping it completely. Carbon filament formation takes place under conditions where, in the absence of the 'catalyst,' no carbon deposition would take place.

Hairy carbon can easily satisfy two battery electrode applications: (1) a reduction electrode when used independent of other cathode mixes; and, (2) a conductive additive to otherwise nonconductive or low conductivity cathode mixes such as manganese dioxide and carbon monofluoride. For the former application, the submicron filamentous nature of the carbon can provide a novel means for controlling connectivity, porosity and surface area. These attributes, along with the improved physical properties, offer advantages over state-of-the-art carbon electrodes. Regarding the latter application, hairy carbon, being more graphitic and exhibiting high aspect ratio, in addition to improving electrical conductivity, could result in the addition of a smaller volume fraction for conductivity enhancement allowing for addition of more active cathode material or reduction in overall cathode size. The end result is high power and high energy density composite cathodes with more energy output from the same package design or equal energy output from more compact designs. This could prove beneficial to implantable device manufacturers, space exploration programs and original equipment manufacturers requiring size and weight constraints or increased energy from current design packages. This paper focuses on the former application, that is, the carbon reduction electrode. Discharge testing was conducted in BCX electrolyte. BCX is a codepolarizer of the interhalogen, bromine chloride, in thionyl chloride.[11]

EXPERIMENTAL

The electrochemical behavior of the hairy carbons was studied using cyclic voltammetry (CV). A Bioanalytical Systems CV cell, Figure 2, was used in conjunction with the Headstart Electrochemistry program (developed by EG&G Princeton Applied Research), a potentiostat and an IBM personal computer. A saturated calomel electrode served as reference with a platinum wire used as the auxiliary electrode. The working electrode was a purchased holder typically used for carbon paste electrodes. The hairy carbon filled the cavity as does carbon paste, however, was used without the conventional paraffin oil binder. Testing was conducted in 6 mM potassium ferrocyanide as the electroactive species in 1 M potassium nitrate in water as the supporting electrolyte. This solution allowed study of the Fe^{2+}/Fe^{3+} redox couple.

To assess the discharge capability of hairy carbon, constant current plate to plate discharge testing was conducted using the apparatus shown in Figure 3. A cut-down AA battery case was used as the positive electrode current collector. The hairy carbon was placed inside the case and separated from the lithium by a nonconductive glass fiber paper. Insulative polymer disks were placed on top of the assembly and held in place with a metal clip. The assembly was immersed in the BCX electrolyte. A Keithley power source was used to apply current. Data was collected on a Tandy computer.

RESULTS AND DISCUSSION

Compared in Figures 4a - f are the voltammetric responses for hairy versus plain graphite powder, hairy versus plain carbon black and hairy versus plain carbon fibers. The addition of hair dramatically improves electrochemical performance. Note the increase in electron transfer rate and enhanced reversibility of the redox reactions. The improvements are attributed to increased surface area and particulate connectivity which translates into improved conductivity. Figures 5a and b compare a cyclic voltammogram of conventional carbon paste using paraffin oil with dry hairy graphite powder. The graphite powder used to grow hairs for this experiment was the same powder used to manufacture the carbon paste commercially available for analytical electrodes. The results indicate that the electrochemical response of the dry hairy graphite powder surpasses that of current carbon paste technology.

Discharge performance using hairy versus plain graphite powder is shown in Figure 6. An improvement in cell capacity per unit area of greater than 100% was achieved using hairy graphite powder. The substantial increase in capacity is attributed to increased electrode surface area as well as conductivity. The significance in this result is the fact that the graphite powder tested would never be considered for lithium battery use primarily because of its low surface area. Given these results and that many varieties of carbon forms can be made hairy, a new group of materials become available for research by battery manufacturers.

In addition to surface area, pore size and distribution are of importance for carbon reduction electrodes. Carbon blacks traditionally exhibit high surface areas. Electrode preparation methods are developed to achieve optimum electrode pore size and distribution. To maintain good electrode pore size and distribution, yet assess the effect of increased electrode conductivity, discharge testing of carbon black electrodes employed blends of plain carbon black with hairy carbon black. The plain carbon black provided retention of good pore size and distribution while the hairy carbon black contributed to electrode conductivity. Figure 7 compares discharge performance of plain carbon black with a blend of 50 weight percent hairy carbon black and 50 weight per cent plain carbon black. An improvement of approximately 40 mA•h per unit density was achieved when discharged to 2 volts.

CONCLUSIONS

Hairy carbon is electrochemically superior to plain carbon whether in the form of carbon black, graphite powder or carbon fibers. Hairy carbon can improve electrode performance as observed by plate to plate discharge testing. Compared to plain graphite powder deemed unusable for battery applications, hairy graphite powder used in a lithium soluble cathode system, BCX, as a reduction electrode shows increased capacity by greater than 100%. The capacity of electrodes made with a blend of hairy carbon black and plain carbon black was also improved. Capacity improvements due to hairy carbon, however, are larger for graphite powder than for carbon black. The difference in improvement is attributed to increased electrode surface area as well as conductivity on graphite powder whereas conductivity alone is increased for hairy carbon black. Hairy carbon is a new material. Its electrochemical behavior shows it to be attractive for electrode use. In addition to offering a variety of new materials for research by battery manufacturers, the improved electrochemical responses make hairy carbon desirable candidates for analytical electrodes, be they chemical or biomedical. Other potential applications include electronic thermal conductors and conductive composites.

ACKNOWLEDGMENTS

The authors would like to thank New York State Energy Research and Development Authority for funding this work and Professor Carl R. F. Lund of SUNY/Buffalo for technical assistance in hair growth.

REFERENCES

1. Tibbetts, G. G., Cryst, J., *Growth*, **66**, 632 (1984).

2. Tibbetts, G. G., DeVour, M. G., and Rodda, E. J., *Carbon*, **25**, 367 (1987).

3. Bradley, J. R., and Tibbetts, G. G., *Carbon*, **23**, 423 (1985).

4. Keep, C. W., Baker, R. T. K., and France, J. A., *Journal of Catalysis*, **47**, 232 (1977).

5. Baker, R. T. K., Barber, M. A., Harris, P. S., Feates, F. S., and Waite, R. J., *Journal of Catalysis*, **26**, 51 (1972).

6. Rostrup-Nielsen, J. R., *Journal of Catalysis*, **27**, 343 (1972).

7. Oberlin, A., Endo, M., and Koyama, T., *Journal of Crystal Growth*, **32**, 335 (1976).

8. Jackson, S. D., Thompson, S. J., and Webb, G., *Journal of Catalysis*, **70**, 249 (1981).

9. Audier, M., and Coulon, M., *Carbon*, **23**, 317 (1985).

10. Lobo, L. S., and Trimm, D. L., *Journal of Catalysis*, **29**, 15 (1973).

11. C. C. Liang, P. Krehl, D. A. Danner, *Journal of Applied Electrochemistry*, **11**, (1981) 563-571.

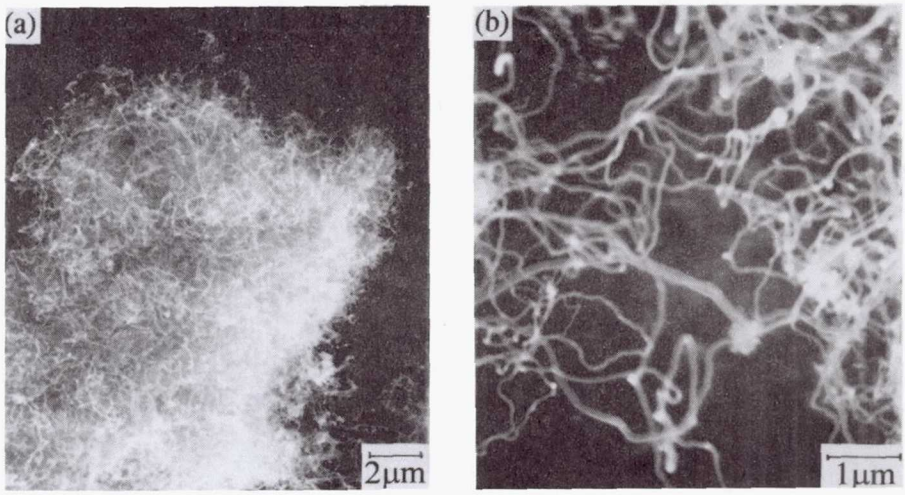

Figure 1 - Scanning electron photomicrographs of hairy carbon black. A portion of a cluster of hairy carbon black is shown in (a). The submicron nature of the hairs is readily observed in the higher magnification view in (b).

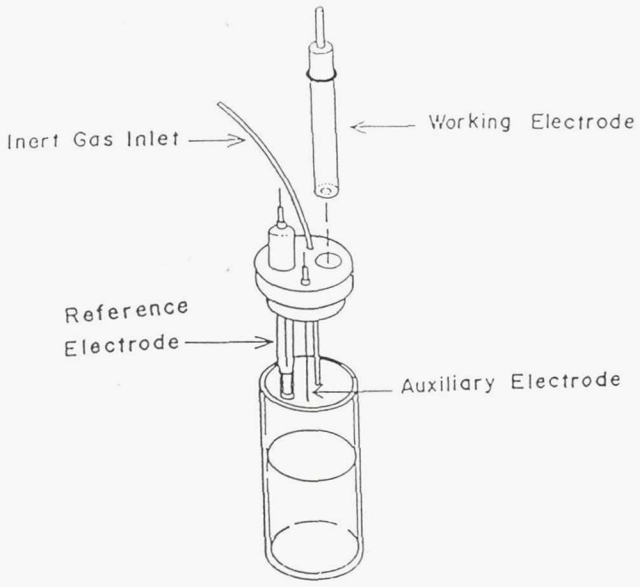

Figure 2 - The cyclic voltammetry cell used to study the Fe^{2+}/Fe^{3+} redox couple.

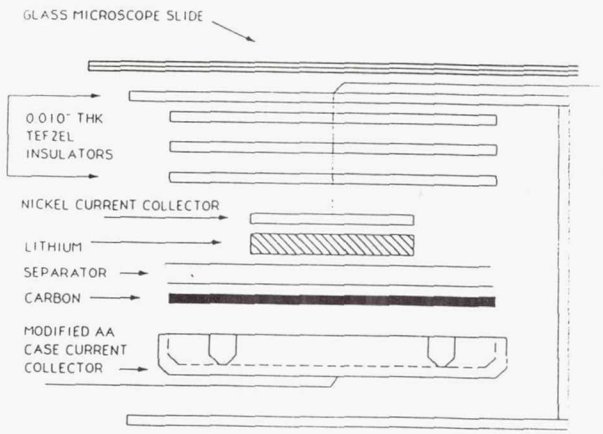

Figure 3 - Hairy carbon discharge test cell. Capacity comparisons were made by conducting plate to plate discharge testing.

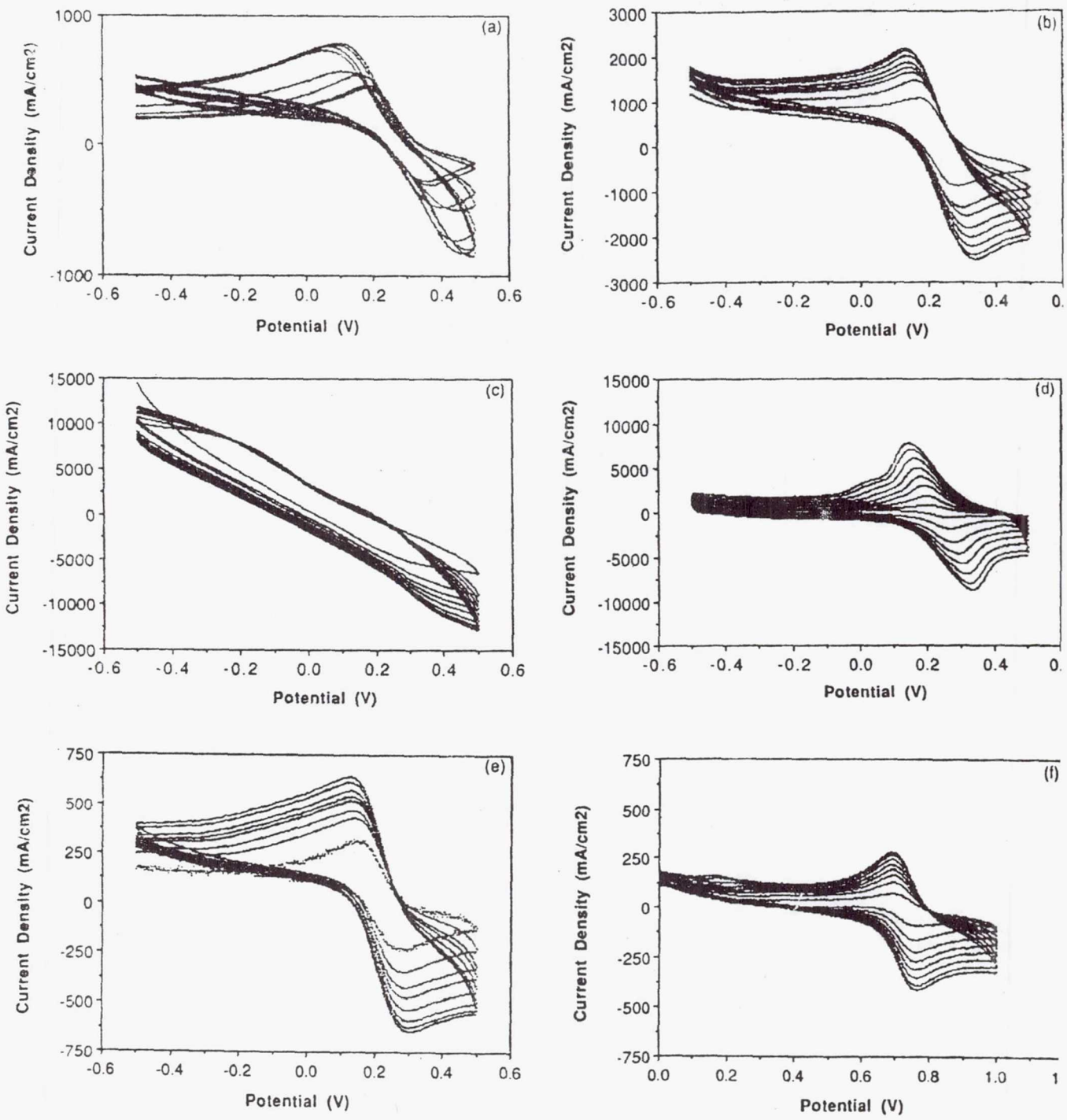

Figure 4 Cyclic voltammograms of plain versus hairy carbon substrates. Plain versus hairy graphite powder is compared in (a) and (b) respectively, plain versus hairy carbon black in (c) and (d) respectively, and plain versus hairy carbon fibers in (e) and (f) respectively.

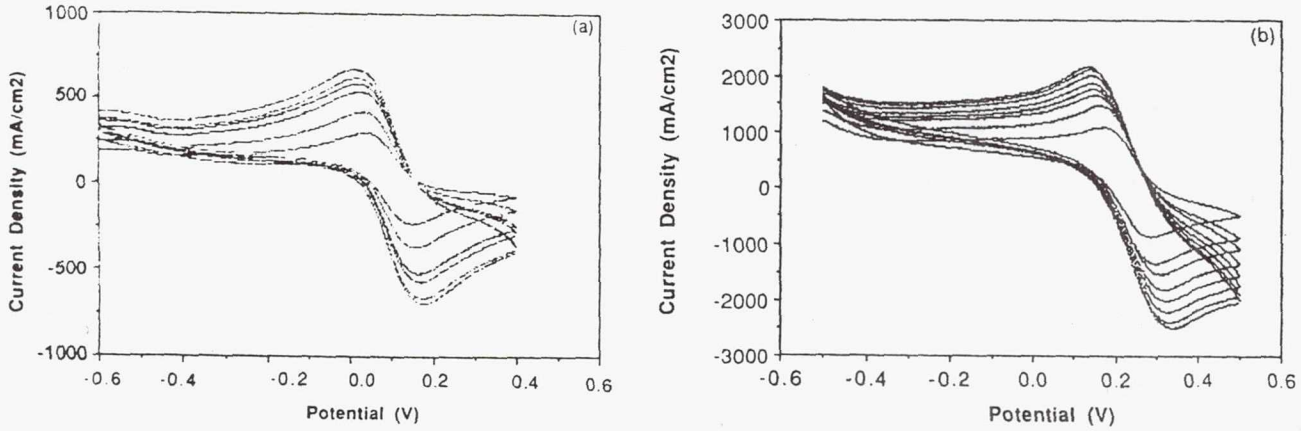

Figure 5 - Cyclic voltammetry comparison between conventional carbon paste using paraffin oil binder (a) and dry hairy graphite powder (b). The graphite powder for both (a) and (b) is the same except that the powder in (b) is hairy.

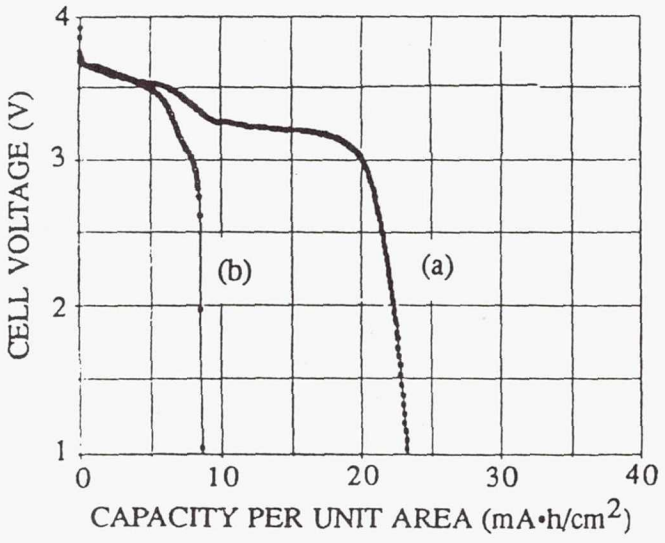

Figure 6 - Plate to plate discharge test results for (a) hairy and (b) plain graphite powder. The plain graphite powder is not used by battery manufacturers because of its low surface area.

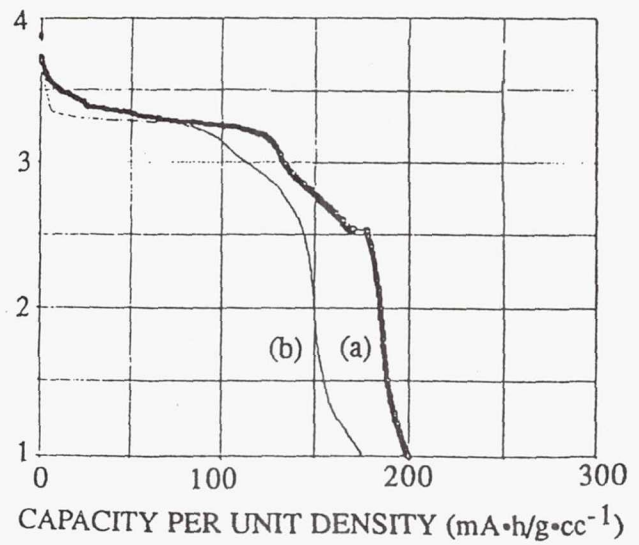

Figure 7 - Plate to plate discharge test results for (a) hairy and (b) plain carbon black. The hairy carbon black electrode is a 50:50 blend by weight of hairy carbon black with plain carbon black.

REPORT DOCUMENTATION PAGE

Form Approved
OMB No. 0704-0188

1. AGENCY USE ONLY (*Leave blank*)	2. REPORT DATE	3. REPORT TYPE AND DATES COVERED
	November 1993	Conference Publication

4. TITLE AND SUBTITLE

Space Electrochemical Research and Technology

5. FUNDING NUMBERS

WU–506–41–21

6. AUTHOR(S)

7. PERFORMING ORGANIZATION NAME(S) AND ADDRESS(ES)

National Aeronautics and Space Administration
Lewis Research Center
Cleveland, Ohio 44135–3191

8. PERFORMING ORGANIZATION REPORT NUMBER

E–8075

9. SPONSORING/MONITORING AGENCY NAME(S) AND ADDRESS(ES)

National Aeronautics and Space Administration
Washington, D.C. 20546–0001

10. SPONSORING/MONITORING AGENCY REPORT NUMBER

NASA CP–3228

11. SUPPLEMENTARY NOTES

Responsible person, Margaret A. Reid, (216) 433–5253.

12a. DISTRIBUTION/AVAILABILITY STATEMENT

Unclassified - Unlimited
Subject Categories 44 and 02

12b. DISTRIBUTION CODE

13. ABSTRACT ***(Maximum 200 words)***

This document contains the proceedings of NASA's fourth Space Electrochemical Research and Technology (SERT) Conference, held at the NASA Lewis Research Center on April 14–15, 1993. The objective of the conference was to assess the present status and general thrust of research and development in those areas of electrochemical technology required to enable NASA missions into the next century. The conference provided a forum for the exchange of ideas and opinions of those actively involved in the field, in order to define new opportunities for the application of electrochemical processes in future NASA missions. Papers were presented in three technical areas: advanced secondary batteries, fuel cells, and advanced concepts for space power. This document contains the papers presented.

14. SUBJECT TERMS

Electrochemistry; Batteries; Fuel cells

15. NUMBER OF PAGES

269

16. PRICE CODE

A12

17. SECURITY CLASSIFICATION OF REPORT	18. SECURITY CLASSIFICATION OF THIS PAGE	19. SECURITY CLASSIFICATION OF ABSTRACT	20. LIMITATION OF ABSTRACT
Unclassified	Unclassified	Unclassified	